Examining hydrogen trapping in steels by using advanced microscopy and modelling techniques

Pang-Yu Liu

THE UNIVERSITY OF SYDNEY

A thesis submitted in fulfilment of
the requirements for the degree of
Doctor of Philosophy

Supervised by:

Prof. Julie Cairney, Drs. Yi-Sheng (Eason) Chen, Patrick A. Burr, and Ranming Niu

School of Aerospace, Mechanical, and Mechatronic Engineering

Faculty of Engineering

The University of Sydney

Australia

12 December 2023

“All these people, all these things came into my life, and they're all blessings from God. And now that I look back, I realize that these are His fingerprints all over my story.”

Table of Contents

Acknowledgements

As I sit down to write these acknowledgments, a memory floods back—a memory from when I was just 11 years old, walking to elementary school. I can still picture the gray tiles beneath my feet, and I remember saying to myself, 'Hold on, it's only seven more years until I'm done with studying.' And now, fast forward to today, where I'm on the cusp of completing an extraordinary journey. 16 years later, not only did I earn my bachelor's degree, but I'm here submitting my doctoral thesis. This isn't about disliking learning—back then, I always ranked first. It's about the pressure I felt during those years, an overwhelming feeling that studying was too much. So, what brought about this transformation? Undoubtedly, it was the people who entered my life, becoming guiding lights and steadfast pillars of support. And as I stand here, ready to achieve this academic milestone, it's only right to express my gratitude and credit each of them.

Firstly, my heartfelt thanks go to Prof. Julie M. Cairney, my supervisor. Despite your busy schedule, your quick responses to my queries have been invaluable. Your support extended beyond research and shaped the way I approach problems. I'd also like to express my deep appreciation to my co-supervisor, Dr. Yi-Sheng (Eason) Chen. Your unwavering support and guidance have been instrumental in my growth. Thank you for bringing me into this fantastic research group and teaching me all I needed for my own research. A special acknowledgment goes to Dr. Patrick A. Burr, another co-supervisor. Your mentorship has honed my modelling skills. Your innovative thinking continues to inspire me. Lastly, to Dr. Ranming Niu, my final co-supervisor, thank you for your consistent advice and encouragement during this journey. I also want to extend my gratitude to every member of Julie’s research group. Your advice has been invaluable in completing my thesis.

A big thank you goes to the ACMM staff for their support and instrument training. Special thanks to Dr. Takanori Sato and Dr. Leigh Stephenson for their insightful guidance on atom probe experiments.

I'm grateful to Prof. Hung-Wei (Homer) Yen from National Taiwan University for welcoming me into his research group during my first PhD year. Thank you for supporting my thermal desorption experiment. To your group members, particularly Mr. Shao-Lun Lu and Ms. Yi-Shuan Sun, I've learned immensely from you.

My appreciation extends to Mr. Chih-Wei Sung from National Tsing Hua University, not only as a great roommate but also for our valuable scientific discussions. Best wishes for your own PhD journey.

To Prof. Hsin-Yi (Tiffany) Chen, you were the finest supervisor during my undergraduate years, inspiring me to pursue further education abroad. My gratitude also goes to Prof. Shun-Chi Wu, Prof. Tsan-Yao Chen, Prof. Fan-Yi Ouyang, Prof. Chien-Chun Chen, and Prof. Peng-Wei Chu from the Department of Engineering and Systems Science at National Tsing Hua University, Taiwan. Your suggestions and guidance have been invaluable.

Above all, I want to express my deep gratitude to my family. This achievement is a result of your unwavering support.

Statement

Candidate's statement

I hereby declare that this submission represents my work and that, based on my knowledge and belief, it does not include any materials that have been previously published by another person, nor does it contain materials that have been substantially accepted for the award of any other degree or diploma from this or any other institution of higher learning.

Some parts in this thesis are from either the published papers or the manuscripts being considered for publications in peer-reviewed journals, where I have significant contributions as detailed in the next section. In the cases where I am not the corresponding author of a published item or the person conducting the experiments, permission to include the results and figures has been granted by the related personnel.

Computational tools like ChatGPT were occasionally used only for language polishing. All the assistance received in preparing this thesis and sources have been acknowledged.

I certify that I understand if my candidature is successful, my thesis will be lodged with the University Libraries and made available for use.

_____(signature)
Pang-Yu Liu
12 December 2023

Lead supervisor's statement

This thesis is well presented to be examined and does not exceed the prescribed word limit.

As supervisor for the candidature upon which this thesis is based, I can confirm that the authorship attribution and other statements above are correct.

_____(signature)
Julie Cairney, Professor
12 December 2023

Related publications and author contributions

1) Hydrogen Trapping and Embrittlement in Metals – A Review
This manuscript related to Chapter 1 is under consideration at the ***International Journal of Hydrogen Energy***

Authors: Yi-Sheng Chen*, Chao Huang, **Pang-Yu Liu**, Hung-Wei Yen, Ranming Niu, Patrick Burr, Katie L. Moore, Emilio Martínez-Pañeda, Andrej Atrens, Julie Cairney*
*Corresponding authors: Yi-Sheng Chen (yi-sheng.chen@sydney.edu.au); Julie Cairney (julie.cairney@sydney.edu.au)

The content of this review article was mainly produced by the first author. As a co-author, my contribution was drafting the sections relating to the hydrogen embrittlement, hydrogen trapping, applications of atom probe tomography and density function theory for characterizing the behaviors of hydrogen in metals.

2) Atom probe tomography for the observation of hydrogen in materials: a review
This paper related to Chapter 1 and Chapter 2 has been published in ***Microscopy and Microanalysis***, Volume 29, Issue 1, February 2023, Pages 1–15, https://doi.org/10.1093/micmic/ozac005

Authors: Yi-Sheng Chen*[,+], **Pang-Yu Liu**[+], Ranming Niu, Arun Devaraj, Hung-Wei Yen, Ross K. W. Marceau, Julie M. Cairney
+ The authors contributed equally to this work
* Corresponding author: Yi-Sheng Chen (yi-sheng.chen@sydney.edu.au)

This review article was initially drafted by me and then significantly revised by Yi-Sheng-Chen, noting my co-first-author contribution.

3) Engineering metal-carbide hydrogen traps in steels
This manuscript related to Chapter 3 has been accepted by ***Nature Communications***.

Authors: **Pang-Yu Liu**[+], Boning Zhang[+], Ranming Niu[+], Shao-Lun Lu, Chao Huang, Maoqiu Wang, Fuyang Tian, Yong Mao, Tong Li, Patrick A. Burr, Hongzhou Lu, Aimin Guo, Hung-Wei Yen, Julie M. Cairney*, Hao Chen*, Yi-Sheng Chen*
+ The authors contribute equally to this work.
* Corresponding authors: Yi-Sheng Chen (yi-sheng.chen@sydney.edu.au); Hao Chen (hao.chen@mail.tsinghua.edu.cn); Julie Cairney (julie.cairney@sydney.edu.au)

This original research article has my contribution in conducting experiments, analyzing data, writing the first draft, presenting data and drafting the responses to reviewer comments.

4) Hydrogen-enhanced deformation in pearlite
This manuscript related to Chapter 4 is under consideration at ***Acta Materialia***.

Authors: Ranming Niu[+], Hanyu Li[+], **Pang-Yu Liu**[+], Patrick Burr, Yi Feng, Hung-Wei Yen, Mintu Ma, Aimin Guo, Hongzhou Lu*, Yi-Sheng Chen*, Julie M. Cairney*
+ The authors contribute equally to this work.
* Corresponding authors: Julie Cairney (julie.cairney@sydey.edu.au); Yi-Sheng Chen (yi-sheng.chen@sydney.edu.au); Hongzhou Lu (luhz@citic.com)

This original research article has my co-first-author contribution in conducting theoretical simulations, measuring hydrogen content, supporting atom probe tomography experiment, and drafting manuscript.

5) A computationally efficient method to address the gap between dilute and concentrated calculations

This manuscript related to Chapter 5 is under consideration at ***Computational Materials Science***.

Authors: **Pang-Yu Liu***, Julie M. Cairney, Yi-Shen Chen*, Patrick A. Burr*
*Corresponding authors: Pang-Yu Liu (pang-yu.liu@sydney.edu.au); Yi-Sheng Chen (yi-sheng.chen@sydney.edu.au); Patrick A. Burr (p.burr@unsw.edu.au)

This original research article includes my sole first-author contribution in conceptualization, conducting simulations, analyzing data, presenting data, and drafting manuscript.

Abstract

The presence of hydrogen in high-strength steels leads to hydrogen embrittlement (HE), causing premature cracking and posing challenges for hydrogen infrastructure amid the global push for decarbonization. With hydrogen crucial for net-zero emissions, addressing HE is imperative for a secure and environmentally sound hydrogen economy. One strategy involves introducing hydrogen traps into alloy microstructures, limiting HE. While promising, a comprehensive atomic-scale understanding is vital. This study combines advanced microscopy and modeling to investigate hydrogen distribution in steel microstructures. A difference in trapping mechanisms is observed between titanium carbide (TiC) ferritic steel and Ti(Mo)C, formed with the addition of a small amount of Molybdenum. Findings highlight the importance of additional carbon vacancies in Ti(Mo)C, enabling hydrogen transit within the carbide's interior.

Beyond investigating hydrogen trapping within steel precipitates, this study explores hydrogen interactions with pearlitic steel, crucial for steel gas pipes. Hydrogen shows a predilection for the interior regions of ferrite and cementite phases in pearlite, but does not accumulate at interfaces, a different result to what had been predicted in the literature. This complex interplay underscores the significance of understanding hydrogen behavior in steel microstructures.

Atomic-scale simulations are now standard for theoretical understanding, covering defect concentrations. However, addressing intermediate concentrations is challenging. To overcome this, a computationally streamlined approach, inspired by cluster expansion and ensemble statistics techniques, bridges the gap, offering an effective means to tackle complexities associated with intermediate concentration levels. This innovation is crucial for designing HE-resistant alloys and creating safer materials in the hydrogen era, aligning with global net-zero targets.

Chapter 1 - Literature review

Hydrogen (H), the simplest and the most abundant element in the universe, can be used to store, transport, and deliver energy. The hydrogen molecule (H_2) has an energy density of 120 MJ/kg which is 3 times higher than that of gasoline and is the highest among all known fuels [1]. Hydrogen already plays an essential role in chemical processing [1], but recent years have seen a dramatic increase in its use in emerging energy technologies.

Hydrogen electrolysis and hydrogen fuel cells consume and produce electricity on demand, thus providing a load-demand management service to intermittent renewable energy grids. Hydrogen fuel can be used for combustion and electrification and is free of intrinsic carbon emission. It can hence facilitate the decarbonization of the transportation sector, which currently depends heavily on fossil fuels. Hydrogen can also be used as a reductant or fuel to decarbonize hard-to-abate high-emission sectors such as steelmaking [2–4].

It is possible to produce hydrogen at scale from a variety of sources, including natural gas, coal, biomass, waste plastics, water electrolysis [5], and nuclear power [6]. The production methods having carbon footprint may be combined with carbon capture and storage technologies to reduce the embodied carbon emissions of hydrogen production [1]. Hydrogen is being increasingly considered as an essential commodity to replace fossil fuels in a future decarbonized society [1,5]. Worldwide, national and international initiatives are underway to develop a 'hydrogen economy', including in the USA [5,7], Japan [8], UK [9], Germany [10], Norway [11], Canada [12], China [13], and Australia [14]. Many challenges must be addressed to enable this vision. Hydrogen is flammable in air at a concentration above the lower explosive limit [15] and requires careful handling [1]. Moreover, hydrogen can degrade metallic materials significantly, reducing their fracture toughness, fatigue resistance and ductility in a phenomenon referred to as hydrogen embrittlement (HE).

HE is one of the biggest obstacles for the deployment of hydrogen energy infrastructure. This includes the repurposing of natural gas pipelines for the transport of gaseous hydrogen [5,9,12,14,16–19]. Failure of energy infrastructure due to HE could lead to life-threatening accidents – just one major incident could cause a setback in the worldwide application of hydrogen for decarbonization [20–22]. In fact, a recent Australian national survey has indicated that safety is the most important

factor in determining people's willingness to use hydrogen [23]. On a 5-point scale where 5 signifies the highest level of importance, the safety of using hydrogen received an average rating of 4.5 from 906 respondents, which is highest among the considered factors including reliability (4.27), cost (4.18), and convenience (3.64). As such, HE is a major challenge for delivering public acceptance. Beyond the energy sector, HE is an ongoing issue for the use of high-strength materials in defense, transport, energy, and construction [24–26].

Although HE is a longstanding industrial problem, improved characterization and modelling tools have yielded new perspectives in recent years, including potential mitigation approaches based on microstructural hydrogen trapping.

1.1 Hydrogen embrittlement

Hydrogen can embrittle metals and alloys, a phenomenon that was first reported almost 150 years ago. In 1875, Johnson [27] found significant decreases in the breaking strain of steel and iron specimens after immersion in hydrogen-bearing solutions. This mechanical degradation was recovered after the hydrogen was fully desorbed, demonstrating that this degradation was a result of hydrogen uptake. Johnson also found that HE in higher-strength specimens was more significant than for those with similar compositions but with lower strength. Since this report, over 38,000 papers have been published on the subject [28], reflecting the engineering importance, multidisciplinary nature, and high complexity of HE. Many review articles have provided a depiction of the HE phenomena and some understanding of the mechanistic causes [16,26,29–59].

Before going into detail, it is necessary to distinguish between internal hydrogen embrittlement (IHE) and environmental hydrogen embrittlement (EHE). IHE refers to hydrogen-induced failure caused by the presence of pre-existing hydrogen and is typically limited by hydrogen supply. EHE is the response of the material to hydrogen when a specimen is subject to a mechanical load with simultaneous hydrogen charging. For EHE, the extent of hydrogen uptake depends on the charging time and the hydrogen diffusivity of the material. EHE failure typically initiates at the specimen surface, where environmental effects are most severe.

1.1.1 Variables and metrics

Hydrogen content

HE only occurs when a specimen is subjected to a sufficiently high stress or stress intensity factor (either applied or residual) and contains a hydrogen content above a critical level. The exact critical stress and hydrogen content depend on the type of alloy. Metals that require energy to absorb hydrogen (i.e., endothermic hydrogen solution), such as Fe and Ni, have low hydrogen solubility at ambient temperatures and pressures. These metals generally have a low critical hydrogen content, as low as parts per million in weight (wt. ppm, wppm, or mg/g). **Figure 1-1**A shows the ultimate tensile strength (UTS) of a martensitic steel as a function of hydrogen content, which shows that only 5 wt. ppm of hydrogen significantly reduces the UTS, but that less than 1 wt. ppm has little influence [60]. The hydrogen contents in this figure were measured using hydrogen thermal desorption analysis (TDA) [61] and the notched UTS was determined by using a slow strain rate tensile test (SSRT) on ex-situ electrolytically hydrogen-charged specimens [45]. **Figure 1-1**A shows that hydrogen-induced fracture for hydrogen concentrations above 7 wt. ppm occurred at a stress 20% of the UTS in air. **Figure 1-1**B shows the threshold stress intensity factor (K_{TH}) versus diffusible hydrogen content for a martensitic steel (AerMet 100) [62], showing decreased K_{TH} with increasing hydrogen content.

The service environment determines the hydrogen content in a particular material, and the measured HE susceptibility of the material may be low if that environment causes a hydrogen content that is below the critical value for that material. For example, the advanced high-strength steel of **Figure 1-1**A is unlikely to experience HE in automotive applications because the hydrogen concentration in service is generally lower than 1 wt. ppm [63]. Note also that hydrogen uptake is sensitive to the mechanical stress state, as the solubility depends on the hydrostatic stress [64,65].

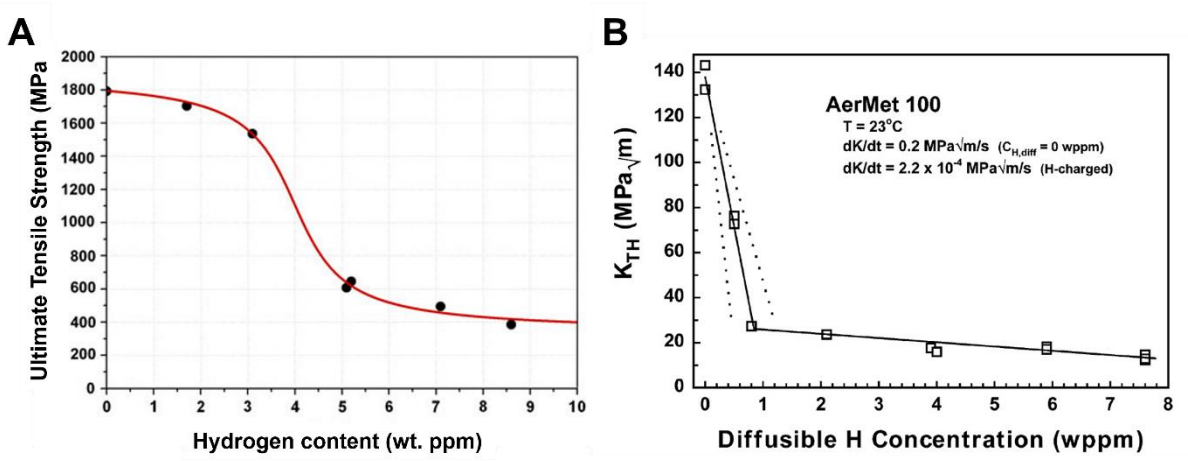

Figure 1-1. Hydrogen content in common metals and HE susceptibility. (A) The material notch strength (defined by ultimate tensile strength) of a hydrogen-charged untempered martensitic steel decreased with increasing hydrogen content, reaching low values for hydrogen contents above 5 wt. ppm, reproduced from [60]. (B) The threshold stress intensity factor (K_{TH}) decreased with increasing diffusible hydrogen content for a AerMet 100 martensitic steel in the near peak aged condition with 1765 MPa yield strength. Hydrogen was charged with increasing cathodic potential to produce an increasing hydrogen concentration. Reproduced from [62]

Mechanical properties

HE can reduce alloy strength and/or ductility in tensile tests. **Figure 1-2**A and B provide examples of decreases of UTS and elongation. Commonly used metrics for HE susceptibility for tensile type specimens are strength and ductility loss are:

$$Strength\ loss\ index = \frac{\sigma_{ref}-\sigma_H}{\sigma_{ref}} \qquad (1\text{-}1)$$

$$Ductility\ loss\ index = \frac{RA_{ref}-RA_H}{RA_{ref}} \qquad (1\text{-}2)$$

where σ_H (or RA_H) is the strength (reduction in area) in hydrogen and σ_{ref} (RA_{ref}) is the strength in a hydrogen-free condition (typically air or inert gases). Increased susceptibility to HE is manifested by a lower strength σ_H or reduced ductility RA_H in hydrogen, and a larger value for the strength or ductility loss index. HE may also cause faster fatigue crack growth. This is shown in **Figure 1-2**C for an austenitic steel with and without hydrogen charging, which required around half the number of cycles in the presence of hydrogen to reach the same crack length [66]. Strength and ductility loss indices are used throughout this paper to compare HE susceptibility, although we note issues with their suitability as HE metrics when the applied stress intensity factor is greater than the threshold stress intensity factor, which can lead to sub-critical crack growth [67–70].

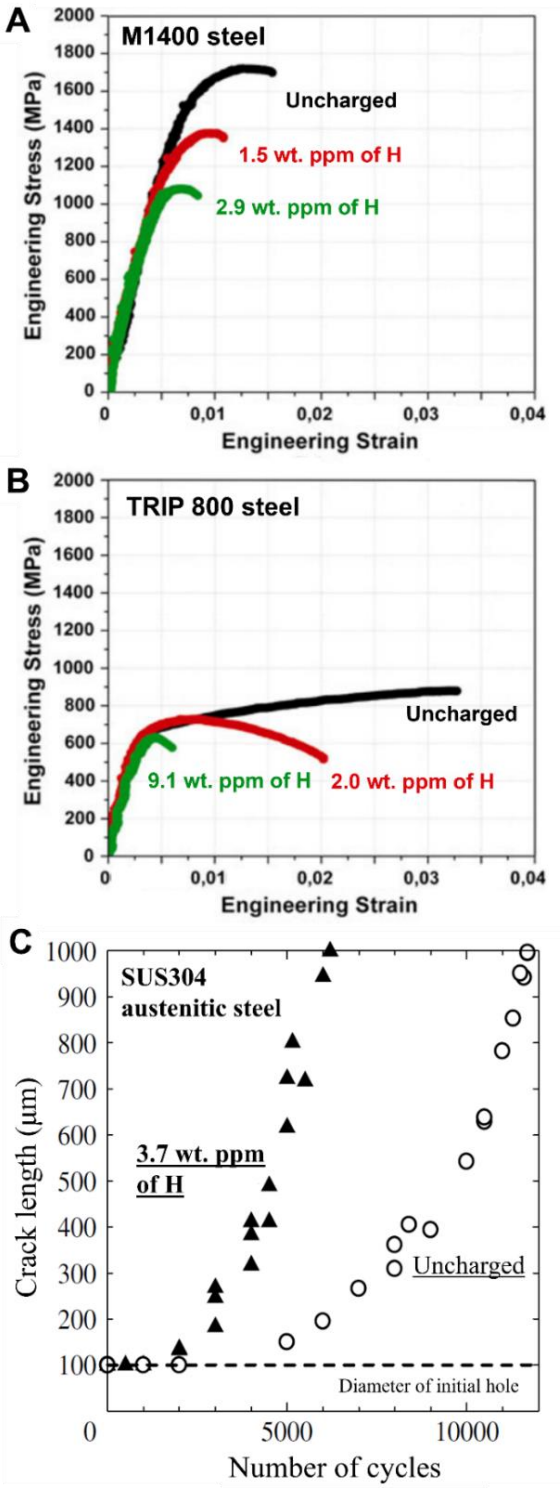

Figure 1-2. The effect of HE on strength, ductility, and fatigue resistance. HE of (A) M1400 martensitic steel and (B) TRIP 800 ferritic/bainitic/austenitic showing reduction of UTS and elongation, respectively, characterized by slow strain rate test. The samples were ex-situ charged with hydrogen and the hydrogen content measured by thermal desorption analysis. (A) and (B) are reproduced from [60]. (C) HE of a SUS304 austenitic steel manifested by constant-loading fatigue test. The mechanical loading was applied at an amplitude of 280 MPa in both tension and compression and a frequency of 1.2 Hz. (C) is reproduced from [66].

HE can also manifest as hydrogen-induced delayed fracture, which can be characterized by the time-to-fracture of a U-bend test under constant loading, where the time-to-fracture decreases with increasing hydrogen content, stress, and/or strain [71,72]. A threshold time-to-fracture is generally defined (e.g., 300 hours in the case of **Figure 1-3**A) with a given bending radius (R in the insert figure), and this information informs the time required for manufacturing the high-strength steel products in the automotive industry. The U-bend test is able to establish a HE fracture map as shown in **Figure 1-3**B, offering a guide for the manufacturing conditions that would avoid HE. This is useful for material suppliers and manufacturers to enhance product reliability and manufacturability. These tests that load the specimen below the UTS (hence without immediate failure) indicate that the presence of hydrogen can decrease the threshold stress intensity factor required for crack growth or cause sub-critical cracking at certain stress conditions [31,42,43,55,73]. This type of HE can occur at approximately half of the yield stress with crack velocities up to 10^{-4} m/s [55,73].

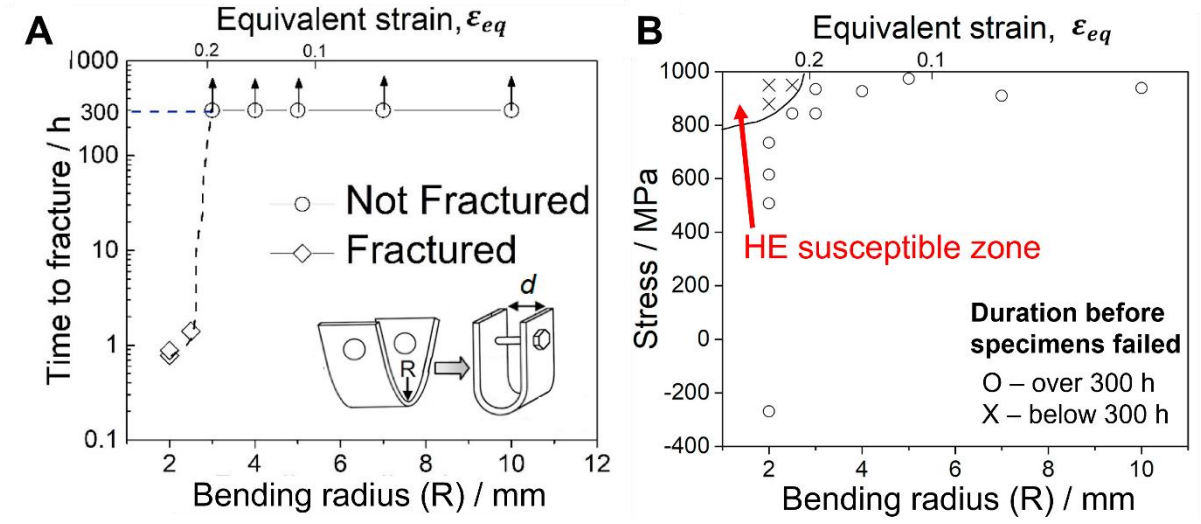

Figure 1-3. U-bend test for characterizing H-induced fracture. (A) Time-to-fracture as a function of strain using a 300-hour up limit. (B) Stress-strain HE fracture map with the stress evaluated by either X-ray measurement or finite element calculation. Reproduced from [71]

The effects of hydrogen on alloys are not always detrimental. Exposure to hydrogen occasionally results in an increase in yield strength and ductility, particularly in the materials with relatively hydrogen-soluble matrix such as face-centered cubic (FCC) iron. An example is shown in **Figure 1-4**A for an annealed commercial stable Fe-24Cr-19Ni-0.02C austenitic FCC steel [74]. **Figure 1-4**B shows

that the fracture surfaces were cup and cone, consistent with ductile dimple rupture (see the next section for the discussion of fracture mode). Higher hydrogen levels led to smaller dimples, indicating that hydrogen facilitated ductile fracture. This hydrogen-induced strengthening was attributed to solid-solution strengthening, and the increase in ductility was attributed to the facilitation of mechanical twinning by the hydrogen in solution in the austenite [74,75].

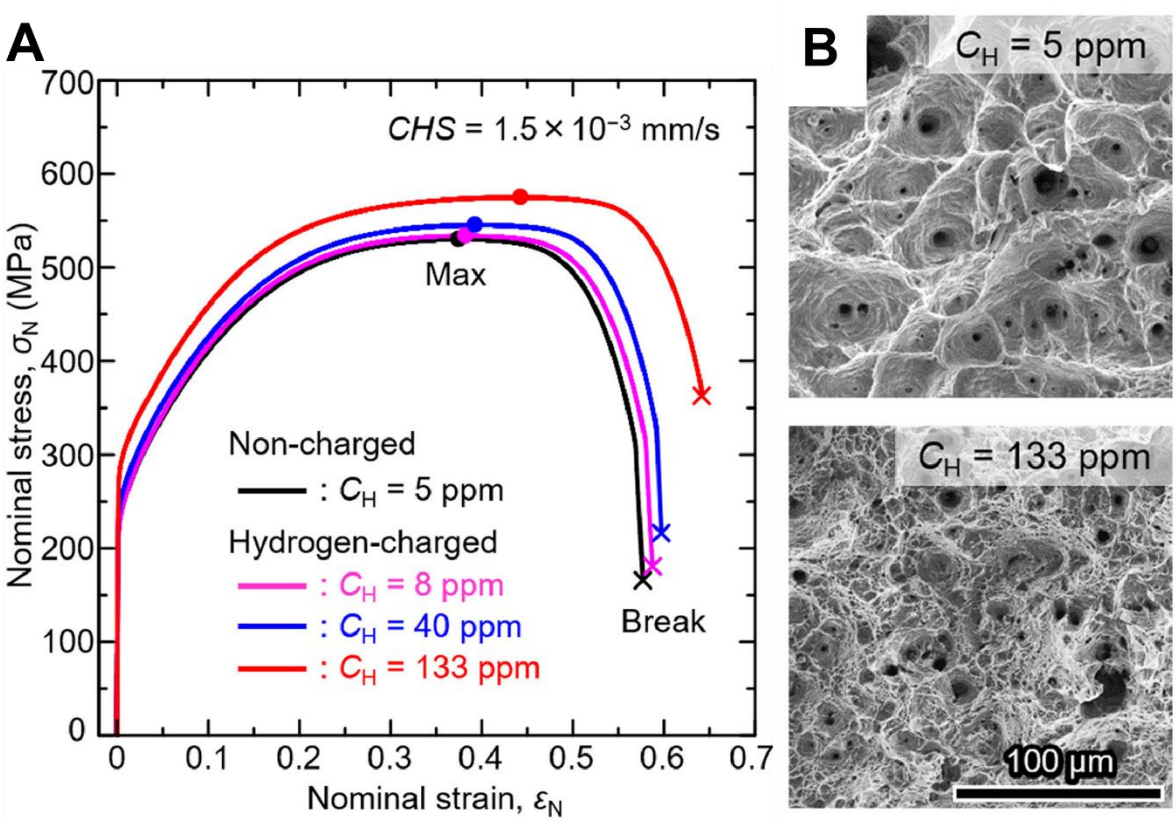

Figure 1-4. Hydrogen-induced strengthening and enhanced ductility in an austenitic steel. (A) Stress-strain curves for an annealed, stable commercial Fe-24Cr-19Ni-0.02C austenitic steel with hydrogen concentrations from 5 wt. ppm to 133 wt. ppm, showing that both strength and ductility increased with increasing hydrogen content. (B) The fractography indicates cup and cone fracture. The fracture in the specimen with more hydrogen has a smaller dimple size, indicating that hydrogen facilitated the ductile dimple rupture fracture mechanism. Reproduced from [74]

Hydrogen has even been proposed as a temporary alloying element to increase the formability of Ti alloys [76,77]. The Ti alloy is held at a relatively high temperature in hydrogen. The absorbed hydrogen induces a phase transformation from α-Ti (hexagonal close-packed, HCP) to more ductile β-Ti (body-center cubic, BCC). The Ti alloy is then mechanically worked at a high temperature and

subsequently, the hydrogen is removed by exposure to a low hydrogen fugacity (in a vacuum or an inert gas).

Fracture mode

The fracture modes of embrittled alloys are normally characterized by taking scanning electron microscope (SEM) images of the fracture surface from above (i.e., fractography) or in cross-section. Examples are presented in **Figure 1-5**A (top view) and B (cross-section), respectively, showing a hydrogen-induced intergranular fracture along prior-austenite grain boundaries (GBs) in a tempered martensitic steel [31]. Best practice for the examination of fracture surfaces requires observations at a tilted angle and at a high resolution so that critical but subtle HE features can be properly captured and correctly linked with associated mechanisms, as detailed in Section 0 [30,31]. For example, **Figure 1-5**C provides a low-magnification image that may be considered as a manifestation of brittle fracture; however, a high-resolution image from the same specimen indicated the presence of fine dimples, as shown in **Figure 1-5**D, indicating some plastic deformation during the hydrogen-induced fracture [78]. HE typically causes a macroscopic loss of ductility; nevertheless, there are many microscopic fracture modes, including voiding, brittle fracture, and transgranular quasi-cleavage with micro-ridges as shown in **Figure 1-5**E and F [79]. For ductile fracture, as shown in **Figure 1-6**A (H-charged) and B (H-free), increased density of dimples in HE-affected specimens indicates that hydrogen facilitates micro-void nucleation and growth.

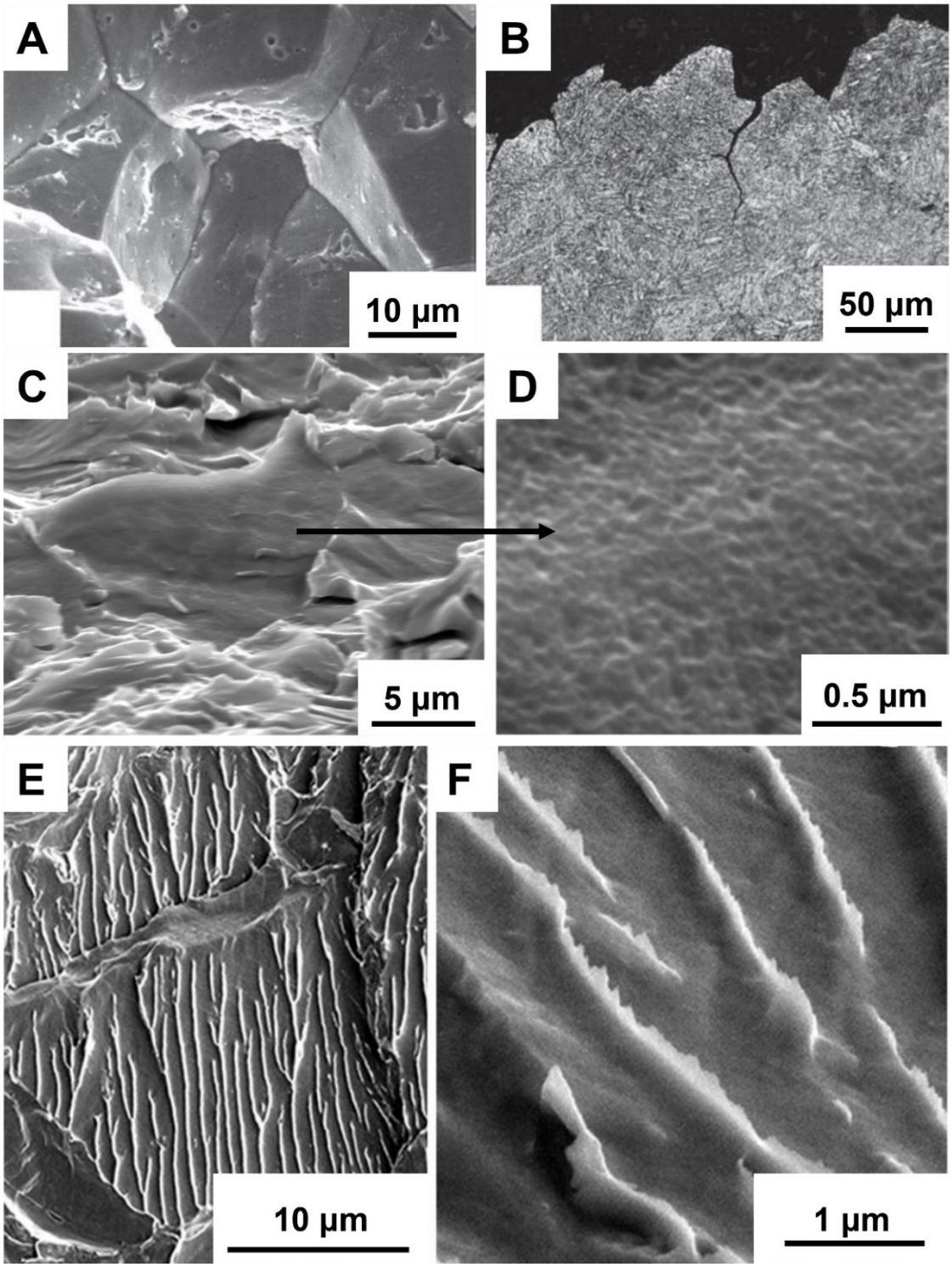

Figure 1-5. Fractography of hydrogen-induced macroscopically brittle fractures. (A) and (B) SEM surface and cross-sectional images of a hydrogen-embrittled tempered martensitic steel, showing mainly intergranular failure due to HE. Source: [31]. (C) and (D) low- and high-magnification SEM images of a hydrogen-embrittled API X60 pipeline steel, showing how tilting and high-resolution imaging reveals dimples on the fracture surface. Source: [66]. (E) and (F) low- and high-magnification SEM images of a hydrogen-embrittled API X60 pipeline steel specimen, showing the quasi-cleavage fracture surface and its micro-ridges. Source: [79]

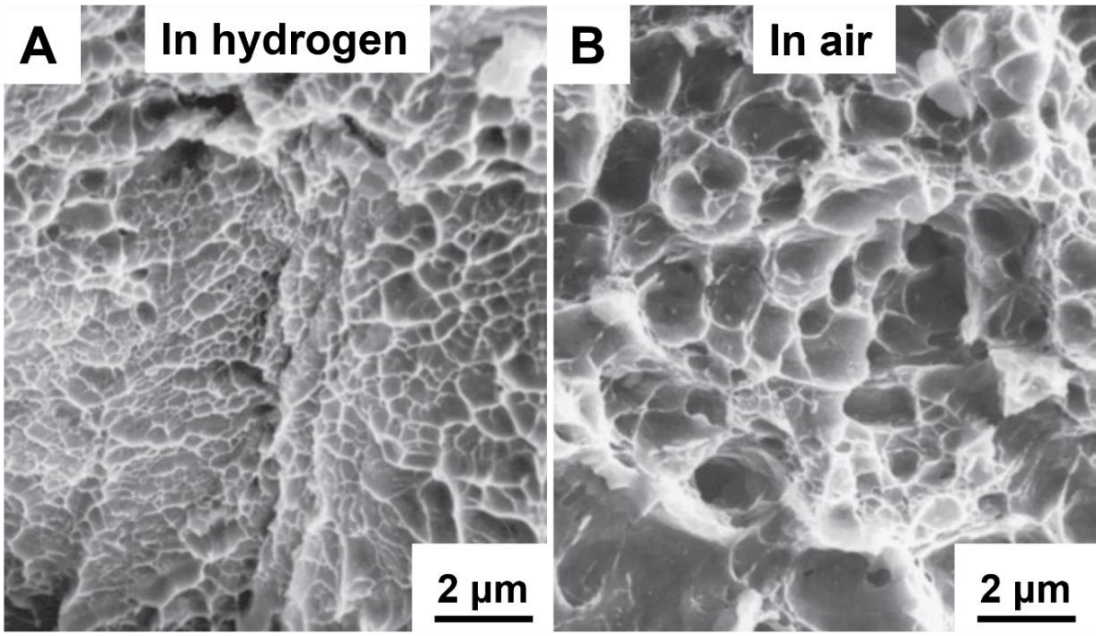

Figure 1-6. Fractography of ductile fracture. SEM images of fracture surface morphologies from martensitic steel specimens tested in (A) gaseous hydrogen environment and (B) air. Changes in the dimple size indicate that hydrogen facilitates micro-void nucleation. Reproduced from [31]

Temperature and strain rate

HE susceptibility depends on temperature and is typically most severe at close to ambient temperature, as shown in **Figure 1-7** [80]. This influence of temperature can be correlated with the kinetics of hydrogen diffusion and transport toward susceptible areas in the material microstructure [80,81]. At a low temperature, hydrogen does not have sufficient mobility to reach the critical locations to facilitate the diffusion-controlled HE mechanisms that lead to fracture, although HE can still take place through a mechanism that does not require hydrogen diffusion (such as grain boundary decohesion) [82]. At a high temperature, hydrogen is too mobile to be pinned by dislocations, and the material is too ductile. Similar to temperature, the kinetics of hydrogen movement can result in varied HE susceptibility at different strain rates. **Figure 1-8**A shows that, in the presence of hydrogen, the UTS and the elongation (ductility) of a martensitic steel were lower (more susceptible to hydrogen) at low strain rates [83]. Fractographic analysis (**Figure 1-8**B) indicated a higher fraction of the embrittled (intergranular) characteristics at lower strain rates.

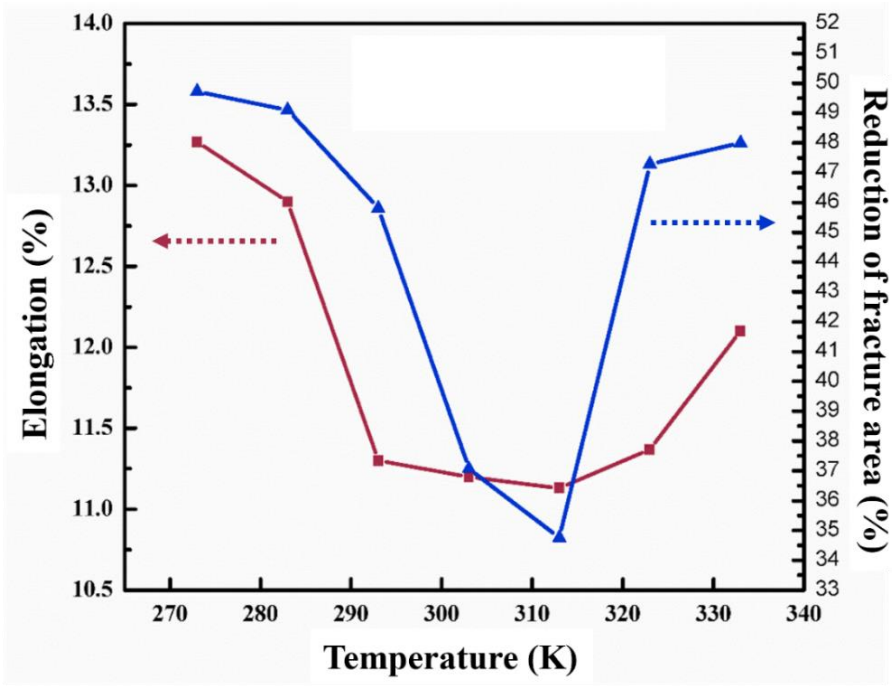

Figure 1-7. Temperature window for HE. The extent of HE of hydrogen-charged ferritic/bainitic X90 pipeline steel specimens in terms of the reductions of elongation (red) and fracture area (blue). The HE reaches a maximum (300-320 K) close to room temperature (293 K). The elongation and the fracture-area reduction were measured using slow strain rate tests with continuous hydrogen charging as loading applied. Reproduced from [80]

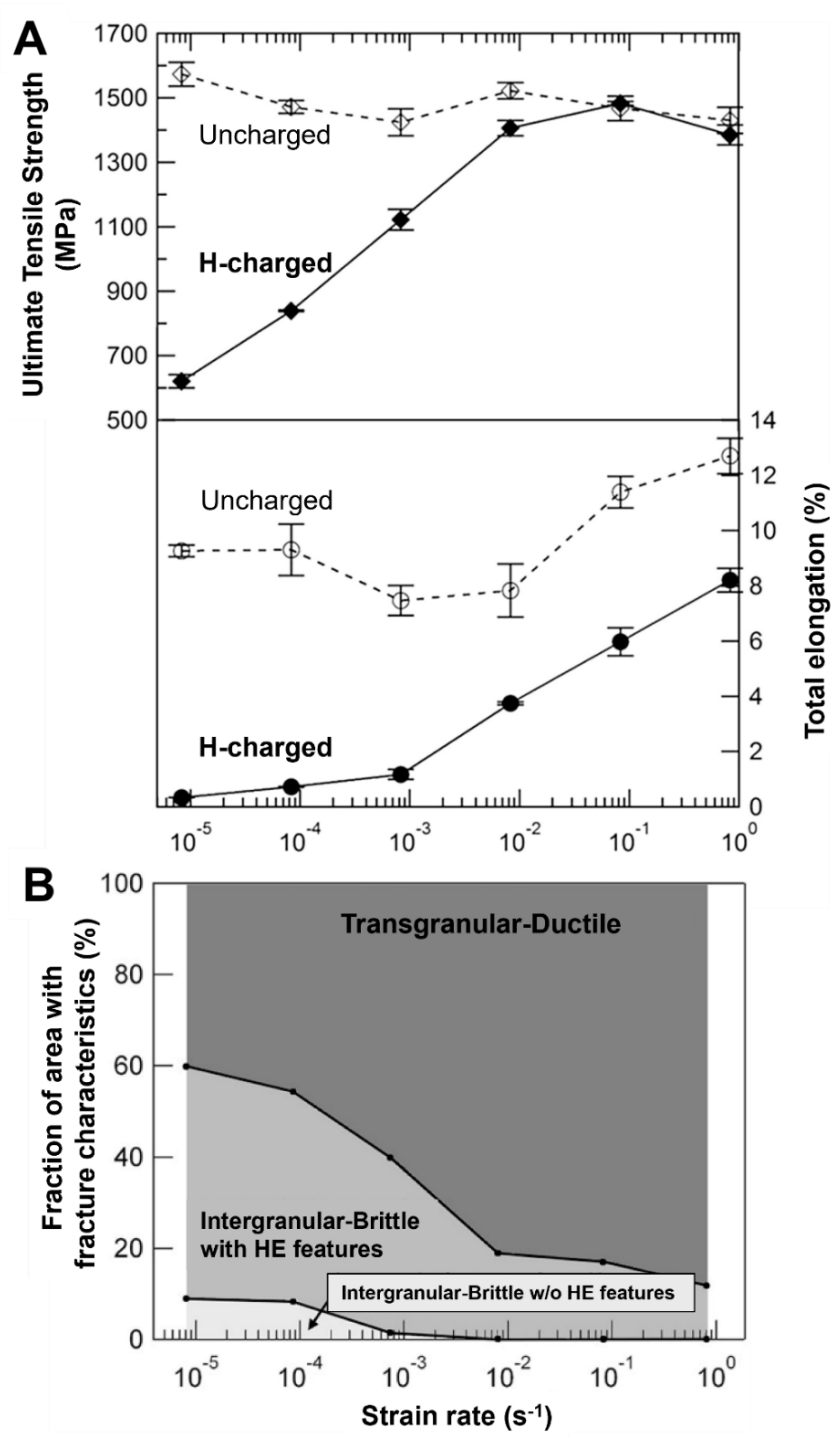

Figure 1-8. The effect of strain rate on HE. (A) The UTS and the elongation of hydrogen-charged and uncharged low-carbon martensitic steel specimens decreased with decreasing strain rate in uniaxial tensile tests, showing HE is more significant at lower strain rates. (B) Fractographic analysis of the specimens in (A) showing the surface area fraction of ductile and brittle features, indicating a change from transgranular-ductile to intergranular-brittle fracture with decreasing strain rate. Reproduced from [83]

Strength

As a rule-of-thumb within a class of alloys, the alloys with higher strength are generally more susceptible to HE [31,35]. As such, extreme care should be taken when considering the use of steel with a strength greater than 1 giga pascal (GPa) in a hydrogen-containing environment. This strength-susceptibility relationship can be attributed to higher stresses (and thus hydrogen concentrations) attained in the fracture region [58,84,85], and by the strong interaction of hydrogen with crystal defects such as dislocations and GBs, which largely determine the strength of the material [29–31,36,50,86–89]. Correlations of EHE susceptibility with dislocation density and grain size, for a wide range of bainitic and martensitic steels with similar strengths, are shown in **Figure 1-9**A and B, respectively.

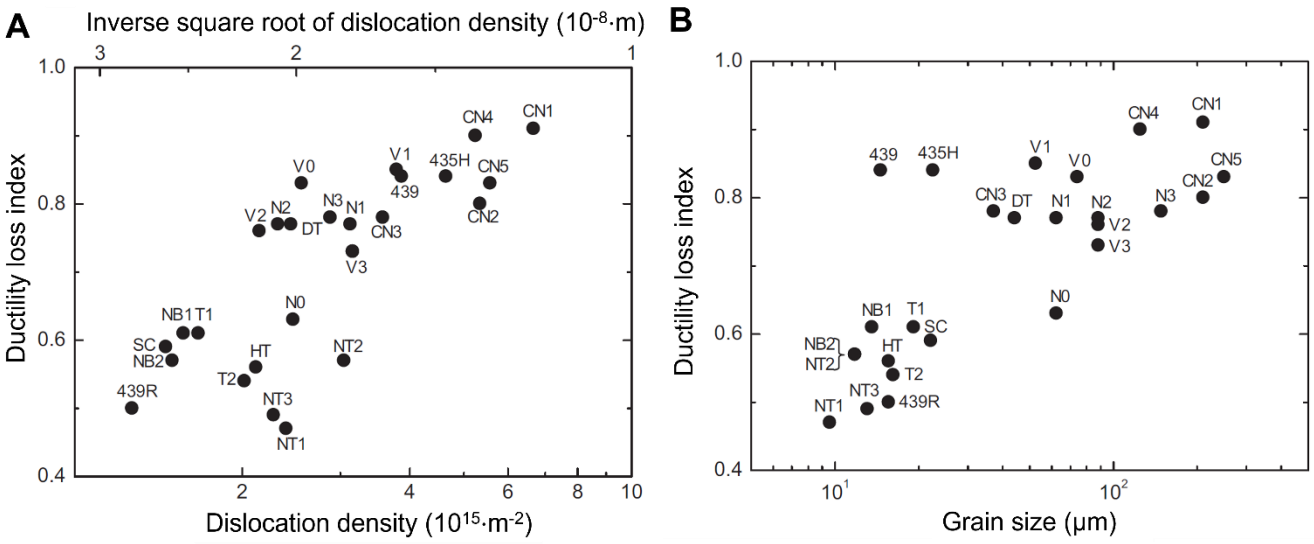

Figure 1-9. Dislocation and grain size vs. environmental hydrogen embrittlement susceptibility. Ductility loss index (HE susceptibility) as a function of (A) dislocation density and (B) grain size in a range of bainitic and martensitic steels with similar strengths (853-1142 MPa). The ductility differences were measured by comparing the SSRT results in a gaseous hydrogen environment of 45 MPa and in air. Reproduced from [90]

1.1.2 Hydrogen embrittlement mechanisms

Many mechanisms have been proposed to explain HE, based on the macro- and microscale evidence, but agreement has not been reached on a universally applicable mechanism. The mechanisms most commonly used to explain hydrogen-induced sub-critical crack growth are discussed below and in [29–32,40]. These mechanistic interpretations are used to build predictive models and to provide a post-experiment rationalization of the results, particularly for fractography [70,91–93]. In recent years

it has become increasingly accepted that several mechanisms may operate simultaneously. [29–31,56,94].

Hydride formation

Westlake proposed in 1969 [95] that HE was the result of brittle hydride formation. This HE mechanism is most relevant to alloy systems that have a high tendency to form hydrides such as Zr [41,96,97], Nb [98], Ti [35,78,99], and Mg [38,100,101]. Hydrogen is an interstitial solute in the metal lattice and can rapidly diffuse and segregate to the zone of high hydrostatic stress at the crack tip (**Figure 1-10**A). Hydrides form when the hydrogen content exceeds the solubility (**Figure 1-10**B), and cleavage of the brittle hydride subsequently occurs along the preferred crystallographic direction of hydride formation (**Figure 1-10**C). The crack is arrested when it meets the ductile matrix (**Figure 1-10**C), and another round of this sequence begins. Crack propagation can be further facilitated by the presence of pre-existing hydrides within the microstructure along the crack path. For non-hydride forming alloys such as Fe or Ni, theoretical models have attempted to relate their transgranular and intergranular failures of HE with the presence of hydrides [102–105]. However, hydride formation at ambient temperature in these alloy systems requires extremely high hydrogen fugacities (e.g., 3.5 GPa for iron [106]), which are unlikely to be relevant in most in-service conditions.

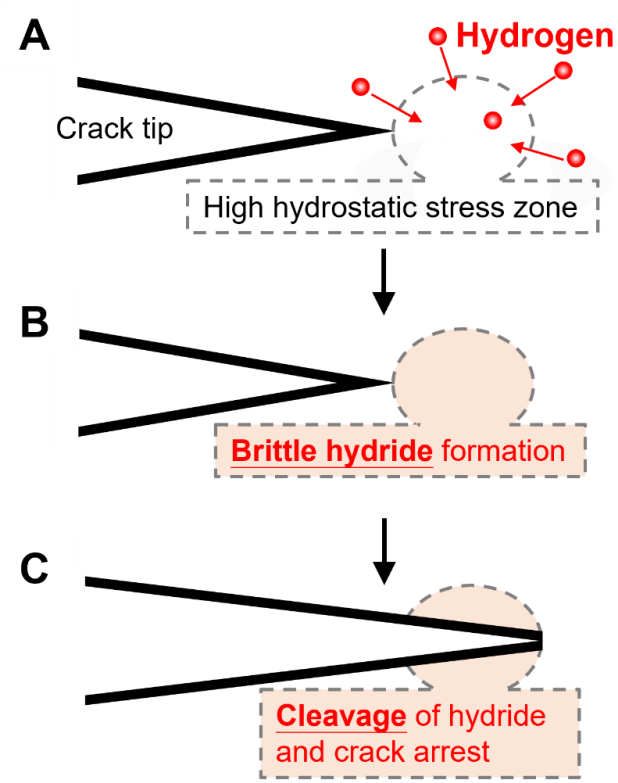

Figure 1-10. Schematic of hydride-induced hydrogen cracking mechanism for sub-critical crack growth

Hydrogen-enhanced decohesion

In the 1960s and 1970s, Troiano and Oriani proposed the hydrogen-enhanced decohesion (HEDE) theory, which postulates that hydrogen can directly reduce the cohesive strength of the atomic bonds in the metal lattice, leading to brittle fracture, as illustrated in **Figure 1-11**A [107,108]. While earlier atomistic studies suggested reductions in fracture energy and cohesive strength of up to 90% [109,110], recent studies suggest that any reduction is limited to 20-40% [111–113]. Given that the lattice / grain boundary strength is roughly 10 times of the yield stress across a broad temperature range (as the material systems and measurement methods varied), a 20-40% reduction in the cohesive strength is insufficient to trigger decohesion in the context of conventional continuum theories [114]. However, theoretical predictions that account for the role of geometrically necessary dislocations and plastic strain gradients lead to much higher stresses and hydrogen levels at the crack tip [115,116], providing a modern mechanistic rationale for HEDE.

HEDE is most widely accepted in the context of inducing intergranular failure (**Figure 1-11**B) or phase-boundary failure (**Figure 1-11**C) [115,117,118], particularly

for high-strength materials [33,119–123]. Atomistic modeling suggests that the presence of more than one atomic layer of solute segregation can lead to a higher degree of cohesive strength reduction [117]. Experimental evidence of HEDE includes the intergranular failure observed in a hydrogen-charged Ni alloy tested at a cryogenic temperature, where hydrogen-dislocation interactions are effectively suppressed, suggesting that hydrogen-induced GB decohesion is responsible for the HE [82].

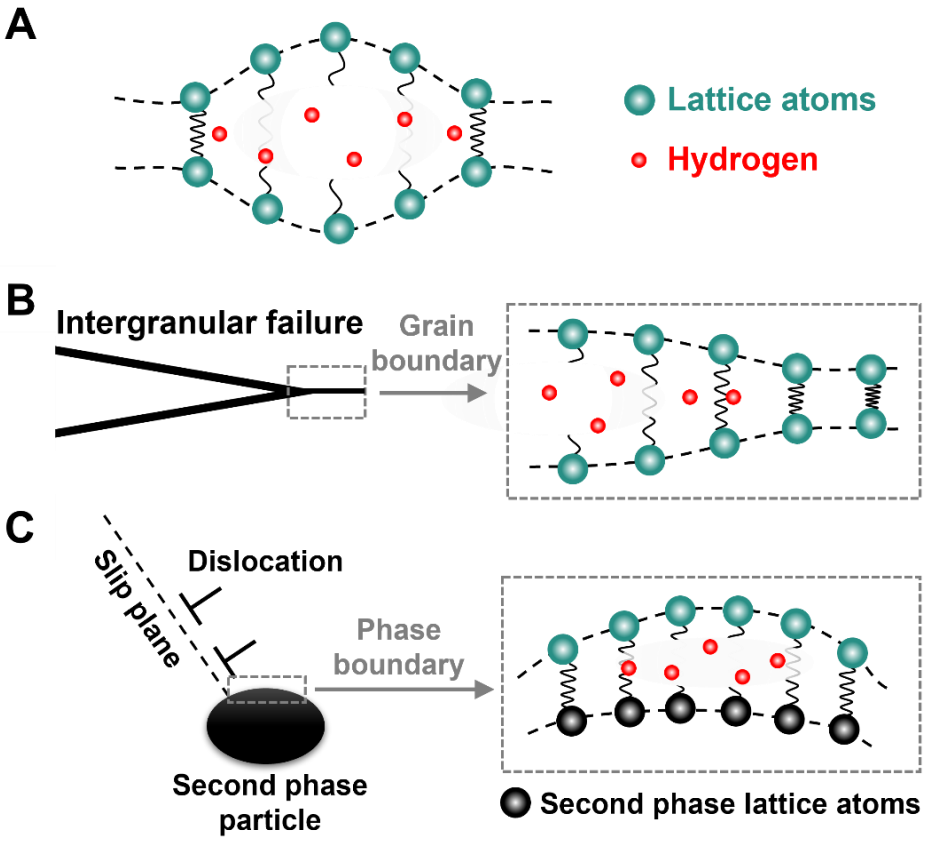

Figure 1-11. Schematics of the hydrogen-enhanced decohesion mechanism (A) in the lattice, (B) at a grain boundary, and (C) at a phase boundary.

Hydrogen-enhanced local plasticity

Hydrogen-enhanced ductile fracture with dimpled fracture surfaces (e.g., **Figure 1-6**A) was described by the hydrogen-enhanced local plasticity (HELP) mechanism by Beachem in 1970s. The theory is that i) interstitial hydrogen atoms concentrate at high tensile hydrostatic stress zones, and ii) hydrogen segregates to lattice defects such as dislocations [124,125], and increases their mobility [126]. This hydrogen segregation is a Cottrell atmosphere, a known effect that reduces the strain energy around dislocations [119,127,128]. **Figure 1-12** illustrates this process. Facilitation of

the generation and motion of dislocations promotes the formation of microvoids and their coalescence, allowing sub-critical hydrogen-induced cracks to propagate, resulting in dimpled fracture surfaces.

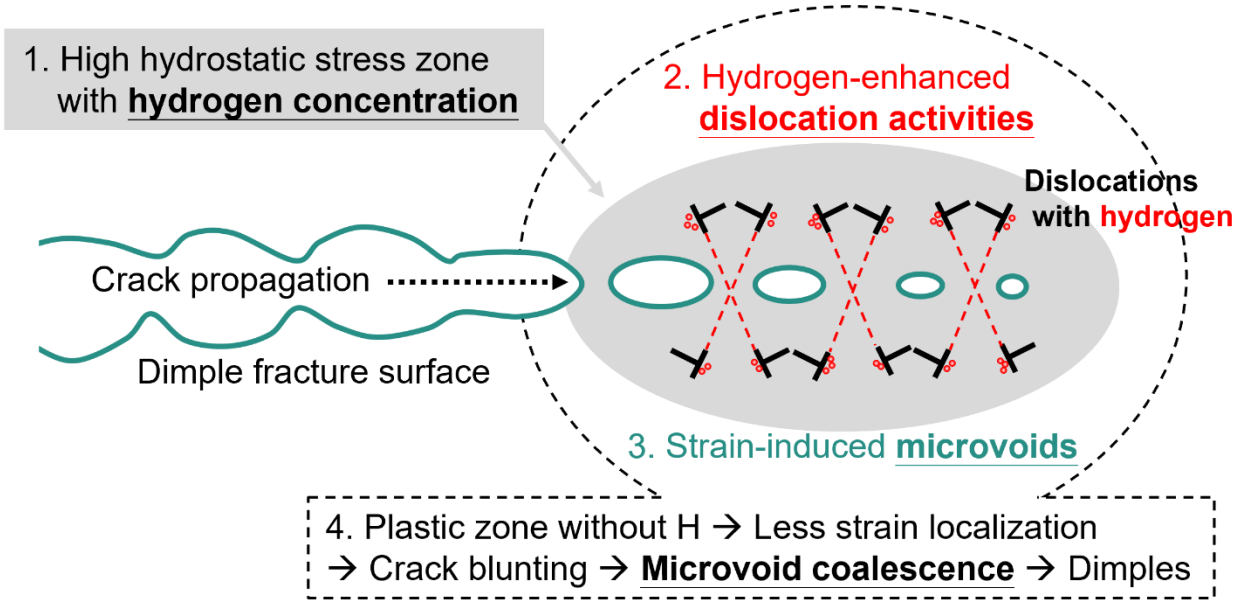

Figure 1-12. Schematic of the hydrogen-enhanced local plasticity mechanism

A critical hypothesis of HELP is that hydrogen atmospheres enhance dislocation mobility (Step 2 in **Figure 1-12**). This was experimentally shown by using environmental transmission electron microscopes (E-TEM) with in-situ mechanical loading on a specimen in a hydrogen atmosphere [126,129,130]. A derivative model of HELP was proposed that associates the crack path with failure along low energy dislocation cell walls that form as a result of the enhanced dislocation mobility in nanoprecipitation-strengthened steels [94]. HELP is now the most popular approach to interpreting HE in non-hydride forming alloys, particularly steels and materials of low to mid-strength. Noting here again that grain boundary decohesion can still take place in the absence of hydrogen-dislocation interactions in some alloy systems such as nickel alloy [82]. The HELP mechanism is a qualitative description of the effects that lead to embrittlement and does not directly provide a means of evaluating the extent of HE.

Adsorption-Induced Dislocation Emission

The adsorption-induced dislocation emission (AIDE) mechanism proposed by Lynch describes HE that arises from hydrogen adsorption at the surface, instead of hydrogen in solution in the bulk [31]. **Figure 1-13** illustrates the mechanism: HE is caused by

the hydrogen adsorption in the metal subsurface [131], which facilitates dislocation activity and boosts dislocation emission from a stressed surface. This dislocation emission facilitates inward strain and leads to the formation of microvoids in the crack-front plastic zone, which coalescence for crack propagation, resulting in a dimpled fracture surface. The AIDE mechanism can explain ductile H-induced crack growth that is induced by an external source of hydrogen, particularly prevalent in specimens with pre-existing surface damage. A similar mechanism 'hydrogen-assisted micro-fracture' was proposed by Atrens and co-workers [132], which also attributes HE to the hydrogen effect at specimen surface but stresses that the fracture propagation in the HE of steels (at the UTS) can be as fast as a velocity of 61-130 m/s, which exceeds the typical velocity of ductile fracture of 46 m/s, suggesting the possible presence of another process that led to the bulk HE [133].

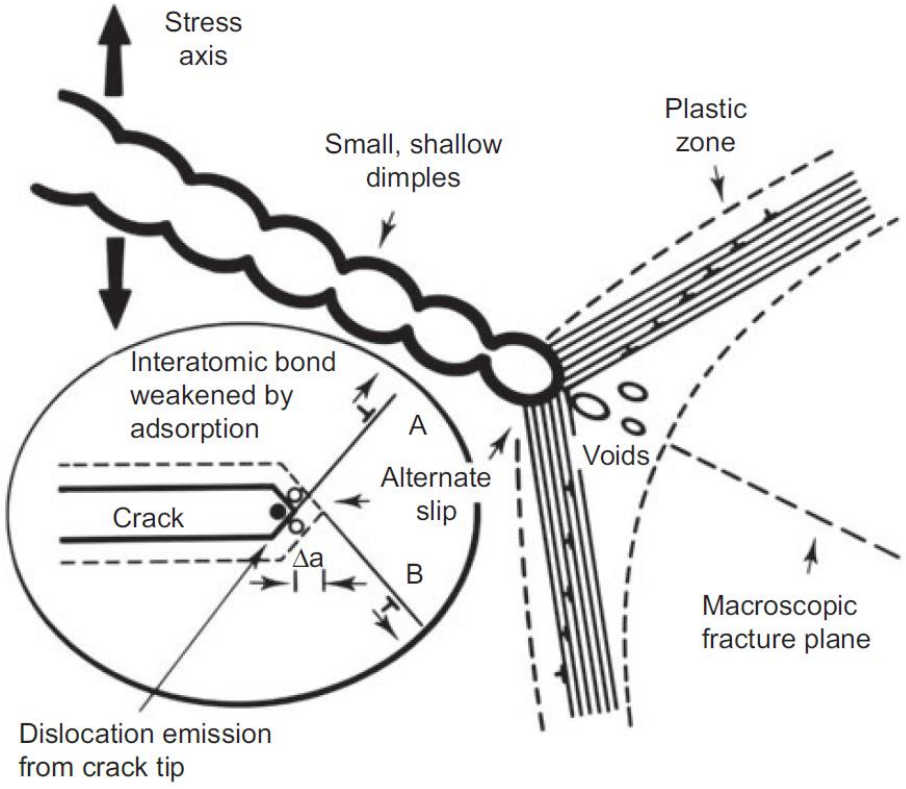

Figure 1-13. Schematic of the AIDE mechanism. Reproduced from [31]

Hydrogen-enhanced strain-induced vacancies

Based on the fact that hydrogen facilitates the formation of vacancies [119,127], Nagumo and Takai proposed the hydrogen-enhanced strain-induced vacancies (HESIV) mechanism, which attributes the observed dimpled fracture surface (e.g., **Figure 1-6**A) to an abundance of hydrogen-stabilized vacancies that are transported

by hydrogen-activated dislocations and subsequently combined into nano-voids during deformation [47]. Nagumo and co-workers combined thermal desorption analyses with delicately controlled straining and annealing that could introduce and remove vacancies, respectively, in steel specimens. Hydrogen-vacancy interactions were correlated with HE. Positron annihilation spectroscopy, which can detect both hydrogen and vacancies, was also used to provide supportive evidence of the relation between hydrogen-vacancy interaction and HE [134–136].

1.1.3 Hydrogen uptake and inhibition

Understanding how hydrogen enters materials, and how to inhibit uptake, is essential for developing strategies against HE. This section provides an overview of hydrogen entry and how it can be managed, finishing by introducing methods to relate laboratory test results with HE problems in the field.

Internal hydrogen embrittlement: hydrogen uptake and liberation

Hydrogen is a byproduct of various material production processes, and its uptake can lead to IHE [128,129]. An example occurs in the application of an aluminum-silicon (Al-Si) alloy coating, a common anti-corrosion treatment in automotive hot-stamped steels [137–139]. Al and Si can oxidize in the presence of ambient moisture, producing surface hydrogen, which can dissolve into the coated material [140]:

$$2Al + 3H_2O \rightarrow Al_2O_3 + 6H \qquad (1\text{-}3)$$

$$Si + 2H_2O \rightarrow SiO_2 + 4H \qquad (1\text{-}4)$$

This problem is of particular concern in the automotive industry, where high-strength steel is desirable for weight reduction [140]. Another example is the exposure of hot or molten steel to air humidity during steel production. Hydrogen can be generated and absorbed by the steel when the surfaces contact ambient moisture at high temperatures [110,113]:

$$3Fe + 4H_2O \rightarrow Fe_3O_4 + 8H \qquad (1\text{-}5)$$

$$2Fe + 3H_2O \rightarrow Fe_2O_3 + 6H \qquad (1\text{-}6)$$

$$Fe + 4H_2O \rightarrow FeO + 8H \qquad (1\text{-}7)$$

Other treatments that can lead to hydrogen uptake by steels are acidic pickling, electroplating for chromium [141], zinc or cadmium [142–146], welding [46,147–149], and in-service corrosion [63]. A famous example of HE following electroplating is the catastrophic failure of tightening bolts during the construction of the San

Francisco Bay bridge span in California, USA, which costs 40 million US dollars for rectification [150].

Hydrogen uptake during steel production can be removed by pre-service baking [142,151]. **Figure 1-14** shows how baking at 100-200 ℃ removed hydrogen (**Figure 1-14**A-C) from hydrogen-bearing hot-stamped martensitic steel specimens with an Al-Si coating, leading to an incremental recovery of the elongation with both annealing time and temperature (**Figure 1-14**D-F). The results suggested baking at 200 ℃ for 10 min was sufficient to remove the pre-existing hydrogen. This approach requires consideration of the effect of the heat treatment on the microstructure and mechanical properties, which may be problematic for some high-strength alloys [143,152].

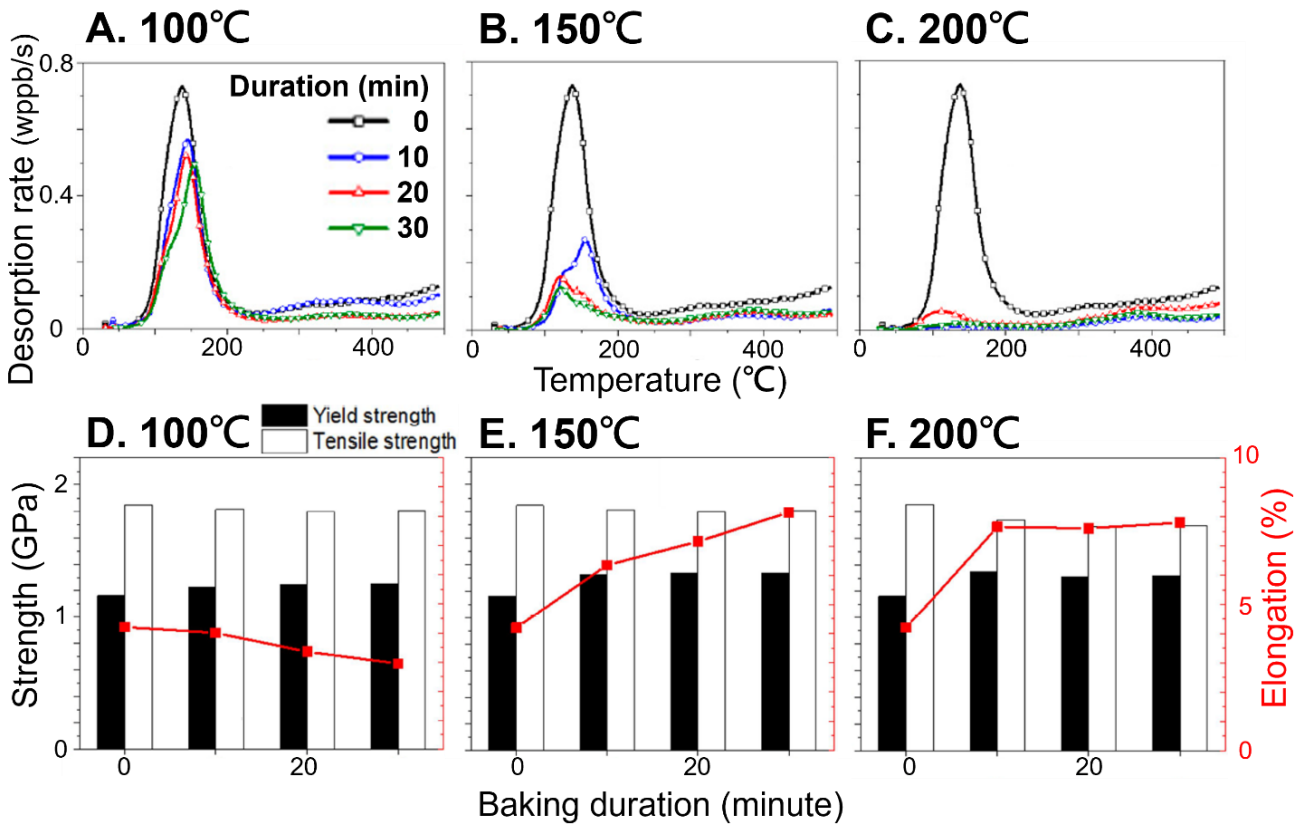

Figure 1-14. Reduced HE after hydrogen removal. Hydrogen desorption and mechanical properties of an Al-Si-coated cold-rolled hot-stamped martensitic steel after baking for 0-30 minutes at 100 ℃ (Figure A and D), 150 ℃ (Figure B and E), and 200 ℃ (Figure C and F). The thermal desorption analyses were conducted at a rate of 20 ℃/min. The mechanical properties were measured by slow strain rate tests, and the elongation was used to define the extent of HE. Reproduced from [151]

Environmental hydrogen embrittlement: hydrogen surface entry and inhibition

Hydrogen in the environment can be absorbed through the metal surface and can lead to EHE [153]. The hydrogen supply can be either finite, leading to conditions similar to those of IHE, or infinite (relative to the solubility in the material at the relevant fugacity), as is the case for gas transmission pipelines carrying hydrogen. Hydrogen from H_2 gas molecules in the local environment dissociate, adsorb on the surface, and are absorbed into the metal lattice. The process can be formulated as:

$$\frac{1}{2}H_2(g) \leftrightarrow H_{ads} \leftrightarrow H_{abs} \leftrightarrow H_{lattice} \qquad (1\text{-}8)$$

The absorbed hydrogen content in the material (c_H) follows the modified Sieverts' law relating to the solubility constant (S), which is specific to the material and its surface condition, the hydrogen pressure or fugacity (f_{H2}) in a material, and the amount of pre-existing and trapped hydrogen (c_T):

$$c_H = c_T + S\sqrt{f_{H_2}} \qquad (1\text{-}9)$$

The hydrogen fugacity is the hydrogen pressure that would apply if the hydrogen acted as an ideal gas and is essentially equal to the hydrogen pressure for hydrogen pressures up to 200 bar. **Figure 1-15** indicates that the hydrogen concentration in the specimen follows the modified Sieverts' Law for the hydrogen pressures up to 200 bar [154–156]. Hydrogen traps are filled rapidly with as hydrogen it becomes available (i.e., at hydrogen pressures less than 1 bar), which explains the apparent y-axis intercept in Equation (1-9) and **Figure 1-15**. The low hydrogen content in the annealed iron sample indicates that the intrinsic hydrogen solubility in pure iron is quite low, where the more substantial hydrogen solubility in steels is associated with hydrogen in traps. Sieverts' law, i.e., Equation (1-9), can be derived using statistical mechanics, as shown in [154], assuming i) the hydrogen in the steel is in equilibrium with the hydrogen in the gas phase, ii) N_H hydrogen atoms occupy N_S sites in the steel lattice having N_t trap sites; and iii) only one hydrogen atom can occupy each of the N_S sites. Note that in many applications (e.g., pipelines, pressure vessels, pumps) the metal is exposed to H_2 gas for prolonged periods (relative to temperature and fugacity) and the dissociation/adsorption/absorption reaches a dynamic equilibrium (Reaction (1-8)). This means that hydrogen atoms also recombine at the surface, and the dissolved hydrogen also desorbs back out of the surface. This is not the case for alloys exposed to transients of high hydrogen fugacity but is the case when the source

of environmental hydrogen is from corrosion of the alloy.

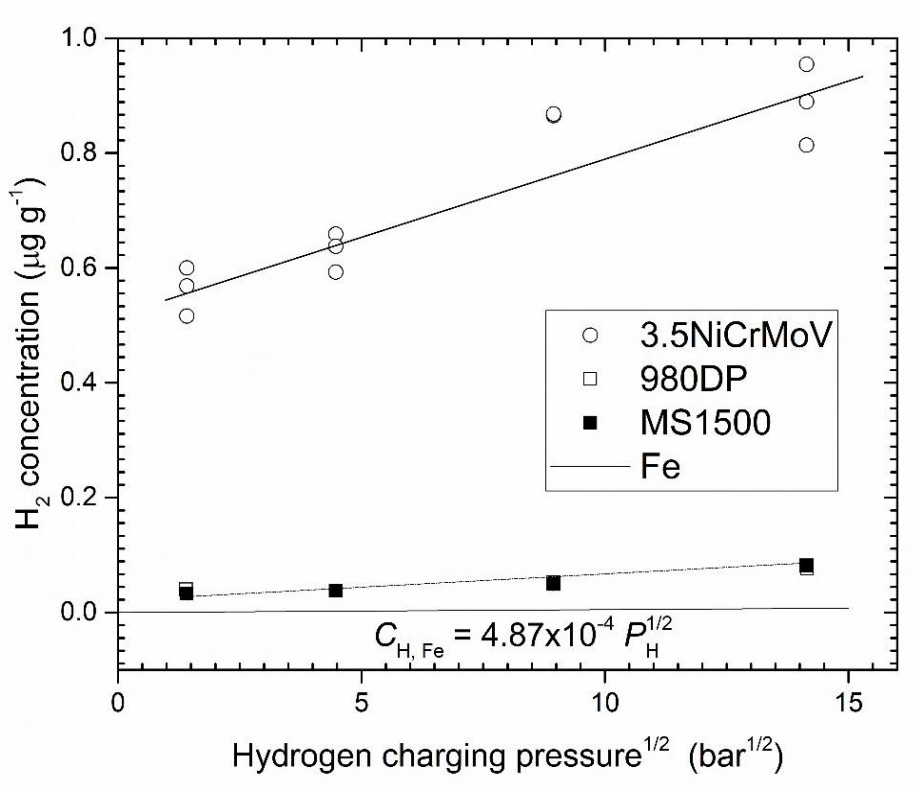

Figure 1-15 Equilibrium hydrogen concentration versus charging pressure in 3.5NiCrMoV steel, 980DP and MS1500 steels for various pressures of gaseous hydrogen from 1 to 200 bar at room temperature, measured using gaseous hydrogen charging [154–156], compared with annealed pure Fe [157].

In addition to the simplest case of direct contact with gaseous hydrogen, contact with hydrogen-bearing gases such as hydrogen sulfide (H_2S) can also lead to HE [17,44,53,59,158]. For an inert gas like methane, the hydrogen solubility in the steel can be determined by Sieverts' law using the hydrogen partial pressure in the gas phase. The hydrogen solubility is much higher (up to an order of magnitude higher) in the presence of an active gas like hydrogen sulfide that inhibits the recombination of hydrogen atoms into hydrogen molecules at the metal surface, thereby increasing the hydrogen fugacity at the metal surface. For this reason, HE due to hydrogen sulfide is a major concern in gas and oil pipes. The usual approach to tackle H_2S embrittlement is to impose a hydrogen gas pressure in service that is one or several orders of magnitude lower than the hydrogen content that causes HE [159]. An alternative approach is to use thicker pipe walls of low-strength steels that are less susceptible to HE, but this can lead to reduced gas transmission efficiency and results in higher weight and installation costs [159].

In contrast, some gases such as oxygen (O_2), carbon monoxide (CO), and sulfur dioxide (SO_2) can inhibit EHE. **Figure 1-16**A first shows that the fracture toughness of X42 and X72 steels in gaseous hydrogen is significantly lower than that measured in inert gases like N_2 and CH_4. However, when the gases are combined, the fracture toughness in both hydrogen and CO (indicated by the red arrows) is similar to the fracture toughness in an inert gas, indicating that the CO in the gas mixture inhibits EHE [160]. Similarly, **Figure 1-16**B shows that O_2, CO, and SO_2 inhibit hydrogen fatigue crack growth [131]. These inhibitor gases, particularly oxygen, absorb preferentially at active sites on the surface and prevent hydrogen from reaching the steel surface and being adsorbed [161–164]. Based on the compelling laboratory evidence for gas inhibition of EHE, additional research is now required to properly quantify this effect to allow for the use of a gas mixture strategy to address HE problems in gas transmission pipelines.

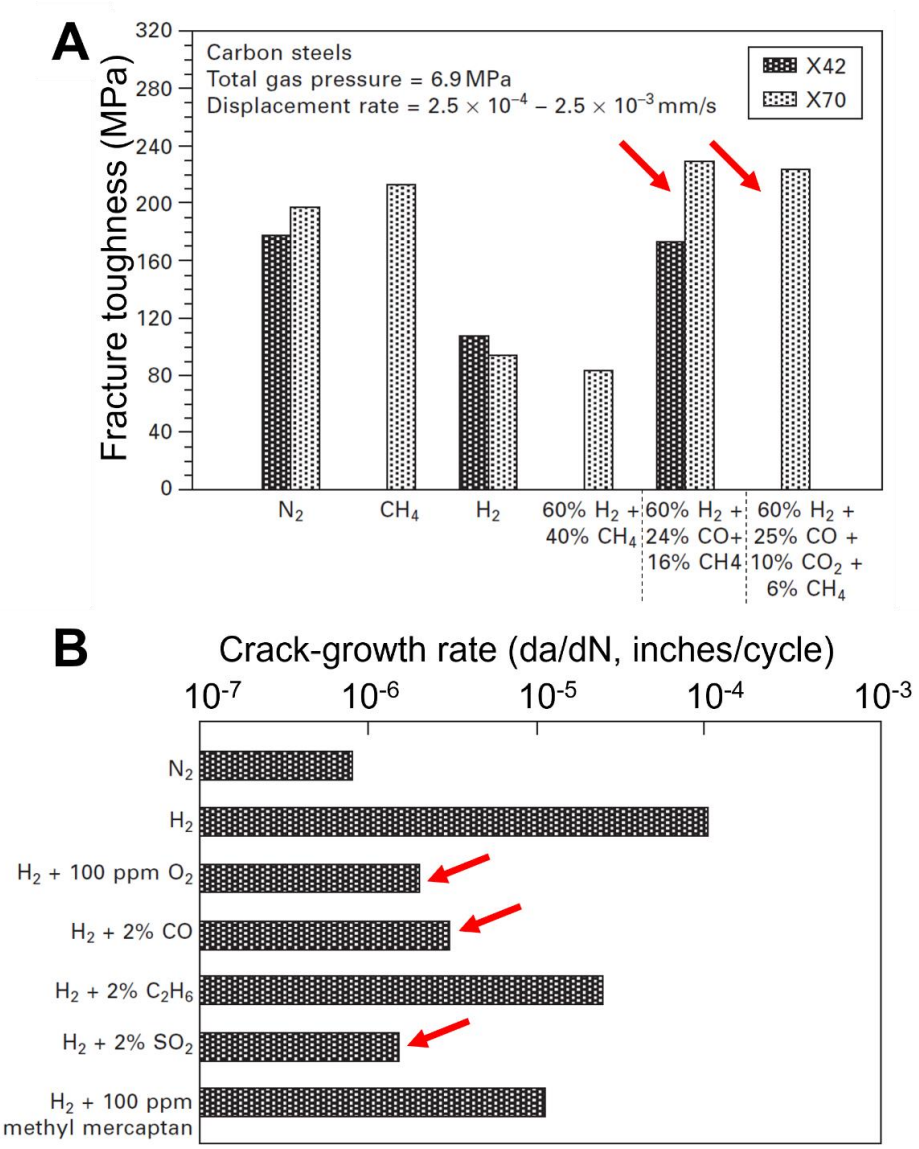

Figure 1-16. EHE susceptibilities for pipeline steels exposed to different gas mixtures with hydrogen. (A) The fracture toughness of X42 and X70 pipeline steels and (B) fatigue crack growth of X42 steel in the gases that contain various contents of hydrogen, showing the inhibition of EHE by O_2, CO, SO_2. Reproduced from [131].

Surface coatings such as iron oxide and aluminum oxide have also been found to reduce EHE by preventing hydrogen entry [28,165–169]. This approach has the advantage that it can be applied to existing structures. However, hydrogen is an effective reductant, so the surface oxides tend to be reduced by hydrogen which may limit the coating life. This reduction reaction occurs slowly at room temperature [170]. Metallic coatings and mechanical surface treatments can also be used to increase HE resistance, as demonstrated in [110,140] and [171–173], respectively. However, coatings can crack (particularly in aggressive environments), and surface

modification is ineffective for abrasive environments such as bearings [28]. In addition, surface diffusion barriers and gas mixtures only reduce the kinetics of hydrogen uptake and do not alter the thermodynamic factors [154]. Unless hydrogen entry kinetics are sufficiently low, materials will eventually become saturated with hydrogen with continuous hydrogen contact, such as in a gas transmission pipeline that might be used for over 30 years .

Laboratory hydrogen charging

Laboratory tests use in-situ and ex-situ hydrogen charging [31,45] to simulate service environments. In-situ charging during a mechanical test (and also beforehand to achieve a uniform hydrogen content) is optimal for evaluating HE susceptibility. Ex-situ charging is simpler to achieve in practice, but hydrogen loss can affect the quality of results for materials with low diffusivity or where long-duration tests (e.g., fatigue) are required. Erroneously high HE resistance can result from hydrogen depletion at the surface, where hydrogen cracking typically initiates. During hydrogen charging, surface oxides present on the metal surface may prevent hydrogen uptake, which can be mitigated by an activation procedure. Gaseous charging generally requires a high pressure and/or high temperature to enable hydrogen uptake [174]. This approach is thus demanding in terms of laboratory safety and equipment.

In contrast, cathodic charging requires only an electrolytic cell, which allows the specimen (the cathode) to be charged in an acidic, neutral, or alkaline solution [144]. Cathodic charging allows for easy generation of high fugacity hydrogen (at the level of GPa) within the specimen with an overpotential of less than 1 volt [154,175,176]. Much higher hydrogen fugacities are possible if a hydrogen recombination poison is also added to the cathodic charging solution. The simplicity and effectiveness have led to widespread use of cathodic charging for HE tests [146], despite the fact that quantifying hydrogen uptake is not as straightforward as it is for gaseous charging. Hydrogen can also be introduced by charging from a plasma [177,178], but this approach is less common and remains uncertain whether the low pressure required allows for the introduction of sufficient hydrogen to trigger HE [179,180].

To better understand the effective cathodic charging fugacity, Atrens and co-workers developed a method to relate the hydrogen fugacity to the equivalent hydrogen pressure during gaseous charging [154–156,176]. The approach is based on the assumptions that i) the hydrogen inside the metal has no memory of whether it

originates from gaseous charging or cathodic charging and ii) the fugacity during cathodic charging is equivalent to the fugacity during gaseous charging for the same hydrogen concentration. The hydrogen fugacity (f_{H_2}) for pure iron is related to the applied electric potential (E_c) by:

$$f_{H_2} = \alpha \times exp\left[\frac{-(E_c - E_H^0) \times F}{\beta RT}\right] \qquad (1\text{-}10)$$

where F, R, and T are the Faraday constant, gas constant, and absolute temperature, respectively. E_H^0 is the equilibrium potential of the hydrogen evolution reaction at the sample surface for hydrogen charging at 1 atm of fugacity, hence ($E_c - E_H^0$) is the overpotential that controls the hydrogen fugacity. The constants α and β relate to the hydrogen evolution reaction (i.e., the acidity of the charging solution) at the steel surface. These constants can be determined for pure iron, which does not have hydrogen traps, based on literature value of the Sieverts' constant *S* in Equation (1-9) (**Figure 1-15**). For a steel, the hydrogen solubility data (e.g., **Figure 1-15** in which hydrogen concentration is measured for each cathodic charging condition) can be used to experimentally establish the relationship between hydrogen content and hydrogen fugacity [176].

This quantification provides the hydrogen fugacity (and equilibrium hydrogen content) at the specimen surface. Time is required to establish a uniform hydrogen concentration throughout the specimen. The penetration can be predicted using hydrogen diffusion equations. Often measurements of the overall hydrogen content in the specimen are used to assess the rate of penetration. In addition to the charging parameters, the hydrogen content in the specimen can be influenced by the surface condition, particularly surface oxides, which can affect the hydrogen uptake [154]. Another important experimental consideration is time-to-test after hydrogen charging, which will affect the extent of hydrogen desorption [181]. Even quite short times can alter the measured degree of HE in some materials. Where possible, in-situ charging during mechanical testing is ideal. When reporting HE results using hydrogen charging, it is necessary to give a clear and complete description of the experimental conditions to enable comparison with the literature.

1.2 Hydrogen trapping

In addition to *extrinsic* approaches to mitigate HE hydrogen degassing or surface coating, a popular *intrinsic* approach is to introduce additional hydrogen traps into the

alloy microstructure. Pressouyre [153] proposed the concept of introducing microstructural hydrogen traps for mitigating HE in the 1980s. Certain microstructural features act as hydrogen traps, reducing the amount of hydrogen is available to reach the location of the crack tip. This concept assumes that the trapped hydrogen is passive and that it is the lattice hydrogen or diffusible hydrogen that leads to HE [27,28,31,32]. However, as shown in **Figure 1-15**, the presence of hydrogen traps increases the solubility of hydrogen in all alloys, including commercial steels, which can also provide a future source of hydrogen available for HE.

An optimal microstructure to resist hydrogen embrittlement will be one in which the microstructure, including the traps themselves, is resistant to embrittlement and in which the traps do not provide an easy source of hydrogen that can contribute to embrittlement effects. Here we overview the fundamental understanding of hydrogen trapping in metals and alloys to establish a scientific ground to underpins the design of a HE-resistant microstructure.

1.2.1 Principle

A hydrogen atom in an alloy can either be a free-moving solute in the lattice or it can reside in a trap. **Figure 1-17** shows the energy landscape for a hydrogen atom. It depicts the activation energy for classical migration of hydrogen in a lattice site (E_d), the activation energy for migration close to a trapping site (E_s), the de-trapping energy for a trapped hydrogen atom to diffuse in the lattice (E_a), and the binding energy of the hydrogen atom to a trapping site (E_b). These energies can be understood in terms of a simple reaction model where the rate $\frac{dx}{dt}$ is given by [182]:

$$\frac{dx}{dt} = A(1-x)exp\left(\frac{-E}{RT}\right) \qquad (1\text{-}11)$$

where x is the fraction of free (detrapped) hydrogen, and R and T are the gas constant and absolute temperature, respectively.

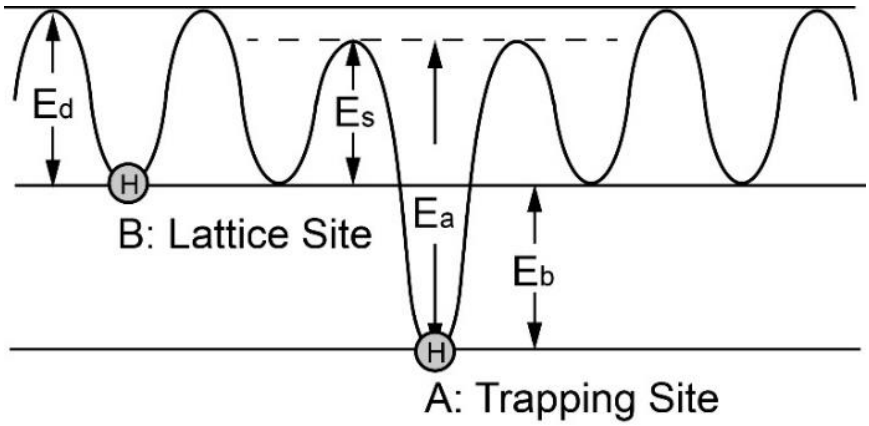

Figure 1-17. Schematic energy profile of hydrogen in the lattice and in a trap. Classical lattice diffusion of hydrogen requires E_d to hop between interstitial sites. This may vary near trapping sites to E_s. Detrapping of hydrogen requires an energy of $E_a = E_b + E_s$.

In BCC, at room temperature interstitial hydrogen atoms prefer to occupy tetrahedral sites over the octahedral site [183–185]. In FCC alloys, hydrogen atoms tend to reside in octahedral sites, which are larger and have lower multiplicity for hydrogen migration [183]. This leads to a lower diffusivity and a larger E_d for hydrogen (e.g., 44 kJ/mol for FCC iron [186]) for FCC compared to other crystal lattices (e.g., 4.5-5.5 kJ/mol for BCC iron [187]).

Negative trapping energies reflect that the hydrogen atom in the potential well is more stable and will sit in the site longer than it does in a lattice site. Both E_a and E_b in **Figure 1-17** have been defined as the 'hydrogen trapping energy' in the literature, depending on the measurement techniques. Their difference, E_s, differs from E_d due to local atomic-structural heterogeneity near microstructural traps with respect to an ideal lattice, such as the strain field around a dislocation [188]. This E_s may also be affected by multiple trapping sites in a single microstructural feature, e.g., the interface and the precipitate structure in second-phase precipitates [88,189,190].

The value of E_a is often used to indicate the reversibility of a hydrogen trap. At room temperature, a trap with $-E_a$ larger than 50 kJ/mol is considered as 'irreversible' since there is a negligible probability of escape of a trapped hydrogen atom [28,153]. Irreversible trap can act sinks until they are saturated, whereas reversible traps can act either as sinks or sources of hydrogen. For example, if a dislocation (a mobile trap) passes a reversible trap that has a trap strength lower than that of the dislocation, then the hydrogen in the reversible trap can be transferred to the dislocation and be carried along with the dislocation [153]. Hydrogen trapping/de-trapping is a thermally

activated process, so a higher trap strength is needed to confine hydrogen at a higher temperature. This is an important consideration in certain application environments, such as in components of a nuclear reactor which are typically operated at approximately 300 °C [191].

Considering that hydrogen is highly mobile, equilibrium between the hydrogen in the lattice and in trapping sites can be reached rapidly in most circumstances [42,43]. The relationship between mobile and trapped hydrogen concentrations can be plotted against trap strength, as shown in **Figure 1-18** [192]. When there is 10^{-2} wt. ppm hydrogen in BCC iron lattice (at the bottom of **Figure 1-18**), traps with 50 kJ/mol trapping energy will be > 90% occupied ($\theta_T > 0.9$); whereas those with 10 kJ/mol are less than 10% full ($\theta_T = 0.1$), leaving most of the hydrogen in the lattice.

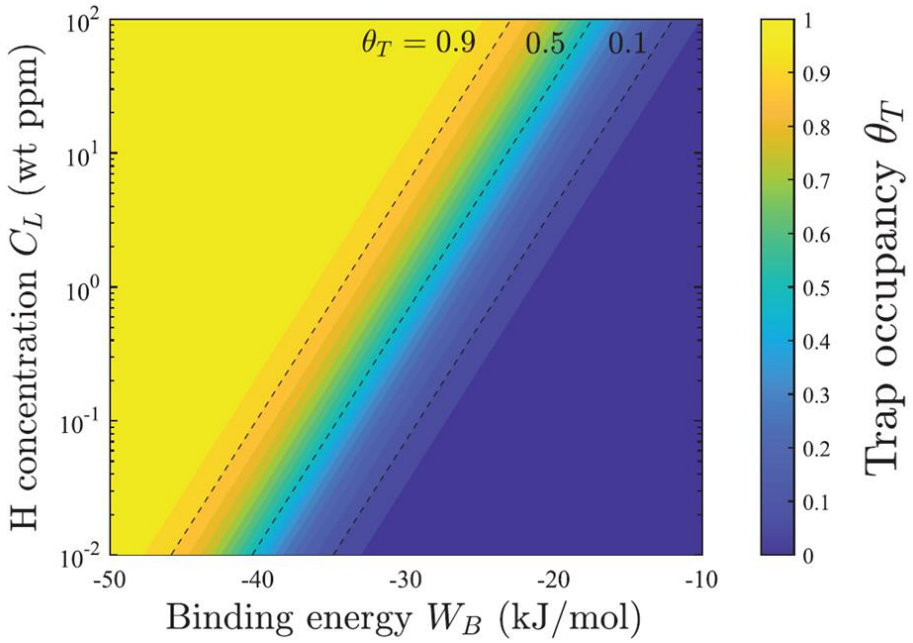

Figure 1-18. Relationship between hydrogen content and trap occupancy as a function of trapping/binding energy. As the lattice hydrogen concentration (C_L) increases, traps with low binding energies (W_B) are filled and the trap occupancy (θ_T) start to increase. Reproduced from [192]

Finally, it is important to note that **Figure 1-17** only depicts a classical view of the hopping mechanism of atomic migration. Hydrogen is sufficiently light that quantum tunneling, and nuclear quantum effects can play a significant role in its migration [188,193–196]. Recent computational work showed that quantum tunneling can result in a non-linear Arrhenius diffusivity of hydrogen in BCC iron at 400–500 K [197,198]. Nuclear quantum effects were also demonstrated to influence hydrogen solubility, mobility, and trapping in the presence of strain [198,199]. It has been

shown that nuclear quantum effects can increase the rate of trapping and decrease the rate of escape when hydrogen atoms interact with vacancies in BCC iron at low temperatures [200]. Similar findings were obtained in diamond [201,202], and it is likely that the consideration of quantum effects is essential for the behavior of hydrogen in other material systems. Quantum effects should be considered in the study of hydrogen behavior, especially in cases where the effects are most significant, such as in low temperature hydrogen trapping, high-pressure phase stability, mixed hydrogen isotopic composition, and hydrogen migration [203,204].

Overall, hydrogen behaves similarly to other interstitial elements in a metallic matrix, i.e., segregation occurs to any location where energy is lower [120,205], or where atoms are dragged by vacancies, dislocations, or other mobile defects. In fact, 'hydrogen trapping' is just a term that highlight the uniquely high mobility of hydrogen compared to other interstitial solute atoms with larger atomic volumes and masses. **Figure 1-19** illustrates the wide array of microstructural features of engineering alloys that can act as hydrogen traps, across several length scales. Hydrogen trapping can take place at many feature types, including dislocations, vacancies, second phase interfaces, and grain boundaries [131].

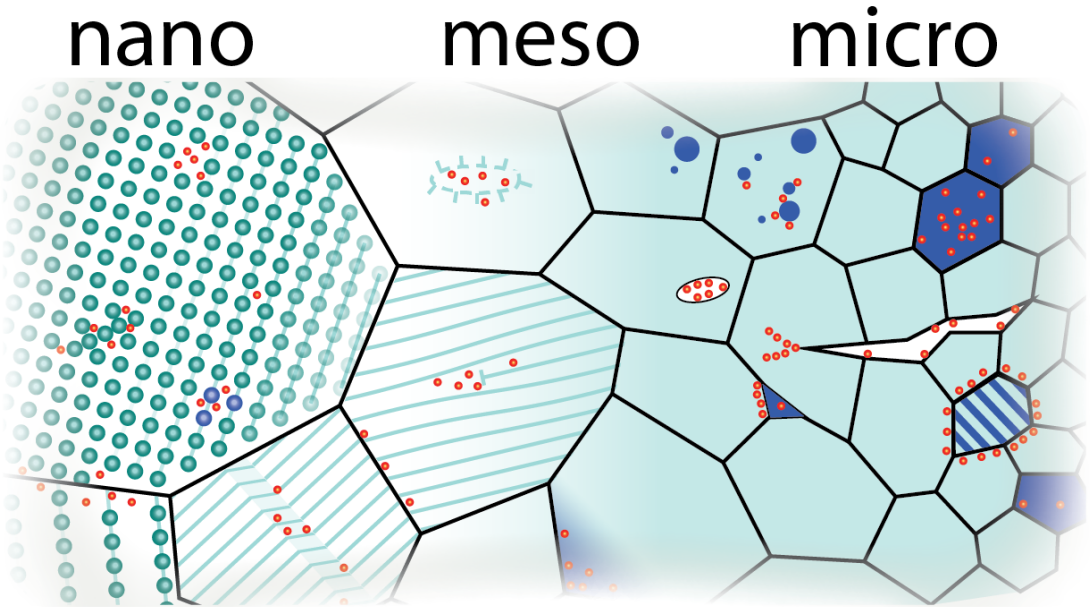

Figure 1-19. Illustration of various microstructural hydrogen traps in an alloy. Hydrogen can be trapped at interstitial lattice sites, grain boundaries, vacancies, alloying solutes, stacking fault, twins, dislocations and their cell walls, strain field, voids, second phases and their boundaries, and the free surfaces of microcracks.

1.2.2 Microscopy techniques for characterizing hydrogen trapping

Characterizing H in materials is challenging [87]. H in solution is interstitial and has high diffusivity in most materials, with a few exceptions that have strong chemical affinities for H such as vanadium (V), titanium (Ti), and zirconium (Zr) [206]. H as a solute that is not part of a stable hydride phase can easily desorb at ambient temperature, and this desorption happens rapidly in smaller specimens that have a high surface-area-to-volume ratio [181]. Fast H desorption is particularly problematic in microscopic characterization experiments where small specimens are required. In addition, H is difficult to remove from vacuum chambers, which are required for many high-resolution microscopes to operate [207–209]. Residual H gas in vacuum can cause confusion about the source of detected H, complicating data interpretation [210,211]. Lastly, although electron-probing techniques such as scanning and transmission electron microscopes (SEM and TEM) have been of great use for both structural and chemical imaging in materials research, electron beams are not very sensitive to H due to its low atomic mass. H can normally only be detected if it is in the form of well-defined H-containing phases in specimens [212–215]. The lack of electron–H interactions largely rules out the use of electron microscopy for studying the distribution of H in materials [87]. For materials such as Zr that react with H to form hydrides, techniques such as ultrafast laser-induced breakdown spectroscopy can be used, but they lack the spatial resolution to analyze H segregation to specific microstructural features[216,217].

To provide unambiguous spatial and chemical information about H in materials, several techniques have been developed and applied. Using a neutron beam, neutron radiography can locate H segregation in materials [218,219]. Silver microprint deposits a layer of silver bromide on the specimen surface, which can react with desorbed H from the bulk and form metallic silver particles that help visualize H distribution [220,221]. Similarly, a scanning Kelvin probe deposits a layer of palladium that is reactive to H on the specimen surface and probes changes in conductivity due to the formation of palladium hydride from H desorption, resulting in a resistivity map that represents H distribution [222,223]. Lastly, mass-spectroscopy-based techniques such as secondary ion mass spectroscopy (SIMS) [224–227] and atom probe tomography (APT) [87,228,229] can provide high spatial resolution and the ability to detect all elements, including H. Among these techniques

for H mapping, APT has the highest spatial resolution at a near-atomic level, which is particularly useful for mapping H distribution at interfaces and other defects within material microstructures [87].

In 2010, a breakthrough in using APT to observe the hydrogen trapping behaviour in materials was achieved by Takahashi et al. [230], who used a custom APT with an attached gas deuteration cell to significantly enhance D retention, leading to the first three-dimensional observation of D trapping in TiC precipitates in a ferritic steel matrix. Their unique instrumentation then led to the successful observations of D trapping in vanadium carbides, mainly V_4C_3 precipitates, which are also transition-metal carbides and have the same NaCl-rocksalt structure as TiC precipitates but a carbon-deficit stoichiometry that suggests the presence of more carbon vacancies in the bulk [190,231].

Chen et al. [189] utilized cryo-APT combined with electrolytic charging, which can generate higher fugacity in charging and introduce more H/D into specimens than gas charging to further enhance D detectability. This approach was used to study V-Mo carbide (V-Mo-C, NaCl-type) precipitates with semi-coherent interfaces with the matrix to better understand their H trapping mechanism in steels. The findings of this work can be combined with a later publication [88] that regards the H trapping in Nb carbide (NbC, also NaCl-type) precipitates with incoherent interfaces, as shown in **Figure 1-20**. The two NaCl-type carbides have the same crystal structure but different metal-to-carbon stoichiometries. The V-Mo-C precipitates contain less carbon and more carbon vacancies in the bulk than NbC precipitates [232], and this characteristic was related to the APT-observed H trapping mechanisms. **Figure 1-20**A and B provide, respectively, the overall APT reconstruction with two NbC precipitates and charged D in a deuterated ferritic sample and the two-dimensional slice views of the NbC precipitates and trapped D. The trapped D atoms in NbC precipitates are located at the carbide-matrix interfaces. In contrast, the D-charged V-Mo-C precipitates, using the same charging method, were found to have D trapping in the carbide bulk (**Figure 1-20**C), as evidenced by **Figure 1-20**D, which is a statistical result of the distribution of D from over 30 V-Mo-C precipitates, and shows that the trapped D is mainly distributed within the carbide bulk. This phenomenon of carbide bulk H trapping agrees well with the works of Takahashi et al. [233] and Zhu et al. [234] in epsilon carbide precipitates, which are often hypo-stoichiometric and have a relatively high carbon vacancy content in bulk form. The combination of these results indicates

that near-stoichiometric NbC precipitates mainly use their interface with the matrix to trap H, whereas the carbides with a higher carbon vacancy content such as V-Mo-C precipitates use bulk carbon vacancies as H traps. These H trapping mechanistic findings are also in good agreement with predictions using first-principle models [235–237]. These modelling results confirm that both interface and carbon vacancies in the carbide bulk can act as strong traps that function independently of each other, though the carbon vacancy has a stronger trapping energy than the interface sites. These findings imply that the H atoms trapped in the carbon vacancies may have a higher probability of being retained in the microstructure than H atoms trapped at the interfaces during the sophisticated sample handling and cryo-transfer processes that are unlikely to retain cryogenic temperatures throughout the entire sample handling and transfer process. Considering this, H atoms trapped at the interface may still exist following H charging for the dataset in **Figure 1-20**C, but these atoms may not be as easy to retain in the structure during the transfer to APT measurements and thus are not as easily observed as the H atoms trapped in the carbide bulk. However, confirmation of this argument requires additional in-depth analysis. Nonetheless, whilst the essential role of interfacial sites in H trapping is acknowledged, **Figure 1-20**C and D provide clear evidence of H trapping in the carbide bulk that were not previously available to the research community.

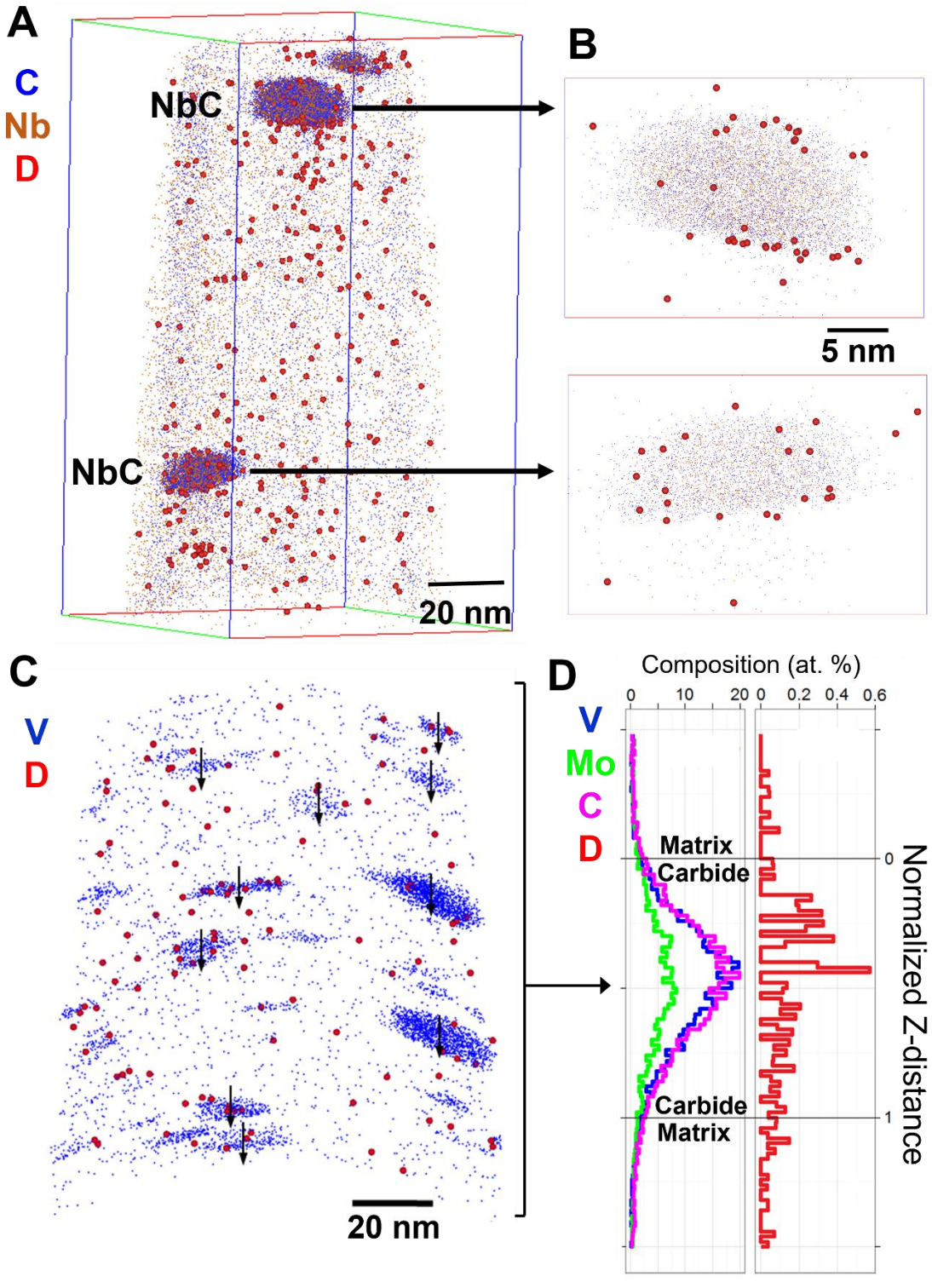

Figure 1-20 APT observations of D trapping of NaCl-type carbides in ferritic steels. (A) is the APT data overview of a NbC-containing steel after D charging. Nb, C, and D are shown in brown, blue, and red, respectively. (B) shows the 10-nm-thick slices of the NbC precipitates that exhibit the interfacial D trapping of the carbides. The experiment used a LEAP 4000 Si with 200 kHz pulse frequency, 20% pulse fraction, and 50 K sample temperature. (C) is a 10-nm-thick slice from a D-charged V-Mo-C-containing steel. (D) shows a one-dimensional composition profile as a

result of collecting over 30 V-Mo-C precipitates in the dataset, dimensionally normalizing the spatial distribution of the constituent element carbides and superimposing all the individual profiles. The APT experiment was from a LEAP 4000 XR with all other experimental parameters the same as the data in (A)–(B). (A)–(B) and (C)–(D) are reproduced from [88] and [189], respectively.

In addition to second-phase precipitates, a retained austenite in steel microstructure can also be an effective H trap, given the higher solubility of H in face-centered cubic (FCC) austenite than in both body-centered cubic (BCC) ferrite and body-centered tetragonal (BCT) martensite [238,239]. H trapping by austenite has also been evidenced by using APT (**Figure 1-21**A) on a steel specimen that contains an austenite (γ)-ferrite (α) phase boundary delineated by a carbon isosurface [238]. **Figure 1-21**B is a one-dimensional composition profile from the light blue region of interest (ROI) in **Figure 1-21**A, quantitatively showing the higher H content in austenite (left) than in martensite (right). Moreover, APT was used to investigate the trapping effect of lattice defects in steels [88]. **Figure 1-21**C is an overall APT reconstruction showing D atoms (red) trapped at dislocations that are decorated with carbon (blue isosurfaces) in a martensitic steel. **Figure 1-21**C also contains a two-dimensional slice view that better shows the colocalization of D and carbon, where the carbon highlights the locations of dislocations. In **Figure 1-21**D, an overall reconstruction incorporating GBs (left) decorated with carbon, as highlighted by carbon isosurfaces (pink), is shown together with slice views (right) showing the colocalization of D and the carbon at GBs. These D maps provide experimental verifications of existing HE models that attribute HE to the H-shielding effect for dislocation movement and H-enhanced GB decohesion [30].

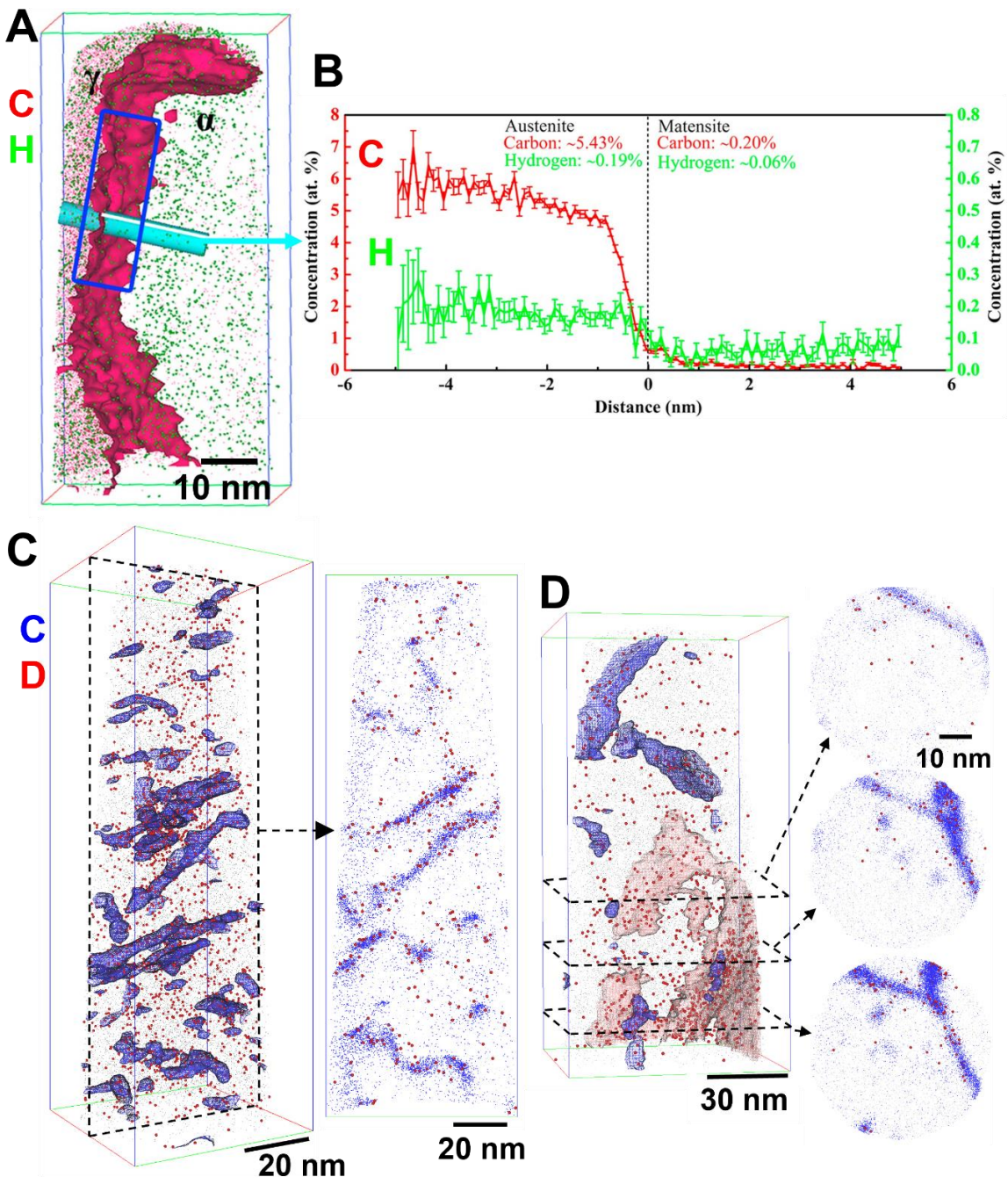

Figure 1-21. APT observations of H trapping at (A)–(B) retained austenite, (C) dislocations, (D) GBs. (A) shows a γ/α interface delineated by a carbon isosurface (red). (B) is a one-dimensional composition profile of carbon (red) and H (green) from the light blue box in (A). The experiment was conducted in a LEAP 3000 HR at a sample temperature of 60–100 K with a 20% pulse fraction and pulsing rate of 2 kHz. (C) provides the overall APT reconstruction containing a carbon isosurface (blue clouds) to delineate the carbon-decorated dislocations and a two-dimensional slice view of carbon (blue) and D (red). (D) is the reconstruction and sliced views of a dataset containing carbon-decorated GBs. Both experiments for (C) and (D) used a LEAP 4000 Si with a 200 kHz pulse frequency, 20% pulse fraction, and 50 K sample temperature. (A)–(B) and (C)–(D) are from [238] and [88], respectively.

1.2.3 Atomic-scale modelling for hydrogen trapping

When performing atomic-scale simulations of hydrogen in metals, it is important to consider the complex chemical binding that hydrogen often displays, especially with transition metals. Additionally, hydrogen is amphoteric and can take charge states of –1 (hydride ion), 0 (atomic hydrogen) and +1 (proton). Thus, atomic-scale simulations of hydrogen require a level of theory capable of capturing these nuanced chemical interactions. For this reason, first-principle simulations using density functional theory (DFT) have been the main approach for understanding hydrogen tapping, as they rely on a quantum mechanical description of the electronic system. DFT provides both thermodynamic and kinetic information by determining the ground state energy of hydrogen in crystal lattices and at traps, and the activation energy for migration, dissociation, adsorption, and absorption. An example is shown in **Figure 1-22**A regarding the energy landscape for absorption of hydrogen atoms into the tetrahedral interstitial site of BCC iron from the (100) surface [240]. Another example in **Figure 1-22**B is a comparison of trapping/solution energies of single and multiple hydrogen atoms in various positions in a ferrite matrix containing vanadium carbide (V_4C_3) [235]. This result indicates that hydrogen is preferentially trapped in the carbon vacancy of V4C3 as compared to the interstitial sites of ferrite or V4C3. This result also shows that it is possible for a vacancy to accommodate up to two hydrogen atoms, which is a behavior observed in many other materials, in some cases with a single vacancy accommodating up to 12 hydrogen atoms [241–246]. DFT has also been widely used for studying the interaction of hydrogen atoms with alloying solute atoms [185,247,248], GBs [249–251], and other second phase precipitates [184,185,235,252–258].

Recent DFT studies have shown that the ground state energy of hydrogen in an interstitial site is strongly dependent on the composition of its immediate surroundings and is relatively insensitive to crystal features and defects beyond the first shell of nearest neighbors [185,248,257,259–262]. This insight is being used to develop a high throughput simulation method based on DFT simulations of the local environment, thus avoiding the computational burden of modeling a large simulation cell representative of the true alloy [185].

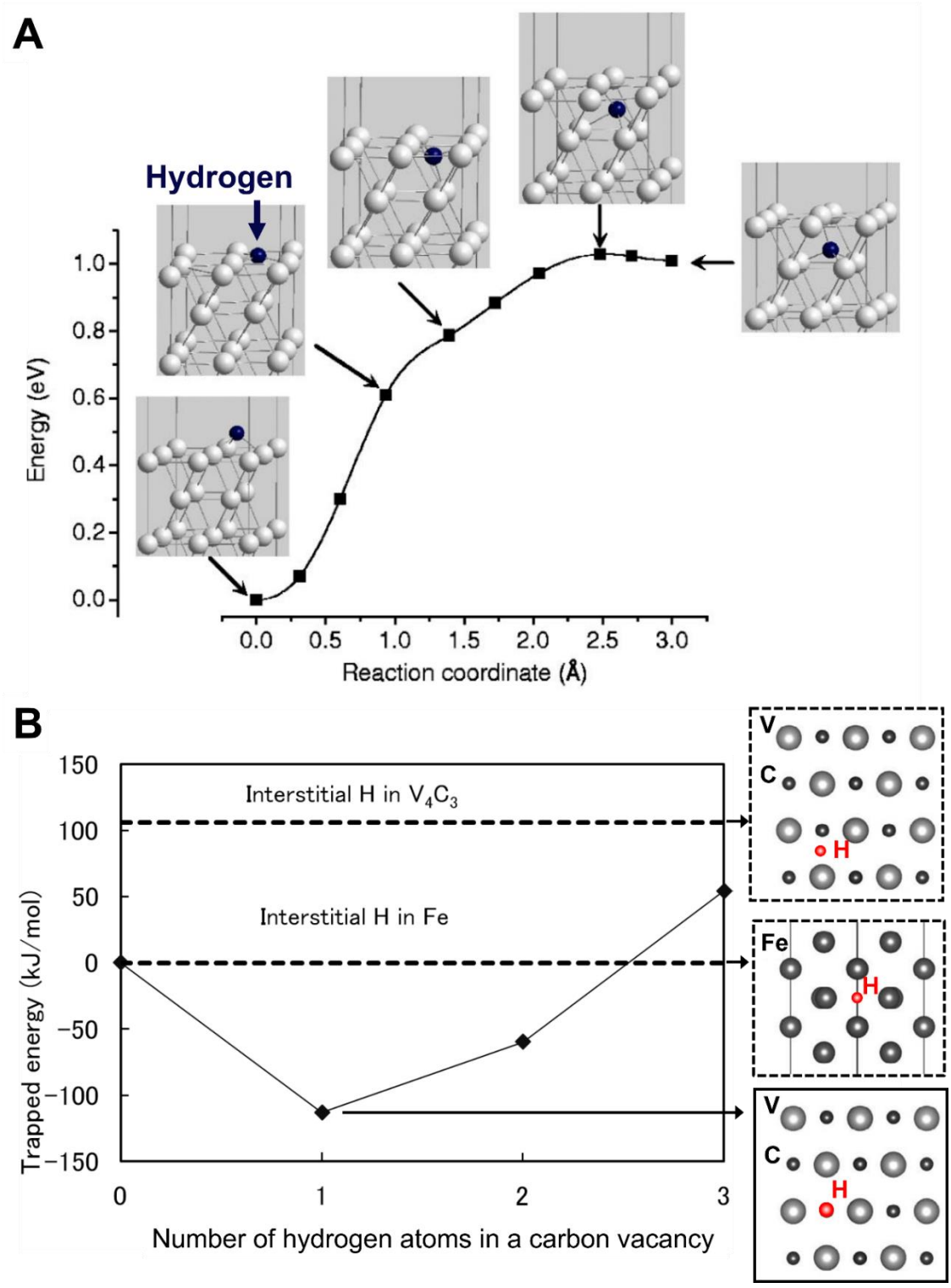

Figure 1-22. DFT calculation of hydrogen solute energy. (A) At the ferrite surface [240]. (B) At an interstitial site or a carbon vacancy of vanadium carbide (V4C3) [235].

A limitation of DFT is the significant computational cost, which limits the scale to a few hundred atoms. This size of the model does not allow a full description of

many of the microstructural features involved in HE mechanisms and hydrogen trapping. Even a simple dislocation requires over 1,000 atoms for a full description of the core and local structure. For longer length scales, one can resort to classical molecular dynamics (MD) or tight-binding, which is an approximation of DFT with a tunable degree of assumptions and thus a sliding scale between DFT and classical MD [263]. However, a recent study of Zr-H potentials showed that reliable Zr-H tight-binding simulations require a similar level of computational cost as DFT [185]. Also, there are few tight-binding codes available, and these are typically not as evolved or approachable as DFT codes. On the other hand, classical MD lacks the chemical accuracy and transferability of DFT because it relies on a pre-defined description of inter-atomic forces. Some of the more complex and advanced interatomic potentials can describe multiple charge states of hydrogen [264,265], but these come at greater computational cost and have shown limited robustness and transferability. Recent developments of machine-learning potentials for MD also show good promise to facilitate HE research [266–268].

In contrast, the hybrid quantum mechanics-molecular mechanics (QM-MM) method is a promising development for larger-scale simulations of hydrogen in metals. In this approach, a simulation cell is divided into two or three concentric regions. In **Figure 1-23**, an inner region centered around the hydrogen atoms uses DFT to describe the chemical interactions with quantum mechanical accuracy, while the outer region uses classical potentials to describe the long-range structure of the microstructural feature of interest. An intermediate “buffer” region where both DFT and classical potentials are used is often also added to provide convergence and eliminate artifacts of discontinuity between the two regions. While QM-MM has proven successful for molecular and biological systems [269], it has only recently started to be used for solid-state metallic systems, for example, in the investigation of the interaction between hydrogen and dislocation in BCC Fe [270]. More applications of this new method with the continuing increase of computational power can be expected in near future.

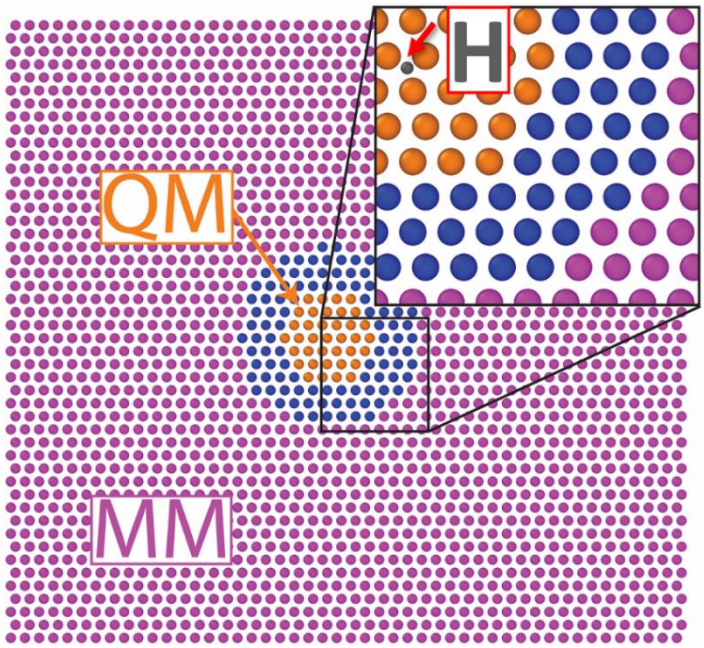

Figure 1-23. 2D slice of a MM/QM model to simulate a hydrogen atom. The small grey sphere in the inset is the hydrogen atom in a screw dislocation of an FCC lattice, where the color indicates the level of theory used to compute forces on those atoms: orange indicates quantum mechanics (typically DFT), purple indicates classical molecular mechanics potentials (e.g., embedded atom method, EAM), and blue indicates a buffer region where both approaches are used to avoid discontinuities.

The modeling methods above can be paired with other techniques when nuclear quantum effects are important. An example is path integral molecular dynamics (PIMD) [271,272], which has made remarkable progress in the last decade to make it approachable even at the DFT level of theory [203,273–278]. In PIMD, instead of following one trajectory of motion dictated by Hook's and Newtown's laws, the simulation follows several imaginary trajectories and integrates between them to yield a probability of hydrogen position and vector. These additional aspects indicate changes to the properties of hydrogen. **Figure 1-24** shows that the predicted diffusivity of hydrogen in BCC iron can be underestimated by several orders of magnitudes if nuclear quantum effects are not included [199], and this is supported by the findings of others [197,198,279]. The same study found that approximately 30% of the hydrogen binding to a vacancy in BCC iron is due to finite temperature effects, and about half of that arises from nuclear quantum fluctuations [199]. In addition to PIMD, the Many-Interactive-World theory of Hall, Deckert, and Wiseman [280], recently implemented by Sturniolo [281], has received increasing attention in hydrogen modeling. As a complement to PIMD, this approach describes the ground

state rather than a dynamic state at a finite temperature. These approaches provide a path to include quantum effects in our understanding of hydrogen trapping.

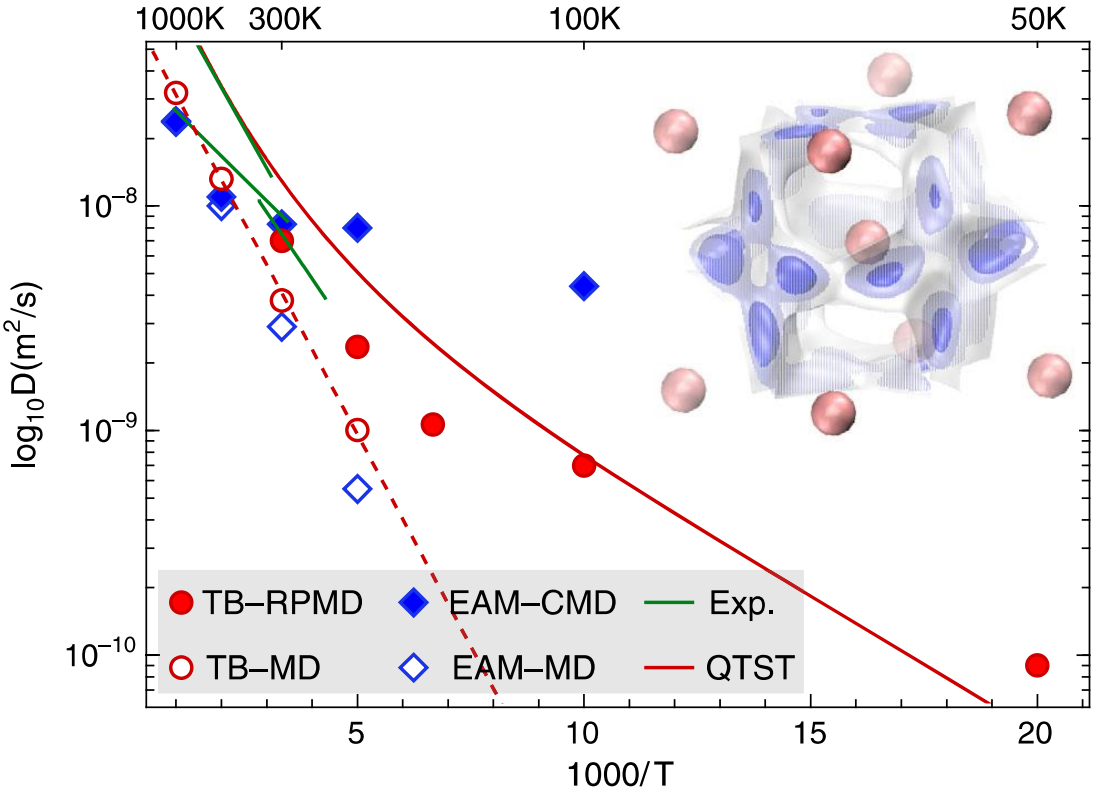

Figure 1-24. Effect of including nuclear quantum effects (including tunneling) on the calculated diffusivity of hydrogen in BCC-Fe. Hollow points only consider classical mechanisms (classical molecular dynamics), while filled points include nuclear quantum effects through path integral methods. Red points use tight-binding to describe inter-atomic interaction from [199], blue points use classical potentials from [197]. The green line is experimental data from [157,282] and the red line is quantum transition state theory (which also accounts for quantum tunneling) from [279]. Inset is the density distribution of hydrogen (blue iso-surfaces) in the BCC-Fe lattice (red sphered). Reproduced from [199]

1.3 Aims and Scope of this thesis

This thesis is dedicated to investigating the hydrogen distribution and its interaction with the microstructure in steels through characterization and modelling techniques. The following content is divided into four chapters: Firstly, the recent progress and the development for mapping hydrogen by high resolution microscope technique, mainly atom probe tomography with cryogenic workflow. Secondly, an engineering method is proposed to increase the hydrogen trapping capacity by introducing more carbon vacancies into the transition carbide. Two titanium-microalloyed ferrite steels are being observed: one is a steel acting as a benchmark with stoichiometric titanium carbide (TiC), the other is an experimental steel with a small addition of molybdenum (Mo) to form Ti-Mo carbides. The change of the microstructure and the hydrogen trapping capacity are examined by several microscopy techniques and first principle computational method (mainly density functional theory). Thirdly, the hydrogen interaction in pearlitic steel is observed, and the origin of hydrogen distribution is explained by density functional theory. Last, a simulation method to calculate the middle-ground defect concentration in atomic-scale is derived. As the difficulty for simulate the defect system for concentration range between the dilute and concentrated calculation haven't been addressed yet, we propose a computational efficient method to account for the concentration with a continuous energy profile. The method is verified with two systems i.e. hydrogen in hypo-stoichiometric cementite and hydrogen in bcc ferrite.

To summarize, this thesis is aiming to:

- Review the use of high resolution microscopy techniques for hydrogen mapping in fundamental scale. (Chapter 2)
- Propose a protocol to largely increase the hydrogen trapping capacity, which have the potential to mitigate the hydrogen embrittlement. (Chapter 3)
- Provide an experimental and simulation insight for hydrogen distribution in pearlite. (Chapter 4)
- Propose a new computationally efficient method to calculate the middle-ground defect concentration, derived from density functional theory calculation results. (Chapter 5)

Chapter 2 - Generic methods

As mentioned in the literature review session, atom probe tomography possesses the highest spatial resolution for mapping the hydrogen at a near-atomic level among all the techniques. In this chapter, the principle of hydrogen detection in APT and the requirements of using it for reliable analysis of hydrogen are introduced.

2.1 Atom probe tomography (APT)

An APT experiment requires a high positive voltage (*V*) applied to a very sharp needle-shaped specimen (with a tip radius less 100 nm) in an ultra-high vacuum (UHV, < 10^{-9} Pa) environment (**Figure 2-1**A). An intense electrostatic field (*F*) is thus generated at the apex of the tip [283,284]. The strength of this electrostatic field is proportional to the applied voltage and inversely proportional to the radius of the tip (*R*), which can be formulated as:

$$F = \frac{V}{k_f R}$$

where *kf* is the field factor with a value between 2 and 4 that accounts for the reduction of the actual field from the theoretical value due to the geometry of the tip and the local electrostatic environment. With the application of a high voltage, the potential energy state of the atoms at the tip surface is deformed, rendering a polarised surface that is deficit in electrons (**Figure 2-1**B). When the voltage is high enough and the field at the tip reaches a critical value that depends on the individual elements within the specimens (e.g., 52 V/nm for tungsten, 33 V/nm for iron, and 19 V/nm for aluminium [283]), the tip atoms are field-evaporated and leave the specimen with a positive charge (**Figure 2-1**B). The evaporated ions are then projected following the electrostatic field lines toward a position-sensitive digital detector, which provides the positions of evaporated ions for later data reconstruction. As illustrated in **Figure 2-1**A, data reconstruction is carried out using a simplified back-projection reconstruction geometry. By applying a high standing voltage to the specimen in combination with an additional voltage pulse (typically in the range of 5% to 25% of the standing voltage) applied to the hollow conical local electrode that allows the evaporated ions to pass through (**Figure 2-1**A), time-controlled field evaporation of individual atoms can be achieved. The measured time-of-flight of the detected ions is converted into the mass-to-charge-state ratio (unit: Dalton, Da), where the chemical identities of the ions, assuming full energy conversion from the electrical potential to

the kinetic energy of the ions [283], ultimately provides quantitative compositional analysis of the specimen.

The chemical identities and positions of the ions are computationally reconstructed into a three-dimensional atom map with knowledge of the experimental configuration, including the turn-on voltage for field evaporation, ion flight path, and the primary element within the specimen. In addition to the electrostatic field, time-controlled field evaporation can also be achieved by combining standing voltage with pulsed thermal energy provided by a focused and pulsed laser beam [285]. This laser-pulsing setup available in the commercial local electrode atom probe (LEAP) modules [284] enables APT analysis on less conductive materials such as oxides, semiconducting materials, and even organic specimens [229,283,284]. APT experiments require a cryogenic cooling unit ("cold finger" hereafter) (**Figure 2-1**A) to keep the specimen at cryogenic temperatures, supressing thermal atomic vibrations that can significantly reduce APT spatial resolution [283]. Cryogenic cooling and a programable heater allow the specimen temperature to be controlled between ~30–80 K, as required for APT [284]. To reach UHV, the LEAP uses a three-chamber specimen loading workflow, including the evacuations from 1) ambient to ~10^{-5} pascal (Pa) (~10^{-7} Torr) in a "loadlock" chamber, 2) ~10^{-5} to ~10^{-7} Pa (~10^{-7} to ~10^{-9} Torr) in an intermediate "buffer" chamber, and 3) < 10^{-9} Pa (10^{-11} Torr) in the ‘Analysis’ chamber where the cold finger is located [284].

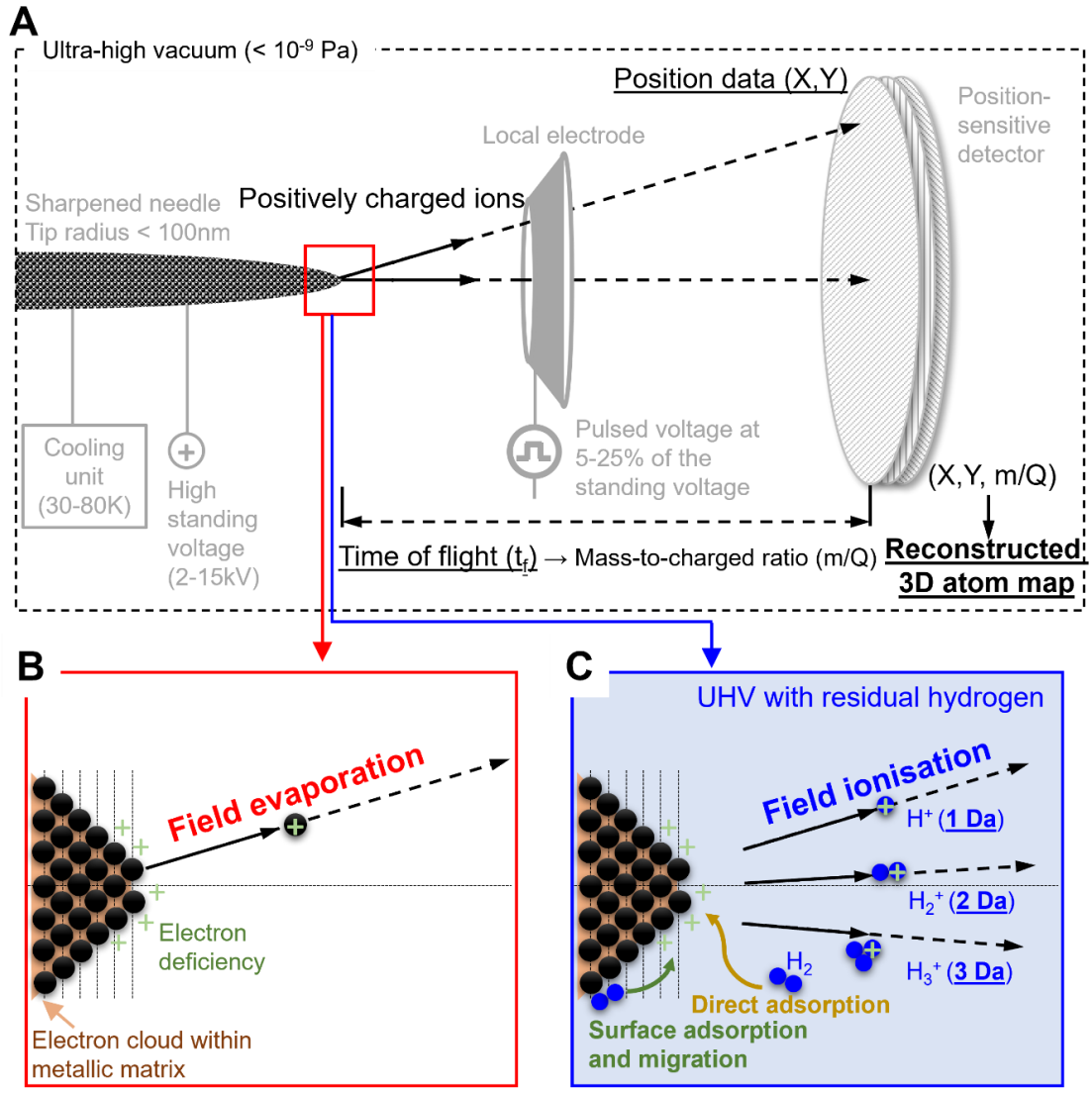

Figure 2-1. Schematic illustrations of (A) the experimental setup of APT, (B) field evaporation at the tip end in APT experiments, and (C) the supply mechanisms of environmental H and the types of H field ionisations that can be seen in APT data.

2.2 Hydrogen background noise in APT

The residual gas in the APT UHV analysis chamber is mainly composed of H [207–209,286], and its presence is mainly due to the use of H-permeable building materials, typically AISI 304 and AISI 316L stainless steels [286]. Felfer et al. [286] recently demonstrated that this residual H can be minimised by building the chamber with titanium, which has characteristically low H desorption, but this design has not yet been widely adapted by other APT laboratories.

In the presence of residual H, molecules of H_2 constantly adsorb onto the tip and its shank during APT experiments at cryogenic temperatures and are ionised from the

tip under the electrostatic field (**Figure 2-1**C). The H supply for such evaporation is derived from 1) direct adsorption onto the apex (dark yellow in **Figure 2-1**C) and 2) an initial adsorption on the shank surface followed by the surface diffusion toward the high-field tip end (dark green in **Figure 2-1**C) [210,287–290]. For specimens constructed from materials that have low H uptake, direct adsorption is dominant because the high field on the tip can enhance adsorption and the surface diffusivity of H at the cryogenic temperature of APT test is generally low [210,288]. In addition, experimental data has shown that increasing the laser energy in APT experiments under a controlled electrostatic field, which should heat up the tip and increase H surface diffusivity, does not lead to an increase of detected H, suggesting that H supply is not governed by surface diffusion [210,288]. In contrast, in the cases where sample materials have strong affinity to environmental H, its uptake and bulk diffusion can contribute a significant amount of H to the resulting APT data [213,291–294].

The adsorption and ionisation of residual H can result in the detection of H^+, H_2^+, and H_3^+ as 1, 2, and 3 Da in APT mass-to-charge spectra, respectively (**Figure 2-1**C) [210,287–290,292,294–296]. The ionisation of H_2^+ is a straightforward result of H_2 losing an electron, while the presence of H^+ involves a more complex dissociation process before ionisation. In addition to the catalytic dissociation of H_2 into H at the metallic surface, followed by H ionisation, H^+ can also be the result of post-ionisation at a critical distance (x_c) away from the tip where the electron of a desorbed ionic molecule can tunnel back to the tip after primary ionisation at the tip end [283,287,297]. Namely, the routes of H^+ formation can be [288,289,297]:

$$H_2 \xrightarrow{post\ ionisation\ at\ x_c} H^+ + H^0 \qquad (2\text{-}1)$$

where H^o is a neutral H atom that cannot be detected in APT with a correct time-of-flight due to the lack of electrostatic force on the atom, and:

$$H_2 \xrightarrow{surface\ ionisation} H_2^+ \xrightarrow{post\ ionisation\ at\ x_c} H_2^{2+} \xrightarrow{field\ dissociation} H^+ + H^+ \qquad (2\text{-}2)$$

It is not yet conclusive which mechanism is more dominant for H^+ formation. For H_3^+, it has been established that H_3 can be stable and present on a surface under a high electrostatic field [288,289,298]. Therefore, the formation of H_3^+ is reasonable when the field is sufficient for ionisation at the tip surface but insufficient for post-ionisation at x_c, which will otherwise generate H_2^+ and H^+. In voltage-pulsing APT experiments, the combined applied electrostatic field is generally high, so the fraction

of H^+ is often high in the APT mass spectrum data [289,292,294]. In contrast, the electrostatic field required for evaporation in laser-pulsing APT experiments can be lowered with the aid of laser energy; thus, detecting undissociated H_2^+ and H_3^+ is more common here than in voltage-pulsing APT [288,289,294,298–302]. **Figure 2-2** shows the changes in the intensities of H^+, H_2^+, and H_3^+ peaks under an increased electrostatic field at the tip in a series of APT experiments using constant laser-pulsing energy [289], confirming that high electrostatic fields (right) tend to dissociate H_2^+ and H_3^+ and produce higher H^+ than lower fields (left). In addition to molecular evaporation, the low-field experiment is known to lead to the detection of metallic hydride ions (e.g., MH^+ and MH_2^+, with M representing metals) in APT mass spectra if the metals have a strong affinity for H [288,298,300,302].

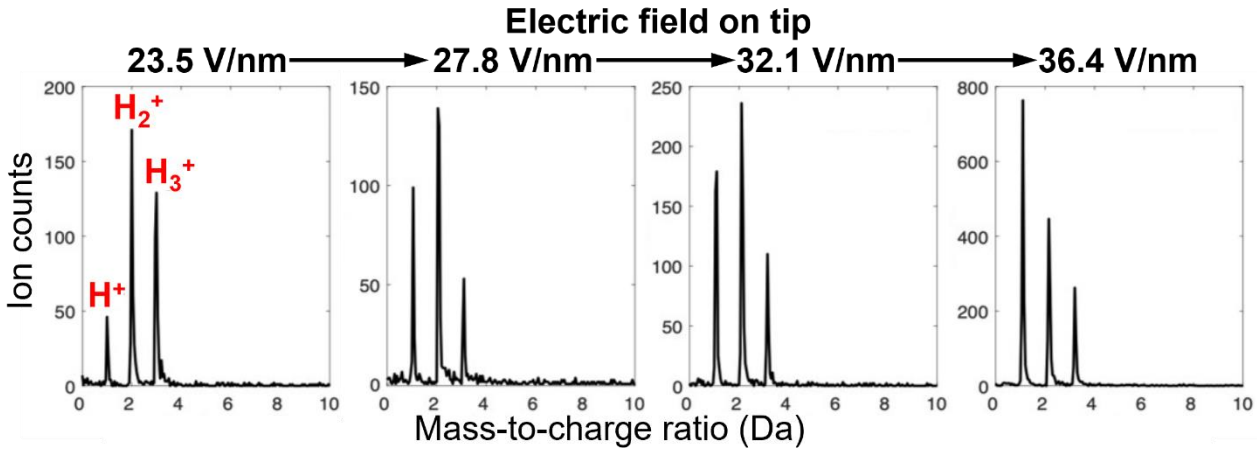

Figure 2-2. Comparison of the H^+, H_2^+, and H_3^+ intensities from low to high electrostatic fields in laser APT using Pt specimens. The experiments were performed in a homemade laser-pulsing APT at 60 K and used a 532 nm wavelength laser at 5 kHz with 2.5 nJ of pulsing energy and 10^{-8} Pa of residual H. Reproduced from [289].

2.3 Using hydrogen isotopes

Given that residual H can cause artefacts and complexity in the mass-to-charge spectra peak interpretation and that APT has an exceptionally high mass resolution, a strategy that has been adopted is to use deuterium (^{2}H or D) as a surrogate for H. D is a H isotope that is less abundant (0.015% natural abundancy) and has a larger atomic mass than the most abundant isotope, protium (^{1}H), but a very similar reactivity and behaviour [189,190,230,231,233,292,294–296,300,301,303]. Due to their different masses, ^{2}H has a slightly lower diffusivity than that of ^{1}H [279]. This difference is typically not significant at ambient temperature and within the small scale of APT

specimens where the diffusion length is limited [304]. Recently, tritium (^{3}H) was also used in an APT experiment in a study concerning the chemical changes of Li-Al-O ceramic specimens after neutron radiation [305].

D charging has been used in both voltage- and laser-pulsing APT experiments [189,190,230,231,233,292,294–296,300,301,303]. However, there has not been a tangible solution to differentiate the contribution of $^{2}H^{+}$ from the artefact H_2^{+} peak at 2 Da (**Figure 2-2**), posing a significant challenge in confidently quantifying the D content and resolving the location of D signal in laser-pulsing APT [295,296,300]. **Figure 2-3** is a comparison between voltage- and laser-pulsing APT analyses using both uncharged and D-charged steel specimens with trapped D [295]. In a voltage-pulsing experiment (top figure), the D-charged specimen (orange) resulted in a significant peak at 2 Da with respect to that from the uncharged specimen (blue). In contrast, in a laser-pulsing APT dataset (bottom figure), both D-charged and uncharged specimens resulted in significant peaks at 2 Da (red arrow), undermining the confidence of peak assignment in APT data analysis. Although significant effort has been made to enable the application of laser-pulsing APT in H analysis by using the metallic deuteride peaks and the $^{2}H_2^{+}$ peak at 4 Da that does not overlap with the peaks of H artefact [289,300–303], it is generally recommended to use a voltage-pulsing setup when the tested materials are sufficiently conductive for good yield under voltage-pulsing analysis.

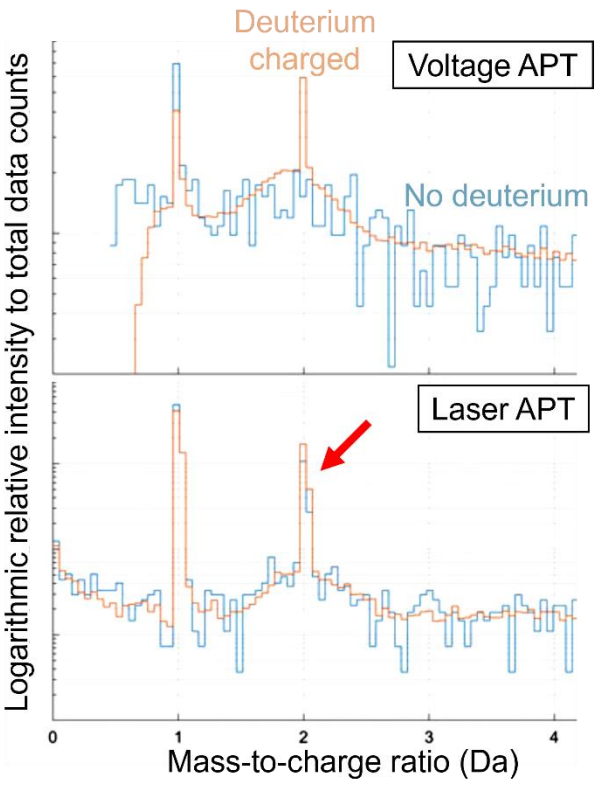

Figure 2-3. Comparison between the mass-to-charge spectra of voltage- (top) and laser- (bottom) pulsing APT from D-charged (orange) and uncharged (blue) steel specimens that contain vanadium carbide H traps. The experiments used a LEAP 3000 HR with a 20% pulse fraction or 532 nm wavelength laser with 0.4 nJ pulse energy, 200 kHz pulse frequency, and 50 K stage temperature. The cryogenic transfer method was used after catholically loading D at 2.1 V in 0.1M NaOH in D_2O to minimise D loss. The signal intensities were normalised to the total data counts. Reproduced with permission from [295].

Whilst residual H in the instrument chamber can generate 1-Da and 2-Da peaks that obscure the observations of H and D introduced into the microstructure, these peaks cannot always be assigned directly to background H. For materials such as titanium that absorb significant amounts of H, utilising APT to uniquely identify signals correlated with H-attracting features, including hydride and phase boundaries, has been shown to be possible using the spatial variation of the 1-Da signal [293,306]. It has also been demonstrated that the 1-Da and 2-Da signals are correlated with H and D, respectively, that diffuse into H traps in steels after electrochemical charging [292]. Therefore, there is clear evidence in the literature that signals from both the 1-Da and 2-Da peaks can be treated as real when materials and experimental conditions are carefully analysed and proven to be different from the background.

2.4 Hydrogen charging

Hydrogen may be intentionally introduced into atom probe specimens through 1) direct ion implantation [285,307,308], 2) water corrosion [309], 3) direct exposure to gaseous H/D (gas charging) [190,230,231,233,310–315], which generally has a safety limit in pressure and often requires additional heat to facilitate H uptake to a practical rate, or 4) water electrolysis (cathodic charging), which uses a straightforward setup to effectively generate high H fugacity at ambient conditions around a conductive specimen. The latter option has been used in the most studies [88,189,294,295,316,317]. For electrolytic deuteration, it has been found that the use of deuterated electrolytes for cathodic charging did not affect the resulting D content [292]. **Figure 2-4** compares the APT mass-to-charge spectra in the voltage-pulsing APT experiments of the specimens catholically charged in 1) heavy water (D_2O) with a deuterated electrolyte (NaOD), 2) D_2O with a normal electrolyte (NaOH), 3) normal water (H_2O) with NaOD, and 4) normal H_2O with NaOH, as shown in black, red, green, and blue, respectively. Using only heavy water and an undeuterated electrolyte (red) is as sufficient as fully deuterated electrolyte (black) to introduce D into the steel specimens with H traps.

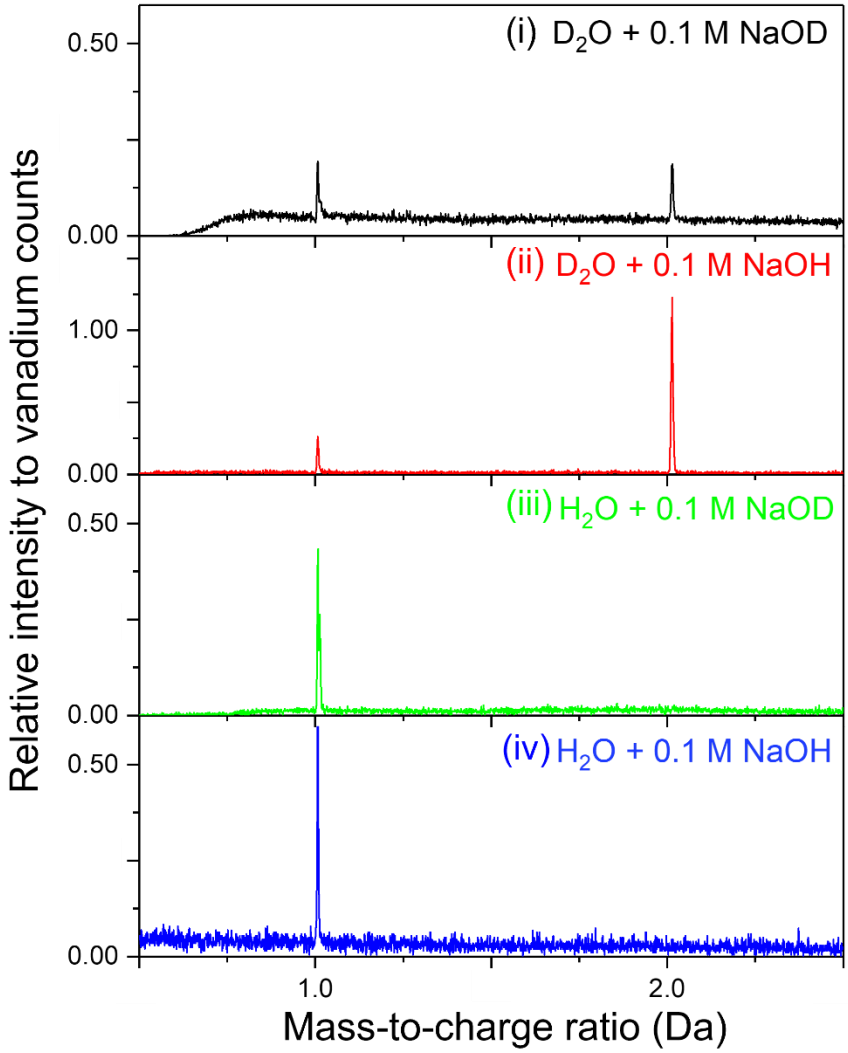

Figure 2-4. Mass-to-charge spectra from four different H charging electrolytes. The APT experimental setup and sample material are the same as those shown in Figure 2-3. The signal intensities were normalised to the vanadium intensities because the material contains a significant number of vanadium-based carbide H traps. Therefore, the vanadium counts can represent the amount of H trapped in the specimens. Reproduced from [292].

2.5 APT with cryogenic-sample transfer capability

To address the fast H desorption/diffusion from specimens with high H diffusivities, custom cryogenic workflows have been developed to account for the scale of the needle-like specimen and the high vacuum sample loading process, leading to the birth of cryogenic APT (cryo-APT) [88,189,292,317–319]. Cryo-APT has also exhibited strong potential to be combined with focused ion beam (FIB) and cryogenic FIB (cryo-FIB) techniques to prepare site-specific specimens [229,301,320–326]. For experiments that use gas charging, cryo-APT can be achieved by adding a cooling

unit onto the sample stage in the gas charging chamber [190,230,231,233,314,315,319]. An example system that functions as an attachment to a commercial LEAP 3000 is shown in **Figure 2-5**A, with its instrument layout diagram shown in **Figure 2-5**B [314]. For cryo-APT workflows involving cathodic charging, a glovebox (**Figure 2-5**C) is important for creating a moisture-free environment to rapidly plunge-freeze the puck in a liquid nitrogen (LN_2) bath after electrolytic deuteration (**Figure 2-5**D). Moisture control can eliminate ice condensation on APT needle samples, which is crucial for achieving the needle apex sharpness required for the success of cryo-APT experiments [292,327]. The glovebox should also include a loadlock (**Figure 2-5**C) to evacuate the cryo-sample to a pressure sufficiently low enough that it can be connected with a sample loading interface in the LEAP. This process involves using a commercially available "suitcase" that can store and transfer the cryo-sample under low pressure between the glovebox loadlock (**Figure 2-5**C) and the LEAP loadlock chamber (**Figure 2-5**E) [88,189,327]. In a commercial LEAP, metallic carousels are used for sample storage and transfer between the loadlock and buffer chambers. Cryo-APT requires a custom carousel with a slot composed of thermally insulating materials such as polyetheretherketone (PEEK) (**Figure 2-5**F) to minimise warming of the sample during the loadlock-buffer transfer. A pre-cooled "piggyback puck" (**Figure 2-5**F) will also be needed to provide additional coldness to the cryo-puck during sample handling in the LEAP. The cryo-transfer workflow is complete when the sample arrives at the cryo-stage in the LEAP analysis chamber, which is typically at 30–80 K. This temperature range is lower than what is achievable using LN_2 as the coolant (100–170 K) [88,324,327].

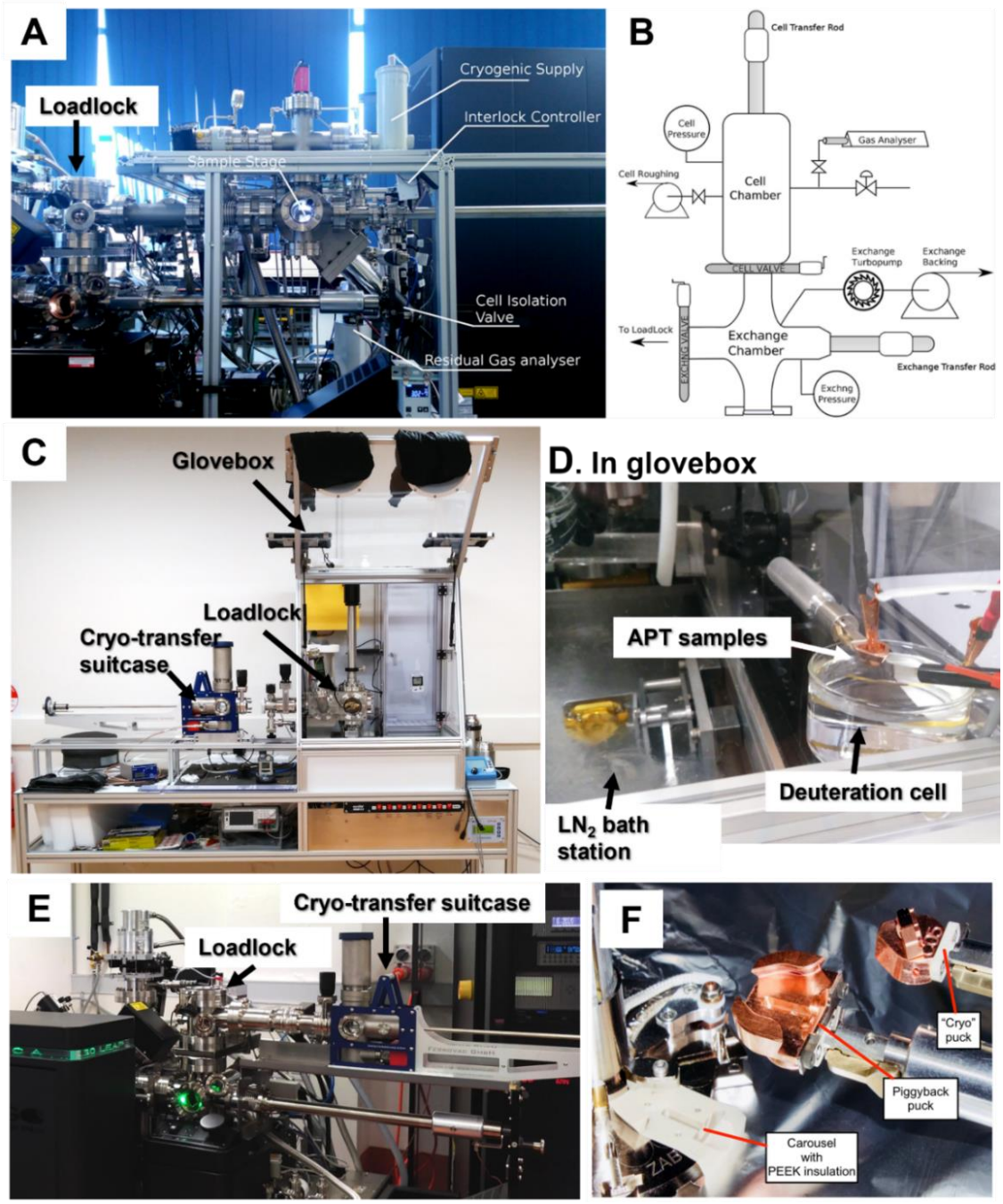

Figure 2-5. Cryo-APT instrumentation. (A) and (B) are photos of a homemade cryo-APT gas charging system attached to a LEAP 3000 HR at the University of Oxford [314]. (C) shows a custom glovebox with a loadlock that can be attached by a commercial cryo-transfer suitcase (Ferrovac), and (D) provides a view of the LN_2 bath and deuteration cell within the glovebox of (C) [88]. (E) shows the attachment of the commercial cryo-transfer suitcase onto a LEAP 4000 Si at the University of Sydney. (F) shows a custom carousel with a PEEK slot and a piggyback puck that can minimise the heat transfer from the LEAP to the cryo-puck [327].

Chapter 3 - Engineering metal-carbide hydrogen traps in steels

3.1 Background

As mentioned in the previous content, one potential solution to mitigate HE is the incorporation of hydrogen traps into the alloy's microstructure. These traps would impede the diffusion of hydrogen towards areas susceptible to HE, such as microcracks. Nanoscale transition-metal carbides like titanium (Ti) and molybdenum (Mo) carbides have shown promise as effective hydrogen traps due to their high number density and even distribution within steels. However, the precise mechanism through which they trap hydrogen remains unclear, specifically whether it's due to the carbide's bulk or its interface with the steel's ferrite structure.

To address this, we employed both theoretical and experimental techniques, including density functional theory, atom probe tomography, and thermal desorption spectroscopy to compare the hydrogen trapping behaviour in two prototype ferritic steels. These steels contained titanium carbide (TiC) and a combination of titanium and molybdenum carbides ((Ti,Mo)C), respectively. In the case of (Ti,Mo)C, the addition of substitutive molybdenum was intentional. This introduction of molybdenum created carbon vacancies that could serve as potential hydrogen traps, providing pathways for hydrogen to penetrate the carbide's bulk. In contrast, stoichiometric TiC, which had fewer carbon vacancies, was expected to exhibit interfacial hydrogen trapping, differing from the behavior observed in (Ti,Mo)C.

The content of this article is largely the product of the work of **Pang-Yu Liu** under the supervision of Julie M. Cairney, Hao Chen and Yi-Sheng-Chen. **Pang-Yu Liu** conducted the atom probe tomography (APT) experiments, the data analyses and drafted the manuscript. Boning Zhang conducted the density functional theory (DFT) simulation, the Thermal desorption spectroscopy (TDS) experiments, and contributed to drafting the manuscript. Ranming Niu conducted the Transmission electron microscopy (TEM) experiments and contributed to the manuscript. Shao-Lun Lu and Chao Huang supported the APT and TEM experiments. Maoqiu Wang supported the TDS experiments. Fuyang Tian supported the DFT simulation. Yong Mao provided the computational resource for the simulation and supported the DFT simulation. Tong Li conceptualized the project and participated in the manuscript development. Patrick A. Burr participated in the data analysis and the manuscript development. Hongzhou Lu,

Aimin Guo and Hung-Wei Yen provided funding support, supervised the project, and participated in the manuscript development. Julie M. Cairney provided the microscope facilities, supervised the project, and finalized the manuscript. Hao Chen initiated and conceptualized the project, provided the samples and funding, supervised the project, and participated in the manuscript development. Yi-Sheng Chen initiated and conceptualized the project, designed the protocols of analyses, provided funding support, supervised the project, contributed to the manuscript, and finalized the manuscript.

Results are presented in the form of a manuscript that has been accepted by '***Nature Communications***'.

3.2 Submitted manuscript

Engineering metal-carbide hydrogen traps in steels

Pang-Yu Liu[1,2,#], Boning Zhang[3,4,#], Ranming Niu[1,2,#], Shao-Lun Lu[1,5], Chao Huang[1,2], Maoqiu Wang[6], Fuyang Tian[7], Yong Mao[4], Tong Li[8], Patrick A. Burr[9], Hongzhou Lu[10], Aimin Guo[10], Hung-Wei Yen[5,11,*], Julie M. Cairney[1,2,*], Hao Chen[3,*], Yi-Sheng Chen[1,2,5,*]

[1] Australian Centre for Microscopy and Microanalysis, The University of Sydney, Sydney, NSW 2006, Australia
[2] School of Aerospace, Mechanical and Mechatronic Engineering, The University of Sydney, Sydney, NSW 2006, Australia
[3] School of Materials Science and Engineering, Tsing Hua University, Beijing 100084, China
[4] Materials Genome Institute, School of Materials and Energy, Yunnan University, Kunming 650091, China
[5] Department of Materials Science and Engineering, National Taiwan University, Taipei 10617, Taiwan
[6] Central Iron & Steel Research Institute Company Limited, Beijing 100081, China
[7] Institute for Applied Physics, University of Science and Technology Beijing, Beijing 100083, China
[8] Institute for Materials, Ruhr-Universität Bochum, Bochum 44801, Germany
[9] School of Mechanical and Manufacturing Engineering, University of New South Wales, Sydney, NSW 2052, Australia
[10] CITIC Metal Co., Beijing 100027, China
[11] Advanced Research Center For Green Materials Science and Technology, National Taiwan University, Taiwan

[#] The authors contribute equally to this work.
[*] Corresponding authors: Yi-Sheng Chen (yi-sheng.chen@sydney.edu.au); Hao Chen (hao.chen@mail.tsinghua.edu.cn); Julie Cairney (julie.cairney@sydney.edu.au); Hung-Wei Yen (homer.yen@ntu.edu.tw)

Abstract
Hydrogen embrittlement reduces the durability of the structural steels required for the hydrogen economy. Understanding how hydrogen interacts with the materials plays a crucial role in managing the embrittlement problems. Theoretical models have indicated that carbon vacancies in metal carbide precipitates are effective hydrogen traps in steels. Increasing the number of carbon vacancies in individual metal carbides is important since the overall hydrogen trapping capacity can be leveraged by introducing abundant metal carbides in steels. To verify this concept, we compared a reference steel containing titanium carbides (TiCs), which lack carbon vacancies, with an experimental steel added with molybdenum (Mo), which form Ti-Mo carbides comprising more carbon vacancies than TiCs. We employed theoretical and experimental techniques to examine the hydrogen trapping behavior of the carbides, demonstrating adding Mo alters the hydrogen trapping mechanism, enabling hydrogen to access carbon vacancy traps within the carbides, leading to an increase in trapping capacity.

Key words: Steel, hydrogen embrittlement, hydrogen trapping, atom probe

tomography, carbide precipitate

Introduction

Hydrogen is a carbon-free energy carrier that can be produced without carbon footprint at scale, offering a solution to meet the world's increasing energy demand and the goal of transition to net zero emissions by 2050 [1]. A significant challenge to delivering hydrogen energy at scale is hydrogen embrittlement [2]. This problem can cause unpredictable failures of metallic components, adding significant costs for monitoring and maintaining infrastructural integrity [3].

Steel is a cost-effective material for constructing large-scale infrastructure, despite its susceptibility to hydrogen embrittlement [3]. There are four methods that have been considered to manage hydrogen embrittlement in steels [4]. The first is pre-service hydrogen desorption, which can remove pre-existing hydrogen in materials [5]. However, this method is not suitable for most services where hydrogen pickup occurs during service, such as bearing [6] and gas pipes [7].The second is adding hydrogen-impermeable coatings onto the steel surface to decrease the kinetics of hydrogen uptake [8]. However, the effectiveness of this method depends on the quality and durability of the coatings, which may have defects, or develop them in service through scratching, erosion or corrosion. The third method is mixing passivating gases, such as oxygen, into the bulk transmitting gas to reduce the probability of hydrogen adsorption on the surface and absorption in materials [9]. But there are additional costs associated with the separation of the gases before being used for applications such as fuel cells, where hydrogen purity is crucial. Finally, hydrogen traps can be introduced into the material microstructure to immobilize or trap absorbed hydrogen, limiting the amount of hydrogen participating in the embrittling process [10–12]. This approach provides materials with intrinsic resistance to hydrogen embrittlement and can be applied synergistically in parallel with other approaches [4]. Embrittlement-resistant alloy design must consider not only hydrogen trapping but also other application requirements, such as strength, ductility, corrosion resistance, and thermal stability [4].

To design a steel microstructure that can effectively trap hydrogen and decrease embrittlement, three criteria must be considered: 1) the susceptibility of incorporated traps to hydrogen embrittlement, 2) trap density, which determines the

efficiency of the microstructure in hindering hydrogen diffusion, and 3) trapping energy, which measures how effectively a trap can retain hydrogen atoms [4,13].

Microstructural features in steel lattice, such as vacancies, dislocations, grain boundaries, and second phases (both their bulk and surfaces) can act as hydrogen traps [4,14]. However, not all of these traps are effective in resisting hydrogen embrittlement. For instance, dislocation and vacancy traps can be produced in high density but are weak traps and can actually contribute to hydrogen embrittlement in steels [15,16]. Hydrogen trapped at dislocations can reduce the stress required for dislocation gliding, leading to increased plastic deformation under high load (near yield strength) [17]. This effect is called hydrogen-enhanced local plasticity (HELP) and explains many characteristics of hydrogen embrittlement, including the dependence on strain rate and hydrogen diffusivity [17,18]. Vacancies can attract and stabilize hydrogen atoms, leading to the formation of more vacancies under load, known as hydrogen-enhanced strain-induced vacancies (HESIV) [19,20]. This effect can lead to the formation, growth, and coalescence of microvoids under high load, causing early failure in the steel, like for HELP[19,20].

Hydrogen can also be trapped at grain boundaries and phase boundaries. However, there has been suspicion around whether such trapped hydrogen under high loads can cause hydrogen-enhanced decohesion (HEDE), leading to micro-crack initiation at the interface and resulting in macroscale embrittlement [18,21,22]. In addition, under high loads, hydrogen can be trapped at the crack tip where load is concentrated and lattice is expanded, forming a quasi-hydride phase that impedes the emission of dislocations, causing macroscopic cleavage in consequence [23]. So far, it is understood that the exact cause of hydrogen embrittlement is subject to many factors of material service conditions (such as applied load and hydrogen content) and hydrogen-susceptible microstructure (such as inclusions). High caution is always required when associating hydrogen-induced failures with a single mechanism. In some specific cases, it is even found that multiple mechanisms can operate synergically and simultaneously [24]. As such, developing a universally applicable mitigation strategy has been a challenging task.

Second phase precipitates, like carbides, can be strong traps, can contribute to material strength, and can be produced in high density [4]. In body-centered cubic (BCC) ferritic steels, transition metal carbides (with M as Ti, V, Mo, Nb, etc.) are of interest for hydrogen trapping as they can be produced at exceptionally high density

with excellent dispersion. For this purpose, a metallurgic phenomenon called 'interphase precipitation' is useful to form high-density carbides in steels. This involves isothermal tempering between 600 and 800 °C immediately after austenization (i.e., without quenching prior to tempering) [25–27], so that precipitates are generated on the interphase boundary during the austenite-to-ferrite phase transformation, leading to the formation of a high density of nanosized metal carbides aligned in bands. As the density and spacing between the resulting metal carbides are sensitive to the isothermal temperatures used [27,28], it is possible to achieve engineering steel microstructures with a desired hydrogen trap density to achieve good embrittlement resistance. Furthermore, since the transition metals have low solubility in ferrite, the production of high-density metal carbides generally requires only a modest amount of alloying (typically at 0.1 to 0.3 weight percent, wt.%). This level of alloying is described as 'microalloying' and is a very cost-effective method for steel strengthening [29].

For the most effective trapping, it is desirable to create a high density of traps, but also to maximize the trapping energy and capacity. Two microstructural factors can influence this: metal carbide matrix-interface coherency and carbon vacancy in carbide. For coherent and semi-coherent interfaces, lower coherency of the ferrite-metal carbide interface means a higher number of dislocations, which can act as hydrogen traps, leading to a higher overall trapping capacity [30,31]. However, taking advantage of this effect requires coarsening (over-ageing) the metal carbides, which reduces the overall number carbides and the mechanical strength of the alloy. Additionally, excess hydrogen trapped at incoherent interfaces under high loads can cause micro-cracks through HEDE [18,21,22]. Manipulation of interface coherency is therefore a double-edged sword when it comes to designing hydrogen traps to increase hydrogen embrittlement resistance.

Computational studies suggest that carbon vacancies in metal carbides are a promising hydrogen trap due to their high trapping energy compared to interface misfit dislocations [32–35]. When a carbon vacancy is located near a metal carbide surface, it can trap hydrogen near the interface, even if the interface is fully coherent [36]. However, theoretical models indicate that a high kinetic energy is required for hydrogen atoms to overcome the diffusion barrier near the metal carbide-matrix interface and reach the carbon vacancies inside [32–35]. Di Stefano et al. [33] have used first-principle calculations to demonstrate that it is possible to reduce this barrier by

increasing the concentration of near-interface and interior carbon vacancies in titanium carbide (TiC) to create a diffusion path for hydrogen to reach strong carbon vacancy traps inside the metal carbide. A similar strategy was proposed in Kirchheim's work [37], which considers the near-interface carbon vacancy traps in vanadium carbide and is in agreement with other research [34,38]. The number of carbon vacancy sites is greater than the number of interface misfit dislocations, particularly so in transition metal carbides that have a high interface coherency and a low number of misfit dislocations at the interface. Therefore, a potential strategy for increasing hydrogen trapping capacity is to create a type of metal carbide with a very high density of 'accessible' and strong carbon vacancy traps to accommodate abundant hydrogen atoms per metal carbide. This strategy can be further leveraged against the high metal carbide number density achieved by interphase precipitation to potentially create a steel microstructure with exceptional hydrogen trapping capacity.

In this work, to explore the effectiveness of increasing the carbon vacancy concentration in metal carbides, we created two ferritic steels with a high-density of metal carbides: one with TiC and another with titanium-molybdenum carbides ((Ti,Mo)C). Both have a NaCl rock salt structure [39]. Mo, a VI-B element, substitutes for Ti, in the (Ti,Mo)C and, importantly, creates additional carbon vacancies to maintain the electron valency balance within the metal carbide lattice. We then compared the hydrogen trapping behavior of each type of metal carbide at multiple length scales. At the atomic level, we used first-principle calculations based on density functional theory (DFT) to examine the hydrogen inward migration and the presence of excess energetically stable carbon vacancies in the carbides containing Mo. At the macroscale, we employed thermal desorption spectroscopy (TDS) to measure the increased amount of trapped hydrogen in the (Ti,Mo)C steel compared to the TiC steel. The TDS specimens were intentionally left at room temperature for a long period of time to desorb the hydrogen trapped by lattice defects and to leave only carbide-trapped hydrogen for measurement. At the nanoscale, we verified that both metal carbides had similar lattice and interface structures using scanning transmission electron microscopy (STEM), showing that they had a similar size, number density, and lattice structure. Finally, we used cryogenic atom probe tomography (cryo-APT) to study the hydrogen trapping mechanisms of both metal carbides in detail, a technique developed in our previous work [40,41]. Cryo-APT allowed us to preserve the hydrogen distribution in charged samples by handling hydrogen-charged samples at

cryogenic temperature [42]. This allowed us to compare the hydrogen near (Ti,Mo)C and TiC interfaces. Our findings highlight the crucial role of carbon vacancies in transition metal carbides, forming through the addition of Mo, for a remarkable increase in hydrogen trapping capacity.

Results

First-principle simulations of hydrogen migration, carbon vacancy stability, and hydrogen trapping in metal carbides

To test and verify the approach of using carbon vacancies to facilitate the internalization of hydrogen trapped at a metal carbide-matrix interface, we created a DFT model to probe the behavior of hydrogen at a phase boundary between BCC ferrite and a NaCl-structured metal carbide, specifically a $Ti_{1-x}Mo_x$ carbide where x represents the number of substitutional Mo atoms in a TiC unit cell. The model is depicted in Figure 1A, which shows Fe, Ti, Mo, and C atoms in black, green, blue and magenta, respectively. Fig. 1a is a 2-dimensional (2-D) view of a 3-D $(Ti_{0.75}Mo_{0.25})C_{0.875}$ supercell in the $[0\ 1\ 0]_{ferrite}$ direction, which corresponds to the $[1\ 1\ 0]_{carbide}$. This orientation relationship (OR) between ferrite and the NaCl-structure metal carbide is known as the Baker-Nutting (B–N) OR [25–27], and occurs due to the covalent bond between Fe and C atoms at the interface, leading to a highly coherent interface, as outlined by a grey dot line in Fig. 1a. The DFT model contains randomly distributed Mo atoms occupying Ti sites in the metal carbide lattice, generated using the similar atomic environment (SAE) method [43]. Three consecutive carbon vacancy sites were created (magenta broken squares, V1-3) to simulate hydrogen diffusion toward the interior of the metal carbide at the proximity of the interface. In Fig. 1a, we placed a solute hydrogen atom (depicted as a red sphere) initially in a ferrite interstitial site near the interface, and the location of which is denoted as 0. We then analyzed the energy required for hydrogen migration (indicated by red arrows) in the presence of the three consecutive carbon vacancies.

Fig. 1b is a group of 3-D models showing various sites: 0, V1, V2, and V3, with the hydrogen solute and surrounding Fe, Ti, and Mo atoms. Site 0 is a tetrahedral interstitial site in a BCC lattice near a B–N OR interface. V1 is a quasi-octahedral carbon-centered unit in a NaCl lattice near the interface, and V2 and V3 are both octahedral carbon-centered units in a NaCl lattice. We placed two Mo atoms adjacent

to the vacancy, so the compositions of the models can be consistent with the bulk chemistry, i.e., $(Ti_{0.75}Mo_{0.25})C_{0.875}$. Similar models were created (not shown) to study the hydrogen migration in TiC counterpart structures. To establish the energy profile of the hydrogen atom migrating in these models, we used climbing image nudged elastic band (CI-NEB) modeling [44] and the results are shown in Fig. 1c. This figure shows the solution energy profiles of the hydrogen atom at 0, V1, V2, and V3 sites and their corresponding saddle points. We examined the cases of a Mo-doped TiC lattice (blue) and a pure TiC lattice (green), both of which have connected carbon vacancy structures. We found that the addition of Mo reduces the energy barrier for the hydrogen atom to diffuse from one carbon vacancy site to another (0.85 eV and 0.8 eV with Mo compared to 1.02 eV and 1.08 eV for Mo-free TiC), while the carbide-entering energy barrier is only slightly increased by 0.08 eV for the Mo-containing carbide (0.38 eV versus 0.30 eV). We consider this difference is insignificant given that the diffusion energy of interstitial hydrogen in BCC iron lattice is 0.088 eV [45].

Note that our model only considered single hydrogen occupancy in each carbon vacancy. As per Di Stefano et al. [33], the diffusion barrier for a hydrogen atom decreases when a second hydrogen is present in the same carbon vacancy due to the intrinsic repulsion between ionic hydrogen particles. Their finding is particularly relevant to situations with a substantial hydrogen supply that is the regime in the hydrogen trapping observation experiments presented in later discussion.

As the quantity of carbon vacancies plays a crucial role in allowing hydrogen to access traps inside metal carbides, we used DFT to examine the effect of Mo addition on both the formation of carbon vacancies and the hydrogen trapping energy. By using SAE, we developed 6 random 3 x 3 x 3 metal carbide bulk supercells, each containing 108 metal (either Ti or Mo) sites and 108 carbon sites. The supercells for the interface models are illustrated in Supplementary Figure 1. The compositions of both bulk metal carbide and metal carbide-ferrite interfaces are listed in Fig. 1d, and the octahedral unit cells are shown in Fig. 1e as parts of the entire supercells, where metal, carbon, and Fe sites are presented in light blue, magenta, and black, respectively. These result in the light blue and black data points, respectively, in Figs. 1f and 1g. We studied the carbon vacancy formation energy by removing carbon atoms in the models that have differing numbers of adjacent Mo atoms around a carbon site. As a result, Fig. 1f provides the carbon vacancy formation energy as a

function of number of adjacent Mo atoms, where a more negative value indicates greater stability. Fig. 1f reveals that, regardless of whether in bulk or at an interface, a carbon vacancy tends to be more stable in the presence of proximal Mo atoms, which is consistent with existing literature [46–50].

To determine the hydrogen trapping energy (i.e., the energy difference between hydrogen at traps and in a ferrite lattice), we then placed a hydrogen atom in each of the carbon vacancies, with their varying numbers of neighboring Mo atoms, resulting in Fig. 1g. We did not find that increasing the number of adjacent Mo resulted in higher trapping energy. Instead, more adjacent Mo atoms reduces the stability of the trapped hydrogen (i.e., the carbon vacancy hydrogen trapping energy), which is consistent with literature [34,51,52]. The dotted line at -0.5 eV in Fig. 1g indicates the energy below which hydrogen traps are unlikely to trap a hydrogen atom for a meaningful duration in a material service at room temperature [4]. Considering both the carbon vacancy stability and the hydrogen trapping strength, our sample with moderate Mo doping in (Ti,Mo)C, with a 1:2 Mo-to-Ti ratio (i.e., 2 Mo every 4 Ti in an octahedral cell), highlighted by the orange shade in Fig. 1G, is expected to achieve good overall synergy. Furthermore, previous research has shown that (Ti,Mo)C with this 1:2 Mo-to-Ti ratio (or $Ti_{1-x}Mo_xC$ with x = 0.33) is the most abundant carbide type in an interphase-precipitate Mo-added TiC steel, regardless of the amount of Mo addition [46]. This type of metal carbide is therefore suitable to verify the effect of incorporating a high density of carbon vacancies on the hydrogen trapping in a metal carbide-containing steel.

In summary, our modelling suggests that the addition of Mo increases the accessibility of internal carbon vacancies to hydrogen by reducing the diffusion energy barrier between the carbon vacancies in the metal carbide bulk (Fig. 1c). This diffusion barrier reduction is in addition to the formation of high-density carbon vacancies (Fig. 1f), which are likely interconnected in metal carbide bulk. Also, our model shows that the Mo-associated carbon vacancy traps have sufficient trapping strength (Fig. 1g). We consider the combination of the above can facilitate the access of hydrogen to the carbon vacancy traps in metal carbide bulk, opening up more trapping sites to the readily available carbide interface traps. [53]

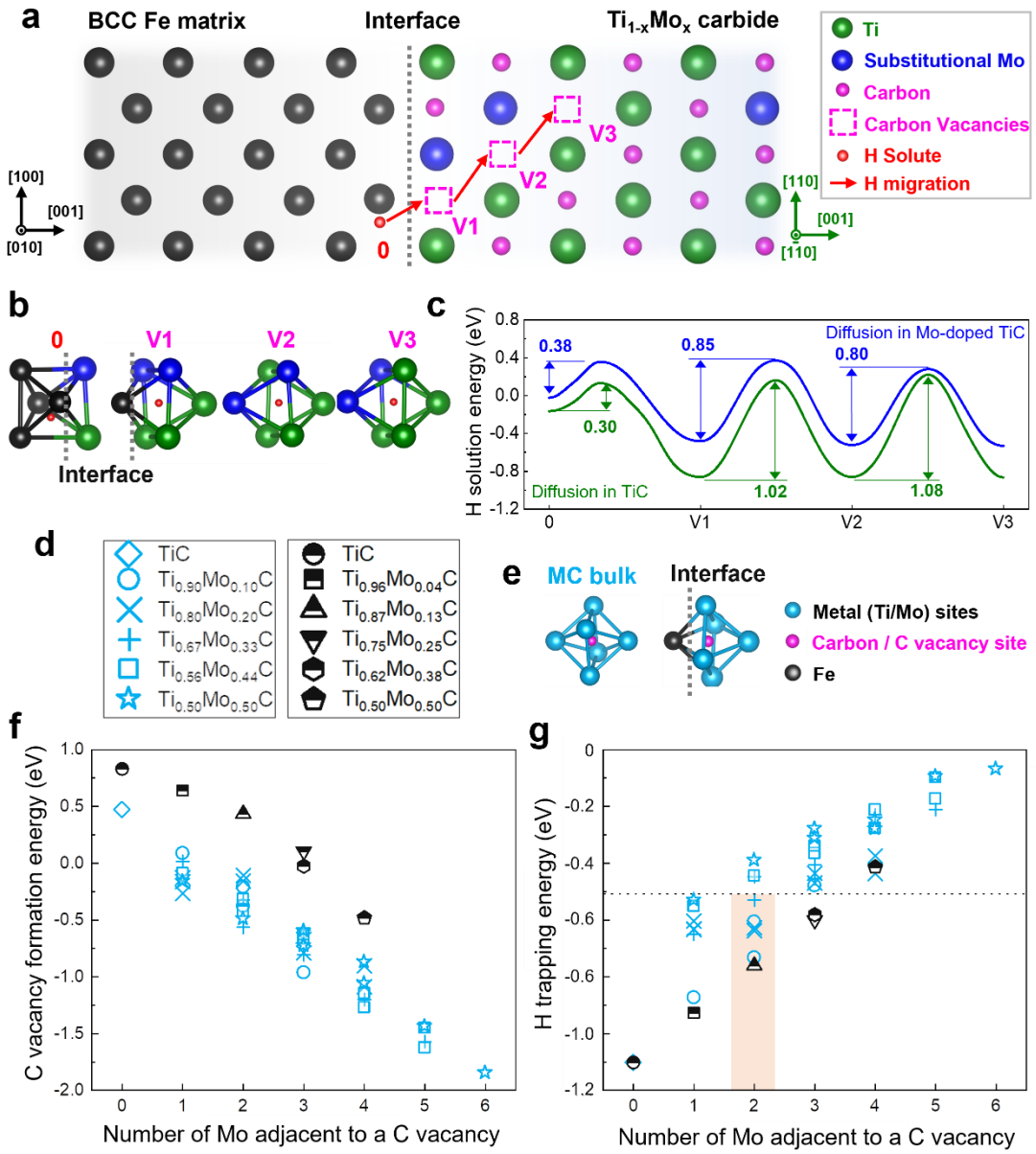

Fig. 1. First-principle simulations showing the effect of Mo addition on hydrogen diffusion, trapping, and carbon vacancy stability in a NaCl-structure metal carbide. (a) 2-D conceptual sketch of a coherent ferrite-metal carbide interface 3-D model with 3 connected carbon vacancies (magenta dashed squares as noted V1-3), a hydrogen solute atom (red sphere at the '0' position), Fe (black spheres), Ti (green spheres), Mo (blue spheres), and C atoms (magenta spheres). The sketch is displayed along $[0\ 1\ 0]_{ferrite}$ which is also $[1\ 1\ 0]_{carbide}$ due to the orientation relationship of the two phases. (b) 3-D illustrations of the atomic coordinate configurations corresponding to the 0 and V1-3 sites in Fig. 1A. (c) Solution energy profiles corresponding to (b) for a hydrogen atom at the ferrite-carbide interface and in the connected carbon vacancies with (blue) and without (green) the adjacent Mo atoms in the NaCl-structure metal carbide models. (d) Compositions and annotations of the metal carbide supercells used to create Figs. (f) and (g) in the case where the vacancy is inside the carbide (light blue) and at the ferrite-carbide interface (black). (e) 3-D model sketches of the carbon-site-centered unit cells considered for the TiC bulk and at the ferrite-carbide interface. (f) Energy to form a carbon vacancy as a function of the number of adjacent Mo atoms. (g) Hydrogen trapping energy in a carbon vacancy

as a function of the number of adjacent Mo atoms. The dotted line at -0.5 eV, indicates the energy required to trap hydrogen for the long term in structural service at room temperature. The orange shade is the composition of the carbides in this research.

Model steel design and macroscale quantification of hydrogen trapping

In accordance with the carbide design strategy described above, we used a model steel containing 0.05% carbon, 1.5% manganese, 0.2% silicon, and 0.1% titanium (by weight) and compared it to another model steel of the same composition, but with an additional 0.2% molybdenum. Both specimens have a simple microstructure with a high density of metal carbides. The moderate addition of Mo is important because excessive amounts can lead to the formation of hexagonally close-packed (HCP) Mo_2C precipitates in the ferrite [28], which have lower hydrogen trapping abilities than NaCl-structure metal carbides [34].

The steels were austenitized at 1200 °C for 5 minutes to dissolve the carbide-forming alloying elements. They were then placed in an isothermal salt bath at 650 ± 20 °C for 60 minutes to form nanosized metal carbides, followed by water-quenching. Mo alloying can influence the temperatures of austenite and martensite formation and the kinetics of the austenite-ferrite phase transformation, leading to variations in the final ferrite grain size, metal carbide density, and the regularity of the metal carbide distribution [27,28]. We therefore anticipated a slight difference in microstructure, although the thermal histories of two samples are identical. Evidence of a smaller grain size of the (Ti,Mo)C steel (140 μm) than that of the TiC steel (195 μm) is provided in Supplementary Information (Supplementary Figure 2) in the form of electron backscatter diffraction (EBSD) orientation maps and is consistent with the literature [28]. The EBSD results in Supplementary Figure 2 also confirmed that the (Ti,Mo)C steel does not contain any detectable residual austenite that is known to be a strong hydrogen trap [4] and could cause confusion when interpreting hydrogen TDS data of carbide-containing steels.

To quantify the amount of trapped hydrogen in both steels, we carried out TDS on samples that were electrochemically charged with hydrogen. The TDS results from the TiC steel and the (Ti,Mo)C steel are shown in green and blue, respectively, in Fig. 2. After hydrogen charging, specimens were left at room temperature for either 1 or 24 hours, corresponding to the data labelled with squares or triangles, respectively, in Fig. 2. Holding at room temperature was intended to release the hydrogen that was weakly trapped in lattice defects such as dislocations and grain boundaries [4], so we

can better correlate the TDS results with stronger traps such as the metal carbides in our specimens. This treatment also addresses the variance in grain size in the two specimens. To establish hydrogen-free references, we tested the hydrogen-charged specimen desorbed for 720 hours and the uncharged specimen, the corresponding data labelled as plus signs and circles, respectively, in Fig. 2. We found that (Ti,Mo)C steel (blue) preserves much larger quantities of hydrogen than TiC (green) in the steel regardless of the duration of room-temperature desorption. In the 1-hour desorption datasets (squares), the overall released hydrogen for the (Ti,Mo)C steel is 1.685 wt. ppm, which is much higher than for the TiC steel at 0.169 wt. ppm. The addition of Mo in the steel therefore increases hydrogen trapping capacity significantly. We also conducted experiments with other desorption durations, as shown in Supplementary Figure 3 in Supplementary Information, which agree well with the data in Fig. 2. We also compared the macroscopic hydrogen permeabilities of the two specimens (Supplementary Figure 4), revealing that the (Ti,Mo)C steel has a lower hydrogen permeability, which suggests that there are more effective hydrogen traps in the (Ti,Mo)C steel. In summary, macroscale evidence supports our hypothesis that Mo in TiC can increase hydrogen trapping capacity of steels. We then continue with microscopic analyses for revealing the origin of the enhanced hydrogen trapping.

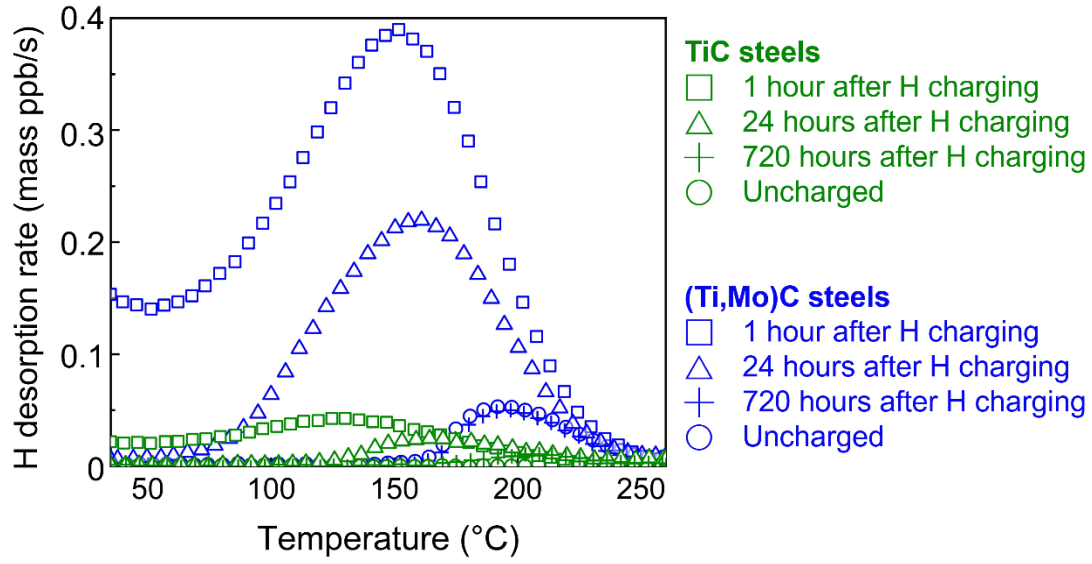

Fig. 2. Quantitative measurement of hydrogen trapping in the interphase-precipitate-containing ferritic steels by thermal desorption spectroscopy (TDS). The steels with TiC (green) and (Ti,Mo)C (blue) after charging and room-temperature desorption for 1 hour (square), 24 hours (triangle) and 720 hours (plus sign), compared to the uncharged sample (circle).

Microstructural characterization

We utilized bright-field TEM, atomic-resolution annular bright-field (ABF) STEM, and atomic structure simulator to examine the interphase-precipitation metal carbides in the BCC ferrite matrix, using the $[0\ 1\ 0]_{ferrite}$ zone axis that is most suitable for observing interphase-precipitation carbides [21–23], resulting in Figs. 3a-d from the TiC steel and Figs. 3e-h from the (Ti,Mo)Cs steel. Figs. 3a and 3e show the TiCs and (Ti,Mo)Cs as the dark and linearly aligned features in the BCC ferrite matrix, respectively[25–27]. We examined the diffraction patterns from the TiCs and (Ti,Mo)C steels, as shown in Figs. 3b and 3f, confirming the presence of the diffraction spots associated with the metal carbides as highlighted by green and blue circles, respectively, as well as their B–N OR with the ferrite matrix [25–27]. We also used the metal carbides' diffraction spots to conduct dark-field imaging in TEM, as an example shown in Supplementary Figure 5 for the TiC. However, we found this imaging method does not provide the most straightforward micrograph to exhibit the presence of metal carbides since the resulting image can also include other structural defects (Supplementary Figure 5b).

As we aim to produce the metal carbides that have the same lattice structure (and are only different in carbon vacancy concentrations), we used ABF STEM to further confirm the atomic structure of the metal carbides and their OR with the ferrite matrix, which resulted in Figs. 3c and 3g. Due to the small size of the carbides relative to the specimen thickness (illustrated in Supplementary Figure 6), the observed Ti (or substitutional Mo) atoms from the metal carbides overlap with the atomic lattice of ferrite, as highlighted by the red squares in Figs. 3c and 3g, hindering observations of the metal carbides. Note that the C atoms (with a low atomic mass) in the Fe matrix (with a high atomic mass) are not resolvable in our imaging condition (using 300 kV for electron acceleration). Moiré fringes, sometimes seen in conventional high-resolution TEM images of metal carbides [27,28], are absent in these STEM images because the ultra-fine scanning electron beam in STEM is less conducive to the electron beam interference that leads to Moiré fringes at the inclusions (see Supplementary Figure 6).

In order to confirm the atomic structure of the metal carbides embedded in the BCC ferrite matrix in the STEM images, we simulated the atomic structures of NaCl-like metal carbides embedded in a BCC iron matrix, as shown in Figs. 3d and 3h, and compared them with the STEM images (Figs. 3c and 3g), using the same atomic

structure coordinates with respect to the imaging direction of $[0\ 1\ 0]_{\text{ferrite}}$ zone axis. The simulated atomic models assumed the B–N OR, i.e., $\{0\ 0\ 1\}_{\text{ferrite}}//\{0\ 0\ 1\}_{\text{metal carbide}}$ and $<1\ 0\ 0>_{\text{ferrite}}//<1\ 1\ 0>_{\text{metal carbide}}$ reported in literature [27,28]. Ti/Mo atom columns are aligned (green/blue spheres) along $(\mathbf{1\ 1\ \bar{1}})$ planes in the simulated structures, as shown by the green and blue shades in Figs. 3d and 3h, respectively. Also, planes of Fe atom columns along $(\mathbf{1\ 0\ \bar{1}})$ are highlighted by grey shades in Figs. 3d and 3h. Similar atomic structures in the STEM images confirm the presence of the embedded metal carbides. In the Figs. 3c and 3g STEM images, atom columns corresponding to the $(\mathbf{1\ 1\ \bar{1}})_{MC}$ atom planes are highlighted by the green and blue broken lines, respectively. We also found that these $(\mathbf{1\ 1\ \bar{1}})_{MC}$ atom columns have the same angle with respect to the $(\mathbf{1\ 0\ \bar{1}})_{ferrite}$ planes (black broken lines in Figs. 3c and 3g), which is in agreement with the simulated data in Figs. 3d and 3h. This agreement also confirms the B–N OR between the metal carbides and the BCC ferrite matrix.

We also carried out STEM imaging along the $[1\ 0\ 0]_{\text{ferrite}}$ zone axis (in parallel with $[1\ 1\ 0]_{\text{metal carbide}}$ under the B–N OR), i.e., turning 90 degrees along the $[1\ 0\ 0]_{\text{ferrite}}$ axis toward the viewing direction of Fig. 3 (viewing from left to right in the coordinate of Fig. 3), resulting in Supplementary Figure 7 in Supplementary Information. We found coincident locations of metal carbide and ferrite atom columns (Supplementary Figure 7b and 7e), as predicted in the simulated structures in Figs. S7C and S7F. This is in contrast to Figs. 3b and 3e showing the atom columns from the $(\mathbf{1\ 1\ \bar{1}})_{MC}$ and $(\mathbf{1\ 0\ \bar{1}})_{ferrite}$ planes and a nominal angle between them, suggesting the observed inclusions are indeed the metal carbides with the expected NaCl crystal structure. In summary, our TEM and STEM results are consistent with previous literatures [27,28], indicating both metal carbides are NaCl type and have the B–N OR with the BCC ferrite matrix.

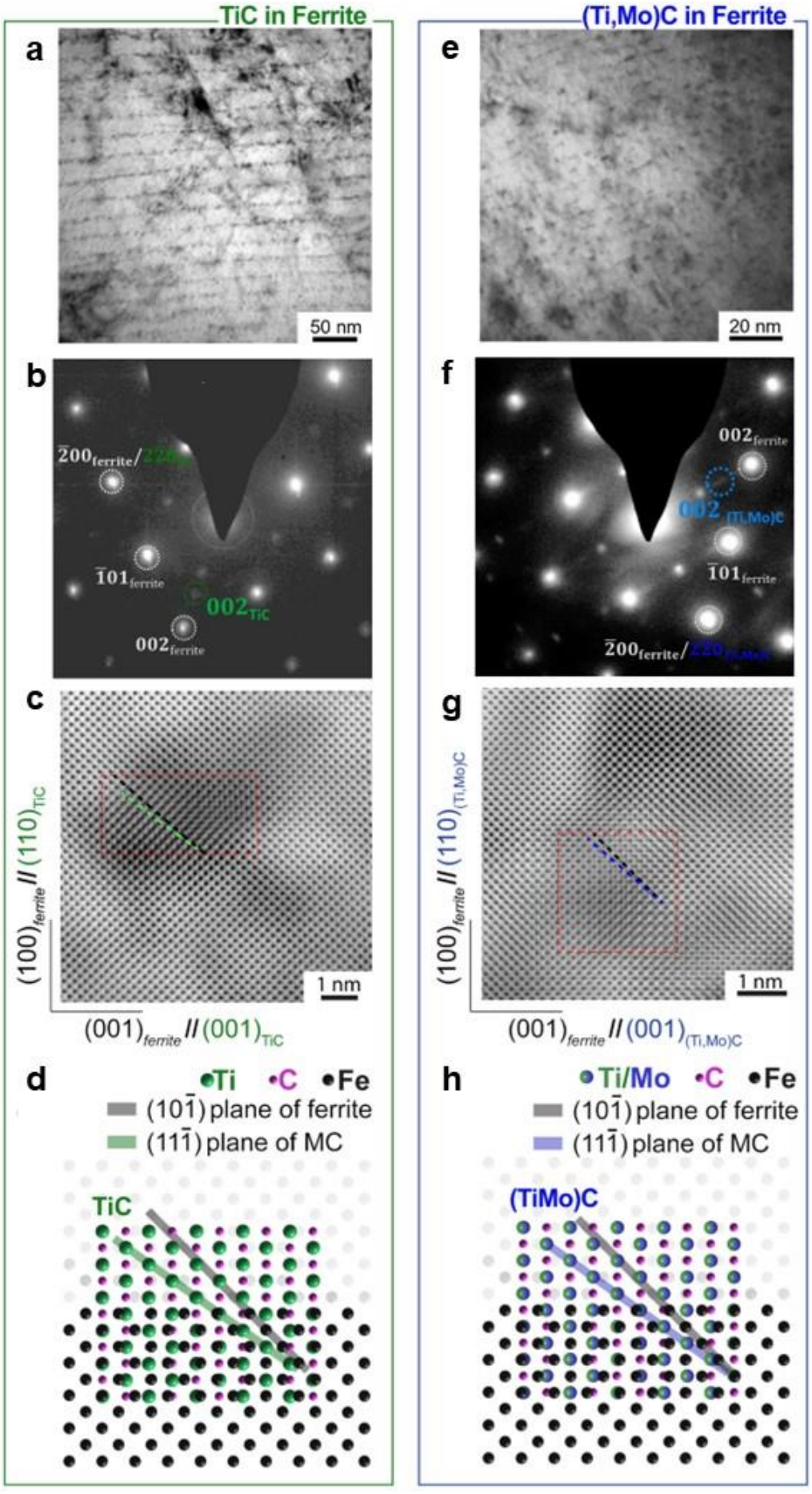
TiC in Ferrite
(Ti,Mo)C in Ferrite
a
e
50 nm
20 nm
b
f
$\bar{2}00_{ferrite}$/220TiC
$\bar{1}01_{ferrite}$
002TiC
$002_{ferrite}$
$002_{ferrite}$
002(Ti,Mo)C
$\bar{1}01_{ferrite}$
$\bar{2}00_{ferrite}$/220(Ti,Mo)C
c
g
$(100)_{ferrite}$ // $(110)_{TiC}$
$(001)_{ferrite}$ // $(001)_{TiC}$
$(100)_{ferrite}$ // $(110)_{(Ti,Mo)C}$
$(001)_{ferrite}$ // $(001)_{(Ti,Mo)C}$
1 nm
1 nm
d
h
Ti C Fe
Ti/Mo C Fe
$(10\bar{1})$ plane of ferrite
$(11\bar{1})$ plane of MC
$(10\bar{1})$ plane of ferrite
$(11\bar{1})$ plane of MC
TiC
(TiMo)C

Fig. 3. TEM and STEM observations of the carbide morphology, structure, and orientation relationship with ferrite matrix along [0 1 0]$_{ferrite}$ zone axis. (a)-(d) are from the TiC steel, and (e)-(h) are from the (Ti,Mo)C steel. (a) and (e) are bright-field TEM images showing the morphology of the carbides (dark and linearly aligned features). (b) and (f) are the diffraction patterns of both steel specimens, which are indexed with the spots associated with the ferrite matrix and the metal carbides. (c) and (g) are the high-resolution annular bright-field STEM images, showing the atomic structures of the NaCl-structure carbides and the BCC ferrite matrix indexes. The $(\mathbf{1\,1\,\bar{1}})$ planes of the carbides were marked by green and blue broken lines in (c) and (g), respectively, whereas $(\mathbf{1\,0\,\bar{1}})$ planes of ferrite were marked by black broken lines. (d) and (h) are corresponding atomic models illustrating the corresponding atomic structures in the observations of Figs. c and g, showing the nominal atomic structures of the metal carbides embedded in the BCC ferrite matrix in the STEM images. These results are in consistent with previous literature [27,28], indicating the metal carbides have a NaCl structure and the B–N OR with the BCC ferrite matrix.

High-resolution observations of hydrogen trapping in metal carbides

We then used cryo-APT to examine how hydrogen is trapped in the two metal carbides, specifically focusing on whether hydrogen atoms locate at the metal carbide-ferrite interface or within the carbide bulk, and whether this changes when additional carbon vacancies are present due to Mo in the carbides [46–50]). We utilized a cryogenic sample transfer protocol developed from a previous study [41]. Using cryo-transfer in APT analyses of hydrogen is crucial because the small needle-shaped samples have a very high surface-area-to-volume ratio and are susceptible to hydrogen desorption due to the high diffusivity of hydrogen in steels [54,55]. We charged our samples with deuterium (D or ^{2}H), instead of normal hydrogen that contains mostly protium (^{1}H). This allows us to circumvent any ambiguity around the origin of hydrogen signal in the APT data, distinguishing the hydrogen within the sample from noise induced by the residual hydrogen in the APT ultra-high-vacuum chamber [40,41,55–57]. We used electrolytic D charging (i.e., electrolysis of heavy water), which allows a significant dose of D to maximize its signal. Details of the D charging can be found in Supplementary Information.

The APT 3-D reconstructed data of the deuterium-charged TiC and (Ti,Mo)C containing steels are shown in Figs. 4 and 5, respectively. The corresponding APT mass spectra, their D-free counterparts, and the ion peak assignments are provided in Supplementary Figure 8 and 9. Fig. 4a is a visualization of the reconstructed tip-shaped sample with the interphase-precipitate TiC carbides highlighted by 2 atomic percent (at. %) Ti isoconcentration surfaces (isosurfaces) [58] shown in green. Fig. 4b shows the same volume with the Ti, C, and D atoms displayed in green, magenta, and

red, respectively. To better observe the distribution of D in relation to carbide locations, we extracted a 10-nm-thick slice along the Y-Z plane, from the area highlighted by the broken line in Fig. 4b, and this data is shown in Fig. 4c.

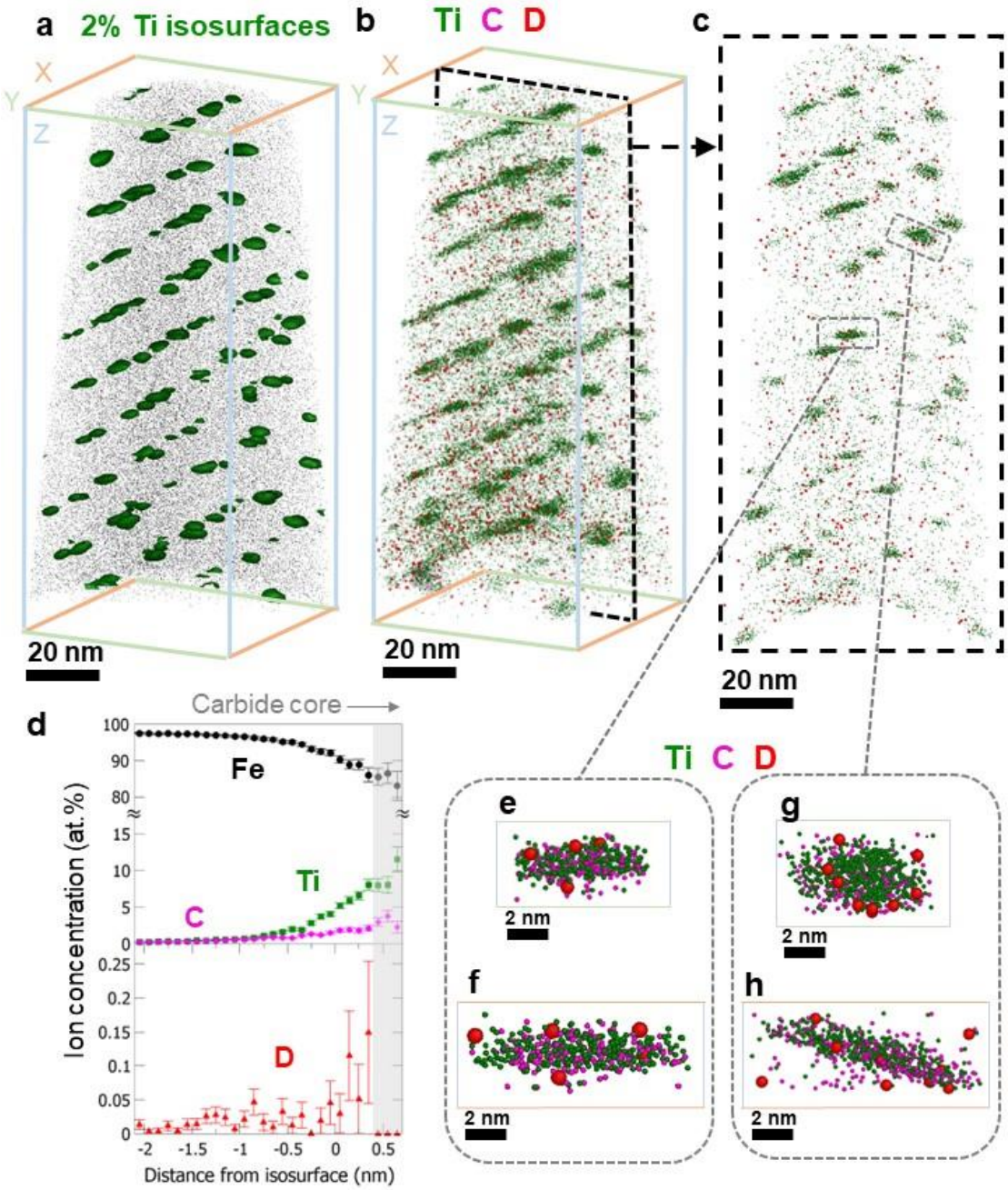

Fig. 4. APT analysis of deuterium-charged TiC steel. (a) Reconstructed APT data showing the TiC distribution, highlighted by 2 at. % Ti isosurfaces. (b) Atom map with Ti (green), C (magenta), and D (red) displayed. (c) A 10-nm-thick slice from the broken-line-highlighted region in (B). (d) An integrated proxigram from all the isosurfaces with complete shapes in (a), showing the concentration change as a function of the distance from the defined isosurfaces. Error bars depict the statistical precision associated with each element's count. (e)-(h) Magnified views of two carbides selected from (c), each from two perspectives.

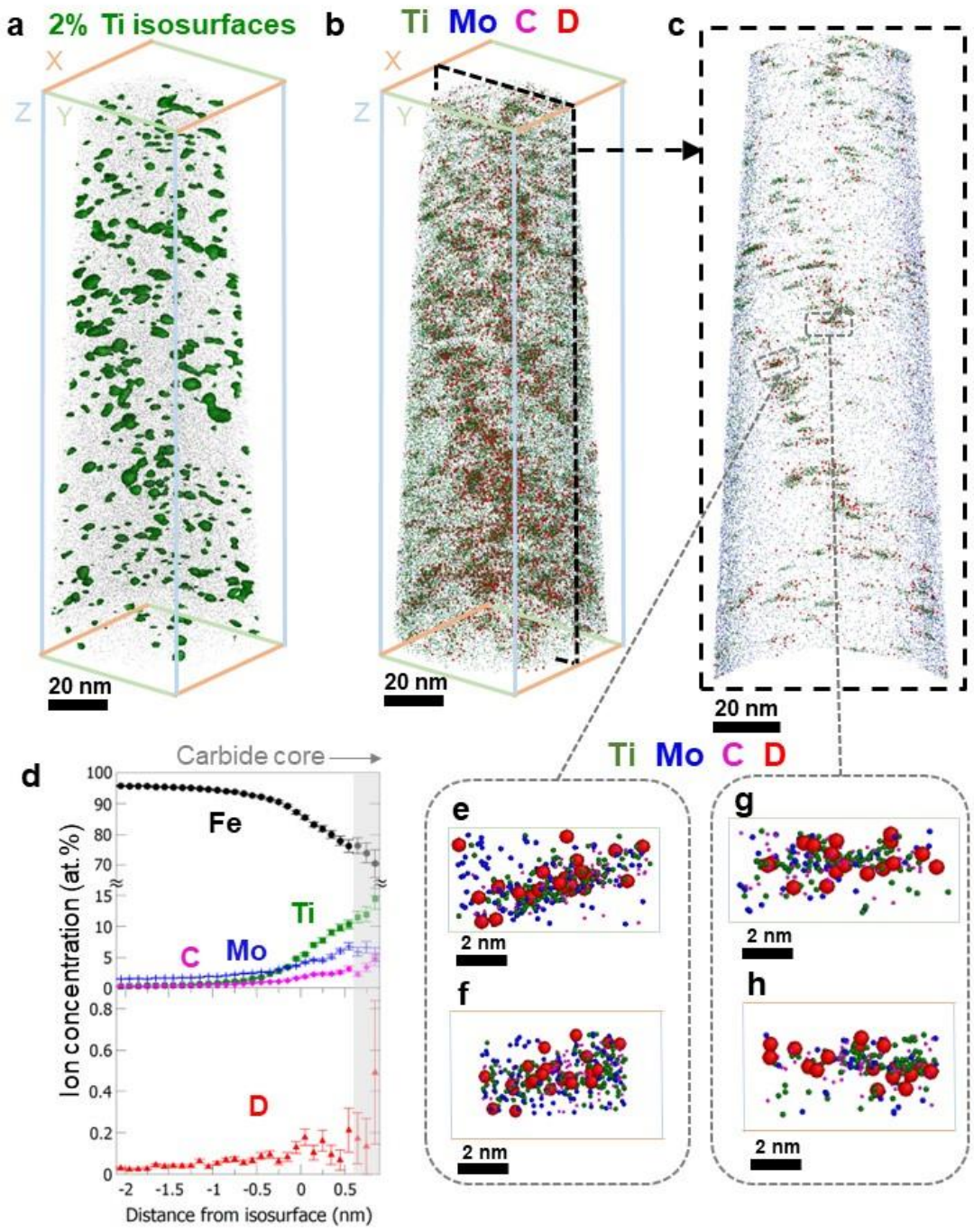

Fig. 5. APT analysis of deuterium-charged (Ti,Mo)C steel. (a) Reconstructed data showing the (Ti,Mo)Cs highlighted by 2 at. % Ti isosurfaces. (b) Atom map with Ti (green), Mo (blue), C (magenta), and D (red) displayed. (c) A 10-nm-thick slice from the broken-line-highlighted region in (B). (d) An integrated proxigram from all the isosurfaces in (A). Error bars depict the statistical precision associated with each element's count. (e)-(h) Magnified views of two carbides selected from (c), from two different perspectives.

We used the isosurfaces defined in Fig. 4a to develop a statistical overview of the D distribution around the carbides relative to the distributions of the other elements present. Fig. 4d is an integrated proximity histogram (proxigram[59]), which

averages all of the proxigram data from the 52 geometrically intact isosurfaces (i.e., those not located at the edge of APT reconstruction). The proxigram shows how the concentration of different elements changes as a function of the distance from the isosurfaces. In Fig. 4d the 2 at. % Ti isosurface is the zero point on the X-axis and the more positive values are closer to the carbide core. The interfacial region corresponds to a decrease in the content of Fe (black) and increases in Ti (green) and C (magenta), with plateaus at the approximate location of carbide cores (grey shade). Note that the ratio of C to Ti in the carbide core shown in Fig. 4d is not representative of the actual carbide composition for two reasons. First, the $^{48}Ti^{2+}$ peak overlaps with $^{12}C_2^+$ peak at 24 mass-to-charge ratio (Da) in the APT mass spectra (Supplementary Figure 8 and Supplementary Figure 9), impeding precise quantification of C and Ti. Second, the presence of covalently-bonded carbon atoms in carbides leads to complex field ionization and carbon-molecule dissociation in APT experiments [60–63], causing a loss of the carbon count that also affects the measured carbon concentration. Therefore, the hypo-stoichiometric C-to-Ti ratio in Fig. 4d may not relate directly to the presence of carbon vacancies in carbide core, although their presence is theoretically predicted [47–49,64]. We observed the expected changes in Fe, Ti, and C, as well as an increase in the D content (red) at or near the carbide surface. Interestingly, the D content drops to a very low value in the region of carbide core. The observation of higher D near the metal carbide-ferrite interface is consistent with existing literature [36], which correlates trapped D with the presence of carbon vacancy traps near the metal carbide-matrix interface. Herein we additionally show the absence of D at the metal carbide core, which we attribute to the inability of D atoms to access the metal carbide interior. Proxigram analysis is useful for providing an overview of element distribution with respect to defined isosurfaces. However, the creation of proxigram involves a data voxelization process (i.e., binning considerable numbers of atoms into cubic-nanometer voxels to aggregate the atomic compositions within each voxel [59]), and this can compromise the nominal atomic resolutions in APT. To determine the hydrogen trapping sites more precisely, direct high-resolution observations of D locations were conducted, as shown in Figs. 4e to 4h, which are from two TiCs indicated in Fig. 4c. These atomic views show that D atoms (red) are mainly located near the metal carbide-matrix interfaces, rather than inside the metal carbide. Several previous studies have used D charging to show D atoms trapped at metal carbide interfaces [41,65], substantiating these observations. More high-resolution atomic views of TiCs

with trapped D atoms are provided in Supplementary Figure 10A. A fly-through view of the dataset shown in Fig. 4, using 10-nm slices, is available in the online version (Supplementary Movie1). The experiment was repeated to verify the result, as shown in Supplementary Figure 11. These results confirm that the interface is the main hydrogen trapping site for TiC, which agrees with existing literature [55].

We then examined the hydrogen trapping in (Ti,Mo)C, as shown in Fig. 5a, and obtained an overview of the carbide distribution in the sample with the same 2 at. % Ti isosurfaces (green) used for Fig. 4a. The atom map with Mo (blue), Ti (green), C (magenta), and D (red) is shown in Fig. 5b with a 10-nm slice extracted from the region highlighted by the broken line in Fig. 5c. The (Ti,Mo)C precipitates were slightly smaller than the TiCs in Fig. 4, which is consistent with previous research that used TEM and carbon extraction replica to determine carbide sizes [46]. To gain an overview of the elemental distributions around the interface and carbide core, we again created an integrated proxigram that included the statistics of 260 isosurfaces with round geometries (see Fig. 5a), which is shown in Fig. 5d. The Mo-to-Ti ratio was measured as approximately 0.5, which is consistent with previous research [46]. We observed a high concentration of D atoms (red) within the carbide core (grey shade), unlike for the TiC shown in Fig. 4d, in which hydrogen trapping occurs only at the interface.

We took a close look at the carbides with trapped D, and the views of two representative carbides are displayed in Figs. 5e-5h, which are from two axial perspectives. Both show D atoms located in the carbide bulk, where carbon vacancies can exist. Additional close-up images of the (Ti,Mo)Cs with trapped D atoms are provided in Supplementary Figure 10B. A fly-through view of the Fig. 5 dataset, using a 10-nm slice is available in the online version (Supplementary Movie 2). A repeat experiment was conducted to verify these observations in relation to the (Ti,Mo)C steel, shown in Supplementary Figure 12. These observations provide evidence that the core of (Ti,Mo)C is the main trapping site of hydrogen, unlike that for TiC. Moreover, we observed a large difference in overall D composition between the TiC and (Ti,Mo)C steel datasets, at 0.006 at. % (Fig. 4 dataset, TiC) and 0.02 at. % (Fig. 5 dataset, (Ti,Mo)C), which is consistent with the TDS result in Fig. 2.

We also calculated the carbide number density in each APT dataset (Table 1). The carbide number densities in the two steels are of the same order of magnitude, indicating that the more trapped hydrogen in the (Ti,Mo)C steel is not simply the

result of a higher carbide number density. Combining with the moderate difference in grain boundary density (Supplementary Figure 2), the increased hydrogen trapping capacity of the (Ti,Mo)C steel is therefore attributed to the ability of the carbides to incorporate hydrogen in their bulk.

Table. 1. Carbide number density from APT analyses

Sample	Related figure	Data volume (10^{-22} m^3)	Carbide number*	Number density (10^{-23} m^{-3})
TiC steel	Fig. 4	8.47	129	**1.52**
	Supplementary Figure 11	10.98	293	**2.67**
(Ti,Mo)C steel	Fig. 5	9.11	284	**3.12**
	Data provided	14.46	164	**1.13**

*Carbides were defined by using the protocol developed in [66]

Considering the limited spatial resolution that proxigrams can achieve with voxelised data, we also examined D composition near the carbides by using a different statistical approach. For consistency between the two specimens, which have different average carbide sizes, we only compared carbides with diameters smaller than 5 nm. This helps to minimize any errors that could arise from trajectory aberrations in APT experiments, which would affect smaller carbides to a greater extent. These carbides have high interface coherency, so using the smaller precipitates for this analysis also minimizes the contribution of hydrogen trapped by misfit dislocations at the interface [30], allowing a more direct comparison of the hydrogen trapped by carbon vacancies. Fig. 6a shows the carbide size distribution for TiC and (Ti,Mo)C, corresponding to the datasets in Figs. 4 and 5, respectively. The carbide sizes were defined using the Cluster Analysis algorithm in the commercial APT software (APSuite 6.0, CAMECA) [59], and the cluster-defining parameters were selected based on a protocol from the literature [66], described in Supplementary Information. The defined clusters are displayed in Supplementary Figure 13a and 13b for the TiC steel and (Ti,Mo)C steel, respectively. We used the largest radius of gyration (R_g) among the axes to define the radius of carbide, and the carbide size distributions in Fig. 6a are consistent with previous research using similar materials [46].

We created integrated 1-D atomic concentration profiles along the Z-axis from a centered cylindric region for all considered carbides with trapped D atoms, as

conceptually illustrated in Fig. 6b. Analyses along the Z axis allow us to use the direction with the highest spatial resolution in APT, thereby reducing ambiguity when defining the locations of carbide core and interface [59]. Using the cylindric regions of interest across the carbide center allows us to exclude D atoms trapped at the lateral edges of carbide (Fig. 6b), which could be miscounted as being located in carbide core if the entire carbide is incorporated in the cylindric measurement. After collecting individual concentration profiles with a measuring step size of 1 nm, we normalized the profiles to their Ti spatial span (i.e., their size), and then superimposed the dimensionless profiles into the overall 1-D Z-axis profiles as shown in Figs. 6c and 6d.

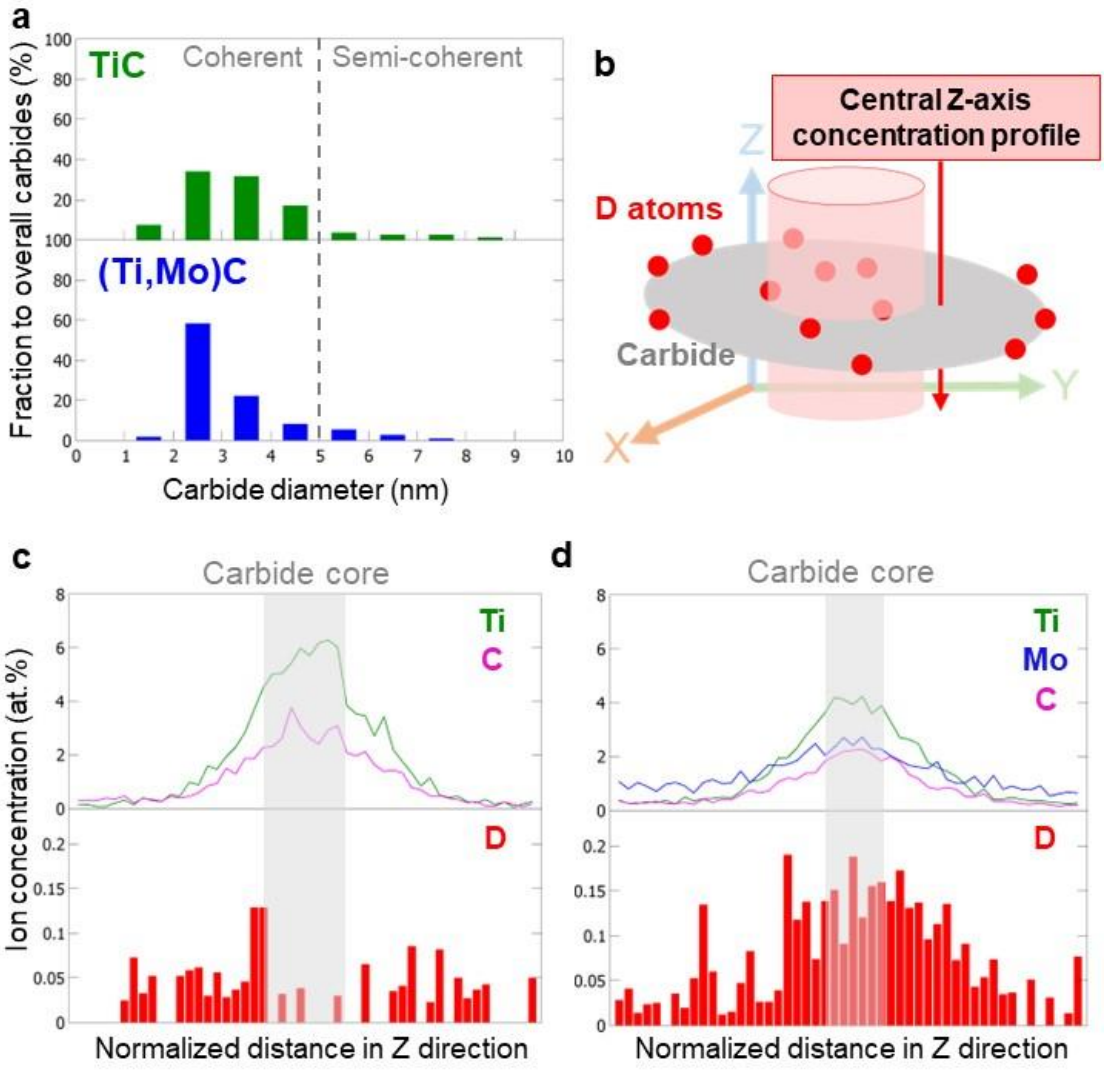

Fig. 6. Statistical analyses of deuterium distributions in relation to interface and carbide core locations from Figs. 4 and 5 results. (a) presents the carbide size histograms of TiC (green) and (Ti,Mo)C (blue) from the Figs. 4 and 5 datasets, respectively. (b) is a schematic illustration of the method to extract a 1-D Z-axis

concentration profile from the center of a carbide in APT dataset. 1-nm step size was used to generate the profiles. (c) is the overall Z-axis profile from the TiC steels shown in Fig. 4 after normalizing each profile with corresponding carbide size and superimposing all the resulting dimensionless profiles. (d) is the counterpart of (c) for (Ti,Mo)C from Fig. 5.

Fig. 6c, from the TiC APT data, shows a drop in D in the carbide core region, consistent with the proxigram data, again suggesting that TiCs are unable to trap hydrogen in their core. In contrast, Fig. 6d, from the (Ti,Mo)C steel, shows D is present in the carbide core, which is attributed to accessible carbon vacancies leading to the higher hydrogen trapping capacity, also seen in the TDS data (Fig. 2). Fig. 6d also shows that the Mo-to-Ti ratio is approximately 0.5, consistent with the proxigram analysis (Fig. 5d) and previous research [46]. Although carbon quantification in APT is difficult, we believe the detected carbon contents in the two APT experiments using the identical instrument, parameters, and ion ranging method are still qualitatively comparable. In Fig. 6d, we found that the ratio of carbon content to metal (i.e., Ti plus Mo) content at the carbide core is lower than that of carbon content to Ti content in Fig. 6c. This result supports our prediction of more carbon vacancies in (Ti,Mo)C than TiC. We note that it is also possible that changes in the phase-transformation kinetics of metal carbide formation from Mo additions could also affect the carbon content. Further research to quantify the vacancies may provide a better quantitative correlation between hydrogen trapping with carbon vacancy concentration.

In summary, we have used first-principle simulations and state-of-the-art microscopic tools to demonstrate a successful materials engineering alloy design strategy to enhance the ability of steels to trap hydrogen. This is achieved by increasing the number of carbon vacancy traps that are accessible within carbide precipitates. Our microscopic observations agree well with the macroscopic analyses by thermal desorption analysis and permeation tests. This strategy can be easily implemented through microalloying and is not limited to Mo; other carbide forming elements in steel are likely to have the same effect. This microalloying is cost-effective and applicable for a broad range of precipitate-strengthened steels.

Methods

First-principles calculations

To construct the interface and bulk models for $Ti_{1-x}Mo_x$ carbide, the similar atomic

environment (SAE) method [43] that generates quasi-random structures through calculating binary and ternary clusters was used. Different concentrations of alloying atoms ranging from 0.125 to 0.50 in the Ti sub-lattice were selected according to chosen number of atoms in supercells. The calculation of H trapping energetics is consistent with that in [51]. The formation energy of C vacancies in various sites was calculated according to [67]:

$$\Delta E_{C-Vac} = E_{system}^{C-Vac} - E_{system} + \mu_C \quad (1)$$

where E_{system}^{C-Vac} (E_{system}) is the total energy of the system with (without) a C vacancy, μ_C is the referenced chemical potential of C, which is equal to the single-atom energy of graphite. The formula describes the off-stoichiometric tendency in the carbides under C-rich conditions.

Ab-initio calculations based on DFT were carried out using the VASP code [68].The projector augmented wave (PAW) potentials and the generalized gradient approximation (GGA) [69] with the Perdew-Burke-Ernzerhof (PBE) [70] parametrization of exchange-correlation functionals were adopted. A plane-wave cutoff energy of 450 eV and Monkhorst-Pack [71] k-point sampling was used for atomic relaxations until the forces are smaller than 0.01 eV/Å. The climbing image nudged elastic band (CI-NEB) method [44] was used to find the energy barrier of H migration, where five images were used with the relaxation criterion set at 0.05 eV/Å.

Scanning electron microscopy and electron backscatter diffraction experiments

The steel samples were polished using SiC polishing papers of 30, 15, 5, and 1 micron grades, followed by a final 1-minute polishing in the Struers Inc TegraPol-25 instrument using active oxide polishing suspensions. The surface of the samples was then cleaned using Ar ion beam polishing with a Gatan PECS ll machine, using two 2 kV beams with an inclination angle of ± 3°. EBSD experiments were conducted in a Thermofisher G4 Hydra Plasma FIB-SEM, prior to preparing TEM samples using the FIB lift-out method. During the EBSD experiments, a 20kV 1.8 nA electron beam was used, and EBSD patterns were collected using an Oxford Instruments Symmetry S1 EBSD Detector. The Kikuchi patterns were indexed using both the 'fcc iron' and 'bcc iron' phases in the embedded database in the EBSD software Aztec. The data presented in Supplementary Figure 2 has an index rate of more than 95%, which were all automatically indexed to the bcc iron phase, indicating that no austenite was detected.

Thermal desorption spectroscopy and hydrogen permeation tests

Mechanically polished specimens with diameters of 5 mm and length of 25 mm were electrochemically H-charged using an aqueous solution of 3% NaCl + 0.3% NH_4SCN with a current of 0.3 mA/cm^2 for 48 h. The H-charged specimens were then exposed at ambient temperature for selected durations from 0 to 720 h before conducting TDS measurements using the HTDS-002 instrument at Central Iron & Steel Research Institute Company. To verify that Mo alloying affects H diffusion through the nano-precipitates rather than the substituted atoms in the ferrite matrix, electro-chemical H permeation tests were conducted on the model steels and compared with that of a commercially pure Fe alloyed with 0.5 wt.% Mo (Fe-0.5Mo). The tests were carried out at a constant potential of 300 mV in an aqueous solution of 0.2 M/L NaOH + 0.3 wt.% NH_4SCN.

Transmission electron microscopy

A Thermo-Fisher G4 Hydra Plasma FIB-SEM with EBSD detector was used to conduct TEM and STEM lift-out sample preparations. Grains with the $[100]_{ferrite}$ crystal orientation were targeted to lift-out 15-micron-thick samples. These lift-out samples were placed on copper grids and thinned by a xenon plasma ion beam, in the sequence of 30 kV-1nA, 30 kV-100 pA, 30 kV-30 pA, and finally 5 kV-30pA. 3 lift-out samples from 3 different grains (with the same crystal orientation) were prepared and examined to confirm the reproducibility of STEM data.

TEM analyses were conducted on a FEI Tecnai G2 F20. STEM analyses were conducted on a Spectra 300 kV STEM and a Thermo-Fisher Themis-Z 300 kV STEM with two aberration correctors for low-resolution and atomic-resolution imaging, respectively. The samples were mounted onto double-tilted holders and were cleaned in Ar plasma before entering the STEM. We imaged the samples in the $<001>_{ferrite}$ zone axis. We used the electron probe aperture of 25.1 mrad in semi-angle and the ABF collection semi-angles between 48 and 200 mrad. We used a monochromator to set the probe current at 80 pA, in order to minimize the electron beam damage.

Atom probe tomography and specimen deuteration

The charging and cryo-transfer methods were adopted from our previous work [41]. We conduct the charging in a custom-designed cryo-transfer glove box. The charging condition for the sample is 30 seconds with 2.2V, followed by the liquid nitrogen bath and the cryo-transfer process. A more comprehensive description of the charging and cryo-transfer method is reported in the supporting document of [40].

For the sample preparation, the steels were cut into 1 x 1 x 15 mm matchstick-shaped bars. We first use the 25% perchloric acid in acetic acid at 10-30 V for rough electropolishing, separating the sample from the middle and yielding two needle-shaped samples. This is followed by fine electropolishing with 2% perchloric acid in butoxyethanol under a 40x optical microscope. The voltage range for the fine polishing is around 5-20V; the higher voltage is used to form the necking and the lower voltage to remove the top part. All the atom probe experiments were analyzed with a Local Electrode Atom Probe (LEAP 4000 Si, CAMECA) with a pulse frequency of 200 kHz, a stage temperature of 50 K and a pulse fraction of 20%. After acquiring the data, the reconstruction was conducted by the atom probe analysis software AP Suite (version 6.1, CAMECA). For the reconstruction parameters, the detector efficiency of 57% and image compression factor 1.40 were used for TiC specimen and 1.44 for (Ti,Mo)C specimen in the APT data reconstructions.

Data and materials availability: All data are available in the main text or the supplementary materials and can be accessed online via https://unisyd-my.sharepoint.com/:f:/g/personal/yi-sheng_chen_sydney_edu_au/EtQResJv6NhJnN9t0RPcep4BiciuE8NSxqhh9s6n6itpzw?e=TQoNzs

Reference

1. International Energy Agency. *Global Hydrogen Review*. https://www.iea.org/reports/global-hydrogen-review-2022 (2022).
2. Martin, M. L., Connolly, M. J., DelRio, F. W. & Slifka, A. J. Hydrogen embrittlement in ferritic steels. *Appl Phys Rev* **7**, 041301 (2020).
3. Gangloff, R. P. & Somerday, B. P. *Gaseous hydrogen embrittlement of materials in energy technologies: the problem, its characterisation and effects on particular alloy classes*. (Elsevier, 2012).
4. Bhadeshia, H. K. D. H. Prevention of hydrogen embrittlement in steels. *ISIJ international* **56**, 24–36 (2016).
5. Kim, H.-J., Park, H.-K., Lee, C.-W., Yoo, B.-G. & Jung, H.-Y. Baking effect on desorption of diffusible hydrogen and hydrogen embrittlement on hot-stamped boron martensitic steel. *Metals (Basel)* **9**, 636 (2019).
6. Alexander Stopher, M. & Rivera-Diaz-del-Castillo, P. E. J. Hydrogen embrittlement in bearing steels. *Materials Science and Technology* **32**, 1184–1193

(2016).
7. Laureys, A. *et al.* Use of existing steel pipeline infrastructure for gaseous hydrogen storage and transport: A review of factors affecting hydrogen induced degradation. *J Nat Gas Sci Eng* **101**, 104534 (2022).
8. Ooi, S. W., Yan, P. & Vegter, R. H. Black oxide coating and its effectiveness on prevention of hydrogen uptake. *Materials Science and Technology* **35**, 12–25 (2019).
9. Atrens, A., Gray, E., Venezuela, J., Hoschke, J. & Roethig, M. Feasibility of the Use of Gas Phase Inhibition of Hydrogen Embrittlement in Gas Transmission Pipelines Carrying Hydrogen: A Review. *JOM* **75**, 232–238 (2023).
10. Pressouyre, G. M. Trap theory of Hydrogen embrittlement. *Acta Metallurgica* **28**, 895–911 (1980).
11. KUSHIDA, T. *et al.* Delayed Fracture and Hydrogen Absorption of 1.3GPa Grade High Strength Bolt Steel. *Tetsu-to-Hagane* **82**, 297–302 (1996).
12. Zhang, S. *et al.* Effect of Nb on hydrogen-induced delayed fracture in high strength hot stamping steels. *Materials Science and Engineering: A* **626**, 136–143 (2015).
13. Fernández-Sousa, R., Betegón, C. & Martínez-Pañeda, E. Analysis of the influence of microstructural traps on hydrogen assisted fatigue. *Acta Mater* **199**, 253–263 (2020).
14. Koyama, M. *et al.* Recent progress in microstructural hydrogen mapping in steels: quantification, kinetic analysis, and multi-scale characterisation. *Materials Science and Technology* **33**, 1481–1496 (2017).
15. Saito, K., Hirade, T. & Takai, K. Hydrogen Desorption Spectra from Excess Vacancy-Type Defects Enhanced by Hydrogen in Tempered Martensitic Steel Showing Quasi-cleavage Fracture. *Metallurgical and Materials Transactions A* **50**, 5091–5102 (2019).
16. Takasawa, K., Ikeda, R., Ishikawa, N. & Ishigaki, R. Effects of grain size and dislocation density on the susceptibility to high-pressure hydrogen environment embrittlement of high-strength low-alloy steels. *Int J Hydrogen Energy* **37**, 2669–2675 (2012).
17. Robertson, I. M. The effect of hydrogen on dislocation dynamics. *Eng Fract Mech* **68**, 671–692 (2001).
18. Robertson, I. M. *et al.* Hydrogen Embrittlement Understood. *Metallurgical and Materials Transactions A* **46**, 2323–2341 (2015).

19. Nagumo, M. & Takai, K. The predominant role of strain-induced vacancies in hydrogen embrittlement of steels: Overview. *Acta Mater* **165**, 722–733 (2019).
20. Nagumo, M. *Fundamentals of Hydrogen Embrittlement*. (Springer Singapore, 2016). doi:10.1007/978-981-10-0161-1.
21. Murakami, Y., Kanezaki, T. & Sofronis, P. Hydrogen embrittlement of high strength steels: Determination of the threshold stress intensity for small cracks nucleating at nonmetallic inclusions. *Eng Fract Mech* **97**, 227–243 (2013).
22. Lynch, S. Hydrogen embrittlement phenomena and mechanisms. *Corrosion reviews* **30**, 105–123 (2012).
23. Song, J. & Curtin, W. A. Atomic mechanism and prediction of hydrogen embrittlement in iron. *Nat Mater* **12**, 145–151 (2013).
24. Djukic, M. B., Bakic, G. M., Sijacki Zeravcic, V., Sedmak, A. & Rajicic, B. The synergistic action and interplay of hydrogen embrittlement mechanisms in steels and iron: Localized plasticity and decohesion. *Eng Fract Mech* **216**, 106528 (2019).
25. Honeycombe, R. W. K. & Mehl, R. F. Transformation from austenite in alloy steels. *Metallurgical Transactions A* **7**, 915–936 (1976).
26. Batte, A. D. & Honeycombe, R. W. K. Strengthening of Ferrite by Vanadium Carbide Precipitation. *Metal Science Journal* **7**, 160–168 (1973).
27. Yen, H.-W., Chen, P.-Y., Huang, C.-Y. & Yang, J.-R. Interphase precipitation of nanometer-sized carbides in a titanium–molybdenum-bearing low-carbon steel. *Acta Mater* **59**, 6264–6274 (2011).
28. Gong, P., Liu, X. G., Rijkenberg, A. & Rainforth, W. M. The effect of molybdenum on interphase precipitation and microstructures in microalloyed steels containing titanium and vanadium. *Acta Mater* **161**, 374–387 (2018).
29. Vervynckt, S., Verbeken, K., Lopez, B. & Jonas, J. J. Modern HSLA steels and role of non-recrystallisation temperature. *International Materials Reviews* **57**, 187–207 (2012).
30. Wei, F. G. & Tsuzaki, K. Quantitative analysis on hydrogen trapping of TiC particles in steel. *Metallurgical and Materials Transactions A* **37**, 331–353 (2006).
31. Shi, R. *et al.* Atomic-scale investigation of deep hydrogen trapping in NbC/α-Fe semi-coherent interfaces. *Acta Mater* **200**, 686–698 (2020).
32. Kawakami, K. & Matsumiya, T. Numerical Analysis of Hydrogen Trap State by TiC and V4C3 in bcc-Fe. *ISIJ International* **52**, 1693–1697 (2012).
33. Di Stefano, D. *et al.* First-principles investigation of hydrogen interaction with

TiC precipitates in α-Fe. *Phys Rev B* **93**, 184108 (2016).
34. Salehin, R., Thompson, G. B. & Weinberger, C. R. Hydrogen trapping and storage in the group IVB-VIB transition metal carbides. *Mater Des* **214**, 110399 (2022).
35. Li, Y. *et al.* First-principles study on the dissolution and diffusion behavior of hydrogen in carbide precipitates. *Int J Hydrogen Energy* **46**, 22030–22039 (2021).
36. Takahashi, J., Kawakami, K. & Kobayashi, Y. Origin of hydrogen trapping site in vanadium carbide precipitation strengthening steel. *Acta Mater* **153**, 193–204 (2018).
37. Kirchheim, R. Changing the interfacial composition of carbide precipitates in metals and its effect on hydrogen trapping. *Scr Mater* **160**, 62–65 (2019).
38. Takahashi, J., Kawakami, K. & Kobayashi, Y. Origin of hydrogen trapping site in vanadium carbide precipitation strengthening steel. *Acta Mater* **153**, 193–204 (2018).
39. Nagakura, S. & Oketani, S. Structure of Transition Metal Carbides. *Transactions of the Iron and Steel Institute of Japan* **8**, 265–294 (1968).
40. Chen, Y.-S. *et al.* Direct observation of individual hydrogen atoms at trapping sites in a ferritic steel. *Science (1979)* **355**, 1196–1199 (2017).
41. Chen, Y.-S. *et al.* Observation of hydrogen trapping at dislocations, grain boundaries, and precipitates. *Science (1979)* **367**, 171–175 (2020).
42. Chen, Y.-S. *et al.* Atom Probe Tomography for the Observation of Hydrogen in Materials: A Review. *Microscopy and Microanalysis* **29**, 1–15 (2023).
43. Tian, F., Lin, D.-Y., Gao, X., Zhao, Y.-F. & Song, H.-F. A structural modeling approach to solid solutions based on the similar atomic environment. *J Chem Phys* **153**, 034101 (2020).
44. Henkelman, G., Uberuaga, B. P. & Jónsson, H. A climbing image nudged elastic band method for finding saddle points and minimum energy paths. *J Chem Phys* **113**, 9901–9904 (2000).
45. Jiang, D. E. & Carter, E. A. Diffusion of interstitial hydrogen into and through bcc Fe from first principles. *Phys Rev B* **70**, 064102 (2004).
46. Dong, H. *et al.* Revealing the influence of Mo addition on interphase precipitation in Ti-bearing low carbon steels. *Acta Mater* **223**, 117475 (2022).
47. Park, N.-Y. *et al.* First-Principles Study of the Interfaces between Fe and Transition Metal Carbides. *The Journal of Physical Chemistry C* **117**, 187–193 (2013).
48. Yu, X.-X., Weinberger, C. R. & Thompson, G. B. Ab initio investigations of the

phase stability in group IVB and VB transition metal carbides. *Comput Mater Sci* **112**, 318–326 (2016).

49. Weinberger, C. R. & Thompson, G. B. Review of phase stability in the group IVB and VB transition-metal carbides. *Journal of the American Ceramic Society* **101**, 4401–4424 (2018).

50. Jang, J. H., Lee, C.-H., Heo, Y.-U. & Suh, D.-W. Stability of (Ti, M)C (M = Nb, V, Mo and W) carbide in steels using first-principles calculations. *Acta Mater* **60**, 208–217 (2012).

51. Zhang, B. *et al.* Atomistic insight into hydrogen trapping at MC/BCC-Fe phase boundaries: The role of local atomic environment. *Acta Mater* **208**, 116744 (2021).

52. Jin, X. *et al.* The effect of undissolved and temper-induced (Ti,Mo)C precipitates on hydrogen embrittlement of quenched and tempered Cr-Mo steel. *Corros Sci* **166**, 108421 (2020).

53. Echeverri Restrepo, S., Di Stefano, D., Mrovec, M. & Paxton, A. T. Density functional theory calculations of iron - vanadium carbide interfaces and the effect of hydrogen. *Int J Hydrogen Energy* **45**, 2382–2389 (2020).

54. Suzuki, H. & Takai, K. Summary of Round-robin Tests for Standardizing Hydrogen Analysis Procedures. *ISIJ International* **52**, 174–180 (2012).

55. Takahashi, J., Kawakami, K., Kobayashi, Y. & Tarui, T. The first direct observation of hydrogen trapping sites in TiC precipitation-hardening steel through atom probe tomography. *Scr Mater* **63**, 261–264 (2010).

56. Sundell, G., Thuvander, M. & Andrén, H.-O. Hydrogen analysis in APT: Methods to control adsorption and dissociation of H2. *Ultramicroscopy* **132**, 285–289 (2013).

57. Chen, Y.-S., Bagot, P. A. J., Moody, M. P. & Haley, D. Observing hydrogen in steel using cryogenic atom probe tomography: A simplified approach. *Int J Hydrogen Energy* **44**, 32280–32291 (2019).

58. Hellman, O. C., Rivage, J. B. du & Seidman, D. N. Efficient sampling for three-dimensional atom probe microscopy data. *Ultramicroscopy* **95**, 199–205 (2003).

59. Gault, B., Moody, M. P., Cairney, J. M. & Ringer, S. P. *Atom probe microscopy*. vol. 160 (Springer Science & Business Media, 2012).

60. Marceau, R. K. W., Choi, P. & Raabe, D. Understanding the detection of carbon in austenitic high-Mn steel using atom probe tomography. *Ultramicroscopy* **132**, 239–247 (2013).

61. Takahashi, J., Kawakami, K. & Kobayashi, Y. Quantitative analysis of carbon content in cementite in steel by atom probe tomography. *Ultramicroscopy* **111**, 1233–1238 (2011).
62. Thuvander, M. *et al.* Quantitative atom probe analysis of carbides. *Ultramicroscopy* **111**, 604–608 (2011).
63. Sha, W., Chang, L., Smith, G. D. W., Liu Cheng & Mittemeijer, E. J. Some aspects of atom-probe analysis of Fe-C and Fe-N systems. *Surf Sci* **266**, 416–423 (1992).
64. Jang, J. H., Lee, C.-H., Heo, Y.-U. & Suh, D.-W. Stability of (Ti, M)C (M = Nb, V, Mo and W) carbide in steels using first-principles calculations. *Acta Mater* **60**, 208–217 (2012).
65. Zhao, H. *et al.* Hydrogen trapping and embrittlement in high-strength Al alloys. *Nature* **602**, 437–441 (2022).
66. Dhara, S. *et al.* Atom probe tomography data analysis procedure for precipitate and cluster identification in a Ti-Mo steel. *Data Brief* **18**, 968–982 (2018).
67. Råsander, M., Hugosson, H. W. & Delin, A. Density functional study of carbon vacancies in titanium carbide. *Journal of Physics: Condensed Matter* **30**, 015702 (2018).
68. Kresse, G. & Furthmüller, J. Efficient iterative schemes for *ab initio* total-energy calculations using a plane-wave basis set. *Phys Rev B* **54**, 11169–11186 (1996).
69. Perdew, J. P. *et al.* Atoms, molecules, solids, and surfaces: Applications of the generalized gradient approximation for exchange and correlation. *Phys Rev B* **46**, 6671–6687 (1992).
70. Perdew, J. P., Burke, K. & Ernzerhof, M. Generalized Gradient Approximation Made Simple. *Phys Rev Lett* **77**, 3865–3868 (1996).
71. Monkhorst, H. J. & Pack, J. D. Special points for Brillouin-zone integrations. *Phys Rev B* **13**, 5188–5192 (1976).

Acknowledgement

Y.-S. C. thanks the support from his family. **Funding:** The authors acknowledge funding from Australian Research Council (LP180100431, LP210300999, IE230100160, FT180100232, and LE190100048), CITIC-CBMM Nb Steel Award Fund Program (2018FWNB30064), the 2019 University of Sydney Postdoctoral Fellowship, Taiwan's Ministry of Education (Taiwan-University of Sydney

Scholarship) and National Science and Technology Council (111-2119-M-002 -020-MBK), China's National Key R&D Program (2022YFE0110800 and 2022YFB3705200) and National Natural Science Foundation (51922054, 52301176, and U1808208), Advanced Computing Center of Yunnan University, National Taiwan University, as well as the research facilities and technical service supported by Microscopy Australia and the University of Sydney's Core Research Facility program.

Author contribution:

P.-Y. L. conducted the APT experiments and the data analyses and drafted the manuscript. B. Z. conducted the DFT simulation, the TDS experiments, and drafted the manuscript. R. N. conducted the TEM experiments and drafted the manuscript. S.-L. L. and C. H. supported the APT and TEM experiments. M. W. supported the TDS experiments. F. T. supported the DFT simulation. Y. M. provided the computational resource for the simulation and supported the DFT simulation. T. L. conceptualized the project and participated in the manuscript development. P. A. B. participated in the data analysis and the manuscript development. H. L., A. G., and H.-W. Y. provided funding support, supervised the project, and participated in the manuscript development. J.M.C. provided the microscope facilities, supervised the project, and finalized the manuscript. H. C. initiated and conceptualized the project, provided the samples and funding, supervised the project, and participated in the manuscript development. Y.-S.C. initiated and conceptualized the project, designed the protocols of analyses, provided funding support, supervised the project, drafted the manuscript, and finalized the manuscript. **Competing interests:** The authors declare no competing interests.

Supplementary Materials (provided as an Appendix to this thesis)

Supplementary Figure 1 to 13

Captions of Supplementary Movies 1 and 2

3.3 Summary

In this chapter, I present an engineering strategy aimed at enhancing the capacity of hydrogen trapping. This is achieved by introducing a higher number of carbon vacancies into transition metal carbides within ferritic steel. Atom probe tomography and first principle calculation results confirm that the sites for trapping hydrogen are affected by both the incorporation of Mo (Molybdenum) and the increased presence of carbon vacancies within the carbide structure.

Importantly, this engineering approach is not limited solely to the Ti and Mo system. Other transition elements also exhibit similar effects, indicating the broader applicability of this strategy. Previous observations using cryogenic atom probe techniques, which investigated hydrogen trapping sites within ferrite for the (V, Mo)C (Vanadium, Molybdenum Carbide) system [189], revealed comparable mechanisms. These mechanisms involve the entrapment of hydrogen within the carbide structure. What sets our work apart is that, for the first time, I present both experimental results and reference material systems. This allows us to systematically eliminate other potential variables, thereby confirming the existence of two distinct hydrogen trapping mechanisms. This discovery offers fresh insights for the design of materials with enhanced resistance to hydrogen embrittlement.

Chapter 4 - Hydrogen-enhanced deformation in pearlite

4.1 Background

In addition to actively incorporating hydrogen trapping sites into the microstructure of steel, there is considerable interest in understanding the intrinsic microstructure of steel itself, particularly in identifying locations where irreversible hydrogen entrapment can occur. Among the various steel microstructures, pearlitic steel stands out as one of the most well-known. This type of steel finds extensive use in products like natural gas pipes. To ensure a cost-effective transition to hydrogen, it's imperative to explore the feasibility of utilizing existing natural gas pipelines for hydrogen transport. However, exposing current pearlitic steel gas pipelines to hydrogen can result in hydrogen embrittlement.

Addressing this issue comprehensively and devising potential solutions are essential steps toward advancing the global adoption of hydrogen for decarbonization efforts. In this chapter, our primary objective is to conduct a comprehensive investigation into the interaction between hydrogen and pearlitic steel, focusing on its distinctive lamella microstructure. This investigation is approached from both experimental and simulation perspectives, including atom probe tomography and first principles calculations. Furthermore, we delve into the phenomenon of hydrogen-induced fracture, employing in-situ micromechanical testing experiments to gain deeper insights.

By undertaking a multifaceted examination of how hydrogen interacts with pearlitic steel and its lamella structure, we uncover crucial insights that can inform the development of strategies to mitigate hydrogen-induced issues. This research is vital for enabling the safe and effective utilization of existing infrastructure, such as natural gas pipelines, during the transition to a hydrogen-based energy landscape.

Results are presented in the form of a manuscript currently under review by '***Acta Materialia***'. The content of this article is largely the product of the work of Ranming Niu under the supervision of Hongzhou Lu, Yi-Sheng-Chen and Julie M. Cairney. Ranming Niu conducted the APT experiment, data analysis and drafted the manuscript. Hanyu Li conducted the in-situ micromechanical testing experiment and draft the manuscript. **Pang-Yu Liu** supported the APT experiment and data analysis, conducted the TDS experiment, DFT simulation and drafted the manuscript. Patrick Burr supported the DFT simulation and participate in the manuscript development. Yi

Feng provided the samples. Hung-Wei Yen participated in the manuscript development. Mintu Ma and Aimin Guo supervised the project and provided funding support. Hongzhou Lu supervised the project, provided the samples, provided funding support, and supervised the project. Yi-Sheng Chen initiated and conceptualized the project, supervised the project, provided funding support, drafted the manuscript, and finalized the manuscript. Julie Cairney provided the microscope facilities, supervised the project, and finalized the manuscript.

4.2 Submitted manuscript

Hydrogen-enhanced deformation in pearlite

Ranming Niu[1,2,7], Hanyu Li[1,2,7], Pang-Yu Liu[1,2,7], Patrick Burr[3], Yi Feng[4], Hung-Wei Yen[5], Chao Huang[1,2,], Yi-Hsuan Sun[5], Mingtu Ma[4], Aimin Guo[6], Hongzhou Lu[6,*], Yi-Sheng Chen[1,2,5,*], Julie M. Cairney[1,2,*]

[1]Australian Centre for Microscopy and Microanalysis, The University of Sydney, Sydney, Australia

[2]School of Aerospace, Mechanical and Mechatronic Engineering, The University of Sydney, Sydney, Australia

[3]School of Mechanical and Manufacturing Engineering, University of New South Wales, Australia

[4]China Automotive Engineering Research Institute Co., Ltd., China

[5]Department of Materials Science and Engineering, National Taiwan University, Taiwan

[6]CITIC Metals Co., Beijing, China

[7]These authors contributed equally to this work: Ranming Niu, Hanyu Li, Pang-Yu Liu.

*Corresponding authors:
julie.cairney@sydey.edu.au (J.M.C.); yi-sheng.chen@sydney.edu.au (Y.S.C.); luhz@citic.com (H.L.)

Abstract

Hydrogen-induced degradation of pipeline steels is a serious safety challenge for the transport of hydrogen. Steel pipes contain a large proportion of the pearlite phase, which consists of lamellar cementite in ferrite. How hydrogen interacts with pearlite and degrades the mechanical properties remains unclear. Here we have studied the deformation behavior of pearlite in hydrogen, with emphasis on the cementite–ferrite interface. In-situ micromechanical results revealed that the plastic deformation of H-charged pearlitic samples occurs predominantly within the ferrite phase, with some shearing of the cementite, while in uncharged samples it takes place by slip at the ferrite-cementite interface. Cryo atom probe tomography confirms that hydrogen is associated with defects in the ferrite away from the interface and is trapped within the

cementite, enhancing dislocation motion in both ferrite and cementite bulk. Hydrogen is not observed at the interface. First principal simulations show the expected influence of lattice strain and cementite vacancies on hydrogen trapping, consistent with the experimental results.

1. Introduction

The use of hydrogen (H) as a decarbonized fuel has the potential to reduce our dependence on fossil fuels for energy or transportation. H is being proposed for energy in many major countries including USA, Japan, Germany, UK, Korea, Australia, China, and Canada [1]. A common assumption is that H will be distributed via the existing natural gas transmission network, allowing for a transition with minimal infrastructural renovation. However, existing gas infrastructure is comprised mainly from steel, and gaseous H can be absorbed by steel, reducing its toughness and potentially leading to catastrophic failure due to a phenomenon known as hydrogen embrittlement (HE) [2,3]. This is an enormous safety concern as H is flammable, even explosive, when combined with oxygen in air [4]. It is paramount to understand how hydrogen leads to HE in gas pipeline steels, both for risk mitigation for existing infrastructure, and to provide guidance for the development of future hydrogen-safe alloys.

HE in steels arises from interactions between solute H and microstructural features, most notably dislocations and grain boundaries. For dislocations, H atoms in the lattice are attracted to the strain field around their cores, forming so-called Cottrell atmospheres [5], which reduce the elastic field required for slip, leading to increased dislocation activity. This increased activity facilitates the formation of microvoids, and eventually their coalescence, leading to subsequent crack propagation in the H-

rich region [6,7]. This process is referred as H-enhanced localized plasticity (HELP) [8]. The fine nature of the dimples on the resulting fracture surfaces can mean that HELP-induced fracture surfaces have a pseudo brittle fracture (quasi-cleavage) appearance [9]. Adsorption-induced dislocation emission (AIDE) also occurs, whereby H enhances dislocation nucleation [10], again leading to micro-voids and quasi-cleavage fracture surfaces [7].

The segregation of H solute to microstructural interfaces and grain/phase boundaries can reduce their strength, leading to H-enhanced decohesion (HEDE) [11]. This segregation not only affects the interface, but also lowers the atomic bonding energy of the matrix lattice, as proposed by Troiano [12] and further developed by Oriani [11]. HEDE is associated with hydrogen-induced brittle cracking.

One of the solutions to mitigate hydrogen embrittlement is to introduce hydrogen ‘traps’ in material microstructures [13–15]. The aim is to create benign repositories of the hydrogen solute atoms that do not participate in the embrittling process in the presence of loading. However, it can be difficult to determine the detrimental or benign roles of microstructural features that attract H. Bulk / macroscale measurements of H susceptibility by mechanical testing [14], or the measurement of H trapping by thermal desorption [16] provide information that can be used to speculate as to the active HE processes. The situation is further complicated by the fact that multiple HE mechanisms can operate simultaneously [17].

American Petroleum Institute (API) X52, X56, X60, and X65 pipeline steels are the most prevalent alloys in gas transmission systems [18]. These steels generally have a low-strength body-centered cubic (bcc) ferrite matrix and 20 to 30 volume

percent pearlite [19], a phase that consists of lamellar cementite (Fe_3C) in ferrite [20,21]. Although it is an important phase in these steels, the role of hydrogen on the deformation behavior of pearlite has been less well studied than it has in simpler phases in these alloys such as ferrite. H-induced property degradation has generally been attributed to HEDE because of the high concentration of cementite–ferrite interfaces in pearlite, which, in theory, are susceptible to HE [22]. It has also been reported that cracks initiate at the cementite–ferrite interfaces, especially at high concentrations of hydrogen [23]. More recently, tearing topography surfaces (stepped flat and dimpled fracture surfaces) observed in H-charged pearlitic steels have been attributed to brittle shear cracking across colonies [24].

These findings have been largely based on fractography and post-mortem transmission electron microscopy investigations. Here we have used in-situ deformation and atom probe microscopy to study a model hypoeutectoid steel sample with a high volume-fraction of pearlite in order to determine how hydrogen affects plastic deformation and where within the microstructure the hydrogen is trapped.

2. Experimental procedures

2.1 Material production and heat treatment

The steel ingot was continuously cast by desulphurization, converter processing, refining in furnace, and vacuum degassing. The ingots were then heat-treated by pre-heating (< 900°C), heating (950 – 1020°C) and homogenizing (1080 – 1120°C) for a total of 8 hours. The steel sheets were hot-rolled in 5 steps between 1100°C and 850°C to reduce the ingot thickness from 40 mm to 6 mm, followed by water-cooling to 600°C. The steel sheets were then cooled in a pit furnace at 350°C. The composition of the steel is given in **Table 1.**

Table 1. Material composition (weight percent, wt.%)

Fe	Mn	C	Si	Cr	V	Zn	Al	S	Cu	Ni	P	N
98.55	1.39	0.44	0.44	0.18	0.085	0.030	0.011	0.038	0.031	0.013	0.011	0.004

2.2 In-situ micro-mechanical compression tests in a scanning electron microscopy (SEM)

Hypoeutectoid steel sheet samples of 10 × 10 × 1 mm were mechanically polished, followed by a dual 8-kV argon ion beam polishing at an angle of 5° for 45 minutes in a precision etching coating system (PECS, Gatan). Pearlitic micropillars were prepared following the steps below as illustrated in **Fig. S1**: electron back scattered diffraction (EBSD) was conducted on the surface of a polished bulk specimen to identify grains with normal orientation parallel to $<110>_{ferrite}$. Rough trenching was carried out at 30 kV-4 nA, in an annular pattern with an outer diameter of 15 μm and an inner diameter of 3 μm. Due to the cementite-ferrite orientation relationship, lamellar cementite are oriented along the {112} planes of the ferrite matrix in the samples. We selected the micropillars with uniform cementite lamellae that are inclined 40-50 degrees to the micro-compression direction, to allow {112} slip to be the primary deformation mode. Final ion milling was carried out at 30 kV-30 pA until the desired geometry was achieved.

The in-situ micro-compression experiments were conducted in a Zeiss Ultra SEM operated at 5-30 kV. Compression was applied by a nanoindenter (PI85, Hysitron) using a diamond punch with a 2-μm-diameter flat tip. Compression experiments were carried out in strain-control mode at a rate of 3 nm/s, which is equivalent to a quasi-static loading at a strain rate of 10^{-3}. The loading and straining data and the sample geometry were used to calculate the stress–strain curves. Resolved shear stress was used to account for the influence of the angles of the

cementite lamellae. H-charged samples were electro-chemically charged in 0.1 M NaOH in H_2O for 1 hour. After a quick dusting, the H-charged samples were immediately loaded into a SEM (Ultra, Zeiss) for testing. The loading takes approximate 10 minutes. The in-situ compression test generally commenced within 30 minutes and was complete within 4 hours.

2.3 Transmission electron microscopy (TEM) experiments

After polishing, TEM specimens were prepared by using a Xenon focused-ion beam (FIB) in three steps: 30 kV-300 pA, 30 kV-30 pA, and 5 kV-30 pA, in a Thermofisher G4 Hydra Plasma FIB-SEM (PFIB) equipped with an EBSD detector (Symmetry, Oxford Instruments). The same procedures were used to prepare the post-mortem TEM samples from the deformed pillars. The TEM sample was imaged by a Thermo-Fisher Themis-Z Double-corrected S/TEM at 300 kV. The convergence angle is 17.9 mrad, while the collection angles under HAADF and ABF are 38 – 200 and 9 – 35 mrad, respectively. The selected-area diffraction pattern was taken with a camera length of 200 mm in a JEOL JEM-2100 TEM at 200 kV.

2.4 Atom probe tomography (APT) experiments

APT samples were prepared from 1 × 1 × 15 mm matchstick bars, starting with rough electropolishing in 25% perchloric acid in acetic acid at 10-30 V until two needle specimens form at the middle of the bar samples. Fine polishing was then conducted in 2% perchloric acid in butoxyethanol under an optical microscope. Polishing was undertaken at 30 V until a neck forms near the apex, and then at 10 V until a new sharp tip was formed. The sharpened tips were then ion-milled in the PFIB to capture the lamellar cementite in the APT field-of-view, by using an in-situ annular milling process as illustrated in **Fig. S2.** Ion milling began with a 30 kV-4 nA beam for

locating the region of interest (ROI) in the tip, followed by a 30 kV-100 pA beam for finer operation, ending with a 2 kV-100 pA beam for final shaping.

Cementite lamellae inclined at ~45° were targeted for an optimized combination of data yield and spatial resolution of elemental mapping at the interface. Although the analysis direction (the z-direction along the length of the tip) gives the highest spatial resolution in APT analysis [25], horizontal cementite in the tips resulted in high tip fracture rate and low data yield in voltage-mode APT.

D charging of APT tip samples was carried out by using 0.1 M NaOH in D_2O for 30 seconds. The D-charged specimens were transferred to the atom probe by using a cryogenic-sample transfer (cryo-transfer) protocol described elsewhere [26].

Data for the uncharged sample was acquired by using a Local Electrode Atom Probe (LEAP 3000 Si, CAMECA), and cryo-APT was conducted using a LEAP 4000X Si (CAMECA) with a cryo-transfer suitcase (Ferrovac). All APT experiments were conducted at a voltage pulse frequency of 200 kHz, a specimen temperature of 50 K, and a pulse fraction of 20%. All APT reconstructions used the default algorithm in AP Suite (Version 6.1, CAMECA) with the settings of 57% detector efficiency and 1.65 image compression factor. 1-D concentration profiles were obtained from cuboid ROIs with fixed bin width of 1 nm without bin overlaps. No 2 Da peak was observed in uncharged data, therefore it is assumed to be associated with charged deuterium ions. Ion-density maps for all APT results (**Fig. S3**) were also examined to confirm that the electric field change between ferrite and cementite has little influence on the D concentration.

2.5 Density function theory (DFT) simulations

DFT simulations were conducted by using the Vienna ab-initio simulation package (VASP) [27]. The simulations employed the Perdew-Burke-Erzerhof (PBE) exchange-correlation functional [28] along with projector augmented-wave (PAW) [29] pseudopotentials. The valence electrons of Fe-3d74s1 and C-2s22p2 were considered, and the plane wave basis set cutoff was set at 500 eV. The simulations included spin polarization to account for the magnetic moment of iron, and a Methessel-Paxton smearing of 0.1 eV. The structures were iteratively minimized until the energy change between three consecutive steps reached below 10-5 eV. The relaxed lattice parameters of cementite, assuming the Pnma space group definition, were found to be a = 5.03 Å, b = 6.71 Å and c = 4.48 Å and the lattice parameter of ferrite was determined to be a = 2.83 Å.

Dilute carbon vacancies and H defects, and pairs of those defects, were simulated in a 192-atom supercell of cementite, built from a 2 x 2 x 3 replica of the Pnma unit cell, and a 128-atom supercell of ferrite, built from a 4 x 4 x 4 replica of the conventional bcc unit cell. K-point sampling for these supercells was through Monkhorst-Pack grids [30] of 4 x 3 x 2 and 4 x 4 x 4, respectively. For higher concentrations, we describe the system using configurational ensembles, which allows us to take into account the various H-vacancy and vacancy-vacancy complexes that may form in a hypo-stoichiometric carbide. The Site-Occupation Disorder (SOD) algorithm [31] was utilized to model the configurational ensembles. Cementite supercells with dimensions of 2 x 1 x 2 containing 64 atoms were employed, and a k-point grid of 4 x 5 x 4 was applied. This resulted in 128 independent configurations at the four stoichiometries considered (6.25%, 12.5%, 18.75% and 25%).

3. Results

Scanning electron microscopy (**Fig. 1A**) reveals that the sample has pearlitic grains that consist of cementite (dark linear features) in a ferritic matrix (grey background). **Fig. 1B** is an annular bright-field scanning transmission electron microscope (ABF-STEM) image of the pearlite taken along [111] zone-axis, from which we measured that the parallel cementite lamellae are 29 ± 6 nm thick with an average spacing of 95 ± 28 nm. Selected area electron diffraction (SAED) (**Fig. 1C**) confirms that the cementite and ferrite follow the Isaichev orientation relationship, $(101)_{cementite} \parallel (11\bar{2})_{ferrite}$ and $[010]_{cementite} \parallel [111]_{ferrite}$ [32]. High-angle annular dark-field scanning transmission electron microscopy (HAADF-STEM) imaging (**Fig. 1D**) confirms the orientation relationship and reveals the atomic structure of the cementite–ferrite interface.

Geometric phase analysis was conducted using the software package Strain++® [33]. The ferrite lattice far from the interface was used as a reference to calculate the elastic strain. **Fig. 1D** is a lattice strain map of the interfacial area shown in **Fig. 1C**. The ferrite region near the interface (orange arrow) is expanded and the cementite near the interface (blue arrow) is compressed due to the lattice misfit between the two phases.

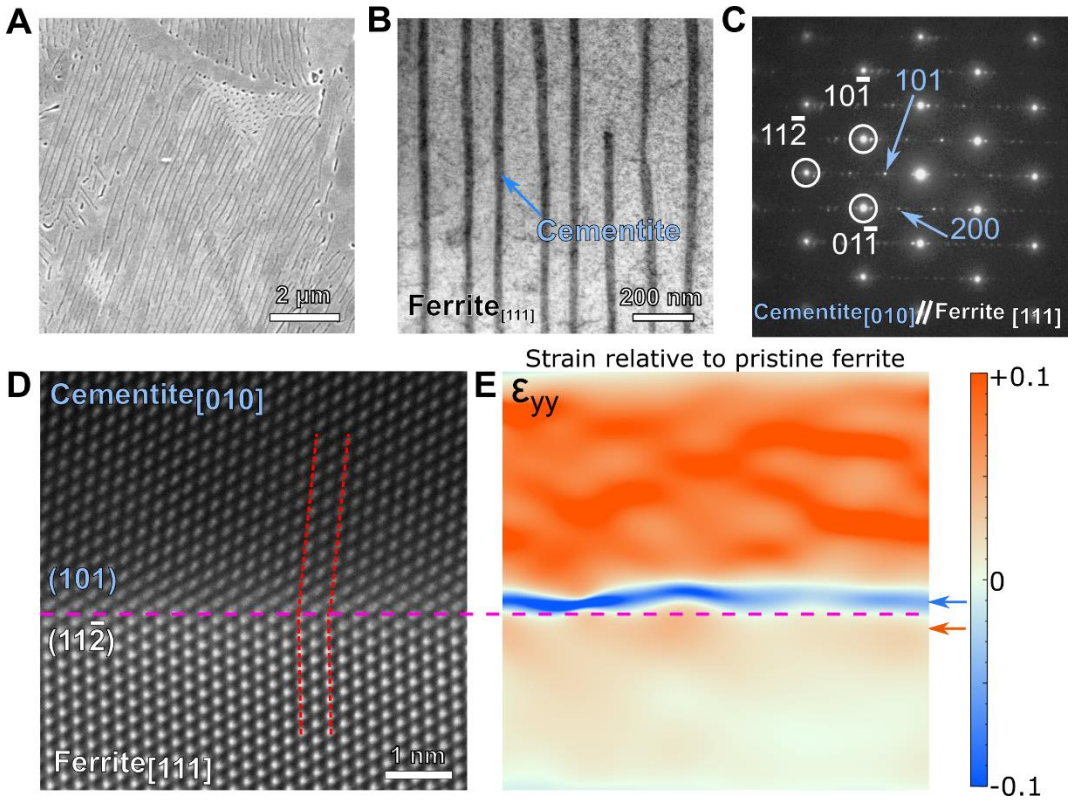

Fig. 1. Microstructure of the designed fine pearlitic steel specimen. (A) Secondary electron scanning electron microscopy (SEM) image and (B) bright-field TEM image showing the pearlitic microstructure containing lamellar cementite. (C) The selected area electron diffraction (SAED) pattern and the atomic resolution HAADF-STEM image in (D) show that ferrite and cementite follow the Isaichev relationship. (E) is a strain map obtained from (D) by using geometric phase analysis, showing an expansion (orange arrow) of the ferrite lattice and a compression (blue arrow) of cementite near the interface. Positive and negative strain values correspond to tension and compression, respectively.

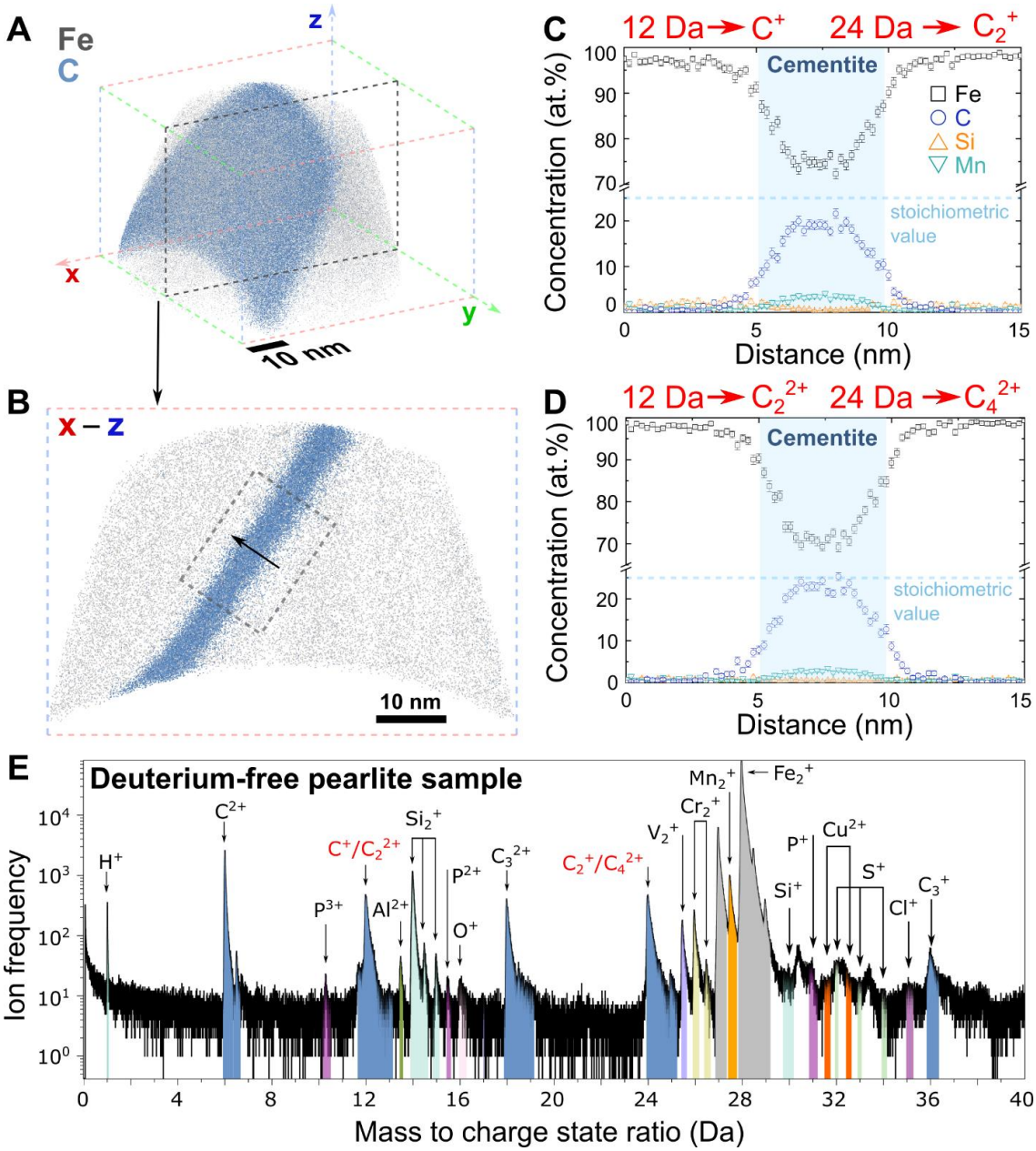

Fig. 2. Atom probe tomography analysis of a single layer of cementite. (A) is an APT 3-D atom map reconstruction with iron (grey) and carbon (blue). (B) is a 10-nm thick slice from the region marked by the broken line in (A). (C) and (D) are 1-D concentration profiles from the region of interest in (B) with the size of size of 15(L) x 20(W) x 20(H) nm^3 along the direction marked with an arrow. Specifically, The lower-bound carbon concentration (19.24 at.%), given in profile (C), is plotted by assigning peak 12Da and peak 24 Da in mass spectrum (E) fully to C^+ and C_2^+, respectively, while the upper-bound carbon concentration (23.16 at.%), given in profile (D), is plotted by assigning 12Da and 24 Da fully to C_2^{2+} and C_4^{2+}. A modest level of manganese (~2.75at.%) and silicon (~0.16 at.%) was also detected in the cementite phase. (E) is a mass spectrum showing the ranges applied to the pearlitic steel sample. Following the C2/C4 assignment, the bulk composition of this dataset is C - 0.06 at.%, Mn - 1.26 at.%, and Si - 0.58 at.%.

We also used atom probe tomography (APT) to measure the composition of the cementite. A needle-shaped sample was fabricated that deliberately contained a cementite lamella angled close to 45° to provide an optimal combination of data yield and interfacial spatial resolution (see experimental methods and **Fig. S2**) [25]. The APT result is shown in **Fig. 2** (**Video S1** for the animated version), where Fe and C atoms correspond to grey and blue dots, respectively. A 10 nm thick slice of data from the highlighted region of **Fig. 1A** is shown in **Fig. 1B**. 1-D concentration profiles from the region highlighted by the black arrow in **Fig. 2B** are provided in **Fig. 2C** and **2D**. Careful evaluation of the atom probe data was undertaken to quantify the carbon concentration in cementite. It's possible that the peaks at 12 and 24 mass-to-charge ratio (Da), assigned to C^+ and C_2^+, respectively, may also contain signals from ions with more carbon, i.e. C_2^{2+} and C_4^{2+} [34,35]. Ion peak assignments in the mass spectrum are given in **Fig. 2E**. To evaluate the effect of carbon peak assignment, we assigned the 12 and 24 Da peaks to C^+ and C_2^+, respectively, to show the lower bound of the estimated carbon content (**Fig. 2C**). In addition, we assigned the 12 and 24 Da peaks to C_2^{2+} and C_4^{2+}, respectively, to deliberately overestimate the overall C content. This led to a maximum possible C content of 23.16 at.% (**Fig. 2D**).

The carbon concentration measured in the cementite (maximum 23.16 at. %) is lower than the nominal 25 at.% for stoichiometric (Fe_3C). This result is consistent with previous observations by APT [36] and neutron diffraction [37]. It has been established by *ab initio* calculations that imposed volumetric strain can lead to C deficiency in carbides [38]. We also examined the distribution of other alloying elements in cementite and did not observe any artefacts relating to the cementite region. It is reasonable to believe that the carbon vacancies in the cementite play a role in the deficiency of carbon.

We used in-situ micro-compression tests on micropillar specimens to examine the effect of H on the deformation mechanism. H-charged micropillars were prepared by cathodic charging (see Materials and Methods). Hydrogen diffuses quickly and can easily escape from microscale specimens [26,39,40], but the bulk specimen acts as a reservoir to supply additional hydrogen. To ensure that the specimens still contained sufficient hydrogen during our experiment, we conducted a series of thermal desorption analysis (TDA) experiments to establish a reference hydrogen content against time in vacuum. The TDA setup is detailed in reference [41]. The tests were conducted at a heating rate of 400 °C per hour on 10 × 10 × 1 mm sheets of our pearlitic steel with cleaned and polished surfaces. This specimen dimension is the same as used for the base specimen for the micro-compression tests. **Fig.3** shows the hydrogen desorption for three conditions: i) uncharged reference sample (black), which was found to have an overall H content of 17 mppb; ii) 60-minute H-charging followed by a 30-minute desorption in the TDS vacuum chamber (blue) which contained 137 mppb H; and iii) 60-minute H-charging followed by a 4-hour desorption in the TDS vacuum chamber (red), which contained 35 mppb H. Note that the H content was estimated by considering only the first peak. The signal from 200 to 300°C are excluded as they could be contributed by surface oxidization or the residual H introduced during heat treatment. These measurements suggest that approximately 137 mass part per billion (mppb) of hydrogen would remain in a specimen the size of ours at the start of the micro-compression tests (0.5 hours after hydrogen charging). 35 mppb of hydrogen would remain in the specimen at the completion of a set of micromechanical tests (4 hours after charging), still significantly more than an uncharged reference of 17 mppb.

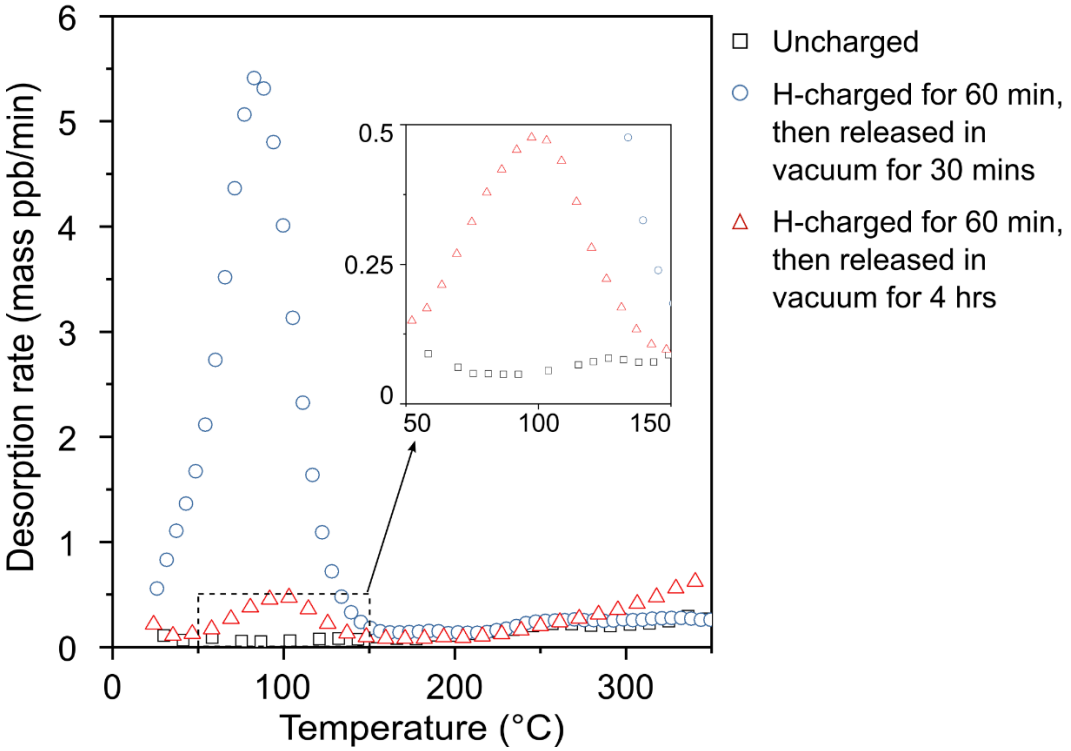

Fig. 3. Thermal desorption analyses. The experiments were conducted on an uncharged specimen (black), a hydrogen-charged specimen tested after waiting 30 min (blue), and a hydrogen-charged tested after 4 h (red) - the maximum time required for the completion of micro-compression tests. Results confirm that hydrogen remains in the specimens for duration of the micro-compression tests.

The micropillars were prepared specifically to investigate slip around the cementite–ferrite interfaces, initially assuming that slip would occur under a lower load at the interfaces as a result of interfacial H segregation, as theoretically predicted by HEDE models [22,42]. We used FIB to fabricate micropillars that were 1 μm in diameter and 3 μm high, containing cementite lamellae angled at approximately 45°, as illustrated in **Fig. 4A**. This orientation encourages slip along the direction of the cementite–ferrite interfaces by maximizing the resolved shear stress along this plane.

We first examined specimens without H, which yielded at a stress of approximately 0.93 GPa. A typical engineering stress–strain curve is shown in black in **Fig. 4A.** Pillars were then tested after cathodic H-charging (see Experimental Methods). A typical engineering shear stress–strain curve is shown in red in **Fig. 4A**.

Although hydrogen diffuses quickly and can easily escape from microscale specimens [26,39,40], we found the bulk pearlitic steel sample acts as a reservoir to supply additional hydrogen, as predicted by TDS. (See **Section 4.1**).

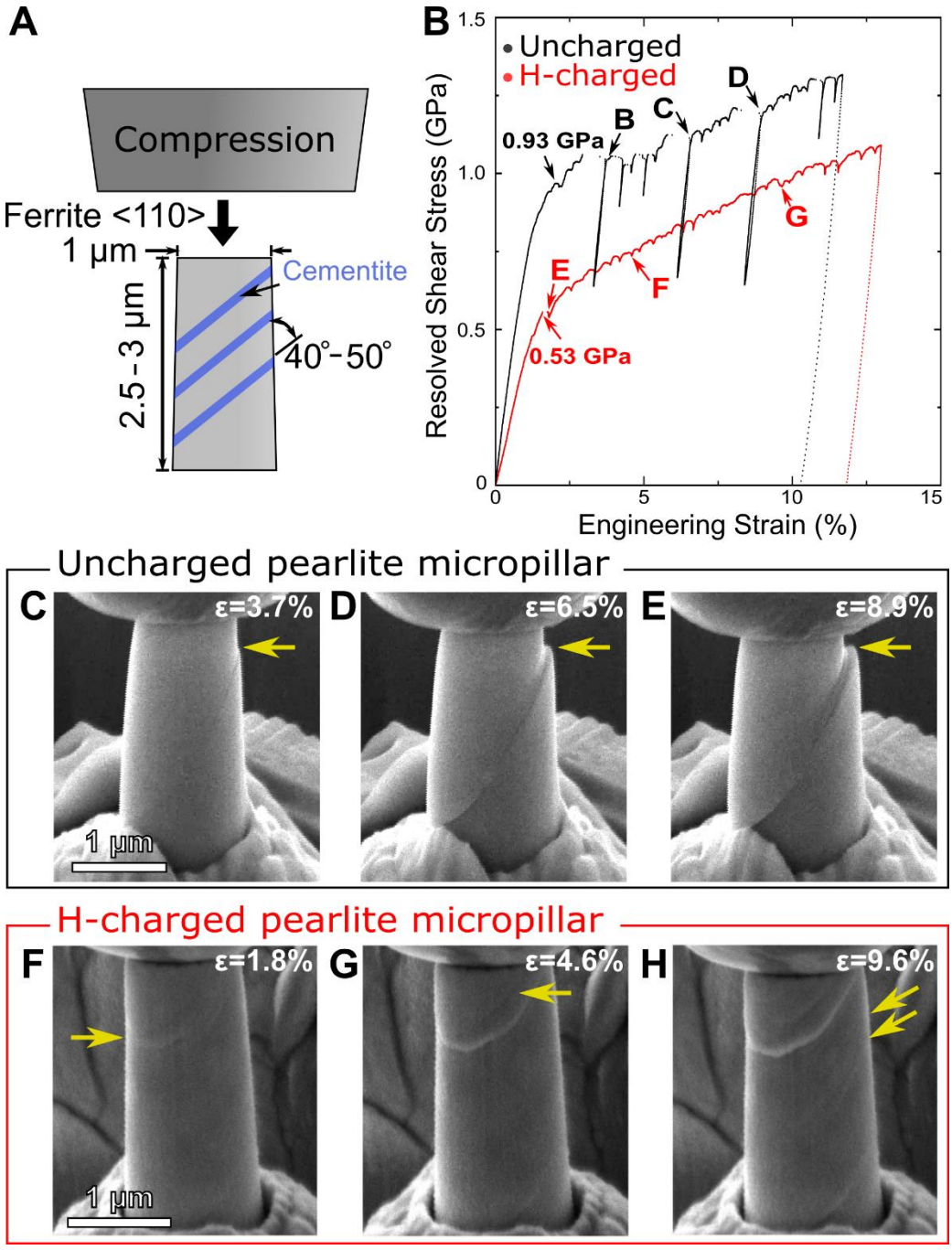

Fig. 4. In-situ micromechanical scanning electron microscopy. (A) Engineering shear strength of uncharged (black) and hydrogen-charged (red) micropillars as a function of their nominal strain. Inset is a schematic of the experimental configuration for the micro-compression test. (B), (C), (D) are still images from **Supplementary Video 2** at the instants noted in (B), showing the deformation of the uncharged pillar. (E), (F),

(G) are from the hydrogen-charged pillar, taken from **Supplementary Video 3.** The yellow arrows in the figures indicate slip bands at the given strain levels.

H-charging lowered the yield stress. For the data shown in **Fig. 4A**, the yield stress after H charging, 0.53 GPa, is approximately 40% less than for the uncharged specimen (0.93 GPa). The experiment was repeated on eight separate samples **(Fig. S4)**, and the average yield stress was 0.56 GPa for the charged samples and 1.02 GPa for the uncharged samples. Examination of the stress–strain curves reveals that both specimens experienced strain bursts that correspond to drops in the stress, but the bursts in the unchanged samples appears were larger and less frequent on the H-charged sample. Different burst behaviour reflects a hydrogen-induced change in the nature of the deformation.

The deformation behaviour is further elucidated with reference to SEM images of the pillar taken during compression. Images of the uncharged pillar are shown in **Figs. 4C–E**, corresponding to the labels B–D after bursts in **Fig. 4B**. The plastic deformation of the uncharged pillar is mainly accommodated by abrupt shearing along specific cementite–ferrite interfaces in the micropillars. Note that the sharp corner of the slipped part of the pillar was still intact, confirming the slipped material does not collide with the base. Plastic deformation in the H-charged pillar was much more homogeneous. As shown by **Fig. 4F–H**, corresponding to the relevant labels on the curve in **Fig. 4B,** the H-charged pillar displayed a smoother straining process that suggests more consistent dislocation slipping across the entire micropillar, possibly due to enhanced dislocation mobility after H charging. **Supplementary Videos 2 and 3** provide a typical comparison of the in-situ micro-compression for the two sample-types.

We examined the microstructure of deformed pearlite micropillars using both SEM and TEM. **Fig. 5A and B** are post-mortem FIB cross-sections of two uncharged samples, prepared edge-on to the cementite layers. Both images reveal steps on the edge of the samples where slip has taken place. **Fig. 5C** is an annular bright-field STEM (ABF-STEM) image of an uncharged specimen prepared (by FIB lift-out) close to the area labelled by the red broken square in **Fig. 5B**. While many dislocations are visible in the ferrite matrix, the surface step on the edge of the sample aligns exactly with the cementite–ferrite interface, demonstrating that interfacial slipping dominates the plastic deformation. For the H-charged pillars, post-mortem SEM cross-sectional images reveal more homogenous deformation, indicated by the smooth edges and mushroom shape seen in **Fig. 5D,** and the more abundant small slip steps in **Fig. 5E**. The ABF-STEM image in **Fig. 5F** shows that the steps on the edge of the H-charged samples do not directly align with the cementite–ferrite interfaces, implying that dislocations predominantly slip within the ferrite phase, rather than along the interface. The dislocations were also observed actively intersecting the cementite lamellae, as indicated by the orange arrow in **Fig. 5F**.

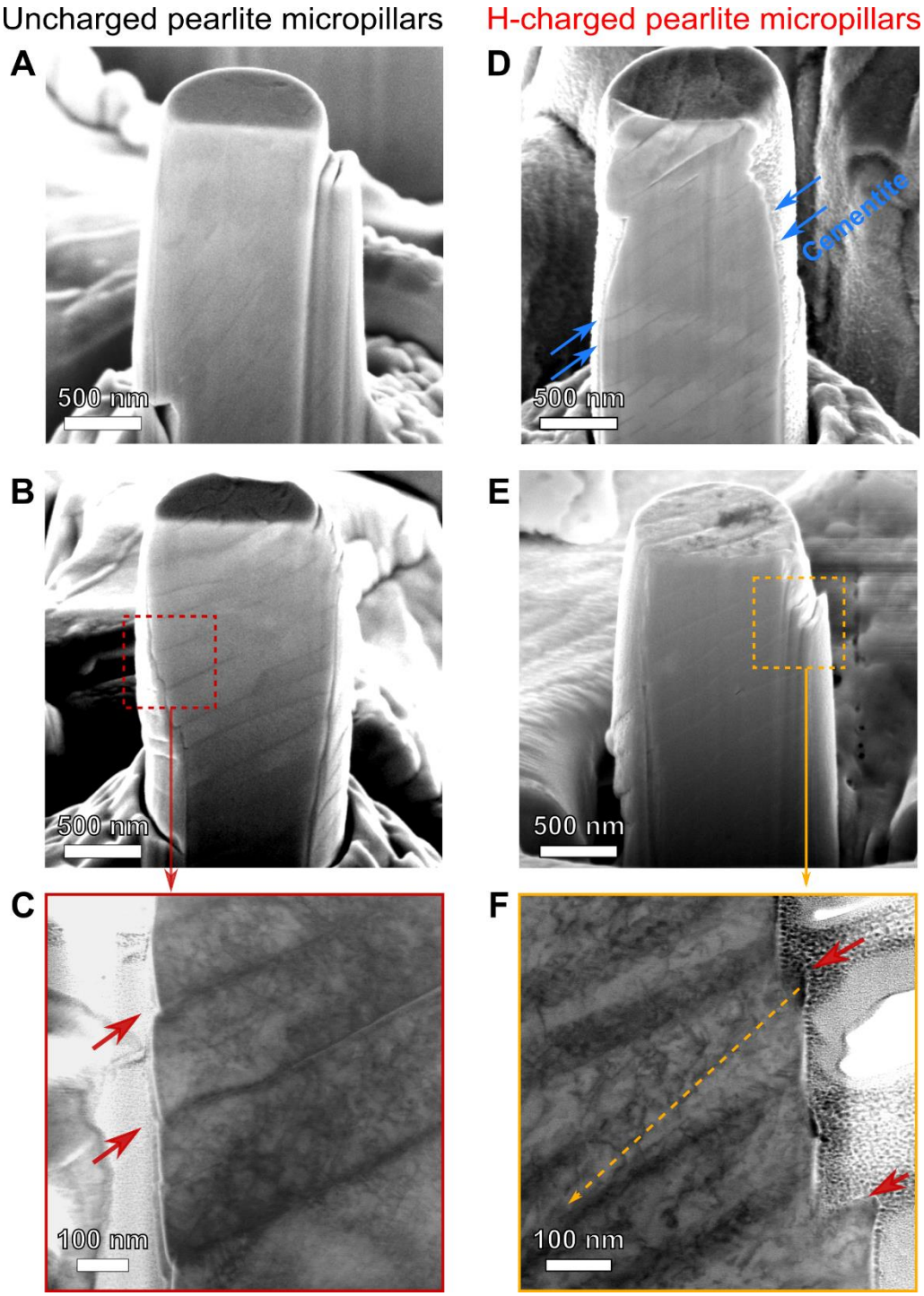

Fig. 5. Post-deformation SEM and TEM images for the uncharged pearlite micropillars (A–C) and H-charged pearlite micropillars (D–F). (A) and (B) are SEM images of FIB-prepared cross-sections. The TEM image in (C) is from the area marked by the red broken square in (B), showing slip steps on the cementite–ferrite interfaces. (D) and (E) are cross-sectional SEM images of two H-charged pearlite micropillars after deformation, while (F) is a TEM image prepared from the region marked by the yellow broken square in (E). Red arrows indicate slip steps.

Fig. 6A is an ABF-STEM image showing the overall microstructure of another charged and deformed pillar, with areas marked by red and yellow enlarged in **Fig. 6B** and **Fig. 6C**, respectively. Multiple slip steps are observed, consistent with the H-charged sample in **Figs. 5D–F**. Moreover, this pillar showcases an example of locations where dislocations appear to have passed through the cementite, as shown by the red arrows in **Fig. 6B**. Dislocation arrays slipping in the ferrite penetrate though the cementite, leading to thinning and fragmenting of the intersected cementite layer. We note that the slip along the interface co-exists with this 'intersecting' slip. **Fig. 6C** captures a regions where dislocations have slipped along the cementite, forming a slip step. Further to the right, an array of dislocations crosses the cementite. We note that the ferrite–cementite interface is parallel to the {112} plane of ferrite (**Fig. 1C**), which is one of the primary bcc slip systems [43], so steps observed on the pillar surface are consistent with H-enhanced dislocation slipping within the ferrite. TEM confirms that the H-charged samples has more abundant dislocation activity in the ferrite with a higher for propensity crossing the cementite lamellae. One would therefore suspect the cementite contributes less to the strength in the H-charged sample. We believe hydrogen reduces the micropillar's strength by enhancing the plasticity of the ferrite and softening the cementite, as supported by HELP, rather than by decreasing the cohesion of cementite–ferrite interfaces, as has been suggested in the literature [44,45].

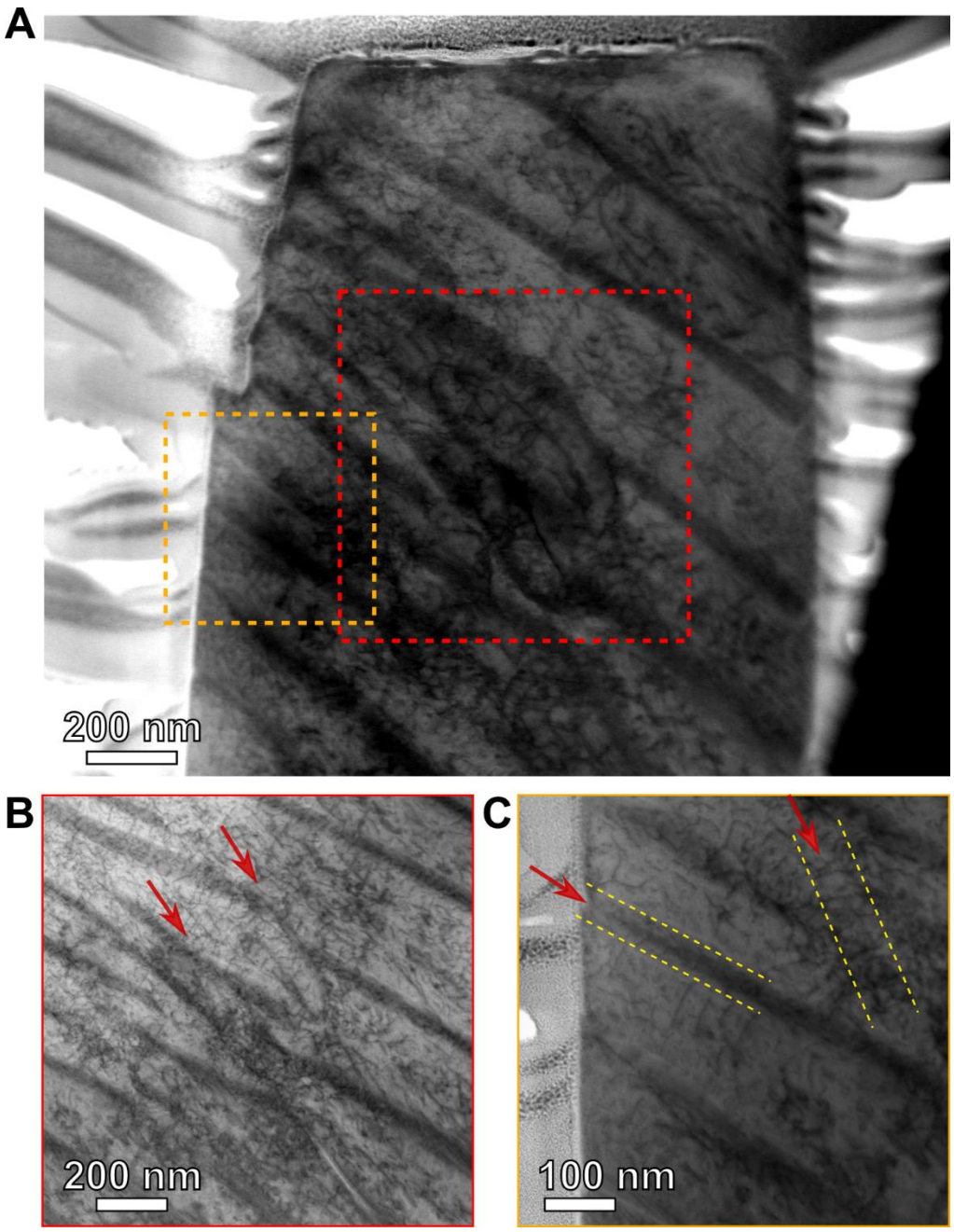

Fig. 6. Post-mortem ABF-STEM of the H-charged pearlite micropillar. (A) ABF-STEM image showing the overall deformation microstructure. (B) and (C) show the area of the same pillar marked by red and yellow squares in (A), respectively.

We also conducted micro-compression tests one day after conducting hydrogen charging experiments, aiming to test the mechanical properties of the pillars after the release of hydrogen. **Fig. 7** shows that the yield strength of the pillars is recovered after hydrogen release. This result is consistent with previous reports on hydrogen embrittlement in bulk pearlitic steels [46]. This experiment also verified that

our results were caused by hydrogen, not other artifacts caused by FIB milling or electro-chemical charging.

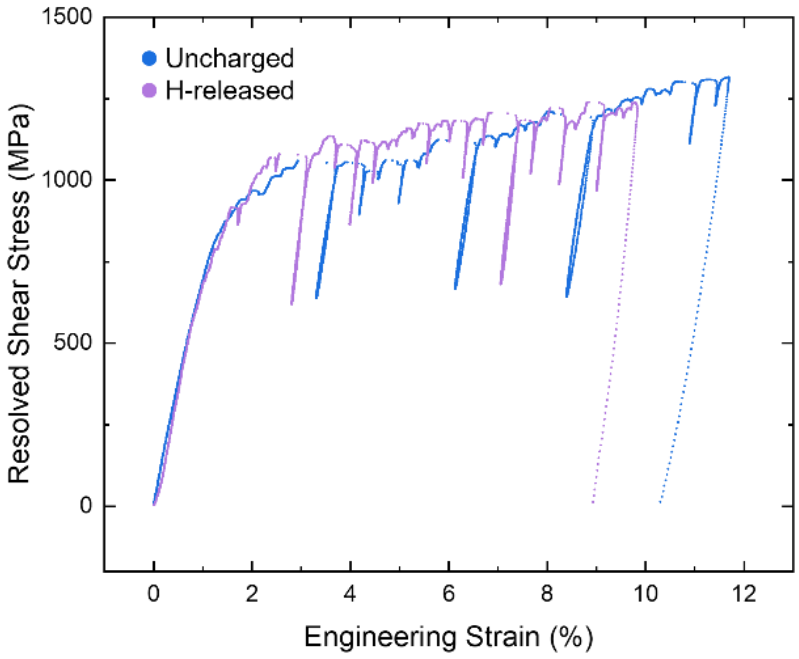

Fig. 7. Engineering stress–strain curves collected from micro-compression tests using uncharged (blue) and H-released (purple) pearlite micropillars tested 24h after charging. The two curves show similar yielding and strain burst behaviours, confirming the reversability of the mechanical effects caused by the presence of hydrogen.

To better understand the H-induced change of deformation mechanism, we used cryogenic APT (cryo APT) to examine the H distribution [26,39,47]. Deuterium ($D/^2H$) charging was used to distinguish the signal from that caused by the H background in the APT vacuum chamber and a custom cryogenic-sample-transfer APT protocol prevented fast D desorption after charging [26]. The D-charged specimen was plunge-frozen in liquid nitrogen (LN_2) and transferred under cryogenic temperatures (< 150 K) into the atom probe chamber, where voltage-pulsing APT experiments were performed at a temperature of 50 K.

Fig. 8 contains the cryo-APT results, showing the trapping of deuterium in the pearlite sample. The experiment was carried out twice to confirm the distribution of deuterium. **Figs. 8A–D** are from *cryo-APT dataset #1*. A 3-D atom map from the

charged sample, **Fig. 8A**, contains a cementite lamella (blue) and D in solution (red). Note that only 0.2% of the total iron ions (grey) are shown in order to visualize the distribution of deuterium and carbon. A 2-D slice (20 nm in thickness) perpendicular to the cementite lamella is shown in **Fig. 8B**, taken from the region marked by the broken frame in **Fig. 8A**. More deuterium ions are distributed inside the cementite than in the ferrite matrix. We did not observe D segregation at the cementite–ferrite interface, despite it being predicted by theoretical models [22,42]. Instead, we found a region of lower D concentration (a depletion zone) in the ferrite near the interface, highlighted by the red arrows in **Fig. 8B** (see also **Video S4** for the 3D animation of the reconstructed APT dataset #1). The D depletion zone can also be seen in a 1-D concentration profile (**Fig. 8C**) prepared from a region that crosses the cementite lamella in the direction indicated by the black arrow in **Fig. 8B**. The profile shows that the cementite, which contains a maximum carbon of 20 at.%, also contains deuterium ions up to 0.9 at.%, which is higher than the amount detected at the nearby interfaces and in the ferrite matrix. The mass spectrum in **Fig. 8D** shows the peak at 2 Da, associated with D, while mass spectra from the uncharged specimens (**Fig. 2E**) do not have a distinguishable peak at 2 Da. We also examined a specimen charged with D and transferred under non-cryogenic conditions. Minimal D was observed, confirming that the D in the tips is almost fully desorbed when transferring at room temperature. We repeated the experiment and obtained a similar result, *cryo-APT dataset #2*, as shown in **Fig. S5** and see also **Video S5**. A difference between this dataset and the one shown in here in the main text is that less deuterium is trapped inside cementite, which is thought to be caused by deuterium desorption as the cementite is located at the apex of the APT sample. We also note that the deuterium in ferrite is only half of that observed in the first sample, consistent with the suggestion

that more deuterium has escaped from *cryo-APT dataset #2*. Cryo-APT captures one moment in time – a delay of only a few seconds when plunge-freezing the D-charged sample may substantially affect the efficiency of capturing deuterium. For this reason, we do not attempt to quantify deuterium across different cryo-APT datasets, but overall, we are able to conclude that deuterium was not present at a detectable level at the interface and is present at a higher level away from the interface in the cementite and ferrite.

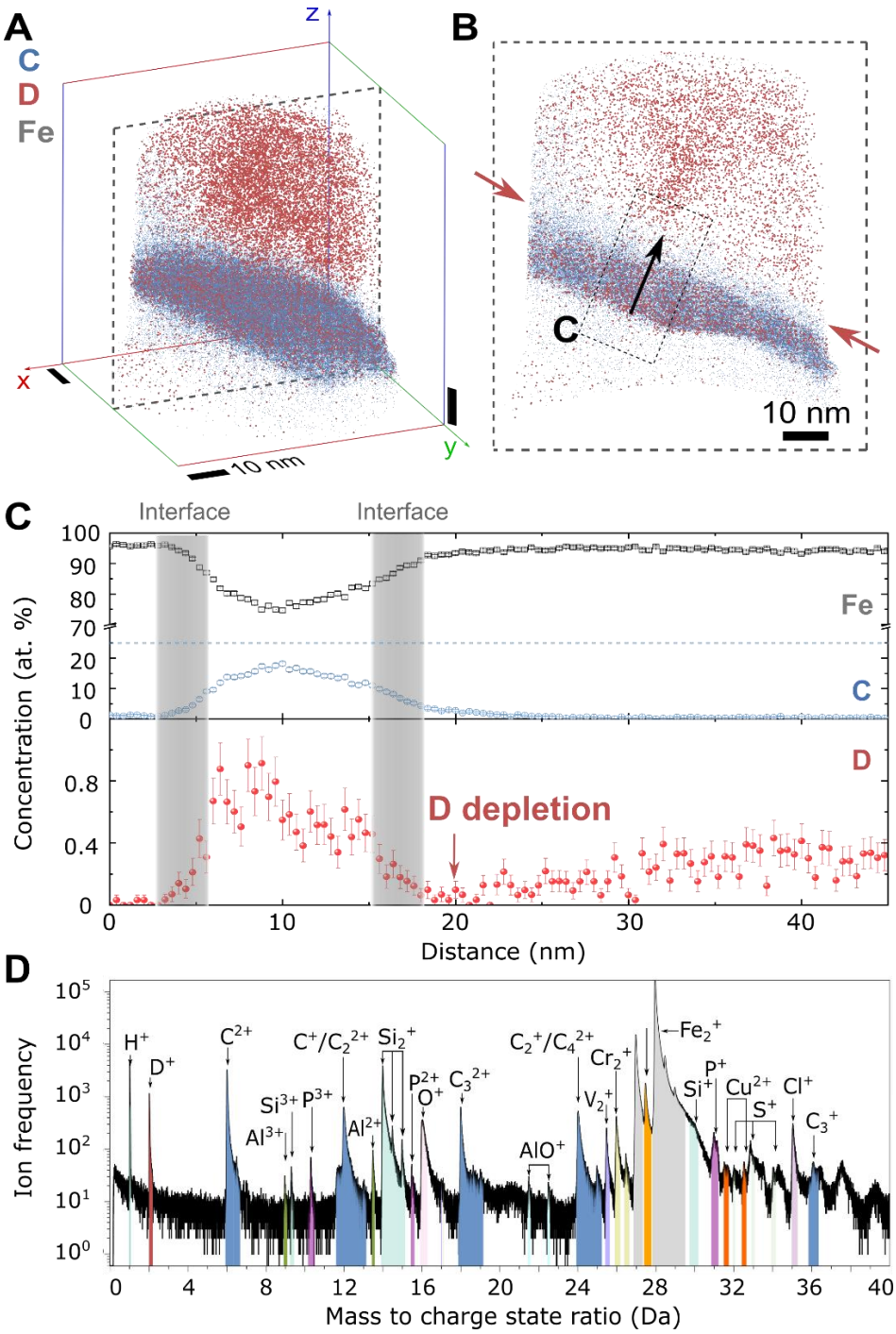

Fig. 8. APT analysis of D-charged pearlitic specimens, *cryo-APT dataset #1*. (A) is a reconstructed 3-D atom map showing the spatial distribution of carbon (blue), deuterium (red), and iron (grey). (B) is a 20-nm thick slice from the cross-section highlighted by the broken line in (A), showing that the D is concentrated in the cementite and ferrite bulk, but appears to be depleted near the cementite–ferrite interface. (C) is a 1-D concentration profile from the region highlighted in (B), showing that the cementite is rich in D, and confirming the existence of the D depletion zone. (D) is the mass spectrum for the APT dataset, showing a the 2 Da peak associated with deuterium that is not present in the data from the uncharged sample.

To understand the reason for the observed spatial distribution of hydrogen, we used density function theory (DFT) to calculate the relative hydrogen trapping potential in the proximity of the cementite–ferrite interface. The formation energy, E_f, of a defect (e.g. a H interstitial atom or a carbon vacancy), was calculated as:

$$E_f = E(\text{host} + n \text{ defects}) - E(\text{host}) \pm n * \mu(\text{defect})$$

Where $E(\text{host})$ is the DFT energy of a perfect supercell, $E(\text{host+defect})$ is the DFT energy of the same supercell with an added defect, and $\mu(\text{defect})$ is the chemical potential of any atoms added (–) or removed (+) from the perfect supercell to form the defect. For carbon vacancies, $\mu(\text{C})$ was taken as the DFT energy of diamond ($Fd\bar{3}m$), while for H interstitial atoms, to sidestep the limitation of DFT in modelling gaseous dimers [48,49], the chemical potential was defined with respect to a dilute H atom in ferrite:

$$\mu(\text{H}) = E(\text{Fe}_{192}\text{H}) - E(\text{Fe}_{192})$$

As such, the defect formation energy for H defects is also the relative change in solution energy between cementite and ferrite, ΔE_{sol}.

The calculated carbon vacancy formation energy in otherwise stoichiometric cementite is 0.65 eV, indicating that the process is endothermic. Considering APT evidence of hypo-stoichiometry of cementite, especially near the cementite/ferrite interface, we believe that carbon vacancies exist in the cementite matrix. Thus, we compute the formation energy of vacancies at higher concentrations, shown in **Fig. 9A**. The lowest energy configuration for each structure is used to investigate the trapping of H.

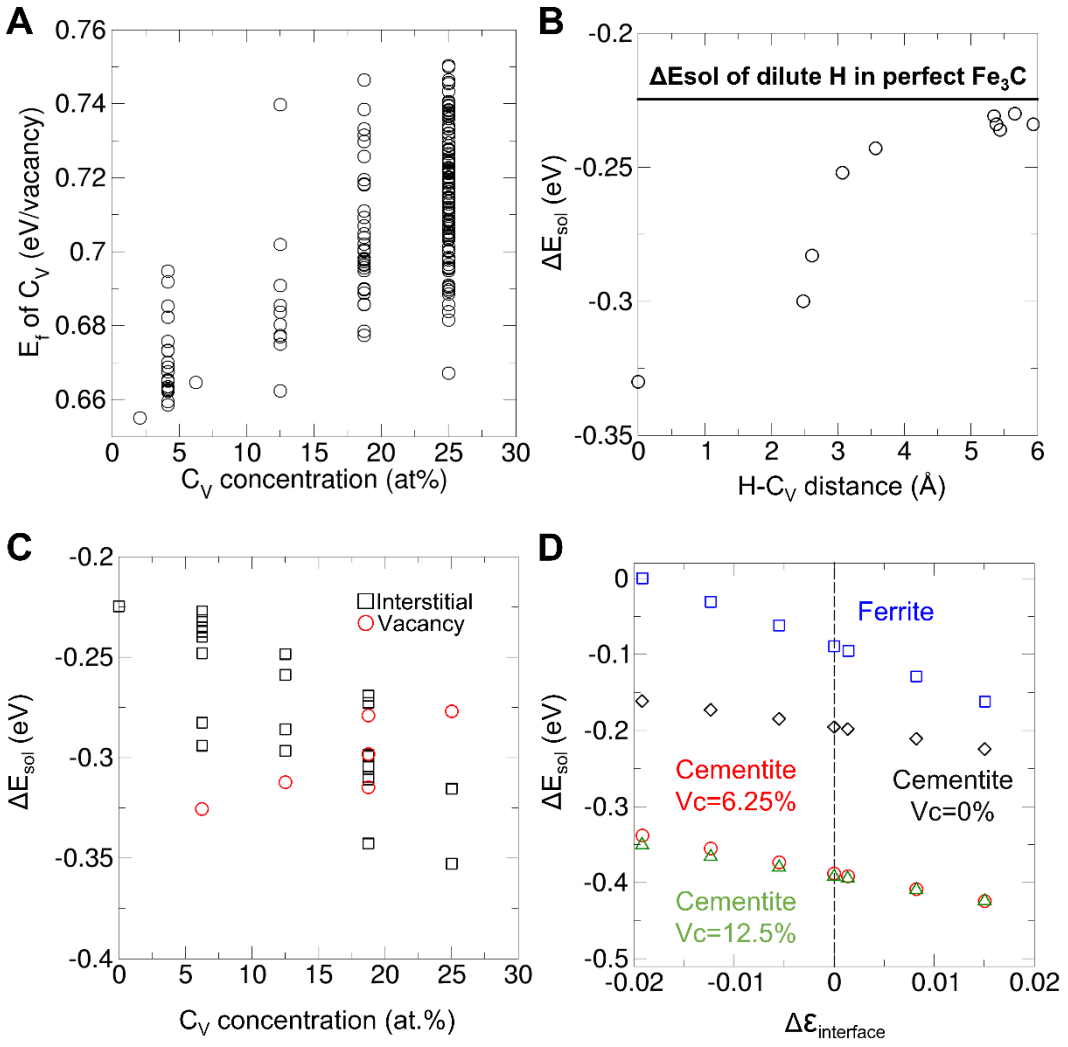

Fig. 9. Hypo-stoichiometric cementite modelling and hydrogen trapping. (A) Vacancy formation energy, per vacancy, for all symmetrically unique configurations modelled. Hydrogen trapping strength of (B) a dilute carbon vacancy in cementite as a function of distance, and (C) higher concentration of carbon vacancies, where multiple local environments are considered, and (D) applied interfacial strain $\Delta\varepsilon_{interface}$, relative to equilibrium interface lattice as described in the text.

Fig. 9B shows the binding energy between a single vacancy and a H atom as a function of distance, modelled in the larger 192-atom supercell. H is attracted to vacancies that are within 3.5 Å, and is preferentially accommodated within the vacancy, where it is strongly bound (binding energy of 0.11 eV). The attrition is short-ranged, with the energy rapidly converging to that of dilute H in a perfect cementite. We further consider the H trapping behavior in the structures with higher

vacancy concentrations by placing a H atom in every interstitial site of the lowest energy SOD (see Experimental Methods) configuration for each composition. The results are shown in **Fig. 9C**. A wide range of solution energies is observed, depending on the local environment of the H atom in the hypo-stoichiometric cementite. At all concentrations, all states for H solution are lower energy than in the stoichiometric cementite, suggesting that vacancies have a strong trapping effect. The presence of 6.25% vacancies leads to a reduction in solution energy of up to 0.1 eV. Interestingly, at low vacancy concentrations, H preferentially occupies the vacancy sites, while at higher vacancy concentration the interstitial sites become lower energy, with the cross-over occurring between 12.5–18.75%.

The interface of cementite is not only characterized by the presence of excess vacancies, but also by a biaxial elastic strain field that accommodates the lattice mismatch in the coherent ferrite/cementite interface, as shown in our HAADF-STEM observations in **Fig. 1**. The lattice mismatch between ferrite and cementite is 2.7% along $[111]_{\text{ferrite}}//[010]_{\text{cementite}}$ and 0.8% along $[1\bar{1}0]_{\text{ferrite}}//[10\bar{1}]_{\text{cementite}}$. We consider a range of strains for both materials, varying linearly between these values and zero strain. We rotate the strain matrix to align them to the coordinates of the conventional unit cells of ferrite and cementite, and then apply them to the $Fe_{192}H$ ferrite supercell and the lowest solution energy structures of cementite shown in **Fig. 9C.**

We define the equilibrium lattice parameter at the interface, $d_f^{\Delta\sigma=0}$ and $d_c^{\Delta\sigma=0}$ for ferrite and cementite respectively, as those for which

$$\sigma_i^f = \sigma_i^c$$

thus,

$$\sum_j c_{ij}^f \varepsilon_j^f = \sum_j c_{ij}^c \varepsilon_j^c$$

With the DFT-derived elastic constants of ferrite and cementite (see **Table 2**), this equates to a 56% of the total strain being accommodated in ferrite, and the resulting lattice spacing on the habit plane of the interface are reported in **Table 3**. The deviation in strain from this equilibrium interface biaxial strain is defined as

$$\Delta\varepsilon_{interface} = \frac{d_1 - {d_1}^{\Delta\sigma=0}}{{d_1}^{\Delta\sigma=0}} + \frac{d_2 - {d_2}^{\Delta\sigma=0}}{{d_2}^{\Delta\sigma=0}}$$

where d_1 and d_2 refer to $[111]_{ferrite}//[010]_{cementite}$ and $[1\bar{1}0]_{ferrite}//[10\bar{1}]_{cementite}$, respectively.

Table 2 The elastic constants of cementite and ferrite in this study

(GPa)	**C_{11}**	**C_{22}**	**C_{33}**	**C_{12}**	**C_{23}**	**C_{13}**	**C_{44}**	**C_{55}**	**C_{66}**
Ferrite	248.96	248.96	248.96	146.22	146.22	146.22	102.52	102.52	102.52
Cementite	387.95	346.63	325.95	158.52	166.23	166.66	13.46	134.50	133.02

Table 3 The relative biaxial strain and the corresponding lattice spacing

$\Delta\varepsilon_{interface}$	**-0.019**	**-0.012**	**-0.005**	**0**	**0.001**	**0.008**	**0.015**
fraction ε accommodate in ferrite	0%	20%	40%	56%	60%	80%	100%
$[111]_f//[010]_c$ (Å)	4.903	4.929	4.956	4.977	4.982	5.009	5.035
$[1\bar{1}0]_f//[10\bar{1}]_c$ (Å)	8.006	8.020	8.033	8.044	8.047	8.060	8.074

Fig. 9D shows that biaxial compression increases the solution energy in both materials, while tension decreases it. In practice this means that the interfacial strain leads to a decrease in H solution energy in ferrite as H approaches the interface from bulk ferrite, and an increment in solution energy in cementite as H approaches the interface from bulk cementite. The presence of vacancies has an even stronger effect on the reduction of H solution energy, overwhelming the effect of strain in cementite.

Fig. 10 shows the calculated potential energy of a H solute atom as a function of its distance to the cementite–ferrite interface. The gradient colors refer to the tension in ferrite (grey) and the compression in cementite (blue) near the interface. As shown by the black solid line in **Fig. 10**, H atoms have a lower potential (are more stable) in the ferrite under tension, so the H solute atoms in the relaxed ferrite lattice would be expected to migrate toward this region. However, we also found that the H solution energy in a perfect cementite lattice is 0.11 eV lower than the ferrite under tension, suggesting that the H solute atoms near the interface might be absorbed by the cementite. We then consider the H energy in the cementite with 6.25% carbon vacancy sites, as shown by the red broken line in **Fig. 10**. In this case, the difference of H solute potential between the ferrite in tension and the vacancy containing cementite increases by 0.3 eV, since the carbon vacancies are strong H traps [22,42]. These modelling results provide a rationale for the presence of a ~5 nm hydrogen depletion zone in ferrite (**Fig. 8C and Fig S5C**), i.e. hydrogen atoms in this zone are drained to cementite where stronger trapping sites are available. Compression of the cementite lattice slightly reduces the hydrogen trapping energy near the interface (red broken line in **Fig. 10**), so when hydrogen atoms enter cementite, they would be expected to continue to penetrate into the cementite core rather than accumulating at the interface, consistent with the experimental data in **Fig. 8 and Fig. S5.** Strong trapping of H within cementite is consistent with some theoretical predictions [50,51] and prior experimental observations [39]. (See discussions in Section 4.2).

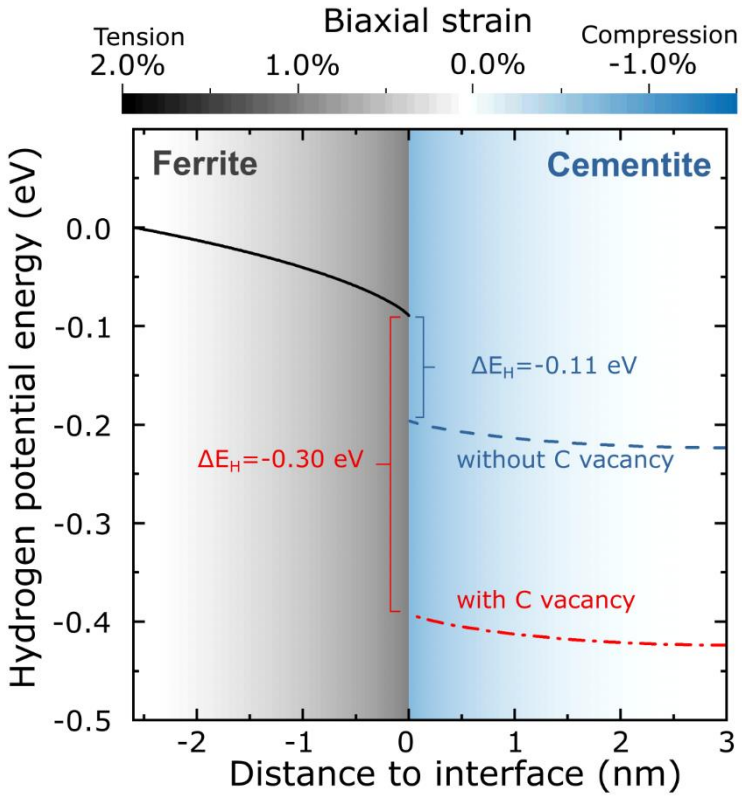

Fig. 10. Hydrogen behavior around the cementite–ferrite interface. DFT-calculated hydrogen potential energy near the cementite–ferrite interface. The gradient colors of grey and blue indicate the strain gradient with respect to distance from the ferrite/cementite interface. The blue and red broken lines delineate the hydrogen potential energy in cementite with 0 and 6.25 at.% carbon vacancies, respectively.

4. Discussion

4.1. Insights from H-charged micromechanical testing

Our micromechanical results provide new information on the influence of hydrogen on the deformation of pearlite. A new protocol was designed to test micropillars containing specific microstructures in order to study local mechanical responses. The cementite lamellae were inclined at ~45° to the loading axis, optimal for interfacial slip, with the intention to quantify the shear strength between cementite and ferrite. The yield strength dropped significantly after the sample was charged with hydrogen, as seen in **Fig. 4**. However, this observation is inconsistent with prior work

that indicates that hydrogen does not affect strength, but is more relevant to ductility loss, see example mechanical data in reference [24]. Due to the small sample volume, the flow stress is very sensitive to the microstructural evolution and the defect activities [52]. For this reason, micromechanical tests are good for directly linking mechanical properties to the activities of crystalline defects. For example, collective dislocation slip activity, or 'dislocation avalanches' can be observed on the stress–strain curve in the form of large strain bursts, both in the literature [53] and in our results (see **Fig. 4A**).

Strain bursts explicitly demonstrated the repetitive physical process of dislocations self-organizing into slip barriers then slipping in a collective cascade. The fact that strain bursts are smaller after H-charging is solid evidence of the fundamental change in dislocation dynamics caused by the presence of hydrogen. The reduced strength and strain burst behavior shed light on two aspects of the role of hydrogen. On one hand, hydrogen enhances the mobility of dislocations in ferrite, consistent with the HELP mechanism [6]; On the other hand, microstructural barriers to dislocations motion, i.e., cementite layers, become less effective in hydrogen. The observed offset of the slip plane from the interface, and evidence of the slip band intersecting and crossing the cementite in the post-mortem TEM results in **Figs 4 and 5** support this point of view**.**

4.2. Factors affecting hydrogen distribution around the cementite–ferrite interface.

Our DFT results demonstrated that the value of hydrogen potential energy is determined by the concentration of vacancies and the lattice elastic strain (see **Figs. 9 and 10**). The hydrogen potential energy landscape establishes an energetic driving force for local hydrogen atoms to diffuse towards the cementite–ferrite interface and

then into the cementite bulk, as illustrated in **Fig. 11.** Close to the cementite–ferrite interface, H is attracted by cementite and migrates toward the cementite–ferrite interface due to the presence of a strain gradient from the lattice misfit (left red arrow). When H enters the cementite, it is strongly trapped in the cementite bulk due to the presence of carbon vacancies (blue broken circles). A strain gradient in the cementite near the interface facilitates the internalization of H solutes (right red arrow). The result is a H depletion zone in the ferrite region near the interface.

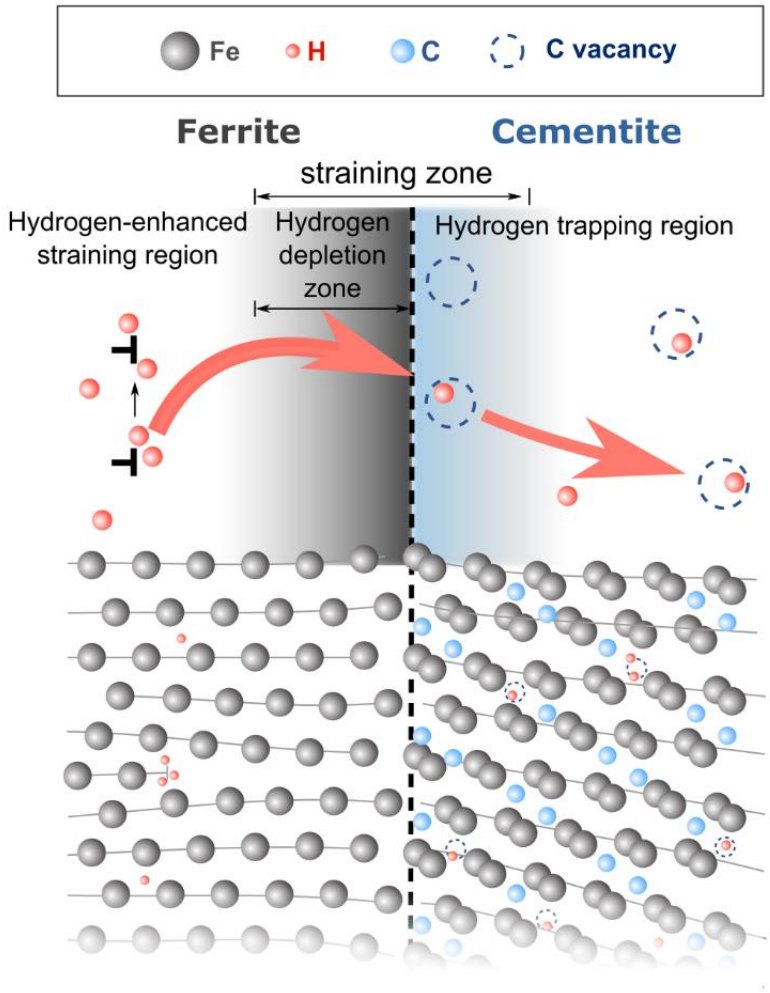

Fig. 11. Hydrogen-dislocation interaction near the cementite–ferrite interface. A schematic illustration of hydrogen migration and trapping. The drawing shows the hydrogen-dislocation interactions in ferrite bulk, hydrogen depletion in ferrite due to a lower potential energy in cementite, the carbon vacancy hydrogen trapping in cementite, and the incorporation of hydrogen inside the cementite phase due to the lower potential energy in the relaxed cementite lattice away from the interface.

As detailed in the DFT results section, our model include 3 key assumptions, established by our experimental work: i) the high coherency of the interface with specific orientation relationship, as per **Fig. 1C**, ii) unique elastic strain field: tension in the ferrite region and compression in cementite region near the interface, both as per **Fig. 1E**, and iii) the presence of carbon vacancies in hypo-stoichiometric cementite, as per **Figs. 2C and 2D** and literature [37]. For ii), the strain was calculated based on classic elastic mechanical models provided in [54]. For iii), we assumed 6.25% carbon vacancies in a cementite lattice (i.e. 1 vacancy per 16 carbon atoms) which is equivalent to an overall 1.47 at.% deficit of carbon, similar to the deficit measured by APT (**Fig. 2**). Changing these factors may affect the hydrogen distribution near the cementite–ferrite interface.

The atomic structure of the cementite–ferrite interface is critical. The APT results in this study showcase the distribution of hydrogen near a coherent phase boundary, or more specifically, a coherent segment on a semi-coherent interface, allowing us to examine the a pristine cementite–ferrite phase boundary. It is reasonable to believe that misfit dislocations on the interface would release local elastic energy, affecting the local strain field and leading to changes on H-distribution. Previous reports on strained pearlite in cold-drawn bridge steel wires, showed H trapped at the interface [55]. H-trapping at cementite–ferrite interface is expected [22,42,55,56], but we argue that the condition of the interface plays a significant role on H-distribution. The cold drawn pearlite may have considerable crystalline defects on the interface [55], which may lead to different results from ours. In addition to the coherency of the interface, future work may reveal whether the nature of the orientation relationship, or indeed whether an orientation relationship is present, may

also change the distribution of hydrogen, as might be expected, as the strain field changes with the orientation relationship.

Moreover, it has been recently reported that the cementite can decompose during the cold drawing process, introducing more carbon vacancies in cementite, as shown by APT using pearlite samples at different drawing strains. More abundant C-vacancies are expected to enhance H-trapping in cementite bulk. No experiments have yet been reported.

Conclusions

By correlating in-situ micromechanics, TEM, APT and DFT, we have obtained some new data that sheds light upon the deformation mechanisms within pearlite in the presence of H and the distribution of hydrogen trapped in pearlite. We have developed a new understanding on how H trapping enhances the deformation, drawing the following conclusions.

1. Lower yield stress in pearlite in the presence of hydrogen is the result of HELP within the ferrite phase and the cementite bulk, and not due to decohesion or slip along the cementite-ferrite interface itself. H enhances dislocations slip in ferrite, and weakens the cementite as a dislocation barrier, leading to higher propensity of dislocations intersecting the cementite. The combination of the easier slip and the penetration of cementite by dislocations leads to the lower measured strength.

2. Hydrogen trapping in this microstructure occurs in the cementite and in the ferrite away from the interface, but not at the cementite–ferrite interface. The distribution of hydrogen is determined by the coherency of the interface, the strain field near the interface, and carbon vacancies in the carbide.

Altogether, these factors establish an energetic driving force for local hydrogen atoms to diffuse towards the cementite–ferrite interface and then become trapped in the cementite bulk.

References

[1] International Energy Agency, Global Hydrogen Review, (2021).
[2] A. Laureys, R. Depraetere, M. Cauwels, T. Depover, S. Hertelé, K. Verbeken, Use of existing steel pipeline infrastructure for gaseous hydrogen storage and transport: A review of factors affecting hydrogen induced degradation, J Nat Gas Sci Eng. 101 (2022).
[3] H. Li, R. Niu, W. Li, H. Lu, J. Cairney, Y.S. Chen, Hydrogen in pipeline steels: Recent advances in characterization and embrittlement mitigation, J Nat Gas Sci Eng. 105 (2022).
[4] R. Rhodes, Explosive Lessons in Hydrogen Safety, NASA ASK Magazine. 41 (2011) 46–50.
[5] A.H. Cottrell, B.A. Bilby, Dislocation Theory of Yielding and Strain Ageing of Iron, Proc Phys Soc Sect A. 62 (1949) 49–62.
[6] I.M. Robertson, P. Sofronis, A. Nagao, M.L. Martin, S. Wang, D.W. Gross, K.E. Nygren, Hydrogen Embrittlement Understood, Metall Mater Trans B Process Metall Mater Process Sci. 46 (2015) 1085–1103.
[7] S. Lynch, Hydrogen embrittlement phenomena and mechanisms, Corros Rev. 30 (2012) 105–123.
[8] H.K. Birnbaum, P. Sofronis, Hydrogen-enhanced localized plasticity-a mechanism for hydrogen-related fracture, Mater Sci Eng A. 176 (1994) 191–202.
[9] M.L. Martin, B.P. Somerday, R.O. Ritchie, P. Sofronis, I.M. Robertson, Hydrogen-induced intergranular failure in nickel revisited, Acta Mater. 60 (2012) 2739–2745.
[10] S.P. Lynch, Metallographic contributions to understanding mechanisms of environmentally assisted cracking, Metallography. 23 (1989) 147–171.
[11] R.A. Oriani, A mechanistic theory of hydrogen embrittlement of steels, Berichte Der Bunsengesellschaft Für Physikalische Chemie. 76 (1972) 848–857.
[12] A.R. Troiano, The role of hydrogen and other interstitials in the mechanical behavior of metals, Trans. ASM. 52 (1960) 54–80.
[13] G.M. Presouyre, Trap theory of hydrogen embrittlement, Acta Metall. 1980 (1979) 895–911.
[14] H.K.D.H. Bhadeshia, Prevention of Hydrogen Embrittlement in Steels, ISIJ International. 56 (2016) 24–36.
[15] R. Fernández-Sousa, C. Betegón, E. Martínez-Pañeda, Analysis of the influence of microstructural traps on hydrogen assisted fatigue, Acta Mater. 199 (2020) 253–263.
[16] M.L. Martin, M.J. Connolly, F.W. Delrio, A.J. Slifka, Hydrogen embrittlement in ferritic steels, Appl Phys Rev. 7 (2020) 041301.
[17] M.B. Djukic, G.M. Bakic, V. Sijacki Zeravcic, A. Sedmak, B. Rajicic, The synergistic action and interplay of hydrogen embrittlement mechanisms in steels and iron: Localized plasticity and decohesion, Eng Fract Mech. 216 (2019) 106528.
[18] A. Laureys, R. Depraetere, M. Cauwels, T. Depover, S. Hertelé, K. Verbeken,

Use of existing steel pipeline infrastructure for gaseous hydrogen storage and transport: A review of factors affecting hydrogen induced degradation, J Nat Gas Sci Eng. 101 (2022) 104534.
[19] K. Nishioka, K. Ichikawa, Progress in thermomechanical control of steel plates and their commercialization, Sci Technol Adv Mater. 13 (2012) 023001.
[20] J.Q. Wang, A. Atrens, D.R. Cousens, N. Kinaev, Microstructure of X52 and X65 pipeline steels, J Mater Sci. 34 (1999) 1721–1728.
[21] E.G. Ohaeri, W. Qin, J. Szpunar, A critical perspective on pipeline processing and failure risks in hydrogen service conditions, J Alloys Compd. 857 (2021) 158240.
[22] E.J. McEniry, T. Hickel, J. Neugebauer, Ab initio simulation of hydrogen-induced decohesion in cementite-containing microstructures, Acta Mater. 150 (2018) 53–58.
[23] Y. Ogawa, H. Nishida, M. Nakamura, V. Olden, A. Vinogradov, H. Matsunaga, Dual roles of pearlite microstructure to interfere/facilitate gaseous hydrogen-assisted fatigue crack growth in plain carbon steels, Int J Fatigue. 154 (2022) 106561.
[24] S. Yu, H. Jeong, G. Hoon, S. Kim, D. Lee, Y. Lee, Origin of tearing topography surface in hydrogen-charged pearlitic steel, Acta Mater. 256 (2023) 119116.
[25] B. Gault, M.P. Moody, J.M. Cairney, S.P. Ringer, Atom Probe Microscopy, 2012.
[26] Y.S. Chen, H. Lu, J. Liang, A. Rosenthal, H. Liu, G. Sneddon, I. McCarroll, Z. Zhao, W. Li, A. Guo, J.M. Cairney, Observation of hydrogen trapping at dislocations, grain boundaries, and precipitates, Science (1979). 367 (2020) 171–175.
[27] G. Kresse, J. Furthmüller, Efficiency of ab-initio total energy calculations for metals and semiconductors using a plane-wave basis set, Comput Mater Sci. 6 (1996) 15–50.
[28] J.P. Perdew, K. Burke, M. Ernzerhof, Generalized gradient approximation made simple, Phys Rev Lett. 77 (1996) 3865–3868.
[29] P.E. Blöchl, Projector augmented-wave method, Phys Rev B. 50 (1994) 17953–17979.
[30] H.J. Monkhorst, J.D. Pack, Special points for Brillouin-zone integrations, Phys Rev B. 13 (1976) 5188.
[31] R. Grau-Crespo, S. Hamad, C.R.A. Catlow, N.H. De Leeuw, Symmetry-adapted configurational modelling of fractional site occupancy in solids, J Phys Condens Matter. 19 (2007) 256201.
[32] Y.T. Zhou, S.J. Zheng, Y.X. Jiang, T.Z. Zhao, Y.J. Wang, X.L. Ma, Atomic structure of the Fe/Fe3C interface with the Isaichev orientation in pearlite, Philosophical Magazine. 97 (2017) 2375–2386.
[33] M.J. Hÿtch, E. Snoeck, R. Kilaas, Quantitative measurement of displacement and strain fields from HREM micrographs, Ultramicroscopy. 74 (1998) 131–146.
[34] M. Thuvander, J. J. Weidow, J. Angseryd, L.K.L. Falk, F. Liu, M. Sonestedt, K. Stiller, H.O. Andrén, Quantitative atom probe analysis of carbides, Ultramicroscopy. 111 (2011) 604–608.
[35] J. Takahashi, K. Kawakami, Y. Kobayashi, Quantitative analysis of carbon content in cementite in steel by atom probe tomography, Ultramicroscopy. 111 (2011) 1233–1238.
[36] P.Y. Tung, X. Zhou, D. Mayweg, L. Morsdorf, M. Herbig, Under-stoichiometric cementite in decomposing binary Fe-C pearlite exposed to rolling contact fatigue, Acta Mater. 216 (2021) 117144.
[37] V.I. Voronin, I.F. Berger, Y.N. Gornostyrev, V.N. Urtsev, A.R. Kuznetsov, A. V. Shmakov, Composition of cementite in the dependence on the temperature. In situ

neutron diffraction study and Ab initio calculations, JETP Lett. 91 (2010) 143–146.
[38] P. Dey, R. Nazarov, B. Dutta, M. Yao, M. Herbig, M. Friák, T. Hickel, D. Raabe, J. Neugebauer, Ab initio explanation of disorder and off-stoichiometry in Fe-Mn-Al-C κ carbides, Phys Rev B. 95 (2017) 1–14.
[39] Y.S. Chen, D. Haley, S.S.A. Gerstl, A.J. London, F. Sweeney, R.A. Wepf, W.M. Rainforth, P.A.J. Bagot, M.P. Moody, Direct observation of individual hydrogen atoms at trapping sites in a ferritic steel, Science (1979). 355 (2017) 1196–1199.
[40] H. Suzuki, K. Takai, Summary of Round-Robin tests for standardizing hydrogen analysis procedures, ISIJ International. 52 (2012) 174–180.
[41] Y.C. Lin, I.E. McCarroll, Y.T. Lin, W.C. Chung, J.M. Cairney, H.W. Yen, Hydrogen trapping and desorption of dual precipitates in tempered low-carbon martensitic steel, Acta Mater. 196 (2020) 516–527.
[42] K. Kawakami, T. Matsumiya, Ab-initio Investigation of Hydrogen Trap State by Cementite in bcc-Fe, ISIJ International. 53 (2013) 709–713.
[43] C. Du, F. Maresca, M.G.D. Geers, J.P.M. Hoefnagels, Ferrite slip system activation investigated by uniaxial micro-tensile tests and simulations, Acta Mater. 146 (2018) 314–327.
[44] Y. Ogawa, H. Nishida, M. Nakamura, V. Olden, A. Vinogradov, H. Matsunaga, Dual roles of pearlite microstructure to interfere/facilitate gaseous hydrogen-assisted fatigue crack growth in plain carbon steels, Int J Fatigue. 154 (2022) 106561.
[45] J. Toribio, HELP versus HEDE in progressively cold-drawn pearlitic steels: Between Donatello and Michelangelo, Eng Fail Anal. 94 (2018) 157–164.
[46] T. Doshida, K. Takai, Dependence of hydrogen-induced lattice defects and hydrogen embrittlement of cold-drawn pearlitic steels on hydrogen trap state, temperature, strain rate and hydrogen content, Acta Mater. 79 (2014) 93–107.
[47] M. Koyama, M. Rohwerder, C.C. Tasan, A. Bashir, E. Akiyama, K. Takai, D. Raabe, K. Tsuzaki, Recent progress in microstructural hydrogen mapping in steels: quantification, kinetic analysis, and multi-scale characterisation, Mater Sci Technol (United Kingdom). 33 (2017) 1481–1496.
[48] P.A. Burr, S.T. Murphy, S.C. Lumley, M.R. Wenman, R.W. Grimes, Hydrogen accommodation in Zr second phase particles: Implications for H pick-up and hydriding of Zircaloy-2 and Zircaloy-4, Corros Sci. 69 (2013) 1–4.
[49] A.Y. Lozovoi, A. Alavi, M.W. Finnis, Surface energy and the early stages of oxidation of NiAl(110), Comput Phys Commun. 137 (2001) 174–194.
[50] D. di Stefano, R. Nazarov, T. Hickel, J. Neugebauer, M. Mrovec, C. Elsässer, First-principles investigation of hydrogen interaction with TiC precipitates in α -Fe, Phys Rev B. 93 (2016) 184108.
[51] S. Echeverri Restrepo, D. di Stefano, M. Mrovec, A.T. Paxton, Density functional theory calculations of iron - vanadium carbide interfaces and the effect of hydrogen, Int J Hydrogen Energy. 45 (2020) 2382–2389.
[52] J.R. Greer, J.T.M. De Hosson, Plasticity in small-sized metallic systems: Intrinsic versus extrinsic size effect, Prog Mater Sci. 56 (2011) 654–724.
[53] F.F. Csikor, C. Motz, D. Weygand, M. Zaiser, S. Zapperi, Dislocation avalanches, strain bursts, and the problem of plastic forming at the micrometer scale., Science (1979). 318 (2007) 251–254.
[54] J.H. Davies, D.M. Bruls, J.W.A.M. Vugs, P.M. Koenraad, Relaxation of a strained quantum well at a cleaved surface, J Appl Phys. 91 (2002) 4171–4176.
[55] A.J. Breen, L.T. Stephenson, B. Sun, Y. Li, O. Kasian, D. Raabe, M. Herbig, B. Gault, Solute hydrogen and deuterium observed at the near atomic scale in high-strength steel, Acta Mater. 188 (2020) 108–120.

[56] S.H. Yu, S.M. Lee, S. Lee, J.H. Nam, J.S. Lee, C.M. Bae, Y.K. Lee, Effects of lamellar structure on tensile properties and resistance to hydrogen embrittlement of pearlitic steel, Acta Mater. 172 (2019) 92–101.

Declaration of Competing Interest

The authors declare that they have no known competing financial interests or personal relationships that could have appeared to influence the work reported in this paper.

Acknowledgments: A. Breen, H.W. Liu, V. Bhatia, T. Sato, S.Y. Huang, N. Holmes, and H.S. Chen (The University of Sydney) are thanked for their technical supports. D.G. Xie (Xi'an Jiao Tong University) is thanked for useful discussion. Y.-S. C. thanks his family. **Funding:** The authors acknowledge funding from Australian Research Council (IE230100160, LP180100431, LP210300999, LE190100048, and FT180100232), the 2019 University of Sydney Postdoctoral Fellowship, CITIC-CBMM Nb Steel Award Fund Program (2018FWNB30064), Taiwan's Ministry of Science and Technology (MOST 110-2119-M-002 -018 -MBK), USyd-NTU Partnership Award, and China Scholarship Council (201506840096). The authors also thank the research facilities supported by Microscopy Australia, the University of Sydney, the Australian National Computational Infrastructure, the Pawsey Supercomputing Centre, and Intersect Australia Limited.

4.3 Summary

In this study, I have achieved a significant breakthrough in comprehending the hydrogen distribution within non-deformed pearlite. Through the innovative utilization of cryogenic APT, we have shed light on the behavior of hydrogen atoms. Our findings show that hydrogen atoms reside within the bulk of the ferrite or cementite phases of pearlite, rather than concentrating at their interfaces. A reduction in the yield strength in charged samples is attributed to H that is present both at dislocations in the ferrite phase and within the cementite phase. The H reduces the energy required for dislocation nucleation and motion, allowing more deformation in the ferrite, and for the dislocations to shear the cementite, resulting in enhanced plasticity and a lowering of the yield strength

To complement our experimental insights, we employed DFT calculations and conducted HRTEM observations. These analytical approaches enabled us to delve into two key factors: 1) the lattice misfits existing between cementite and ferrite, and 2) the influence of carbon vacancies within cementite.

Within the ferrite matrix, solute hydrogen exhibits heightened stability when positioned in proximity to the cementite-ferrite interface. Furthermore, our investigations illustrate the pivotal role of carbon vacancies situated close to the interface, as they enhance the tendency for hydrogen entrapment within the cementite phase.

The culmination of our efforts has laid a robust foundation, amalgamating experimental evidence and theoretical insights. This groundwork holds great promise for informing the design of pipeline steel optimized for hydrogen-based applications.

Chapter 5 - Bridging gap between dilute and concentrated defect calculations

5.1 Background

Atomic-scale simulations of point defects have become routine for characterizing defect concentrations, whether they are extremely dilute or highly concentrated. However, conventional methods often encounter challenges or become impractical when addressing intermediate concentration levels. Unfortunately, these intermediate concentrations frequently hold the utmost relevance in real-world materials, as exemplified by scenarios like hydrogen-induced embrittlement in steel.

To bridge this critical gap, we have introduced an innovative and computationally efficient approach. This novel method draws inspiration from both cluster expansion techniques and ensemble statistics. In its essence, it presents a solution for efficiently studying intermediate concentration levels that was previously lacking in the field.

Results are presented in the form of a manuscript currently under review by '***Computational Materials Science***'. The content of this article is largely the product of the work of **Pang-Yu Liu** under the supervision of Yi-Sheng Chen and Patrick A. Burr. **Pang-Yu Liu** conceptualized the project, conducted the DFT simulation, conducted the data analysis and drafted the manuscript. Julie M. Cairney participated in the manuscript development. Yi-Sheng Chen provided funding support, supervised the project, and revised the manuscript. Patrick A. Burr initiated and conceptualized the project, supervised the project, drafted the manuscript, and finalized the manuscript.

5.2 Submitted manuscript

Bridging gap between dilute and concentrated defect calculations

Pang-Yu Liu[1,2,*], Yi-Sheng Chen[1,2,3,*], Julie M. Cairney[1,2], Patrick A. Burr[4,*]

[1]Australian Centre for Microscopy and Microanalysis, The University of Sydney, Sydney, Australia

[2]School of Aerospace, Mechanical and Mechatronic Engineering, The University of Sydney, Sydney, Australia

[3]Department of Materials Science and Engineering, National Taiwan University, Taipei, Taiwan

[4]School of Mechanical and Manufacturing Engineering, University of New South Wales, Australia

[*]Corresponding authors: pang-yu.liu@sydney.edu.au (P.-Y. L.); yi-sheng.chen@sydney.edu.au (Y.-S. C.); p.burr@unsw.edu.au (P. A. B.)

Abstract

Atomic-scale simulation of structural defects in materials provides a path to understand the behaviors and properties of materials at an *ab initio* level, which is crucial to enable the by-design development of new materials. Existing first-principles modelling methods, especially density functional theory, are well-designed for either low or high concentrations of defects but are computationally inefficient and/or less accurate the further one moves from either limit. This work develops a computationally effective approach to address this gap in developing mid-concentration models, which are the most relevant in real-life alloys. Our model combines the concepts of cluster expansion and ensemble statistics treatment of defect thermodynamics. We demonstrate our method by modelling hydrogen trapping at carbon vacancies in a hypo-stoichiometric cementite and hydrogen clusters in ferrite, which are computationally demanding tasks using conventional methods. The modeling results effectively provide an explanation for the unexpectedly high local hydrogen concentrations observed in the experimental data obtained through atom probe tomography.

Keywords

Atomic simulation, point defects, defect concentrations

1. Introduction

Point defects and impurities control most properties of crystalline materials, and several atomic-scale simulation techniques have been developed to study defects. First-principles calculations, and in particular density functional theory (DFT), are now widely used to supplement experimental data. This is because they possess sufficient accuracy at a reasonable computational cost to serve as a predictive tool. However, methods for studying point defects within DFT simulations are chiefly designed to defect concentrations that are either very low (dilute limit) or very high (concentrated solid solutions), but are less efficient at modelling intermediate defect concentrations.

Atomic scale simulations of defects have been pioneered by the field of semiconductors[1], where ppm level of aliovalent dopants can have a significant effect on the electrical and optical properties of the material[2–4]. Thus, methods for simulating dilute concentrations of defects are highly advanced. When the defect concentration is sufficiently low that defect-defect interactions are negligible, individual defects may be simulated using either the Mott-Littleton approach[5] or the more commonly used supercell approach in conjunction with periodic boundary conditions[6], in which a defect is sufficiently distant from its replica so that the interaction across the boundary is negligible[7–15]. The same technique can be used to simulate clusters of defects, as point defects may cluster into larger defects even in dilute concentrations if the binding energy is sufficiently large and migration kinetics are sufficiently fast.

For high concentrations of defects, where defect-defect interaction dominates the energy of the defects, the contribution of configurational entropy become significant and therefore need to be carefully taken into account[16] at finite temperatures. In the solid-state alloys, the dominant entropic contribution is the configurational entropy, while other source such as electronic entropy, magnetic entropy, and vibrational entropy are expected to have secondary importance[17,18]. Alternative approaches have been developed and proven successful for concentrated solid solutions, such as equimolar binary alloys, disordered or non-stoichiometric ceramics and high entropy alloys[19,20]. Suitable methods include effective medium theories, random sampling[21], quasi-random structures[22,23], configurational ensembles[24,25] and cluster expansion[26]. However, all of these computational methods have limitations when applied to low-but-not-dilute defect concentrations. Effective medium theories

fail to capture the effects of discrete atomic potential variations. In random structure the size of the simulation cell and sample size increases non-linearly with decreasing defect concentration, making them computationally intractable. Quasi-random structures are created which an implicit assumption of ideal mixing, which is unphysical for vacancies and interstitial type defects, and overestimates configurational entropy[27]. Configurational ensembles provide an exact entropic description of the system but are computationally very taxing and thus can only be applied to small systems, even when symmetry operations are exploited[28]. And cluster expansion methods fit the infinite configurational space of disordered solutions using a large finite set of concentration-independent configurations, leading to decreasing computational efficiency (larger clusters require a larger number of simulations) and increasing input data sparsity with increasing concentration of defects/solutes[26,29]. For a thorough review of the merits and pitfalls of these methods, the reader is referred to literature[21,22,25,26].

In essence, while both the diluted and concentrated calculation methods have proven valuable for a range of applications, there is still a specific concentration interval for which there is no established or effective approach. This gap is particularly troublesome as this intermediate defect concentration (i.e. low but not dilute) is often observed in metallic alloys and non-stoichiometric compounds. For example, hydrogen trapping and segregation in metallic alloys is of crucial importance in understanding hydrogen embrittlement. Typically, hydrogen atoms prefer to segregate at lattice defects such as vacancy, dislocation, grain boundary, and the strain field and misfit dislocations near phase boundaries. The local concentration of hydrogen in these regions can be up to 0.4 atomic percent (at.%) in the case of body-centered cubic (BCC) iron (Fe) [30]. Typically, the computational expense dramatically increases for defects that are not dilute (i.e. defect-defect interactions are non-negligible) but have a concentration range below 1 at% if supercell approach is adopted. We consider this as “intermediate concentration range”, and the exact bounds of concentration range vary from material to material.

In this paper, we present a low-cost computational approach to bridge the gap between dilute and concentrated calculations. We demonstrated the usefulness of this method with two case studies. First, as a form of validation, we consider defect energies in hypo-stoichiometric cementite (Fe_3C). Specifically, we look at hydrogen (H) solution energy as a function of carbon (C) stoichiometry, and we calculate this for a continuous

range of different vacancy concentrations and compare it to explicit (and computationally intensive) simulations at two vacancy concentrations. Second, we apply the method to a problem that is currently beyond the reach of existing approaches. We calculated the hydrogen solution energy in ferrite explicitly as a function of hydrogen content. The findings of this case are highly relevant to the hydrogen embrittlement community, showcasing the value of a high-throughput method for intermediate defect concentrations.

2. Computational details

DFT simulations were carried out using the Vienna ab-initio simulation package (VASP)[31]. The simulations employed the Perdew-Burke-Erzerhof (PBE) exchange-correlation functional[32] along with projector augmented-wave (PAW)[33] pseudopotentials. The valence electrons of Fe-$3d^7 4s^1$ and C-$2s^2 2p^2$ were considered, and a plane wave basis set cutoff of 500 eV was utilized. The relaxed lattice parameters of cementite, assuming the Pnma space group definition, were found to be a = 5.03 Å, b = 6.71 Å and c = 4.48 Å. On the other hand, the lattice parameter of ferrite was determined to be a = 2.83 Å. Spin polarization was incorporated in the simulations to consider the magnetic moment of iron, and a Methessel-Paxton smearing of 0.1 eV was applied. All structures were iteratively minimized until the energy change between three consecutive steps reached below 10^{-5} eV. For defective structures, only internal coordinates were relaxed to maintain symmetry and reduce computation cost. The forces on all atoms in the relaxed structure were less than 0.01 eV/Å. The configurational ensembles were modelled with the aid of the Site-Occupation Disorder (SOD) algorithm[34], using 64-atom 2 x 1 x 2 supercells with a 4 x 5 x 4 k-point grid for cementite and 54-atom 3 x 3 x 3 supercells with 4 x 4 x 4 k-point grid for ferrite.

The solution energy, E_s, of different defect types (ex: hydrogen interstitial atom and carbon vacancy), was calculated as:

$$E_s = E(\text{host} + n \text{ defects}) - E(\text{host}) \pm n * \mu(\text{defect})$$

where $E(\text{host})$ is the DFT energy of a perfect supercell, $E(\text{host+defect})$ is the DFT energy of the same supercell with an added defect, and $\mu(\text{defect})$ is the chemical potential of any atoms added (–) or removed (+) from the perfect supercell to form the defect. The chemical potential for the $\mu(\text{C})$ is half the DFT energy of a graphite unit cell, while for the $\mu(\text{H})$ is the half the DFT energy of a hydrogen molecule. We acknowledge that $\mu(\text{H})$ is sensitive to temperature and partial pressure of the H_2 gas,

which could easily be incorporated following the procedure commonly performed for oxygen chemical potential in oxides[35,36]. However, for the purpose of this work, those variables are kept fixed to focus on the enthalpic and entropic effects of H defect-defect clustering in the solid.

3. Theoretical framework

We first consider the probability of a defect existing in the binding range, as illustrated in Figure 1. For a site being occupied by a single defect, the probability could be expressed as:

$$P'(I) = x \tag{1}$$

Where I represents the event in which site i is occupied, and x is the concentration of the defect atom. We define this probability with P' to distinguish it from a different probability, P, which considers the effect of temperature and will be discussed in later sections.

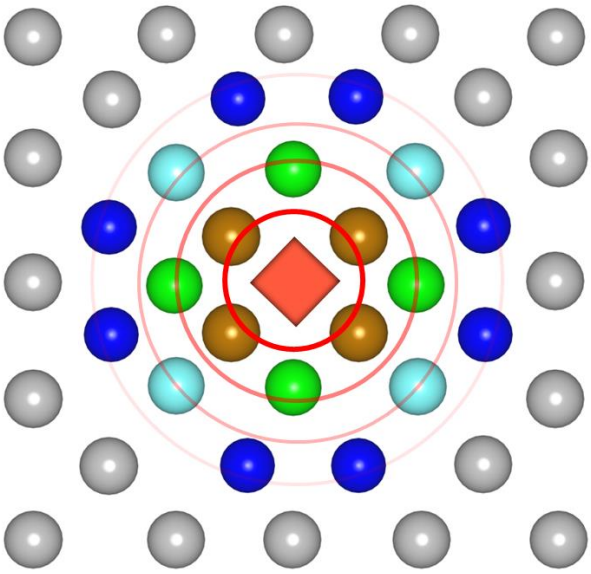

Figure 1. Schematic of nearest neighbour shells of atoms (circles) surrounding a central defect (diamond). The closer shells typically interact more strongly with the defect at the center. The grey circles represent the matrix atom outside the binding range, while other colored circles represent the atoms in different shells within the binding range.

When the distance between two defects is sufficiently large, the interaction between the defects is negligible and thus they are defined as being out of the binding range. In the case of low concentration, defects are always assumed to be further than

their binding range. At higher concentration, two or more objects can fall within the binding range of an individual object. By considering one defect as the center of the cluster, one can define a shell as the collection of sites that are equidistant from the central site and are symmetrically equivalent. All the clusters consisting of a defect in the centre and a defect in any of the sites of a given shell will have identical energy state. Therefore, the number of defect clusters in the binding range can be expressed in terms of the density of states with a given binding energy, and their multiplicity, the density of which is as:

$$D_s = \frac{n_s}{N_s} \tag{2}$$

where n_s is the number of sites within a shell of strong interaction (s) and N_s represent all sites in the binding range, thus $N_s = \sum_s n_s$.

Let I and J represent the events of site i being occupied and site j being occupied, respectively. Thus, the event $J|I$ represents the case in which a second defect occupies site j that is in the binding range of i, given that site i is already occupied (which for convenience we consider to be the central atom of the cluster). For an ideal solid solution, where the enthalpy and volume of mixing are zero, the probability of this event is given by combinatorics:

$$P'(J|I) = \binom{1}{N_s} x(1-x)^{(N_s-1)} = N_s x(1-x)^{(N_s-1)} \tag{3}$$

Similarly, if we restrict the probability only to sites j that reside on a specific shell s, the probability of site j_s being occupied by a defect given that site i is also occupied becomes:

$$P'_s = P'(J_s|I) = D_s \cdot P'(J|I) = n_s x(1-x)^{(N_s-1)} \tag{4}$$

For the event of triplet defects occurring within the binding range, $(K|J|I)$, in an ideal solution, the probability is:

$$P'(K|J|I) = C_2^{Ns} x^2(1-x)^{(N_s-2)} \tag{5}$$

where there is a total of C_2^{Ns} triplet configurations within the binding range. For any given triplet configuration in the binding range, which can be defined uniquely by the pair of neighbour distances $s_1 s_2$, the probability is:

$$P'\left(K_{s_1}\middle|J_{s_2}\middle|I\right) = N_{s_1 s_2} x^2(1-x)^{(N_s-2)} \tag{6}$$

where $N_{s_1 s_2}$ is the multiplicity of the triplet configuration. All higher terms are derived similarly to the above equations. The probability that no other site in the range N_s is occupied, other than i, is

$$P'_{out} = P'(\bar{J}|I) = (1-x)^{N_s} \tag{7}$$

In a dilute solid solution with finite x, two defects are either within binding range of one another or out of range, thus[1]:

$$P'(J|I) + P'(\bar{J}|I) = \frac{P(J \cap I) + P(\bar{J} \cap I)}{P(I)} = \frac{P(I)}{P(I)} = 1 \tag{8}$$

and similarly, for triplets and higher-order terms

$$P'(K|J|I) + P'(\bar{K}|J|I) = 1 \tag{9}$$

Notably, when the concentrations are sufficiently low, the probability of clusters larger than pairs becomes vanishingly small. Thus,

$$P'(\bar{K}|J|I) \cong P'(J|I) \tag{10}$$

Until now we have considered ideal and regular mixtures, where there is no preferential binding of any atom or defect to any other atom or defect. While some alloys are well-approximated by regular solution (e.g. Au-Ag, Zr-Hf, etc.), most systems deviate strongly from ideal laws of mixing – H interstitial clusters and carbon vacancy clusters shown below are two exemplar cases. Our goal is to develop a general method that would apply to any extrinsic and intrinsic defect. For materials that do not exhibit ideal mixing behaviour, the probability of occupying a bound defect state is not merely decided by the multiplicity (or density) of that defect state, but is also dictated by the binding energy E_s of that bound pair defect state, following Boltzmann distribution. Specifically, the probability of occupying the in-range shells s configuration is

$$P_s = \frac{e^{\left(-E_s/k_BT\right)} P'_s}{Z} \tag{11}$$

And the probability of occupying out-of-range configurations is

$$P_{out} = \frac{e^{\left(-E_{out}/k_BT\right)} P'_{out}}{Z} \tag{12}$$

where E_{out} is the energy of two defect atoms that are not in the binding range, and the partition function Z is given by

$$Z = \left[\sum_{1}^{s} e^{\left(-E_s/k_BT\right)} P'(J_s|I)\right] + e^{\left(-E_{out}/k_BT\right)} P'_{out}$$

[1] This can be proven by considering the intersection of I and J in event space:

(13)

If all bound defect states are known, one can compute an average defect energy at a given temperature:

$$E = \left(\sum_s N_s P_s\right) + (E_{out} P_O)$$

(14)

To note, in an ideal solid solution, where the energy state of each shell is identical ($E_{s1} = E_{s2} = \cdots E_{sn}$), this formulation reduces the analytical probability distribution presented above ($P_s = P_s'$ and $P_{out} = P_{out}'$).

4. Results and Discussion

4.1. Case study for validation: hydrogen solution in cementite

In this section, we aim to demonstrate and examine our theory by looking into the hydrogen solution energy in cementite systems with different amounts of carbon vacancies. We first calculate the energy of a dilute hydrogen interstitial in a perfect cementite supercell (in the octahedral site[37]) and in a supercell containing one vacancy, where we consider each of the symmetrically unique configurations of the hydrogen-vacancy pair within the supercell. The solution energy of H is shown in Figure 2 as a function of the distance between the H atoms and the C vacancy. The solution energy gradually converges to that of dilute hydrogen in the perfect cementite when the distance from the carbon vacancy increases, indicating the interaction between the hydrogen and the carbon vacancy becomes weaker. It is evident that by 5 Å the binding energy is negligible, so we consider this distance as the cut-off between two defects being within binding range of each other. As a result, there are only 5 energy states, with the multiplicity n_s of 1, 2, 2, 2 and 2, respectively. In total, there are only 9 available sites within the binding range. These energies and multiplicity are later used to compute the solution energy at arbitrary carbon vacancy concentrations using the theory outlined above, and we validate this for two concentrations that are still (just) tractable with conventional methods for simulating concentrated defects.

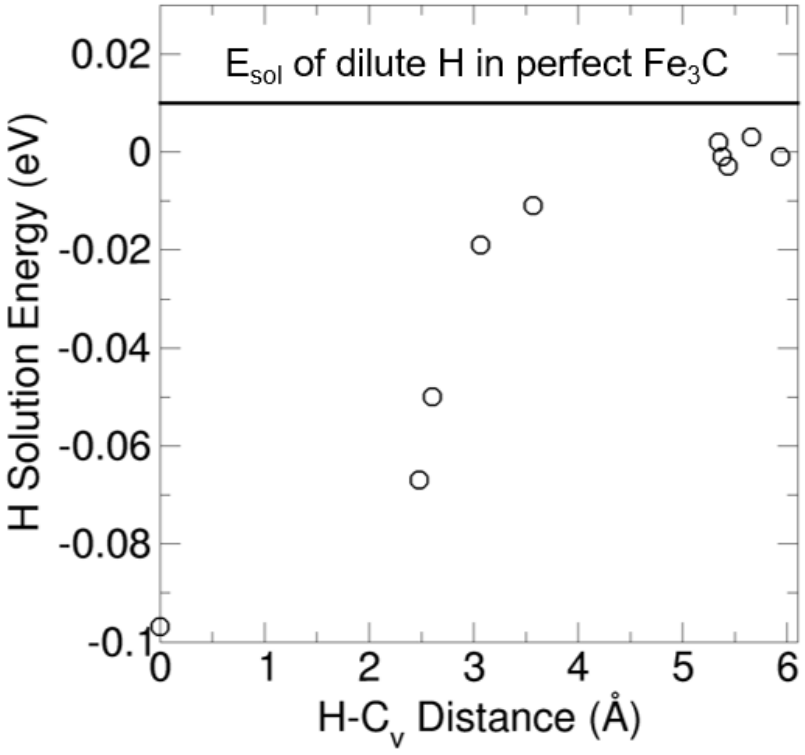

Figure 2. The hydrogen solution energy as the function of the hydrogen-carbon vacancy distance.

Let us first consider what would be the relative probability of having individual defects, pairs triplets and higher order defects, if the system was an ideal or regular mixture. Figure 3 shows the thermal cumulative probability P' as a function of carbon vacancy concentrations. At a concentration of 6.25 at.%, dilute defects account for only 56% of all defects, meaning that the dilute approach is clearly inadequate in this case, even if the material behaved like an ideal mixture. However, when pairs of H-vacancy defects are considered, the cumulative probability of all individual and paired defects is > 90%, at concentrations ≤ 6.25 at.%. In other words, few defect configurations are not taken into account if one includes defect pairs, and this decreases by another order of magnitude if one considers triplets (hydrogen and two vacancies). While the effect of defect-defect binding will cause a deviation from this ideal mixing predictions, the results still provide confidence that considering up to defect pairs is unlikely to neglect important defect configurations that may form in the V_C concentration range of 0–7 at.%.

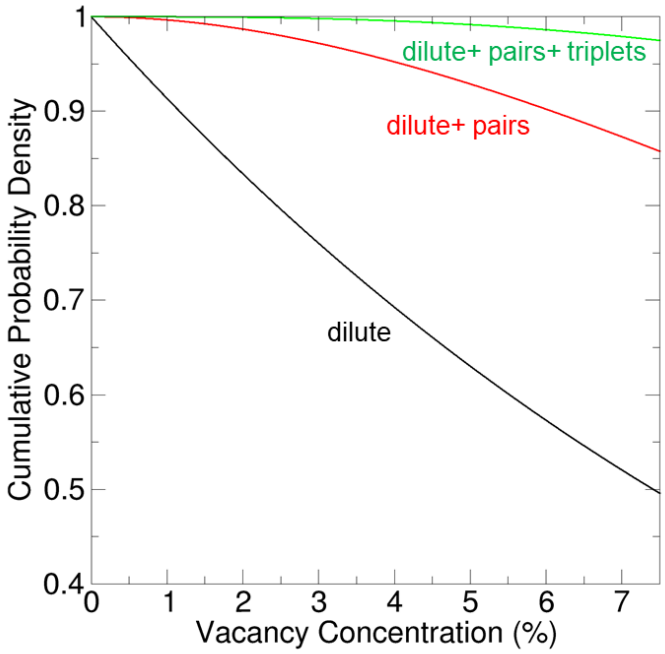

Figure 3. The probability of the different number of carbon vacancy exists in the binding range cumulatively.

Figure 4 shows the predicted defect energy derived from our theory, as a function of vacancy concentration, calculated at 300 and 600 K. The blue and green points are the average energy obtained using the established theory of configurational ensembles for concentrated disordered systems (see computational methodology for details). To aid direct comparison, the DFT simulations for the two methods were kept as similar as possible, and the configurational ensemble was also limited to pairs of defects (adding triplets to the configurational ensemble would be computationally unfeasible at such low concentrations – not so for our approach). Both energy curves drop sharply at the beginning and become flatter when the concentration increases. The 300 K curve is in good agreement with the solution energy, while there is a slight deviation for the 600 K curve. The reason for the slight deviation at 600 K is likely due to the choice of cut-off distance in our approach, or possibly to the lack of defect triplets in the explicit approach (which are accounted for in our method). When calculating defect pair configurations, we set a cut-off distance, defined as the distance where the binding energy was approaching zero. While the results showed strong convergence with little residual energy at the cut-off, these may still contribute to additional uncertainty, embodied in the weight of the "out of binding range" probability. Nevertheless, the result shown in Figure 4 shows that our method is exact at the dilute limit ($[V_C] \sim 0\%$) and is within 90% of established approaches at the relatively high $[V_C]$ of 6.25 at.%.

Additionally, our proposed approach can compute the value for any arbitrary solution within that range at no additional computational cost, and that is precisely the range for which no alternative method is computationally efficient.

It is noteworthy that, by design, the uncertainty of our method increases as the defect concentration increases. So, it is remarkable that a method intended for intermediate concentrations (low-but-not-dilute) retains reasonable agreement even with 6.25 at.% carbon vacancies.

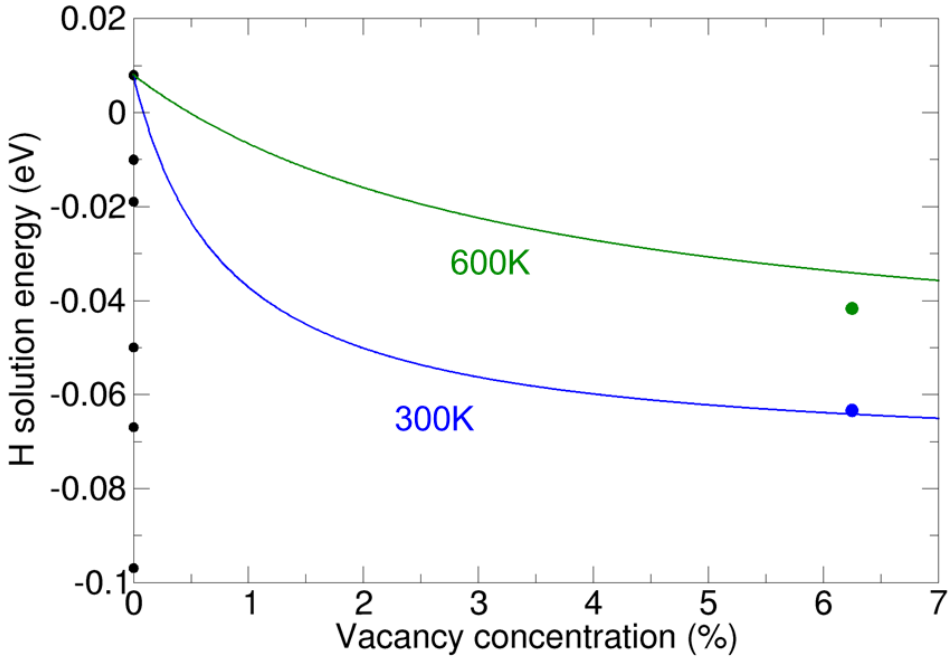

Figure 4. Hydrogen solution energy in cementite containing carbon vacancies, is predicted with the proposed approach (lines) and with configurational ensemble methods (colored dots). The black dots at 0% concentration represent the energy of the individual dilute calculation.

4.2. *Case study for application: Hydrogen solution in ferrite*

Having validated the method for a case where the defect concentration is high enough that it allows comparison with existing approaches for concentrated solutions, we apply the method to predict the solubility and clustering of H at intermediate levels, between dilute and concentrated, for which validation is not possible as no robust alternative simulation method is practicable. The hydrogen solution energy in ferrite is a critical parameter for understanding how hydrogen interacts with one another in the ferrite matrix. Normally, the solubility of hydrogen in the ferrite matrix is less than 10 ppm at ambient temperature[38], which can be accounted for the dilute calculation in this extent of concentration. However, previous studies have found that hydrogen tends to

segregate around the defects in the metal, such as precipitates, dislocations, and grain boundaries[30,39]. For instance, the hydrogen solubility has been observed to be up to 0.4 at.% from atom probe tomography toward the hydrogen segregation around the interface of the niobium carbide and the ferrite matrix[30]. Therefore, in this case, we are aiming to apply our theory to predict the variation of the hydrogen solution energy from dilute to 0.4 at.%, providing the energy landscape of the interaction of hydrogen clusters at the precipitate trapping sites in ferrite.

Hydrogen in ferrite is preferentially accommodated in the tetrahedral interstitial sites[40], of which there are 324 in our 3 x 3 x 3 supercell. Figure 5 shows the solution energy of H-H pairs as a function of distance within this cell, showing a slow convergence towards 0.22 eV. Given the slow convergence, we do not apply any additional cut-off and use all simulated pairs that fit within the 324-atom supercell. Figure 6 shows the probability density (a) and cumulative probability distribution (b) of defect clusters under ideal mixing laws, as a function of cluster size and defect concentration. Due to a large number of available sites in the binding range, dilute defects and pairs of defects account for only 63% of possible configurations at the low H concentrations of 0.4 at.%. Adding triplets to the computation, extend this to 86% of all configurations, at the same concentration of 0.4 at.%. Conversely, when the hydrogen concentration is higher than 1.2 at.%, one would need to consider 6 hydrogen atoms in the binding range in order to capture only 80% of possible configurations, as shown in Figure 6b.

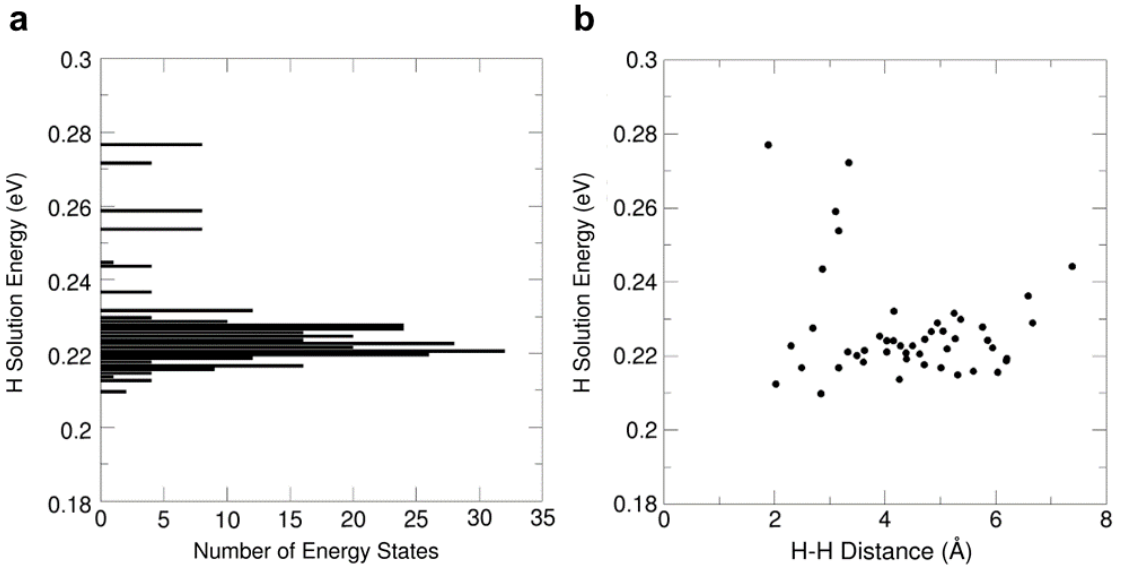

Figure 5. (a)The density of states of hydrogen pairs in ferrite. (b) The distribution of the hydrogen pair solution energy.

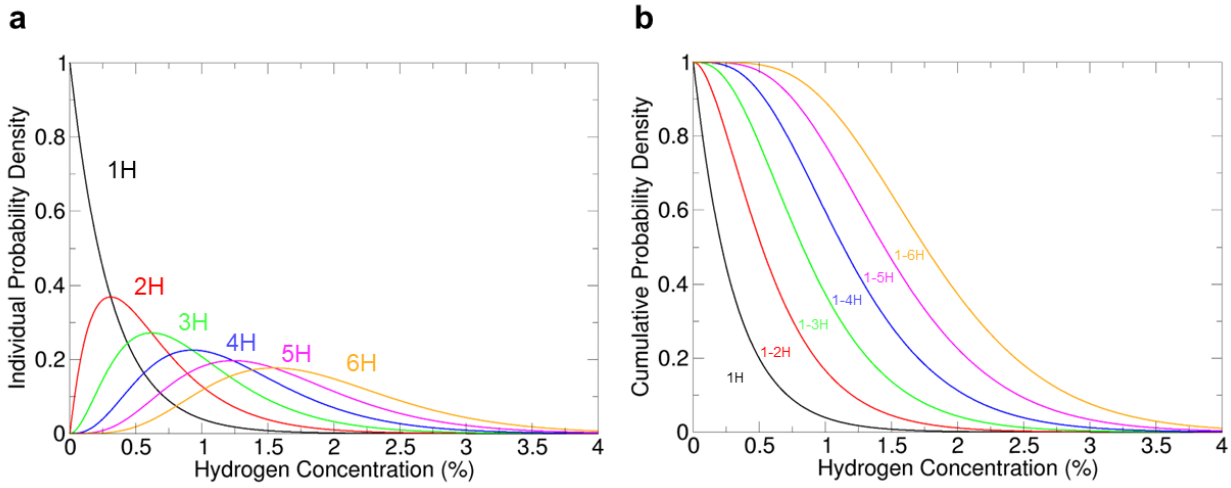

Figure 6. The probability of the different number of hydrogen atoms (defects) exists in the binding range (a) individually and (b) cumulatively.

Figure 7 shows the DOS of triplet hydrogen in the binding range. 2,477 independent configurations are calculated and produce 52,003 configurations in total. Compared to the pair defect DOS, we see a marked shift in the main peak to lower values, now centered around 0.2 eV, with some states as low as 0.18 eV, indicating that neglecting triplets would result in an underestimation of H-H binding, and therefore higher overall solution energies. Triplets also contribute some higher energy states (ΔE around 0.28 eV), with energies higher than those of defect pairs, but these do not contribute significantly to the configurational average at the relevant temperatures of 300 and 600 K, as the probability of occupying these states at those temperatures is negligible.

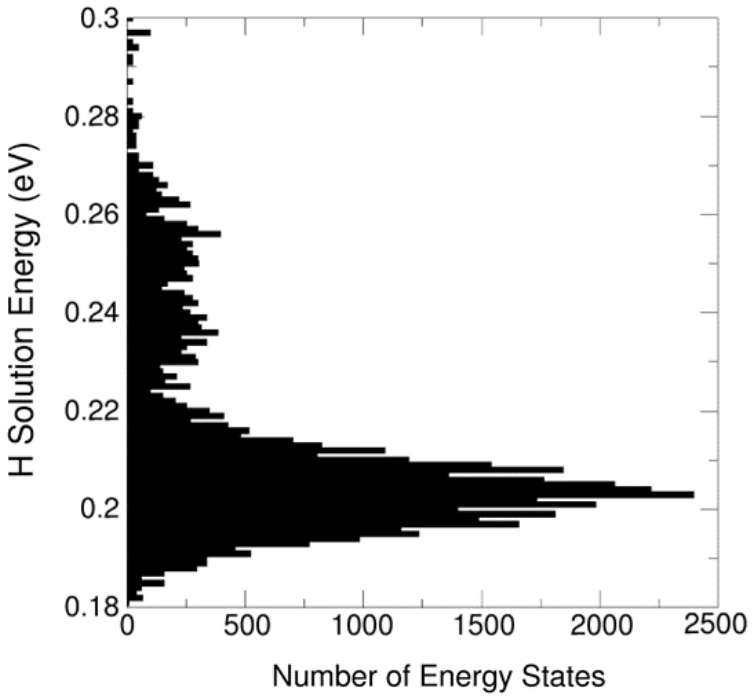

Figure 7. The density of states (DOS) of hydrogen triplet in the binding range.

The result of hydrogen solution energy at different concentrations and temperatures predicted from our method is shown in Figure 8. The results are computed at 300 K (blue) and 600 K (green). The dash lines in Figure 8 are the result derived by our equation with only including hydrogen pairs, while the solid lines include both hydrogen pair and triplet calculations. In both cases, the results converge to the solution energy of a dilute hydrogen atom as the hydrogen concentration decreases. The results of the two approaches remain in good agreement up to 0.025 at.% H, as at this concentration the likelihood of forming a triplet remains low (only 0.02%). However, once triplet clusters form a non-negligible contribution to the overall cluster population, including their energy into the equations makes the predicted solution energy curve more negative compared to the result that considered only up to defect pairs. This essentially means that the true solubility of H is underestimated when calculated from DFT simulations of dilute H solutes, as is conventionally done, and even considering defect pairs slightly underestimates it if the H concentration is above 0.025 at.%. The formation of pairs and later triplets have a non-negligible role in increasing the solubility of hydrogen in ferrite. The formation of quadruplets and larger clusters may have an additional stabilizing effect; however, at this low concentration regime (<0.4 at.%) their contribution is expected to be small.

The trend of the results indicates that the hydrogen solution energy will decrease

as the local hydrogen concentration increases. This phenomenon may affect the distribution of the hydrogen in the ferrite. While the local concentration is higher due to the stress or the presence of nearby microstructural features that attract H, it requires less energy for the higher concentration region to accommodate H, implying an enhanced ability for the ferrite to accommodate more H as the concentration increases. In other words, there appears to be a competing effect on the known repulsion and diffusion towards low-concentration regions. The formation of these hydrogen clusters, which have a lower solution energy, goes some way toward explaining the observed regions of high hydrogen and the segregation behavior around the microstructural features.

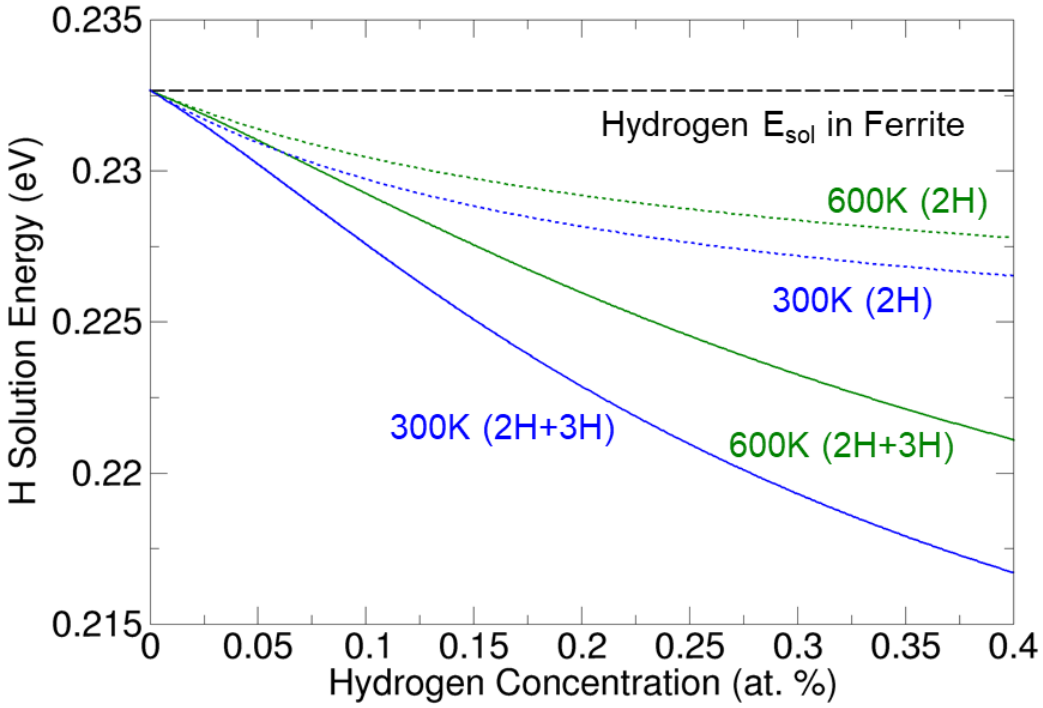

Figure 8. Hydrogen solution energy in ferrite at different concentrations and temperatures predicted by our theory. The blue and green dash lines are the results that include hydrogen pair calculations only, while the solid lines include both the hydrogen pair and triplet calculations.

5. Conclusions

A cost-effectively computational method is proposed in this work to provide a continuous energy profile to bridge the gap between the dilute and concentrated defect calculations. An estimate of uncertainty of the method is also provided by considering the cumulative probability density of each cluster size. The uncertainty decreases when the defect concentration decrease, which is contrary to most methods developed for

concentrated solution, and therefore our approach is especially suitable for intermediate defect concentrations. Our approach was first validated against conventional (and computationally expensive) method for the case of clustering of carbon vacancies and hydrogen in cementite, showing excellent agreement, and then applied to a case that is beyond the reach of other methods. Applying our approach to the case of hydrogen interaction in ferrite, we notice that the hydrogen solution energy will decrease when the local hydrogen concentration increases, implying a feed-forward effect where the energy required to accommodate hydrogen decrease as the concentration increase, driven by other dominant factors like stresses induced by microstructural features.

The novel approach presented here may be applied to other systems where low-but-not-dilute concentration of defects and impurities is important. This method enables accurate and fast predictions of clustering behaviour (and any other ensemble average like defect volumes or stresses) from atomic scale simulations.

6. Acknowledgement

The authors thank the funding supports from Australian Research Council (LP180100431, LP210300999, LP220100031, FT180100232, IE230100160, and IM230100125), the 2019 University of Sydney Postdoctoral Fellowship, and the Taiwan-University of Sydney Scholarship from Taiwan's Ministry of Education.

7. Data Availability

The paper contains all the essential data to assess the conclusions of this study, and relevant data can be provided upon a reasonable request.

8. Reference

[1] C.G. Van de Walle, J. Neugebauer, First-principles calculations for defects and impurities: Applications to III-nitrides, J Appl Phys. 95 (2004) 3851–3879. https://doi.org/10.1063/1.1682673.

[2] Y. Feng, J. Wu, Q. Chi, W. Li, Y. Yu, W. Fei, Defects and Aliovalent Doping Engineering in Electroceramics, Chem Rev. 120 (2020) 1710–1787. https://doi.org/10.1021/acs.chemrev.9b00507.

[3] A. Zunger, O.I. Malyi, Understanding Doping of Quantum Materials, Chem Rev. 121 (2021) 3031–3060. https://doi.org/10.1021/acs.chemrev.0c00608.

[4] A. Walsh, A. Zunger, Instilling defect tolerance in new compounds, Nat Mater. 16 (2017) 964–967. https://doi.org/10.1038/nmat4973.

[5] N.F. Mott, M.J. Littleton, Conduction in polar crystals. I. Electrolytic conduction in solid salts, Transactions of the Faraday Society. 34 (1938) 485. https://doi.org/10.1039/tf9383400485.
[6] C. Freysoldt, B. Grabowski, T. Hickel, J. Neugebauer, G. Kresse, A. Janotti, C.G. Van de Walle, First-principles calculations for point defects in solids, Rev Mod Phys. 86 (2014) 253–305. https://doi.org/10.1103/RevModPhys.86.253.
[7] H.-P. Komsa, T.T. Rantala, A. Pasquarello, Finite-size supercell correction schemes for charged defect calculations, Phys Rev B. 86 (2012) 045112. https://doi.org/10.1103/PhysRevB.86.045112.
[8] C. Varvenne, F. Bruneval, M.-C. Marinica, E. Clouet, Point defect modeling in materials: Coupling *ab initio* and elasticity approaches, Phys Rev B. 88 (2013) 134102. https://doi.org/10.1103/PhysRevB.88.134102.
[9] Y. Kumagai, F. Oba, Electrostatics-based finite-size corrections for first-principles point defect calculations, Phys Rev B. 89 (2014) 195205. https://doi.org/10.1103/PhysRevB.89.195205.
[10] N.D.M. Hine, K. Frensch, W.M.C. Foulkes, M.W. Finnis, Supercell size scaling of density functional theory formation energies of charged defects, Phys Rev B. 79 (2009) 024112. https://doi.org/10.1103/PhysRevB.79.024112.
[11] S. Lany, A. Zunger, Accurate prediction of defect properties in density functional supercell calculations, Model Simul Mat Sci Eng. 17 (2009) 084002. https://doi.org/10.1088/0965-0393/17/8/084002.
[12] G. Makov, M.C. Payne, Periodic boundary conditions in ab initio calculations, Phys Rev B. 51 (1995) 4014–4022. https://doi.org/10.1103/PhysRevB.51.4014.
[13] P.A. Burr, M.W.D. Cooper, Importance of elastic finite-size effects: Neutral defects in ionic compounds, Phys Rev B. 96 (2017) 094107. https://doi.org/10.1103/PhysRevB.96.094107.
[14] Z.-J. Suo, J.-W. Luo, S.-S. Li, L.-W. Wang, Image charge interaction correction in charged-defect calculations, Phys Rev B. 102 (2020) 174110. https://doi.org/10.1103/PhysRevB.102.174110.
[15] T. Gake, Y. Kumagai, C. Freysoldt, F. Oba, Finite-size corrections for defect-involving vertical transitions in supercell calculations, Phys Rev B. 101 (2020) 020102. https://doi.org/10.1103/PhysRevB.101.020102.
[16] I. Mosquera-Lois, S.R. Kavanagh, J. Klarbring, K. Tolborg, A. Walsh, Imperfections are not 0 K: free energy of point defects in crystals, Chem Soc Rev. 52

(2023) 5812–5826. https://doi.org/10.1039/D3CS00432E.
[17] P. Sarker, T. Harrington, C. Toher, C. Oses, M. Samiee, J.-P. Maria, D.W. Brenner, K.S. Vecchio, S. Curtarolo, High-entropy high-hardness metal carbides discovered by entropy descriptors, Nat Commun. 9 (2018) 4980. https://doi.org/10.1038/s41467-018-07160-7.
[18] O.F. Dippo, K.S. Vecchio, A universal configurational entropy metric for high-entropy materials, Scr Mater. 201 (2021) 113974. https://doi.org/10.1016/j.scriptamat.2021.113974.
[19] M.C. Gao, J.-W. Yeh, P.K. Liaw, Y. Zhang, eds., High-Entropy Alloys, Springer International Publishing, Cham, 2016. https://doi.org/10.1007/978-3-319-27013-5.
[20] Y. Zhang, Y.N. Osetsky, W.J. Weber, Tunable Chemical Disorder in Concentrated Alloys: Defect Physics and Radiation Performance, Chem Rev. 122 (2022) 789–829. https://doi.org/10.1021/acs.chemrev.1c00387.
[21] C. Jiang, B.P. Uberuaga, Efficient Ab initio Modeling of Random Multicomponent Alloys, Phys Rev Lett. 116 (2016) 105501. https://doi.org/10.1103/PhysRevLett.116.105501.
[22] A. Zunger, S.-H. Wei, L.G. Ferreira, J.E. Bernard, Special quasirandom structures, Phys Rev Lett. 65 (1990) 353–356. https://doi.org/10.1103/PhysRevLett.65.353.
[23] S.-H. Wei, L.G. Ferreira, J.E. Bernard, A. Zunger, Electronic properties of random alloys: Special quasirandom structures, Phys Rev B. 42 (1990) 9622–9649. https://doi.org/10.1103/PhysRevB.42.9622.
[24] J.M. Sanchez, F. Ducastelle, D. Gratias, Generalized cluster description of multicomponent systems, Physica A: Statistical Mechanics and Its Applications. 128 (1984) 334–350. https://doi.org/10.1016/0378-4371(84)90096-7.
[25] J.M. Sanchez, Cluster expansions and the configurational energy of alloys, Phys Rev B. 48 (1993) 14013–14015. https://doi.org/10.1103/PhysRevB.48.14013.
[26] J.M. Sanchez, Cluster expansion and the configurational theory of alloys, Phys Rev B. 81 (2010) 224202. https://doi.org/10.1103/PhysRevB.81.224202.
[27] C. Oses, C. Toher, S. Curtarolo, High-entropy ceramics, Nat Rev Mater. 5 (2020) 295–309. https://doi.org/10.1038/s41578-019-0170-8.
[28] R. Grau-Crespo, S. Hamad, C.R.A. Catlow, N.H. de Leeuw, Symmetry-adapted configurational modelling of fractional site occupancy in solids, Journal of Physics: Condensed Matter. 19 (2007) 256201. https://doi.org/10.1088/0953-

8984/19/25/256201.
[29] A. Gonis, P.P. Singh, P.E.A. Turchi, X.-G. Zhang, Use of the Ising model in the study of substitutional alloys, Phys Rev B. 51 (1995) 2122–2131. https://doi.org/10.1103/PhysRevB.51.2122.
[30] Y.-S. Chen, H. Lu, J. Liang, A. Rosenthal, H. Liu, G. Sneddon, I. McCarroll, Z. Zhao, W. Li, A. Guo, Observation of hydrogen trapping at dislocations, grain boundaries, and precipitates, Science (1979). 367 (2020) 171–175.
[31] G. Kresse, J. Furthmüller, Efficient iterative schemes for ab initio total-energy calculations using a plane-wave basis set, Phys Rev B. 54 (1996) 11169–11186. https://doi.org/10.1103/PhysRevB.54.11169.
[32] J.P. Perdew, K. Burke, M. Ernzerhof, Generalized Gradient Approximation Made Simple, Phys Rev Lett. 77 (1996) 3865–3868. https://doi.org/10.1103/PhysRevLett.77.3865.
[33] P.E. Blöchl, Projector augmented-wave method, Phys Rev B. 50 (1994) 17953–17979. https://doi.org/10.1103/PhysRevB.50.17953.
[34] R. Grau-Crespo, S. Hamad, C.R.A. Catlow, N.H. de Leeuw, Symmetry-adapted configurational modelling of fractional site occupancy in solids, Journal of Physics: Condensed Matter. 19 (2007) 256201. https://doi.org/10.1088/0953-8984/19/25/256201.
[35] S.T. Murphy, Tritium Solubility in Li2TiO3 from First-Principles Simulations, The Journal of Physical Chemistry C. 118 (2014) 29525–29532. https://doi.org/10.1021/jp508875y.
[36] M.W. Finnis, A.Y. Lozovoi, A. Alavi, THE OXIDATION OF NIAL: What Can We Learn from Ab Initio Calculations?, Annu Rev Mater Res. 35 (2005) 167–207. https://doi.org/10.1146/annurev.matsci.35.101503.091652.
[37] E.J. McEniry, T. Hickel, J. Neugebauer, Ab initio simulation of hydrogen-induced decohesion in cementite-containing microstructures, Acta Mater. 150 (2018) 53–58. https://doi.org/10.1016/j.actamat.2018.03.005.
[38] V. Olden, C. Thaulow, R. Johnsen, Modelling of hydrogen diffusion and hydrogen induced cracking in supermartensitic and duplex stainless steels, Mater Des. 29 (2008) 1934–1948. https://doi.org/10.1016/j.matdes.2008.04.026.
[39] Y.-S. Chen, D. Haley, S.S.A. Gerstl, A.J. London, F. Sweeney, R.A. Wepf, W.M. Rainforth, P.A.J. Bagot, M.P. Moody, Direct observation of individual hydrogen atoms at trapping sites in a ferritic steel, Science (1979). 355 (2017) 1196–1199.

https://doi.org/10.1126/science.aal2418.
[40] W.A. Counts, C. Wolverton, R. Gibala, First-principles energetics of hydrogen traps in α-Fe: Point defects, Acta Mater. 58 (2010) 4730–4741. https://doi.org/10.1016/j.actamat.2010.05.010.

5.3 Summary

In this chapter, we present an innovative method to account for the middle-ground defect concentration calculation. The validity and power of this approach have been established through rigorous validation exercises. Specifically, we have compared our method against conventional, albeit computationally expensive, techniques. In the specific case of hydrogen entrapment by carbon vacancies within hypo-stoichiometric cementite, our approach demonstrates exceptional agreement with the established methods, all while significantly reducing the computational burden. This achievement lends strong credibility to our methodology.

Furthermore, we have extended the application of our approach to investigate hydrogen clustering within ferrite. The insights garnered from our method offer a plausible rationale for the unexpectedly high local concentrations of hydrogen observed in experimental data, acquired through advanced techniques such as atom probe tomography.

In essence, our work introduces an innovative computational avenue that elegantly addresses the complexities of intermediate defect concentrations. By combining cluster expansion with ensemble statistics, we have not only surmounted existing challenges but also provided a powerful tool for unraveling intricate phenomena like hydrogen interactions in materials.

6 Thesis conclusions

In this study, we have measured and predicted the behavior of hydrogen in steel through a combination of advanced microscopy techniques and computational modeling. Recent advances in atom probe tomography techniques, coupled with the implementation of a cryogenic transfer protocol, has enabled us to delve deeper into the hydrogen distribution within steel microstructures, yielding invaluable insights. Simultaneously, atomic-scale simulations, such as density functional theory, have proven immensely valuable. These simulations serve as a bridge between experimental observations and theoretical understanding, facilitating a cohesive correlation between the two domains. By synergistically integrating these experimental and simulation approaches, we've been able to achieve a more comprehensive and accurate comprehension of the behaviour of hydrogen \ within steel materials.

Through an investigation into the hydrogen trapping behavior in both TiC and (Ti,Mo)C ferritic steel, we identified distinct hydrogen trapping mechanisms associated with the presence of carbon vacancies in carbides. The introduction of molybdenum induces a modification in the hydrogen trapping mechanism, whereby H able to access carbon vacancy traps within the carbide precipitates, resulting in a substantial increase in trapping capacity. The observed impact of carbon vacancies on hydrogen trapping offers valuable insights for the development of chemical formulations for carbide-strengthening steels, enhancing their compatibility with hydrogen.

We explored hydrogen distribution within non-deformed pearlite, relevant to gas pipelines. The investigation focused on understanding the effect of lattice misfits between cementite and ferrite, as well as the impact of carbon vacancies within cementite. We discovered that the hydrogen was not located precisely at the cementite-ferrite interface within the ferrite matrix, but instead was clustered in the ferrite at a distance from the boundary, presumably in the form of Cottrell atmospheres around defects/dislocations. Furthermore, the pivotal role of carbon vacancies near the interface was highlighted, amplifying the tendency for hydrogen trapping within the cementite phase. This comprehensive approach, integrating empirical evidence with theoretical insights, establishes a solid foundation with

promising implications for the tailored design of pipeline steel for hydrogen-based applications.

To bridge the gap in theoretical understanding, we introduced a novel computationally efficient approach to encompass intermediate defect concentrations. Our approach, distinctively focused on hydrogen trapping by carbon vacancies within hypo-stoichiometric cementite, was rigorously compared to conventional methodologies. Demonstrating notable alignment with established techniques, our method significantly reduced computational demands, reinforcing its credibility. Expanding its application to investigate hydrogen clustering within ferrite, our approach offered insights explaining elevated hydrogen concentrations in experimental data. Overall, by combining cluster expansion and ensemble statistics, this method allows for exploration of hydrogen behaviors at intermediate concentration levels, something that is challenging to achieve by using conventional techniques.

To summarize, this study not only advances the understanding of hydrogen's role in steel behavior but also contributes to the optimization of material designs for enhanced performance and safety, especially in the context of hydrogen embrittlement and other real-world applications. These suggest future work are listed below in this section.

7 Recommendations for future work

Several areas are identified here that could benefit from further attention in light of the results I've obtained.

- While the introduction of (Ti,Mo)C carbide creates a significant increase in hydrogen trapping capacity within the ferritic steel, it remains imperative to substantiate the true efficacy of these trapping sites in mitigating hydrogen embrittlement through mechanical testing. However, the conventional slow strain tensile test proves unsuitable for directly comparing hydrogen embrittlement resistance between TiC and (Ti,Mo)C ferritic steel samples. This limitation stems from the standard hydrogen charging procedure, wherein samples are charged until they reach saturation, so it is not possible to compare the two samples with the same hydrogen concentration. A nuanced and meticulous approach is necessary to navigate this disparity and ensure the accurate assessment of hydrogen embrittlement resistance in these materials.

- In our exploration of the hydrogen distribution within pearlitic steel using atom probe tomography, it's important to acknowledge that our investigation was conducted solely on samples without any prestrain. We suspect that prestrain might lead to defects/accumulated dislocations at ferrite/cementite interfaces, which may affect the distribution / trapping of hydrogen. To understand the influence of prestrain on hydrogen distribution, it is suggested to examine samples subjected to varying prestrain rates.
- Expanding the scope of the developed simulation method to encompass intermediate defect concentrations is a promising avenue, particularly for delving into the hydrogen trapping behavior within grain boundaries. Notably, our current study centers on hydrogen interaction with the pure ferrite lattice structure, overlooking other defect structures. Delving deeper into the intriguing interaction between hydrogen and grain boundaries using this method could yield valuable insights. The possibility of constructing a continuous energy profile would further enhance our understanding of this interaction and its implications.

References for literature review and generic methods

[1] IEA, The Future of Hydrogen, Paris, 2019.

[2] D. Raabe, C.C. Tasan, E.A. Olivetti, Strategies for improving the sustainability of structural metals, Nature. 575 (2019) 64–74. https://doi.org/10.1038/s41586-019-1702-5.

[3] Y. Ma, I.R. Souza Filho, Y. Bai, J. Schenk, F. Patisson, A. Beck, J.A. van Bokhoven, M.G. Willinger, K. Li, D. Xie, D. Ponge, S. Zaefferer, B. Gault, J.R. Mianroodi, D. Raabe, Hierarchical nature of hydrogen-based direct reduction of iron oxides, Scr Mater. 213 (2022) 114571. https://doi.org/10.1016/j.scriptamat.2022.114571.

[4] K. Daehn, R. Basuhi, J. Gregory, M. Berlinger, V. Somjit, E.A. Olivetti, Innovations to decarbonize materials industries, Nat Rev Mater. 7 (2021) 275–294. https://doi.org/10.1038/s41578-021-00376-y.

[5] S. McQueen, J. Stanford, S. Satyapal, E. Miller, N. Stetson, D. Papageorgopoulos, N. Rustagi, V. Arjona, J. Adams, K. Randolph, D. Peterson, L. Hill, M. Koleva, T. Reinhardt, E. Frye, R. Schrecengost, A. Kokkinos, J. Litynski, R. Conrad, G. Soloveichik, D. Tew, S. Litzelman, J. Vetrano, R. Onuschak, A. Hahn, E. Hsieh, R. Costa, Department of Energy Hydrogen Program Plan, 2020. https://doi.org/10.2172/1721803.

[6] Xing L. Yan, Ryutaro Hino, Nuclear Hydrogen Production Handbook, CRC Press, 2016. https://doi.org/10.1201/b10789.

[7] The U.S. Department of Energy, Hydrogen Shot, Https://Www.Energy.Gov/Eere/Fuelcells/Hydrogen-Shot. (n.d.).

[8] Ministry of the Environment, Summary of Japan Hydrogen Strategy, 2020.

[9] Kwasi Kwarteng, UK Hydrogen Strategy, London, 2021.

[10] The National Hydrogen Strategy, Berlin, 2020.

[11] T. Bru, S. Rotevatn, The Norwegian hydrogen strategy, 2020.

[12] Seamus O'Regan, The Hydrogen Strategy for Canada, Otawa, 2020.

[13] X. Ren, L. Dong, D. Xu, B. Hu, Challenges towards hydrogen economy in China, Int J Hydrogen Energy. 45 (2020) 34326–34345. https://doi.org/10.1016/j.ijhydene.2020.01.163.

[14] A. Finkel, Australia's National Hydrogen Strategy, 2019.

[15] Lessons Learned from a Hydrogen Explosion, Https://Www.Powermag.Com/Lessons-Learned-from-a-Hydrogen-Explosion/ . (2009).

[16] E. Ohaeri, U. Eduok, J. Szpunar, Hydrogen related degradation in pipeline steel: A review, Int J Hydrogen Energy. 43 (2018) 14584–14617.

[17] E.G. Ohaeri, W. Qin, J. Szpunar, A critical perspective on pipeline processing and failure risks in hydrogen service conditions, J Alloys Compd. 857 (2021) 158240. https://doi.org/10.1016/j.jallcom.2020.158240.

[18] A. Laureys, R. Depraetere, M. Cauwels, T. Depover, S. Hertelé, K. Verbeken, Use of existing steel pipeline infrastructure for gaseous hydrogen storage and transport: A review of factors affecting hydrogen induced degradation, J Nat Gas Sci Eng. 101 (2022) 104534. https://doi.org/10.1016/j.jngse.2022.104534.

[19] H. Li, R. Niu, W. Li, H. Lu, J. Cairney, Y.-S. Chen, Hydrogen in pipeline steels: Recent advances in characterization and embrittlement mitigation, J Nat Gas Sci Eng. 105 (2022) 104709. https://doi.org/10.1016/j.jngse.2022.104709.

[20] A. THOMPSON, I. BERNSTEIN, Selection of structural materials for hydrogen pipelines and storage vessels, Int J Hydrogen Energy. 2 (1977) 163–173. https://doi.org/10.1016/0360-3199(77)90007-6.

[21] F. Ustolin, N. Paltrinieri, F. Berto, Loss of integrity of hydrogen technologies: A critical review, Int J Hydrogen Energy. 45 (2020) 23809–23840. https://doi.org/10.1016/j.ijhydene.2020.06.021.
[22] F. Yang, T. Wang, X. Deng, J. Dang, Z. Huang, S. Hu, Y. Li, M. Ouyang, Review on hydrogen safety issues: Incident statistics, hydrogen diffusion, and detonation process, Int J Hydrogen Energy. 46 (2021) 31467–31488. https://doi.org/10.1016/j.ijhydene.2021.07.005.
[23] V. Martin, P. Ashworth, S. Petrova, B. Wade, K. Witt, Public Perceptions of Hydrogen: 2021 National Survey Results, 2021.
[24] H.E. Townsend, K.H. Frank, B. Brignano, C. Choi, Hydrogen embrittlement testing and results of full-size ASTM A354 grade BD rods in the SFOBB, Bridge Structures. 11 (2016) 117–130. https://doi.org/10.3233/BRS-160096.
[25] M. Iordachescu, A. Valiente, M. Pérez-Guerrero, M. Elices, Environment-assisted failure of structural tendons for construction and building applications, Constr Build Mater. 159 (2018) 499–507. https://doi.org/10.1016/j.conbuildmat.2017.11.011.
[26] E.M. Pañeda, Progress and opportunities in modelling environmentally assisted cracking, RILEM Technical Letters. 6 (2021) 70–77. https://doi.org/10.21809/rilemtechlett.2021.145.
[27] W.H. Johnson, II. On some remarkable changes produced in iron and steel by the action of hydrogen and acids, Proceedings of the Royal Society of London. 23 (1875) 168–179. https://doi.org/10.1098/rspl.1874.0024.
[28] H.K.D.H. Bhadeshia, Prevention of hydrogen embrittlement in steels, ISIJ International. 56 (2016) 24–36.
[29] M.L. Martin, M.J. Connolly, F.W. DelRio, A.J. Slifka, Hydrogen embrittlement in ferritic steels, Appl Phys Rev. 7 (2020) 041301. https://doi.org/10.1063/5.0012851.
[30] I.M. Robertson, P. Sofronis, A. Nagao, M.L. Martin, S. Wang, D.W. Gross, K.E. Nygren, Hydrogen embrittlement understood, Metallurgical and Materials Transactions A. 46 (2015) 2323–2341.
[31] S. Lynch, Hydrogen embrittlement phenomena and mechanisms, Corrosion Reviews. 30 (2012). https://doi.org/10.1515/corrrev-2012-0502.
[32] M. Nagumo, Fundamentals of Hydrogen Embrittlement, Springer Singapore, Singapore, 2016. https://doi.org/10.1007/978-981-10-0161-1.
[33] M. Koyama, E. Akiyama, Y.-K. Lee, D. Raabe, K. Tsuzaki, Overview of hydrogen embrittlement in high-Mn steels, Int J Hydrogen Energy. 42 (2017) 12706–12723. https://doi.org/10.1016/j.ijhydene.2017.02.214.
[34] S.K. Dwivedi, M. Vishwakarma, Hydrogen embrittlement in different materials: A review, Int J Hydrogen Energy. 43 (2018) 21603–21616. https://doi.org/10.1016/j.ijhydene.2018.09.201.
[35] Q. Liu, A. Atrens, A critical review of the influence of hydrogen on the mechanical properties of medium-strength steels, Corrosion Reviews. 31 (2013) 85–103. https://doi.org/10.1515/corrrev-2013-0023.
[36] J. Venezuela, Q. Liu, M. Zhang, Q. Zhou, A. Atrens, A review of hydrogen embrittlement of martensitic advanced high-strength steels, Corrosion Reviews. 34 (2016) 153–186. https://doi.org/10.1515/corrrev-2016-0006.
[37] Q. Liu, Q. Zhou, J. Venezuela, M. Zhang, J. Wang, A. Atrens, A review of the influence of hydrogen on the mechanical properties of DP, TRIP, and TWIP advanced high-strength steels for auto construction, Corrosion Reviews. 34 (2016) 127–152. https://doi.org/10.1515/corrrev-2015-0083.
[38] M. Kappes, M. Iannuzzi, R.M. Carranza, Hydrogen Embrittlement of Magnesium and Magnesium Alloys: A Review, J Electrochem Soc. 160 (2013) C168–C178.

https://doi.org/10.1149/2.023304jes.
[39] S. Suman, Mohd.K. Khan, M. Pathak, R.N. Singh, J.K. Chakravartty, Hydrogen in Zircaloy: Mechanism and its impacts, Int J Hydrogen Energy. 40 (2015) 5976–5994. https://doi.org/10.1016/j.ijhydene.2015.03.049.
[40] O. Barrera, D. Bombac, Y. Chen, T.D. Daff, E. Galindo-Nava, P. Gong, D. Haley, R. Horton, I. Katzarov, J.R. Kermode, C. Liverani, M. Stopher, F. Sweeney, Understanding and mitigating hydrogen embrittlement of steels: a review of experimental, modelling and design progress from atomistic to continuum, J Mater Sci. 53 (2018) 6251–6290. https://doi.org/10.1007/s10853-017-1978-5.
[41] T.P. Chapman, D. Dye, D. Rugg, Hydrogen in Ti and Zr alloys: industrial perspective, failure modes and mechanistic understanding, Philosophical Transactions of the Royal Society A: Mathematical, Physical and Engineering Sciences. 375 (2017) 20160418. https://doi.org/10.1098/rsta.2016.0418.
[42] R.P. Gangloff, B.P. Somerday, Gaseous hydrogen embrittlement of materials in energy technologies: the problem, its characterisation and effects on particular alloy classes, Elsevier, 2012.
[43] R.P. Gangloff, B.P. Somerday, Gaseous hydrogen embrittlement of materials in energy technologies: mechanisms, modelling and future developments, Elsevier, 2012.
[44] M. Alexander Stopher, P.E.J. Rivera-Diaz-del-Castillo, Hydrogen embrittlement in bearing steels, Materials Science and Technology. 32 (2016) 1184–1193. https://doi.org/10.1080/02670836.2016.1156810.
[45] D. Rudomilova, T. Prošek, G. Luckeneder, Techniques for investigation of hydrogen embrittlement of advanced high strength steels, Corrosion Reviews. 36 (2018) 413–434. https://doi.org/10.1515/corrrev-2017-0106.
[46] I. Maroef, D.L. Olson, M. Eberhart, G.R. Edwards, Hydrogen trapping in ferritic steel weld metal, International Materials Reviews. 47 (2002) 191–223. https://doi.org/10.1179/095066002225006548.
[47] M. Nagumo, K. Takai, The predominant role of strain-induced vacancies in hydrogen embrittlement of steels: Overview, Acta Mater. 165 (2019) 722–733. https://doi.org/10.1016/j.actamat.2018.12.013.
[48] J.P. Hirth, Effects of hydrogen on the properties of iron and steel, Metallurgical Transactions A. 11 (1980) 861–890. https://doi.org/10.1007/BF02654700.
[49] J. Villalobos, A. Del-Pozo, B. Campillo, J. Mayen, S. Serna, Microalloyed Steels through History until 2018: Review of Chemical Composition, Processing and Hydrogen Service, Metals (Basel). 8 (2018) 351. https://doi.org/10.3390/met8050351.
[50] M. Dadfarnia, A. Nagao, S. Wang, M.L. Martin, B.P. Somerday, P. Sofronis, Recent advances on hydrogen embrittlement of structural materials, Int J Fract. 196 (2015) 223–243. https://doi.org/10.1007/s10704-015-0068-4.
[51] C. Borchers, T. Michler, A. Pundt, Effect of Hydrogen on the Mechanical Properties of Stainless Steels, Adv Eng Mater. 10 (2008) 11–23. https://doi.org/10.1002/adem.200700252.
[52] H.J. Grabke, F. Gehrmann, E. Riecke, Hydrogen in microalloyed steels, Steel Research. 72 (2001) 225–235. https://doi.org/10.1002/srin.200100110.
[53] S. Pillot, L. Coudreuse, Hydrogen-induced disbonding and embrittlement of steels used in petrochemical refining, in: Gaseous Hydrogen Embrittlement of Materials in Energy Technologies, Elsevier, 2012: pp. 51–93. https://doi.org/10.1533/9780857093899.1.51.
[54] A. Atrens, Q. Liu, Q. Zhou, J. Venezuela, M. Zhang, Evaluation of automobile service performance using laboratory testing, Materials Science and Technology. 34

(2018) 1893–1909. https://doi.org/10.1080/02670836.2018.1495903.
[55] A. Atrens, J. Venezuela, Q. Liu, Q. Zhou, K. Verbeken, C. Tapia-Bastidas, E. Gray, F. Christien, K. Wolski, Electrochemical and Mechanical Aspects of Hydrogen Embrittlement Evaluation of Martensitic Steels, in: Encyclopedia of Interfacial Chemistry, Elsevier, 2018: pp. 201–225. https://doi.org/10.1016/B978-0-12-409547-2.13770-9.
[56] M.B. Djukic, G.M. Bakic, V. Sijacki Zeravcic, A. Sedmak, B. Rajicic, The synergistic action and interplay of hydrogen embrittlement mechanisms in steels and iron: Localized plasticity and decohesion, Eng Fract Mech. 216 (2019) 106528. https://doi.org/10.1016/j.engfracmech.2019.106528.
[57] S. Lynch, Discussion of some recent literature on hydrogen-embrittlement mechanisms: addressing common misunderstandings, Corrosion Reviews. 37 (2019) 377–395. https://doi.org/10.1515/corrrev-2019-0017.
[58] R.P. Gangloff, Hydrogen-assisted Cracking, in: Comprehensive Structural Integrity, Elsevier, 2003: pp. 31–101. https://doi.org/10.1016/B0-08-043749-4/06134-6.
[59] J. Hoschke, M.F.W. Chowdhury, J. Venezuela, A. Atrens, A review of hydrogen embrittlement in gas transmission pipeline steels, Corrosion Reviews. 0 (2023). https://doi.org/10.1515/corrrev-2022-0052.
[60] G. Lovicu, M. Bottazzi, F. D'Aiuto, M. De Sanctis, A. Dimatteo, C. Santus, R. Valentini, Hydrogen Embrittlement of Automotive Advanced High-Strength Steels, Metallurgical and Materials Transactions A. 43 (2012) 4075–4087. https://doi.org/10.1007/s11661-012-1280-8.
[61] W.Y. Choo, J.Y. Lee, Hydrogen trapping phenomena in carbon steel, J Mater Sci. 17 (1982) 1930–1938. https://doi.org/10.1007/BF00540409.
[62] R.L.S. Thomas, J.R. Scully, R.P. Gangloff, Internal hydrogen embrittlement of ultrahigh-strength AERMET 100 steel, Metallurgical and Materials Transactions A. 34 (2003) 327–344. https://doi.org/10.1007/s11661-003-0334-3.
[63] S. Ootsuka, S. Fujita, E. Tada, A. Nishikata, T. Tsuru, Evaluation of hydrogen absorption into steel in automobile moving environments, Corros Sci. 98 (2015) 430–437. https://doi.org/10.1016/j.corsci.2015.05.049.
[64] H.P. Van Leeuwen, The kinetics of hydrogen embrittlement: A quantitative diffusion model, Eng Fract Mech. 6 (1974) 141–161. https://doi.org/10.1016/0013-7944(74)90053-8.
[65] E. Martínez-Pañeda, A. Díaz, L. Wright, A. Turnbull, Generalised boundary conditions for hydrogen transport at crack tips, Corros Sci. 173 (2020) 108698. https://doi.org/10.1016/j.corsci.2020.108698.
[66] Y. Murakami, H. Matsunaga, The effect of hydrogen on fatigue properties of steels used for fuel cell system, Int J Fatigue. 28 (2006) 1509–1520. https://doi.org/10.1016/j.ijfatigue.2005.06.059.
[67] E. Martínez-Pañeda, Z.D. Harris, S. Fuentes-Alonso, J.R. Scully, J.T. Burns, On the suitability of slow strain rate tensile testing for assessing hydrogen embrittlement susceptibility, Corros Sci. 163 (2020) 108291. https://doi.org/10.1016/j.corsci.2019.108291.
[68] N.J.H. Holroyd, T.L. Burnett, B.C. Palmer, J.J. Lewandowski, Estimation of environment-induced crack growth rate as a function of stress intensity factors generated during slow strain rate testing of aluminum alloys, Corrosion Reviews. 37 (2019) 499–506. https://doi.org/10.1515/corrrev-2019-0031.
[69] D. Sampath, R. Akid, R. Morana, Estimation of crack initiation stress and local fracture toughness of Ni-alloys 945X (UNS N09946) and 718 (UNS N07718) under hydrogen environment via fracture surface topography analysis, Eng Fract Mech. 191

(2018) 324–343. https://doi.org/10.1016/j.engfracmech.2017.12.010.
[70] A. Golahmar, P.K. Kristensen, C.F. Niordson, E. Martínez-Pañeda, A phase field model for hydrogen-assisted fatigue, Int J Fatigue. 154 (2022) 106521. https://doi.org/10.1016/j.ijfatigue.2021.106521.
[71] H. Li, J. Venezuela, Q. Zhou, Z. Shi, M. Yan, R. Knibbe, M. Zhang, F. Dong, A. Atrens, Effect of plastic strain damage on the hydrogen embrittlement of a dual-phase (DP) and a quenching and partitioning (Q&P) advanced high-strength steel, Materials Science and Engineering: A. 785 (2020) 139343. https://doi.org/10.1016/j.msea.2020.139343.
[72] H. Li, J. Venezuela, Z. Qian, Q. Zhou, Z. Shi, M. Yan, R. Knibbe, M. Zhang, F. Dong, A. Atrens, Hydrogen fracture maps for sheared-edge-controlled hydrogen-delayed fracture of 1180 MPa advanced high-strength steels, Corros Sci. 184 (2021) 109360. https://doi.org/10.1016/j.corsci.2021.109360.
[73] S. Ramamurthy, A. Atrens, Stress corrosion cracking of high-strength steels, Corrosion Reviews. 31 (2013) 1–31. https://doi.org/10.1515/corrrev-2012-0018.
[74] Y. Ogawa, H. Hosoi, K. Tsuzaki, T. Redarce, O. Takakuwa, H. Matsunaga, Hydrogen, as an alloying element, enables a greater strength-ductility balance in an Fe-Cr-Ni-based, stable austenitic stainless steel, Acta Mater. 199 (2020) 181–192. https://doi.org/10.1016/j.actamat.2020.08.024.
[75] K. Wada, J. Yamabe, H. Matsunaga, Mechanism of hydrogen-induced hardening in pure nickel and in a copper–nickel alloy analyzed by micro Vickers hardness testing, Materials Science and Engineering: A. 805 (2021) 140580. https://doi.org/10.1016/j.msea.2020.140580.
[76] D. Eliezer, N. Eliaz, O.N. Senkov, F.H. Froes, Positive effects of hydrogen in metals, Materials Science and Engineering: A. 280 (2000) 220–224. https://doi.org/10.1016/S0921-5093(99)00670-X.
[77] F.H. Froes, O.N. Senkov, J.I. Qazi, Hydrogen as a temporary alloying element in titanium alloys: thermohydrogen processing, International Materials Reviews. 49 (2004) 227–245. https://doi.org/10.1179/095066004225010550.
[78] M.L. Martin, I.M. Robertson, P. Sofronis, Interpreting hydrogen-induced fracture surfaces in terms of deformation processes: A new approach, Acta Mater. 59 (2011) 3680–3687. https://doi.org/10.1016/j.actamat.2011.03.002.
[79] M.L. Martin, J.A. Fenske, G.S. Liu, P. Sofronis, I.M. Robertson, On the formation and nature of quasi-cleavage fracture surfaces in hydrogen embrittled steels, Acta Mater. 59 (2011) 1601–1606. https://doi.org/10.1016/j.actamat.2010.11.024.
[80] X. Xing, R. Cheng, G. Cui, J. Liu, J. Gou, C. Yang, Z. Li, F. Yang, Quantification of the temperature threshold of hydrogen embrittlement in X90 pipeline steel, Materials Science and Engineering: A. 800 (2021) 140118. https://doi.org/10.1016/j.msea.2020.140118.
[81] L. Zhang, M. Imade, B. An, M. Wen, T. Iijima, S. Fukuyama, K. Yokogawa, Internal Reversible Hydrogen Embrittlement of Austenitic Stainless Steels Based on Type 316 at Low Temperatures, ISIJ International. 52 (2012) 240–246. https://doi.org/10.2355/isijinternational.52.240.
[82] Z.D. Harris, S.K. Lawrence, D.L. Medlin, G. Guetard, J.T. Burns, B.P. Somerday, Elucidating the contribution of mobile hydrogen-deformation interactions to hydrogen-induced intergranular cracking in polycrystalline nickel, Acta Mater. 158 (2018) 180–192. https://doi.org/10.1016/j.actamat.2018.07.043.
[83] Y. Momotani, A. Shibata, D. Terada, N. Tsuji, Effect of strain rate on hydrogen embrittlement in low-carbon martensitic steel, Int J Hydrogen Energy. 42 (2017) 3371–3379. https://doi.org/10.1016/j.ijhydene.2016.09.188.

[84] E. Martínez-Pañeda, S. del Busto, C.F. Niordson, C. Betegón, Strain gradient plasticity modeling of hydrogen diffusion to the crack tip, Int J Hydrogen Energy. 41 (2016) 10265–10274. https://doi.org/10.1016/j.ijhydene.2016.05.014.
[85] J.T. Burns, Z.D. Harris, J.D. Dolph, R.P. Gangloff, Measurement and Modeling of Hydrogen Environment-Assisted Cracking in a Ni-Cu-Al-Ti Superalloy, Metallurgical and Materials Transactions A. 47 (2016) 990–997. https://doi.org/10.1007/s11661-015-3315-4.
[86] T. Depover, A. Laureys, D. Pérez Escobar, E. Van den Eeckhout, E. Wallaert, K. Verbeken, Understanding the Interaction between a Steel Microstructure and Hydrogen, Materials. 11 (2018) 698. https://doi.org/10.3390/ma11050698.
[87] M. Koyama, M. Rohwerder, C.C. Tasan, A. Bashir, E. Akiyama, K. Takai, D. Raabe, K. Tsuzaki, Recent progress in microstructural hydrogen mapping in steels: quantification, kinetic analysis, and multi-scale characterisation, Materials Science and Technology. 33 (2017) 1481–1496.
[88] Y.-S. Chen, H. Lu, J. Liang, A. Rosenthal, H. Liu, G. Sneddon, I. McCarroll, Z. Zhao, W. Li, A. Guo, Observation of hydrogen trapping at dislocations, grain boundaries, and precipitates, Science. 367 (2020) 171–175.
[89] T. Depover, D. Pérez Escobar, E. Wallaert, Z. Zermout, K. Verbeken, Effect of hydrogen charging on the mechanical properties of advanced high strength steels, Int J Hydrogen Energy. 39 (2014) 4647–4656. https://doi.org/10.1016/j.ijhydene.2013.12.190.
[90] K. Takasawa, R. Ikeda, N. Ishikawa, R. Ishigaki, Effects of grain size and dislocation density on the susceptibility to high-pressure hydrogen environment embrittlement of high-strength low-alloy steels, Int J Hydrogen Energy. 37 (2012) 2669–2675. https://doi.org/10.1016/j.ijhydene.2011.10.099.
[91] M. Dadfarnia, B. p. Somerday, P.E. Schembri, P. Sofronis, J.W. Foulk, K.A. Nibur, D.K. Balch, On Modeling Hydrogen-Induced Crack Propagation Under Sustained Load, JOM. 66 (2014) 1390–1398. https://doi.org/10.1007/s11837-014-1050-8.
[92] L. Anand, Y. Mao, B. Talamini, On modeling fracture of ferritic steels due to hydrogen embrittlement, J Mech Phys Solids. 122 (2019) 280–314. https://doi.org/10.1016/j.jmps.2018.09.012.
[93] S. SEREBRINSKY, A quantum-mechanically informed continuum model of hydrogen embrittlement, J Mech Phys Solids. 52 (2004) 2403–2430. https://doi.org/10.1016/j.jmps.2004.02.010.
[94] P. Gong, J. Nutter, P.E.J. Rivera-Diaz-Del-Castillo, W.M. Rainforth, Hydrogen embrittlement through the formation of low-energy dislocation nanostructures in nanoprecipitation-strengthened steels, Sci Adv. 6 (2020). https://doi.org/10.1126/sciadv.abb6152.
[95] D.G. Westlake, GENERALIZED MODEL FOR HYDROGEN EMBRITTLEMENT., Argonne National Lab., Ill., 1969.
[96] A.T. Motta, L. Capolungo, L.-Q. Chen, M.N. Cinbiz, M.R. Daymond, D.A. Koss, E. Lacroix, G. Pastore, P.-C.A. Simon, M.R. Tonks, Hydrogen in zirconium alloys: A review, Journal of Nuclear Materials. 518 (2019) 440–460.
[97] Y.-J. Jia, W.-Z. Han, Mechanisms of Hydride Nucleation, Growth, Reorientation, and Embrittlement in Zirconium: A Review, Materials. 16 (2023) 2419. https://doi.org/10.3390/ma16062419.
[98] H.K. Birnbaum, Mechanical properties of metal hydrides, Journal of the Less Common Metals. 104 (1984) 31–41. https://doi.org/10.1016/0022-5088(84)90433-8.
[99] E. Tal-Gutelmacher, D. Eliezer, The hydrogen embrittlement of titanium-based alloys, JOM. 57 (2005) 46–49. https://doi.org/10.1007/s11837-005-0115-0.

[100] N. Winzer, A. Atrens, G. Song, E. Ghali, W. Dietzel, K.U. Kainer, N. Hort, C. Blawert, A Critical Review of the Stress Corrosion Cracking (SCC) of Magnesium Alloys, Adv Eng Mater. 7 (2005) 659–693. https://doi.org/10.1002/adem.200500071.
[101] N. Winzer, A. Atrens, W. Dietzel, G. Song, K.U. Kainer, Evaluation of the delayed hydride cracking mechanism for transgranular stress corrosion cracking of magnesium alloys, Materials Science and Engineering: A. 466 (2007) 18–31. https://doi.org/10.1016/j.msea.2007.03.020.
[102] M.L. Wayman, G.C. Smith, The effects of hydrogen on the deformation and fracture of nickel-iron alloys, Acta Metallurgica. 19 (1971) 227–231. https://doi.org/10.1016/0001-6160(71)90150-7.
[103] J. Song, W.A. Curtin, A nanoscale mechanism of hydrogen embrittlement in metals, Acta Mater. 59 (2011) 1557–1569. https://doi.org/10.1016/j.actamat.2010.11.019.
[104] J. Song, W.A. Curtin, Atomic mechanism and prediction of hydrogen embrittlement in iron, Nat Mater. 12 (2013) 145–151. https://doi.org/10.1038/nmat3479.
[105] S.S. Shishvan, G. Csányi, V.S. Deshpande, Hydrogen induced fast-fracture, J Mech Phys Solids. 134 (2020) 103740. https://doi.org/10.1016/j.jmps.2019.103740.
[106] J. V. Badding, R.J. Hemley, H.K. Mao, High-Pressure Chemistry of Hydrogen in Metals: In Situ Study of Iron Hydride, Science (1979). 253 (1991) 421–424. https://doi.org/10.1126/science.253.5018.421.
[107] H.H. Johnson, J.G. Morlet, A.R. Troiano, Hydrogen, crack initiation, and delayed failure in steel, Trans. Met. Soc. AIME. 212 (1958).
[108] R.A. Oriani, A mechanistic theory of hydrogen embrittlement of steels, Berichte Der Bunsengesellschaft Für Physikalische Chemie. 76 (1972) 848–857.
[109] D.E. Jiang, E.A. Carter, First principles assessment of ideal fracture energies of materials with mobile impurities: implications for hydrogen embrittlement of metals, Acta Mater. 52 (2004) 4801–4807. https://doi.org/10.1016/j.actamat.2004.06.037.
[110] A. Van der Ven, G. Ceder, Impurity-induced van der Waals transition during decohesion, Phys Rev B. 67 (2003) 060101. https://doi.org/10.1103/PhysRevB.67.060101.
[111] A. Tehranchi, W.A. Curtin, Atomistic study of hydrogen embrittlement of grain boundaries in nickel: I. Fracture, J Mech Phys Solids. 101 (2017) 150–165. https://doi.org/10.1016/j.jmps.2017.01.020.
[112] A. Alvaro, I. Thue Jensen, N. Kheradmand, O.M. Løvvik, V. Olden, Hydrogen embrittlement in nickel, visited by first principles modeling, cohesive zone simulation and nanomechanical testing, Int J Hydrogen Energy. 40 (2015) 16892–16900. https://doi.org/10.1016/j.ijhydene.2015.06.069.
[113] I.H. Katzarov, A.T. Paxton, Hydrogen embrittlement II. Analysis of hydrogen-enhanced decohesion across (111) planes in α-Fe, Phys Rev Mater. 1 (2017) 033603. https://doi.org/10.1103/PhysRevMaterials.1.033603.
[114] E. Martínez-Pañeda, V.S. Deshpande, C.F. Niordson, N.A. Fleck, The role of plastic strain gradients in the crack growth resistance of metals, J Mech Phys Solids. 126 (2019) 136–150. https://doi.org/10.1016/j.jmps.2019.02.011.
[115] E. Martínez-Pañeda, C.F. Niordson, R.P. Gangloff, Strain gradient plasticity-based modeling of hydrogen environment assisted cracking, Acta Mater. 117 (2016) 321–332. https://doi.org/10.1016/j.actamat.2016.07.022.
[116] P.K. Kristensen, C.F. Niordson, E. Martínez-Pañeda, A phase field model for elastic-gradient-plastic solids undergoing hydrogen embrittlement, J Mech Phys Solids. 143 (2020) 104093. https://doi.org/10.1016/j.jmps.2020.104093.
[117] A. Tehranchi, W.A. Curtin, The role of atomistic simulations in probing hydrogen effects on plasticity and embrittlement in metals, Eng Fract Mech. 216 (2019)

106502. https://doi.org/10.1016/j.engfracmech.2019.106502.
[118] A. Van der Ven, The thermodynamics of decohesion, Acta Mater. 52 (2004) 1223–1235. https://doi.org/10.1016/j.actamat.2003.11.007.
[119] R. KIRCHHEIM, Reducing grain boundary, dislocation line and vacancy formation energies by solute segregation. I. Theoretical background, Acta Mater. 55 (2007) 5129–5138. https://doi.org/10.1016/j.actamat.2007.05.047.
[120] P. Lejček, M. Šob, V. Paidar, Interfacial segregation and grain boundary embrittlement: An overview and critical assessment of experimental data and calculated results, Prog Mater Sci. 87 (2017) 83–139. https://doi.org/10.1016/j.pmatsci.2016.11.001.
[121] L. Cho, P.E. Bradley, D.S. Lauria, M.J. Connolly, E.J. Seo, K.O. Findley, J.G. Speer, L. Golem, A.J. Slifka, Effects of hydrogen pressure and prior austenite grain size on the hydrogen embrittlement characteristics of a press-hardened martensitic steel, Int J Hydrogen Energy. 46 (2021) 24425–24439. https://doi.org/10.1016/j.ijhydene.2021.05.005.
[122] S. Bechtle, M. Kumar, B.P. Somerday, M.E. Launey, R.O. Ritchie, Grain-boundary engineering markedly reduces susceptibility to intergranular hydrogen embrittlement in metallic materials, Acta Mater. 57 (2009) 4148–4157. https://doi.org/10.1016/j.actamat.2009.05.012.
[123] T. Tsuru, K. Shimizu, M. Yamaguchi, M. Itakura, K. Ebihara, A. Bendo, K. Matsuda, H. Toda, Hydrogen-accelerated spontaneous microcracking in high-strength aluminium alloys, Sci Rep. 10 (2020) 1998. https://doi.org/10.1038/s41598-020-58834-6.
[124] C.D. Beachem, A new model for hydrogen-assisted cracking (hydrogen "embrittlement"), Metallurgical Transactions. 3 (1972) 441–455. https://doi.org/10.1007/BF02642048.
[125] H.K. Birnbaum, P. Sofronis, Hydrogen-enhanced localized plasticity-a mechanism for hydrogen-related fracture.[Ni; NiC], Materials Science and Engineering. A, Structural Materials: Properties, Microstructure and Processing;(Switzerland). 176 (1994).
[126] L. Huang, D. Chen, D. Xie, S. Li, Y. Zhang, T. Zhu, D. Raabe, E. Ma, J. Li, Z. Shan, Quantitative tests revealing hydrogen-enhanced dislocation motion in α-iron, Nat Mater. 22 (2023) 710–716. https://doi.org/10.1038/s41563-023-01537-w.
[127] R. KIRCHHEIM, Reducing grain boundary, dislocation line and vacancy formation energies by solute segregationII. Experimental evidence and consequences, Acta Mater. 55 (2007) 5139–5148. https://doi.org/10.1016/j.actamat.2007.05.033.
[128] A.H. Cottrell, B.A. Bilby, Dislocation Theory of Yielding and Strain Ageing of Iron, Proceedings of the Physical Society. Section A. 62 (1949) 49–62. https://doi.org/10.1088/0370-1298/62/1/308.
[129] I.M. Robertson, The effect of hydrogen on dislocation dynamics, Eng Fract Mech. 68 (2001) 671–692. https://doi.org/10.1016/S0013-7944(01)00011-X.
[130] P.J. Ferreira, I.M. Robertson, H.K. Birnbaum, Hydrogen effects on the interaction between dislocations, Acta Mater. 46 (1998) 1749–1757. https://doi.org/10.1016/S1359-6454(97)00349-2.
[131] A. Pundt, R. Kirchheim, HYDROGEN IN METALS: Microstructural Aspects, Annu Rev Mater Res. 36 (2006) 555–608. https://doi.org/10.1146/annurev.matsci.36.090804.094451.
[132] Q. Liu, Q. Zhou, J. Venezuela, M. Zhang, A. Atrens, Evaluation of the influence of hydrogen on some commercial DP, Q&P and TWIP advanced high-strength steels during automobile service, Eng Fail Anal. 94 (2018) 249–273. https://doi.org/10.1016/j.engfailanal.2018.08.011.

[133] J. Venezuela, T. Hill, Q. Zhou, H. Li, Z. Shi, F. Dong, R. Knibbe, M. Zhang, M.S. Dargusch, A. Atrens, Hydrogen-induced fast fracture in notched 1500 and 1700 MPa class automotive martensitic advanced high-strength steel, Corros Sci. 188 (2021) 109550. https://doi.org/10.1016/j.corsci.2021.109550.
[134] K. Saito, T. Hirade, K. Takai, Hydrogen Desorption Spectra from Excess Vacancy-Type Defects Enhanced by Hydrogen in Tempered Martensitic Steel Showing Quasi-cleavage Fracture, Metallurgical and Materials Transactions A. 50 (2019) 5091–5102. https://doi.org/10.1007/s11661-019-05450-3.
[135] K. SAKAKI, T. KAWASE, M. HIRATO, M. MIZUNO, H. ARAKI, Y. SHIRAI, M. NAGUMO, The effect of hydrogen on vacancy generation in iron by plastic deformation, Scr Mater. 55 (2006) 1031–1034. https://doi.org/10.1016/j.scriptamat.2006.08.030.
[136] A. Oudriss, F. Martin, J. Creus, J. Bouhattate, L. Marchetti, X. Feaugas, Contributions of polarized dislocation walls, internal stresses and vacancies on hydrogen trapping processes in tensile strengthening (100) nickel single crystal, Acta Mater. 245 (2023) 118622. https://doi.org/10.1016/j.actamat.2022.118622.
[137] K.R. Jo, L. Cho, D.H. Sulistiyo, E.J. Seo, S.W. Kim, B.C. De Cooman, Effects of Al-Si coating and Zn coating on the hydrogen uptake and embrittlement of ultra-high strength press-hardened steel, Surf Coat Technol. 374 (2019) 1108–1119. https://doi.org/10.1016/j.surfcoat.2019.06.047.
[138] L. Cho, D.H. Sulistiyo, E.J. Seo, K.R. Jo, S.W. Kim, J.K. Oh, Y.R. Cho, B.C. De Cooman, Hydrogen absorption and embrittlement of ultra-high strength aluminized press hardening steel, Materials Science and Engineering: A. 734 (2018) 416–426. https://doi.org/10.1016/j.msea.2018.08.003.
[139] J. Yoo, S. Kim, M.C. Jo, S. Kim, J. Oh, S.-H. Kim, S. Lee, S.S. Sohn, Effects of Al-Si coating structures on bendability and resistance to hydrogen embrittlement in 1.5-GPa-grade hot-press-forming steel, Acta Mater. 225 (2022) 117561. https://doi.org/10.1016/j.actamat.2021.117561.
[140] K. Mori, P.F. Bariani, B.-A. Behrens, A. Brosius, S. Bruschi, T. Maeno, M. Merklein, J. Yanagimoto, Hot stamping of ultra-high strength steel parts, CIRP Annals. 66 (2017) 755–777. https://doi.org/10.1016/j.cirp.2017.05.007.
[141] L.S. Araujo, L.H. de Almeida, D.S. dos Santos, Hydrogen embrittlement of a hard chromium plated cylinder assembly, Eng Fail Anal. 103 (2019) 259–265. https://doi.org/10.1016/j.engfailanal.2019.04.052.
[142] H. Han, K. Lee, S. Park, S. Park, M. Song, The effect of baking time, fillet radius, and hardness on the lifecycles of pole fastening screws in an electric motor with hydrogen embrittlement, Eng Fail Anal. 48 (2015) 62–77. https://doi.org/10.1016/j.engfailanal.2014.09.008.
[143] S.-H. Yu, A. Lyu, I.-S. Jang, H.S. Park, M. Jang, K.Y. Lee, Y.-K. Lee, Hydrogen absorption, desorption and embrittlement of Zn and ZnNi-electrodeposited bolts, Journal of Materials Research and Technology. 11 (2021) 1604–1610. https://doi.org/10.1016/j.jmrt.2021.02.006.
[144] P. Behera, S.K. Rajagopalan, S. Brahimi, C.A. Venturella, S.P. Gaydos, R.J. Straw, S. Yue, Effect of brush plating process variables on the microstructures of Cd and ZnNi coatings and hydrogen embrittlement, Surf Coat Technol. 417 (2021) 127181. https://doi.org/10.1016/j.surfcoat.2021.127181.
[145] M.J. Carr, M.J. Robinson, The Effects of Zinc Alloy Electroplating on the Hydrogen Embrittlement of High Strength Steels, Transactions of the IMF. 73 (1995) 58–64. https://doi.org/10.1080/00202967.1995.11871060.
[146] S. Laliberté-Riverin, J. Bellemare, F. Sirois, M. Brochu, Internal hydrogen

embrittlement of pre-cracked, cadmium-plated AISI 4340 high strength steel with sustained load tests and incremental step-loading tests, Eng Fract Mech. 223 (2020) 106773. https://doi.org/10.1016/j.engfracmech.2019.106773.
[147] T. An, S. Zhang, M. Feng, B. Luo, S. Zheng, L. Chen, L. Zhang, Synergistic action of hydrogen gas and weld defects on fracture toughness of X80 pipeline steel, Int J Fatigue. 120 (2019) 23–32. https://doi.org/10.1016/j.ijfatigue.2018.10.021.
[148] C. Pandey, M.M. Mahapatra, P. Kumar, N. Saini, Some studies on P91 steel and their weldments, J Alloys Compd. 743 (2018) 332–364. https://doi.org/10.1016/j.jallcom.2018.01.120.
[149] S. Vander Vennet, T. De Seranno, T. Depover, K. Verbeken, Assessment of the hydrogen interaction on the mechanical integrity of a welded martensitic steel, Materials Science and Technology. 37 (2021) 250–257. https://doi.org/10.1080/02670836.2021.1885099.
[150] Y. Chung, Validity of Caltrans' Environmental Hydrogen Embrittlement Tests on Grade BD Anchor Rods in the SAS Span, (2014).
[151] H.-J. Kim, H.-K. Park, C.-W. Lee, B.-G. Yoo, H.-Y. Jung, Baking Effect on Desorption of Diffusible Hydrogen and Hydrogen Embrittlement on Hot-Stamped Boron Martensitic Steel, Metals (Basel). 9 (2019) 636. https://doi.org/10.3390/met9060636.
[152] L. Morsdorf, E. Emelina, B. Gault, M. Herbig, C.C. Tasan, Carbon redistribution in quenched and tempered lath martensite, Acta Mater. 205 (2021) 116521. https://doi.org/10.1016/j.actamat.2020.116521.
[153] G.M. Pressouyre, Trap theory of Hydrogen embrittlement, Acta Metallurgica. 28 (1980) 895–911. https://doi.org/10.1016/0001-6160(80)90106-6.
[154] J. Venezuela, C. Tapia-Bastidas, Q. Zhou, T. Depover, K. Verbeken, E. Gray, Q. Liu, Q. Liu, M. Zhang, A. Atrens, Determination of the equivalent hydrogen fugacity during electrochemical charging of 3.5NiCrMoV steel, Corros Sci. 132 (2018) 90–106. https://doi.org/10.1016/j.corsci.2017.12.018.
[155] J. Venezuela, E. Gray, Q. Liu, Q. Zhou, C. Tapia-Bastidas, M. Zhang, A. Atrens, Equivalent hydrogen fugacity during electrochemical charging of some martensitic advanced high-strength steels, Corros Sci. 127 (2017) 45–58. https://doi.org/10.1016/j.corsci.2017.08.011.
[156] Q. Liu, E. Gray, J. Venezuela, Q. Zhou, C. Tapia-Bastidas, M. Zhang, A. Atrens, Equivalent Hydrogen Fugacity during Electrochemical Charging of 980DP Steel Determined by Thermal Desorption Spectroscopy, Adv Eng Mater. 20 (2018) 1700469. https://doi.org/10.1002/adem.201700469.
[157] K. Kiuchi, R.B. McLellan, The solubility and diffusivity of hydrogen in well-annealed and deformed iron, Acta Metallurgica. 31 (1983) 961–984. https://doi.org/10.1016/0001-6160(83)90192-X.
[158] Y. Long, W. Song, A. Fu, J. Xie, Y. Feng, Z. Bai, C. Yin, Q. Ma, N. Ji, X. Kuang, Combined effect of hydrogen embrittlement and corrosion on the cracking behaviour of C110 low alloy steel in O2-contaminated H2S environment, Corros Sci. 194 (2022) 109926. https://doi.org/10.1016/j.corsci.2021.109926.
[159] L. Briottet, R. Batisse, G. de Dinechin, P. Langlois, L. Thiers, Recommendations on X80 steel for the design of hydrogen gas transmission pipelines, Int J Hydrogen Energy. 37 (2012) 9423–9430. https://doi.org/10.1016/j.ijhydene.2012.02.009.
[160] J.H. Holbrook, H.J. Cialone, E.W. Collings, E.J. Drauglis, P.M. Scott, M.E. Mayfield, Control of hydrogen embrittlement of metals by chemical inhibitors and coatings, in: Gaseous Hydrogen Embrittlement of Materials in Energy Technologies, Elsevier, 2012: pp. 129–153. https://doi.org/10.1533/9780857095374.1.129.

[161] B.P. Somerday, P. Sofronis, eds., International Hydrogen Conference (IHC 2016): Materials Performance in Hydrogen Environments, ASME Press, 2017. https://doi.org/10.1115/1.861387.
[162] A. Staykov, J. Yamabe, B.P. Somerday, Effect of hydrogen gas impurities on the hydrogen dissociation on iron surface, Int J Quantum Chem. 114 (2014) 626–635. https://doi.org/10.1002/qua.24633.
[163] B.P. Somerday, P. Sofronis, K.A. Nibur, C. San Marchi, R. Kirchheim, Elucidating the variables affecting accelerated fatigue crack growth of steels in hydrogen gas with low oxygen concentrations, Acta Mater. 61 (2013) 6153–6170. https://doi.org/10.1016/j.actamat.2013.07.001.
[164] A. Staykov, R. Komoda, M. Kubota, P. Ginet, F. Barbier, J. Furtado, Coadsorption of CO and H2 on an Iron Surface and Its Implication on the Hydrogen Embrittlement of Iron, The Journal of Physical Chemistry C. 123 (2019) 30265–30273. https://doi.org/10.1021/acs.jpcc.9b06927.
[165] S.W. Ooi, P. Yan, R.H. Vegter, Black oxide coating and its effectiveness on prevention of hydrogen uptake, Materials Science and Technology. 35 (2019) 12–25. https://doi.org/10.1080/02670836.2018.1530425.
[166] K.S. Forcey, D.K. Ross, C.H. Wu, The formation of hydrogen permeation barriers on steels by aluminising, Journal of Nuclear Materials. 182 (1991) 36–51. https://doi.org/10.1016/0022-3115(91)90413-2.
[167] D. He, S. Li, X. Liu, C. Zhang, Q. Yu, S. Wang, L. Jiang, Preparation of Cr2O3 film by MOCVD as hydrogen permeation barrier, Fusion Engineering and Design. 89 (2014) 35–39. https://doi.org/10.1016/j.fusengdes.2013.11.005.
[168] F.-D. Duminica, X. Vanden Eynde, M. Mandy, B. Nabi, C. Georges, T. Sturel, P. Drillet, R. Grigorieva, Investigation of PVD thin films as hydrogen barriers in aluminized press hardened steels (PHS), Surf Coat Technol. 397 (2020) 125940. https://doi.org/10.1016/j.surfcoat.2020.125940.
[169] S. Li, D. He, X. Liu, S. Wang, L. Jiang, Deuterium permeation of amorphous alumina coating on 316L prepared by MOCVD, Journal of Nuclear Materials. 420 (2012) 405–408. https://doi.org/10.1016/j.jnucmat.2011.10.040.
[170] M. Li, D.-G. Xie, E. Ma, J. Li, X.-X. Zhang, Z.-W. Shan, Effect of hydrogen on the integrity of aluminium–oxide interface at elevated temperatures, Nat Commun. 8 (2017) 14564. https://doi.org/10.1038/ncomms14564.
[171] X. Li, J. Zhang, M. Ma, X. Song, Effect of shot peening on hydrogen embrittlement of high strength steel, International Journal of Minerals, Metallurgy, and Materials. 23 (2016) 667–675. https://doi.org/10.1007/s12613-016-1279-z.
[172] O. Takakuwa, H. Soyama, Preventing hydrogen embrittlement in stainless steel by means of compressive stress induced by cavitation peening, The Journal of Engineering. 2015 (2015) 106–109. https://doi.org/10.1049/joe.2015.0065.
[173] J. Kim, D. Hall, H. Yan, Y. Shi, S. Joseph, S. Fearn, R.J. Chater, D. Dye, C.C. Tasan, Roughening improves hydrogen embrittlement resistance of Ti-6Al-4V, Acta Mater. 220 (2021) 117304. https://doi.org/10.1016/j.actamat.2021.117304.
[174] C. MARCHI, B. SOMERDAY, S. ROBINSON, Permeability, solubility and diffusivity of hydrogen isotopes in stainless steels at high gas pressures, Int J Hydrogen Energy. 32 (2007) 100–116. https://doi.org/10.1016/j.ijhydene.2006.05.008.
[175] Y. Zhao, J.-M. Park, D.-H. Lee, E.J. Song, J.-Y. Suh, U. Ramamurty, J. Jang, Influences of hydrogen charging method on the hydrogen distribution and nanomechanical properties of face-centered cubic high-entropy alloy: A comparative study, Scr Mater. 168 (2019) 76–80. https://doi.org/10.1016/j.scriptamat.2019.04.025.

[176] Q. Liu, A.D. Atrens, Z. Shi, K. Verbeken, A. Atrens, Determination of the hydrogen fugacity during electrolytic charging of steel, Corros Sci. 87 (2014) 239–258. https://doi.org/10.1016/j.corsci.2014.06.033.
[177] D. Wan, Y. Deng, A. Barnoush, Hydrogen embrittlement effect observed by in-situ hydrogen plasma charging on a ferritic alloy, Scr Mater. 151 (2018) 24–27. https://doi.org/10.1016/j.scriptamat.2018.03.038.
[178] D. Wan, Y. Deng, J.I.H. Meling, A. Alvaro, A. Barnoush, Hydrogen-enhanced fatigue crack growth in a single-edge notched tensile specimen under in-situ hydrogen charging inside an environmental scanning electron microscope, Acta Mater. 170 (2019) 87–99. https://doi.org/10.1016/j.actamat.2019.03.032.
[179] T. Depover, D. Wan, D. Wang, A. Barnoush, K. Verbeken, The effect of hydrogen on the crack initiation site of TRIP-assisted steels during in-situ hydrogen plasma micro-tensile testing: Leading to an improved ductility?, Mater Charact. 167 (2020) 110493. https://doi.org/10.1016/j.matchar.2020.110493.
[180] M. Asadipoor, A. Pourkamali Anaraki, J. Kadkhodapour, S.M.H. Sharifi, A. Barnoush, Macro- and microscale investigations of hydrogen embrittlement in X70 pipeline steel by in-situ and ex-situ hydrogen charging tensile tests and in-situ electrochemical micro-cantilever bending test, Materials Science and Engineering: A. 772 (2020) 138762. https://doi.org/10.1016/j.msea.2019.138762.
[181] H. Suzuki, K. Takai, Summary of round-robin tests for standardizing hydrogen analysis procedures, ISIJ International. 52 (2012) 174–180.
[182] H.E. Kissinger, Reaction Kinetics in Differential Thermal Analysis, Anal Chem. 29 (1957) 1702–1706. https://doi.org/10.1021/ac60131a045.
[183] H. Wipf, ed., Hydrogen in Metals III, Springer Berlin Heidelberg, 1997. https://doi.org/10.1007/BFb0103398.
[184] P.A. Burr, S.T. Murphy, S.C. Lumley, M.R. Wenman, R.W. Grimes, Hydrogen solubility in zirconium intermetallic second phase particles, Journal of Nuclear Materials. 443 (2013) 502–506. https://doi.org/10.1016/j.jnucmat.2013.07.060.
[185] V. Tuli, A. Claisse, P.A. Burr, Hydrogen solubility in Zr–Nb alloys, Scr Mater. 214 (2022) 114652. https://doi.org/10.1016/j.scriptamat.2022.114652.
[186] K. Hirata, S. Iikubo, M. Koyama, K. Tsuzaki, H. Ohtani, First-Principles Study on Hydrogen Diffusivity in BCC, FCC, and HCP Iron, Metallurgical and Materials Transactions A. 49 (2018) 5015–5022. https://doi.org/10.1007/s11661-018-4815-9.
[187] H. Hagi, Y. Hayashi, Effect of Dislocation Trapping on Hydrogen and Deuterium Diffusion in Iron, Transactions of the Japan Institute of Metals. 28 (1987) 368–374. https://doi.org/10.2320/matertrans1960.28.368.
[188] R. Kirchheim, A. Pundt, Hydrogen in Metals, in: Physical Metallurgy, Elsevier, 2014: pp. 2597–2705. https://doi.org/10.1016/B978-0-444-53770-6.00025-3.
[189] Y.-S. Chen, D. Haley, S.S.A. Gerstl, A.J. London, F. Sweeney, R.A. Wepf, W.M. Rainforth, P.A.J. Bagot, M.P. Moody, Direct observation of individual hydrogen atoms at trapping sites in a ferritic steel, Science. 355 (2017) 1196–1199.
[190] J. Takahashi, K. Kawakami, Y. Kobayashi, Origin of hydrogen trapping site in vanadium carbide precipitation strengthening steel, Acta Mater. 153 (2018) 193–204.
[191] G.A. Young, E. Richey, D.S. Morton, Hydrogen embrittlement in nuclear power systems, in: Gaseous Hydrogen Embrittlement of Materials in Energy Technologies, Elsevier, 2012: pp. 149–176. https://doi.org/10.1533/9780857093899.1.149.
[192] R. Fernández-Sousa, C. Betegón, E. Martínez-Pañeda, Analysis of the influence of microstructural traps on hydrogen assisted fatigue, Acta Mater. 199 (2020) 253–263. https://doi.org/10.1016/j.actamat.2020.08.030.
[193] C.P. Flynn, A.M. Stoneham, Quantum Theory of Diffusion with Application to Light

Interstitials in Metals, Phys Rev B. 1 (1970) 3966–3978. https://doi.org/10.1103/PhysRevB.1.3966.
[194] A.M. Stoneham, C.P. Flynn, On the quantum theory of isotope effects in the electromigration and thermomigration of light interstitials, Journal of Physics F: Metal Physics. 3 (1973) 505–512. https://doi.org/10.1088/0305-4608/3/3/008.
[195] A.M. Stoneham, Non- classical diffusion processes, Journal of Nuclear Materials. 69–70 (1978) 109–116. https://doi.org/10.1016/0022-3115(78)90239-8.
[196] H.R. Schober, A.M. Stoneham, Motion of interstitials in metals: Quantum tunneling at low temperatures, Phys Rev B. 26 (1982) 1819–1828. https://doi.org/10.1103/PhysRevB.26.1819.
[197] H. Kimizuka, H. Mori, S. Ogata, Effect of temperature on fast hydrogen diffusion in iron: A path-integral quantum dynamics approach, Phys Rev B. 83 (2011) 094110. https://doi.org/10.1103/PhysRevB.83.094110.
[198] S. Nagase, R. Matsumoto, Volumetric Strain Dependence of Quantum Diffusion of Hydrogen in bcc Iron, ISIJ International. 61 (2021) 1294–1299. https://doi.org/10.2355/isijinternational.ISIJINT-2020-340.
[199] B. Cheng, A.T. Paxton, M. Ceriotti, Hydrogen Diffusion and Trapping in α-Iron: The Role of Quantum and Anharmonic Fluctuations, Phys Rev Lett. 120 (2018) 225901. https://doi.org/10.1103/PhysRevLett.120.225901.
[200] A. Turnbull, Hydrogen diffusion and trapping in metals, in: Gaseous Hydrogen Embrittlement of Materials in Energy Technologies, Elsevier, 2012: pp. 89–128. https://doi.org/10.1533/9780857095374.1.89.
[201] M.J. Shaw, P.R. Briddon, J.P. Goss, M.J. Rayson, A. Kerridge, A.H. Harker, A.M. Stoneham, Erratum: Importance of Quantum Tunneling in Vacancy-Hydrogen Complexes in Diamond [Phys. Rev. Lett. 95, 105502 (2005)], Phys Rev Lett. 95 (2005) 219901. https://doi.org/10.1103/PhysRevLett.95.219901.
[202] A. Kerridge, A.H. Harker, A.M. Stoneham, Quantum behaviour of hydrogen and muonium in vacancy-containing complexes in diamond, Journal of Physics: Condensed Matter. 16 (2004) 8743–8751. https://doi.org/10.1088/0953-8984/16/47/024.
[203] T.E. Markland, M. Ceriotti, Nuclear quantum effects enter the mainstream, Nat Rev Chem. 2 (2018) 0109. https://doi.org/10.1038/s41570-017-0109.
[204] M. Tuckerman, D. Ceperley, Preface: Special Topic on Nuclear Quantum Effects, J Chem Phys. 148 (2018). https://doi.org/10.1063/1.5026714.
[205] J. Svoboda, W. Ecker, V.I. Razumovskiy, G.A. Zickler, F.D. Fischer, Kinetics of interaction of impurity interstitials with dislocations revisited, Prog Mater Sci. 101 (2019) 172–206. https://doi.org/10.1016/j.pmatsci.2018.10.001.
[206] K.T. Møller, T.R. Jensen, E. Akiba, H. Li, Hydrogen-A sustainable energy carrier, Progress in Natural Science: Materials International. 27 (2017) 34–40.
[207] P.A. Redhead, Hydrogen in vacuum systems: An overview, in: AIP Conf Proc, American Institute of Physics, 2003: pp. 243–254.
[208] S.S. Hong, Y.H. Shin, J.T. Kim, Residual gas survey of stainless steel 304 extreme high vacuum chamber with hot cathode ionization gauge, Measurement. 41 (2008) 1026–1031.
[209] M.K. Gupta, A. Priyadarshi, Z. Khan, Hydrogen in stainless steel as killing agent for UHV: A review, Mater Today Proc. 2 (2015) 1074–1081.
[210] G. Sundell, M. Thuvander, H.-O. Andrén, Hydrogen analysis in APT: methods to control adsorption and dissociation of H2, Ultramicroscopy. 132 (2013) 285–289.
[211] F.A. Stevie, C. Zhou, M. Hopstaken, M. Saccomanno, Z. Zhang, A. Turansky, SIMS measurement of hydrogen and deuterium detection limits in silicon: Comparison of

different SIMS instrumentation, Journal of Vacuum Science & Technology B, Nanotechnology and Microelectronics: Materials, Processing, Measurement, and Phenomena. 34 (2016) 03H103.
[212] R. Ishikawa, E. Okunishi, H. Sawada, Y. Kondo, F. Hosokawa, E. Abe, Direct imaging of hydrogen-atom columns in a crystal by annular bright-field electron microscopy, Nat Mater. 10 (2011) 278–281.
[213] Y.-J. Kim, R. Tao, R.F. Klie, D.N. Seidman, Direct atomic-scale imaging of hydrogen and oxygen interstitials in pure niobium using atom-probe tomography and aberration-corrected scanning transmission electron microscopy, ACS Nano. 7 (2013) 732–739.
[214] A. Baldi, T.C. Narayan, A.L. Koh, J.A. Dionne, In situ detection of hydrogen-induced phase transitions in individual palladium nanocrystals, Nat Mater. 13 (2014) 1143–1148.
[215] S. de Graaf, J. Momand, C. Mitterbauer, S. Lazar, B.J. Kooi, Resolving hydrogen atoms at metal-metal hydride interfaces, Sci Adv. 6 (2020) eaay4312.
[216] E.J. Kautz, A. Devaraj, D.J. Senor, S.S. Harilal, Hydrogen isotopic analysis of nuclear reactor materials using ultrafast laser-induced breakdown spectroscopy, Opt Express. 29 (2021) 4936–4946.
[217] E.J. Kautz, E.C.E. Rönnebro, A. Devaraj, D.J. Senor, S.S. Harilal, Detection of hydrogen isotopes in Zircaloy-4 via femtosecond LIBS, J Anal At Spectrom. 36 (2021) 1217–1227.
[218] M. Arif, D.S. Hussey, D.L. Jacobson, Neutron imaging for the hydrogen economy, in: Neutron Imaging and Applications, Springer, 2009: pp. 191–207.
[219] L. Yang, L. He, D. Huang, Y. Wang, Q. Song, L. Zhao, X. Shen, Z. Tian, H. Wang, Three-dimensional hydrogen distribution and quantitative determination of titanium alloys via neutron tomography, Analyst. 145 (2020) 4156–4163.
[220] H.K. Yalçì, D. V Edmonds, Application of the hydrogen microprint and the microautoradiography techniques to a duplex stainless steel, Mater Charact. 34 (1995) 97–104.
[221] K. Ichitani, M. Kanno, S. Kuramoto, Recent development in hydrogen microprint technique and its application to hydrogen embrittlement, ISIJ International. 43 (2003) 496–504.
[222] S. Evers, C. Senöz, M. Rohwerder, Hydrogen detection in metals: a review and introduction of a Kelvin probe approach, Sci Technol Adv Mater. (2013).
[223] M. Koyama, A. Bashir, M. Rohwerder, S. V Merzlikin, E. Akiyama, K. Tsuzaki, D. Raabe, Spatially and kinetically resolved mapping of hydrogen in a twinning-induced plasticity steel by use of scanning Kelvin probe force microscopy, J Electrochem Soc. 162 (2015) C638.
[224] K. Takai, Y. Homma, K. Izutsu, M. Nagumo, Identification of trapping sites in high-strength steels by secondary ion mass spectrometry for thermally desorbed hydrogen, Nippon Kinzoku Gakkaishi/Journal of the Japan Institute of Metals. 60 (1996) 1155–1162.
[225] K. Takai, Y. Chiba, K. Noguchi, A. Nozue, Visualization of the hydrogen desorption process from ferrite, pearlite, and graphite by secondary ion mass spectrometry, Metallurgical and Materials Transactions A. 33 (2002) 2659–2665.
[226] K. Li, J. Liu, C.R.M. Grovenor, K.L. Moore, NanoSIMS imaging and analysis in materials science, Annual Review of Analytical Chemistry. 13 (2020) 273–292.
[227] Y. Aboura, K.L. Moore, NanoSIMS analysis of hydrogen and deuterium in metallic alloys: Artefacts and best practice, Appl Surf Sci. 557 (2021) 149736.
[228] R.K.W. Marceau, Atomic-scale analysis of light alloys using atom probe tomography,

Materials Science and Technology. 32 (2016) 209–219.
[229] B. Gault, A. Chiaramonti, O. Cojocaru-Mirédin, P. Stender, R. Dubosq, C. Freysoldt, S.K. Makineni, T. Li, M. Moody, J.M. Cairney, Atom probe tomography, Nature Reviews Methods Primers. 1 (2021) 1–30.
[230] J. Takahashi, K. Kawakami, Y. Kobayashi, T. Tarui, The first direct observation of hydrogen trapping sites in TiC precipitation-hardening steel through atom probe tomography, Scr Mater. 63 (2010) 261–264.
[231] J. Takahashi, K. Kawakami, T. Tarui, Direct observation of hydrogen-trapping sites in vanadium carbide precipitation steel by atom probe tomography, Scr Mater. 67 (2012) 213–216.
[232] C.R. Weinberger, G.B. Thompson, Review of phase stability in the group IVB and VB transition-metal carbides, Journal of the American Ceramic Society. 101 (2018) 4401–4424.
[233] J. Takahashi, K. Kawakami, Y. Sakiyama, T. Ohmura, Atomic-scale observation of hydrogen trap sites in bainite–austenite dual-phase steel by APT, Mater Charact. 178 (2021) 111282.
[234] X. Zhu, W. Li, T.Y. Hsu, S. Zhou, L. Wang, X. Jin, Improved resistance to hydrogen embrittlement in a high-strength steel by quenching–partitioning–tempering treatment, Scr. Mater. 97 (2015) 21–24.
[235] K. Kawakami, T. Matsumiya, Numerical analysis of hydrogen trap state by TiC and V4C3 in bcc-Fe, ISIJ International. 52 (2012) 1693–1697.
[236] D. Di Stefano, R. Nazarov, T. Hickel, J. Neugebauer, M. Mrovec, C. Elsässer, First-principles investigation of hydrogen interaction with TiC precipitates in α-Fe, Phys Rev B. 93 (2016) 184108.
[237] R. Salehin, G.B. Thompson, C.R. Weinberger, Hydrogen trapping and storage in the group IVB-VIB transition metal carbides, Mater Des. 214 (2022) 110399.
[238] X. Zhu, W. Li, H. Zhao, L. Wang, X. Jin, Hydrogen trapping sites and hydrogen-induced cracking in high strength quenching & partitioning (Q&P) treated steel, Int J Hydrogen Energy. 39 (2014) 13031–13040.
[239] Y.H. Fan, B. Zhang, H.L. Yi, G.S. Hao, Y.Y. Sun, J.Q. Wang, E.-H. Han, W. Ke, The role of reversed austenite in hydrogen embrittlement fracture of S41500 martensitic stainless steel, Acta Mater. 139 (2017) 188–195.
[240] D.E. Jiang, E.A. Carter, Diffusion of interstitial hydrogen into and through bcc Fe from first principles, Phys Rev B. 70 (2004) 064102. https://doi.org/10.1103/PhysRevB.70.064102.
[241] Y. Tateyama, T. Ohno, Stability and clusterization of hydrogen-vacancy complexes in α−Fe: An ab initio study, Phys Rev B. 67 (2003) 174105. https://doi.org/10.1103/PhysRevB.67.174105.
[242] K. Ohsawa, K. Eguchi, H. Watanabe, M. Yamaguchi, M. Yagi, Configuration and binding energy of multiple hydrogen atoms trapped in monovacancy in bcc transition metals, Phys Rev B. 85 (2012) 094102. https://doi.org/10.1103/PhysRevB.85.094102.
[243] Y.-W. You, X.-S. Kong, X.-B. Wu, Y.-C. Xu, Q.F. Fang, J.L. Chen, G.-N. Luo, C.S. Liu, B.C. Pan, Z. Wang, Dissolving, trapping and detrapping mechanisms of hydrogen in bcc and fcc transition metals, AIP Adv. 3 (2013). https://doi.org/10.1063/1.4789547.
[244] M.L. Fullarton, R.E. Voskoboinikov, S.C. Middleburgh, Hydrogen accommodation in -iron and nickel, J Alloys Compd. 587 (2014) 794–799. https://doi.org/10.1016/j.jallcom.2013.10.169.
[245] P. Zhang, J. Zhao, B. Wen, Vacancy trapping mechanism for multiple hydrogen and helium in beryllium: a first-principles study, Journal of Physics: Condensed Matter.

24 (2012) 095004. https://doi.org/10.1088/0953-8984/24/9/095004.
[246] P. Nordlander, J.K. Norskov, F. Besenbacher, Trends in hydrogen heats of solution and vacancy trapping energies in transition metals, Journal of Physics F: Metal Physics. 16 (1986) 1161–1171. https://doi.org/10.1088/0305-4608/16/9/007.
[247] W.A. Counts, C. Wolverton, R. Gibala, First-principles energetics of hydrogen traps in α-Fe: Point defects, Acta Mater. 58 (2010) 4730–4741. https://doi.org/10.1016/j.actamat.2010.05.010.
[248] A.J. Samin, D.A. Andersson, E.F. Holby, B.P. Uberuaga, First-principles localized cluster expansion study of the kinetics of hydrogen diffusion in homogeneous and heterogeneous Fe-Cr alloys, Phys Rev B. 99 (2019) 014110. https://doi.org/10.1103/PhysRevB.99.014110.
[249] Y.A. Du, L. Ismer, J. Rogal, T. Hickel, J. Neugebauer, R. Drautz, First-principles study on the interaction of H interstitials with grain boundaries in α- and γ -Fe, Phys Rev B. 84 (2011) 144121. https://doi.org/10.1103/PhysRevB.84.144121.
[250] X. Zhou, D. Marchand, D.L. McDowell, T. Zhu, J. Song, Chemomechanical Origin of Hydrogen Trapping at Grain Boundaries in fcc Metals, Phys Rev Lett. 116 (2016) 075502. https://doi.org/10.1103/PhysRevLett.116.075502.
[251] H. Momida, Y. Asari, Y. Nakamura, Y. Tateyama, T. Ohno, Hydrogen-enhanced vacancy embrittlement of grain boundaries in iron, Phys Rev B. 88 (2013) 144107. https://doi.org/10.1103/PhysRevB.88.144107.
[252] S. Echeverri Restrepo, D. Di Stefano, M. Mrovec, A.T. Paxton, Density functional theory calculations of iron - vanadium carbide interfaces and the effect of hydrogen, Int J Hydrogen Energy. 45 (2020) 2382–2389. https://doi.org/10.1016/j.ijhydene.2019.11.102.
[253] K. Kawakami, T. Matsumiya, Ab-initio Investigation of Hydrogen Trap State by Cementite in bcc-Fe, ISIJ International. 53 (2013) 709–713. https://doi.org/10.2355/isijinternational.53.709.
[254] D. Di Stefano, M. Mrovec, C. Elsässer, First-principles investigation of hydrogen trapping and diffusion at grain boundaries in nickel, Acta Mater. 98 (2015) 306–312. https://doi.org/10.1016/j.actamat.2015.07.031.
[255] R. Shi, Y. Ma, Z. Wang, L. Gao, X.-S. Yang, L. Qiao, X. Pang, Atomic-scale investigation of deep hydrogen trapping in NbC/α-Fe semi-coherent interfaces, Acta Mater. 200 (2020) 686–698. https://doi.org/10.1016/j.actamat.2020.09.031.
[256] Y. Ma, Y. Shi, H. Wang, Z. Mi, Z. Liu, L. Gao, Y. Yan, Y. Su, L. Qiao, A first-principles study on the hydrogen trap characteristics of coherent nano-precipitates in α-Fe, Int J Hydrogen Energy. 45 (2020) 27941–27949. https://doi.org/10.1016/j.ijhydene.2020.07.123.
[257] C. Jones, V. Tuli, Z. Shah, M. Gass, P.A. Burr, M. Preuss, K.L. Moore, Evidence of hydrogen trapping at second phase particles in zirconium alloys, Sci Rep. 11 (2021) 4370. https://doi.org/10.1038/s41598-021-83859-w.
[258] P.A. Burr, S.T. Murphy, S.C. Lumley, M.R. Wenman, R.W. Grimes, Hydrogen accommodation in Zr second phase particles: Implications for H pick-up and hydriding of Zircaloy-2 and Zircaloy-4, Corros Sci. 69 (2013) 1–4. https://doi.org/10.1016/j.corsci.2012.11.036.
[259] B. Zhang, J. Su, M. Wang, Z. Liu, Z. Yang, M. Militzer, H. Chen, Atomistic insight into hydrogen trapping at MC/BCC-Fe phase boundaries: The role of local atomic environment, Acta Mater. 208 (2021) 116744. https://doi.org/10.1016/j.actamat.2021.116744.
[260] A. Sadoc, E.H. Majzoub, V.T. Huett, K.F. Kelton, Local structure in hydrogenated Ti–Zr–Ni quasicrystals and approximants, J Alloys Compd. 356–357 (2003) 96–99.

https://doi.org/10.1016/S0925-8388(02)01218-5.
[261] J. Radaković, K. Batalović, I. Mađarević, J. Belošević-Čavor, Interstitial hydrogen in Laves phases – local electronic structure modifications from first-principles, RSC Adv. 4 (2014) 54769–54774. https://doi.org/10.1039/C4RA09082A.
[262] S.B. Gesari, M.E. Pronsato, A. Visintin, A. Juan, Hydrogen Storage in AB2 Laves Phase (A = Zr, Ti; B = Ni, Mn, Cr, V): Binding Energy and Electronic Structure, The Journal of Physical Chemistry C. 114 (2010) 16832–16836. https://doi.org/10.1021/jp106036v.
[263] E.L. Simpson, A.T. Paxton, Effect of applied strain on the interaction between hydrogen atoms and 1 2 ⟨ 111 ⟩ screw dislocations in α-iron, Int J Hydrogen Energy. 45 (2020) 20069–20079. https://doi.org/10.1016/j.ijhydene.2020.05.050.
[264] S.R. Phillpot, A.C. Antony, L. Shi, M.L. Fullarton, T. Liang, S.B. Sinnott, Y. Zhang, S.B. Biner, Charge Optimized Many Body (COMB) potentials for simulation of nuclear fuel and clad, Comput Mater Sci. 148 (2018) 231–241. https://doi.org/10.1016/j.commatsci.2018.02.041.
[265] T.P. Senftle, S. Hong, M.M. Islam, S.B. Kylasa, Y. Zheng, Y.K. Shin, C. Junkermeier, R. Engel-Herbert, M.J. Janik, H.M. Aktulga, T. Verstraelen, A. Grama, A.C.T. van Duin, The ReaxFF reactive force-field: development, applications and future directions, NPJ Comput Mater. 2 (2016) 15011. https://doi.org/10.1038/npjcompumats.2015.11.
[266] T. Zubatiuk, O. Isayev, Development of Multimodal Machine Learning Potentials: Toward a Physics-Aware Artificial Intelligence, Acc Chem Res. 54 (2021) 1575–1585. https://doi.org/10.1021/acs.accounts.0c00868.
[267] J. Behler, Perspective: Machine learning potentials for atomistic simulations, J Chem Phys. 145 (2016). https://doi.org/10.1063/1.4966192.
[268] Y. Mishin, Machine-learning interatomic potentials for materials science, Acta Mater. 214 (2021) 116980. https://doi.org/10.1016/j.actamat.2021.116980.
[269] H. Lin, D.G. Truhlar, QM/MM: what have we learned, where are we, and where do we go from here?, Theor Chem Acc. 117 (2007) 185. https://doi.org/10.1007/s00214-006-0143-z.
[270] Y. Zhao, G. Lu, QM/MM study of dislocation—hydrogen/helium interactions in α-Fe, Model Simul Mat Sci Eng. 19 (2011) 065004. https://doi.org/10.1088/0965-0393/19/6/065004.
[271] D. Marx, M. Parrinello, Ab initio path-integral molecular dynamics, Zeitschrift F�r Physik B Condensed Matter. 95 (1994) 143–144. https://doi.org/10.1007/BF01312185.
[272] D. Marx, M. Parrinello, Ab initio path integral molecular dynamics: Basic ideas, J Chem Phys. 104 (1996) 4077–4082. https://doi.org/10.1063/1.471221.
[273] M. Ceriotti, G. Bussi, M. Parrinello, Nuclear Quantum Effects in Solids Using a Colored-Noise Thermostat, Phys Rev Lett. 103 (2009) 030603. https://doi.org/10.1103/PhysRevLett.103.030603.
[274] M. Ceriotti, D.E. Manolopoulos, M. Parrinello, Accelerating the convergence of path integral dynamics with a generalized Langevin equation, J Chem Phys. 134 (2011). https://doi.org/10.1063/1.3556661.
[275] M. Ceriotti, D.E. Manolopoulos, Efficient First-Principles Calculation of the Quantum Kinetic Energy and Momentum Distribution of Nuclei, Phys Rev Lett. 109 (2012) 100604. https://doi.org/10.1103/PhysRevLett.109.100604.
[276] S. Habershon, D.E. Manolopoulos, T.E. Markland, T.F. Miller, Ring-Polymer Molecular Dynamics: Quantum Effects in Chemical Dynamics from Classical Trajectories in an Extended Phase Space, Annu Rev Phys Chem. 64 (2013) 387–413.

https://doi.org/10.1146/annurev-physchem-040412-110122.
[277] M. Ceriotti, J. More, D.E. Manolopoulos, i-PI: A Python interface for ab initio path integral molecular dynamics simulations, Comput Phys Commun. 185 (2014) 1019–1026. https://doi.org/10.1016/j.cpc.2013.10.027.
[278] H.Y. Geng, Accelerating ab initio path integral molecular dynamics with multilevel sampling of potential surface, J Comput Phys. 283 (2015) 299–311. https://doi.org/10.1016/j.jcp.2014.12.007.
[279] A.T. Paxton, I.H. Katzarov, Quantum and isotope effects on hydrogen diffusion, trapping and escape in iron, Acta Mater. 103 (2016) 71–76. https://doi.org/10.1016/j.actamat.2015.09.054.
[280] M.J.W. Hall, D.-A. Deckert, H.M. Wiseman, Quantum Phenomena Modeled by Interactions between Many Classical Worlds, Phys Rev X. 4 (2014) 041013. https://doi.org/10.1103/PhysRevX.4.041013.
[281] S. Sturniolo, Computational applications of the many-interacting-worlds interpretation of quantum mechanics, Phys Rev E. 97 (2018) 053311. https://doi.org/10.1103/PhysRevE.97.053311.
[282] M. Nagano, Y. Hayashi, N. Ohtani, M. Isshiki, K. Igaki, Hydrogen diffusivity in high purity alpha iron, Scripta Metallurgica. 16 (1982) 973–976. https://doi.org/10.1016/0036-9748(82)90136-3.
[283] B. Gault, M.P. Moody, J.M. Cairney, S.P. Ringer, Atom probe microscopy, Springer Science & Business Media, 2012.
[284] D.J. Larson, T.J. Prosa, R.M. Ulfig, B.P. Geiser, T.F. Kelly, Local electrode atom probe tomography, New York, US: Springer Science. 2 (2013).
[285] G.L. Kellogg, T.T. Tsong, Pulsed-laser atom-probe field-ion microscopy, J Appl Phys. 51 (1980) 1184–1193.
[286] P. Felfer, B. Ott, M. Monajem, V. Dalbauer, M. Heller, J. Josten, C. Macaulay, An Atom Probe with Ultra-Low Hydrogen Background, Microscopy and Microanalysis. (2021) 1–9.
[287] G.L. Kellogg, Pulsed laser stimulated field desorption of hydrogen from molybdenum, J Chem Phys. 74 (1981) 1479–1487.
[288] R.P. Kolli, Controlling residual hydrogen gas in mass spectra during pulsed laser atom probe tomography, Adv Struct Chem Imaging. 3 (2017) 1–10.
[289] S. Chen, R. Murakami, K. Araki, M. Owari, Quantitative Analysis of Residual Hydrogen on Platinum Surface by Atom Probe, E-Journal of Surface Science and Nanotechnology. 18 (2020) 127–132.
[290] S.-H. Yoo, S.-H. Kim, E. Woods, B. Gault, M. Todorova, J. Neugebauer, Origins of the hydrogen signal in atom probe tomography: case studies of alkali and noble metals, New J Phys. 24 (2022) 013008.
[291] K. Wu, X. Lu, P. Zhou, W. Li, X. Jin, Improved resistance to hydrogen embrittlement by tailoring the stability of retained austenite, Materials Science and Technology. 33 (2017) 1497–1504.
[292] Y.-S. Chen, P.A.J. Bagot, M.P. Moody, D. Haley, Observing hydrogen in steel using cryogenic atom probe tomography: A simplified approach, Int J Hydrogen Energy. 44 (2019) 32280–32291.
[293] F. Yan, I. Mouton, L.T. Stephenson, A.J. Breen, Y. Chang, D. Ponge, D. Raabe, B. Gault, Atomic-scale investigation of hydrogen distribution in a TiMo alloy, Scr Mater. 162 (2019) 321–325.
[294] A.J. Breen, L.T. Stephenson, B. Sun, Y. Li, O. Kasian, D. Raabe, M. Herbig, B. Gault, Solute hydrogen and deuterium observed at the near atomic scale in high-strength steel, Acta Mater. 188 (2020) 108–120.

[295] M.S. Meier, M.E. Jones, P.J. Felfer, M.P. Moody, D. Haley, Extending estimating hydrogen content in atom probe tomography experiments where H2 molecule formation occurs, Microscopy and Microanalysis. (2021) 1–14.
[296] M.E. Jones, A.J. London, A.J. Breen, P.D. Styman, S. Sikotra, M.P. Moody, D. Haley, Improving the quantification of deuterium in zirconium alloy atom probe tomography data using existing analysis methods, Microscopy and Microanalysis. (2021) 1–10.
[297] D.R. Kingham, The post-ionization of field evaporated ions: A theoretical explanation of multiple charge states, Surf Sci. 116 (1982) 273–301.
[298] T.T. Tsong, T.J. Kinkus, C.F. Ai, Field induced and surface catalyzed formation of novel ions: A pulsed-laser time-of-flight atom-probe study, J Chem Phys. 78 (1983) 4763–4775.
[299] Y.-J. Kim, D.N. Seidman, Atom-probe tomographic analyses of hydrogen interstitial atoms in ultrahigh purity niobium, Microscopy and Microanalysis. 21 (2015) 535–543.
[300] Y.H. Chang, I. Mouton, L. Stephenson, M. Ashton, G.K. Zhang, A. Szczpaniak, W.J. Lu, D. Ponge, D. Raabe, B. Gault, Quantification of solute deuterium in titanium deuteride by atom probe tomography with both laser pulsing and high-voltage pulsing: Influence of the surface electric field, New J Phys. 21 (2019) 053025.
[301] Y. Chang, W. Lu, J. Guénolé, L.T. Stephenson, A. Szczpaniak, P. Kontis, A.K. Ackerman, F.F. Dear, I. Mouton, X. Zhong, Ti and its alloys as examples of cryogenic focused ion beam milling of environmentally-sensitive materials, Nat Commun. 10 (2019) 1–10.
[302] I. Mouton, A.J. Breen, S. Wang, Y. Chang, A. Szczepaniak, P. Kontis, L.T. Stephenson, D. Raabe, M. Herbig, T. Ben Britton, Quantification challenges for atom probe tomography of hydrogen and deuterium in Zircaloy-4, Microscopy and Microanalysis. 25 (2019) 481–488.
[303] A.J. Breen, I. Mouton, W. Lu, S. Wang, A. Szczepaniak, P. Kontis, L.T. Stephenson, Y. Chang, A.K. da Silva, C.H. Liebscher, Atomic scale analysis of grain boundary deuteride growth front in Zircaloy-4, Scr Mater. 156 (2018) 42–46.
[304] K.G. McLennan, E.M. Gray, An equation of state for deuterium gas to 1000 bar, Meas Sci Technol. 15 (2003) 211.
[305] A. Devaraj, B. Matthews, B. Arey, L. Bagaasen, E. Buck, G. Sevigny, D. Senor, Neutron irradiation induced changes in isotopic abundance of 6Li and 3D nanoscale distribution of tritium in LiAlO2 pellets analyzed by atom probe tomography, Mater Charact. 176 (2021) 111095.
[306] Y. Chang, A.J. Breen, Z. Tarzimoghadam, P. Kürnsteiner, H. Gardner, A. Ackerman, A. Radecka, P.A.J. Bagot, W. Lu, T. Li, Characterizing solute hydrogen and hydrides in pure and alloyed titanium at the atomic scale, Acta Mater. 150 (2018) 273–280.
[307] J.A. Spitznagel, S.S. Brenner, M.K. Miller, W.J. Choyke, Deuterium and helium trapping at TiC particles in ferritic steel, Journal of Nuclear Materials. 122 (1984) 252–253.
[308] H. Takamizawa, K. Hoshi, Y. Shimizu, F. Yano, K. Inoue, S. Nagata, T. Shikama, Y. Nagai, Three-dimensional characterization of deuterium implanted in silicon using atom probe tomography, Applied Physics Express. 6 (2013) 066602.
[309] G. Sundell, M. Thuvander, A.K. Yatim, H. Nordin, H.-O. Andrén, Direct observation of hydrogen and deuterium in oxide grain boundaries in corroded Zirconium alloys, Corros Sci. 90 (2015) 1–4.
[310] P. Kesten, A. Pundt, G. Schmitz, M. Weisheit, H.U. Krebs, R. Kirchheim, H-and D distribution in metallic multilayers studied by 3-dimensional atom probe analysis and

secondary ion mass spectrometry, J Alloys Compd. 330 (2002) 225–228.
[311] R. Gemma, T. Al-Kassab, R. Kirchheim, A. Pundt, Studies on hydrogen loaded V–Fe8 at% films on Al2O3 substrate, J Alloys Compd. 446 (2007) 534–538.
[312] R. Gemma, T. Al-Kassab, R. Kirchheim, A. Pundt, APT analyses of deuterium-loaded Fe/V multi-layered films, Ultramicroscopy. 109 (2009) 631–636.
[313] R. Gemma, T. Al-Kassab, R. Kirchheim, A. Pundt, Visualization of deuterium dead layer by atom probe tomography, Scr Mater. 67 (2012) 903–906.
[314] D. Haley, I. McCarroll, P.A.J. Bagot, J.M. Cairney, M.P. Moody, A gas-phase reaction cell for modern atom probe systems, Microscopy and Microanalysis. 25 (2019) 410–417.
[315] H. Khanchandani, A.A. El-Zoka, S.-H. Kim, U. Tezins, D. Vogel, A. Sturm, D. Raabe, B. Gault, L.T. Stephenson, Laser-equipped gas reaction chamber for probing environmentally sensitive materials at near atomic scale, PLoS One. 17 (2022) e0262543.
[316] I. Mouton, Y. Chang, P. Chakraborty, S. Wang, L.T. Stephenson, T. Ben Britton, B. Gault, Hydride growth mechanism in zircaloy-4: Investigation of the partitioning of alloying elements, Materialia (Oxf). 15 (2021) 101006.
[317] H. Zhao, P. Chakraborty, D. Ponge, T. Hickel, B. Sun, C.-H. Wu, B. Gault, D. Raabe, Hydrogen trapping and embrittlement in high-strength Al alloys, Nature. 602 (2022) 437–441.
[318] Y.-S. Chen, M.J. Griffith, J.M. Cairney, Cryo atom probe: Freezing atoms in place for 3D mapping, Nano Today. 37 (2021) 101107.
[319] D.E. Perea, S.S.A. Gerstl, J. Chin, B. Hirschi, J. Evans, An environmental transfer hub for multimodal atom probe tomography, Adv Struct Chem Imaging. 3 (2017) 1–6.
[320] K. Thompson, D. Lawrence, D.J. Larson, J.D. Olson, T.F. Kelly, B. Gorman, In situ site-specific specimen preparation for atom probe tomography, Ultramicroscopy. 107 (2007) 131–139.
[321] D.E. Perea, J. Liu, J. Bartrand, Q. Dicken, S.T. Thevuthasan, N.D. Browning, J.E. Evans, Atom probe tomographic mapping directly reveals the atomic distribution of phosphorus in resin embedded ferritin, Sci Rep. 6 (2016) 1–9.
[322] D.K. Schreiber, D.E. Perea, J. V Ryan, J.E. Evans, J.D. Vienna, A method for site-specific and cryogenic specimen fabrication of liquid/solid interfaces for atom probe tomography, Ultramicroscopy. 194 (2018) 89–99.
[323] A.A. El-Zoka, S.-H. Kim, S. Deville, R.C. Newman, L.T. Stephenson, B. Gault, Enabling near-atomic–scale analysis of frozen water, Sci Adv. 6 (2020) eabd6324.
[324] I.E. McCarroll, P.A.J. Bagot, A. Devaraj, D.E. Perea, J.M. Cairney, New frontiers in atom probe tomography: a review of research enabled by cryo and/or vacuum transfer systems, Mater Today Adv. 7 (2020) 100090.
[325] T.M. Schwarz, E.M. Weikum, K. Meng, E. Hadjixenophontos, C.A. Dietrich, J. Kästner, P. Stender, G. Schmitz, Field evaporation and atom probe tomography of pure water tips, Sci Rep. 10 (2020) 1–14.
[326] C. Macauley, M. Heller, A. Rausch, F. Kümmel, P. Felfer, A versatile cryo-transfer system, connecting cryogenic focused ion beam sample preparation to atom probe microscopy, PLoS One. 16 (2021) e0245555.
[327] L.T. Stephenson, A. Szczepaniak, I. Mouton, K.A.K. Rusitzka, A.J. Breen, U. Tezins, A. Sturm, D. Vogel, Y. Chang, P. Kontis, The Laplace Project: An integrated suite for preparing and transferring atom probe samples under cryogenic and UHV conditions, PLoS One. 13 (2018) e0209211.

Appendix

Supplementary Information for

Chapter 3 - Engineering metal-carbide hydrogen traps in steels

Pang-Yu Liu[1,2,+], Boning Zhang[3,4,+], Ranming Niu[1,2,+], Shao-Lun Lu[1,5], Chao Huang[1,2], Maoqiu Wang[6], Fuyang Tian[7], Yong Mao[4], Tong Li[8], Patrick A. Burr[9], Hongzhou Lu[10], Aimin Guo[10], Hung-Wei Yen[5,11], Julie M. Cairney[1,2,*], Hao Chen[3,*], Yi-Sheng Chen[1,2,5,*]

[+] The authors contribute equally to this work.

[*] Corresponding authors: Yi-Sheng Chen (yi-sheng.chen@sydney.edu.au); Hao Chen (hao.chen@mail.tsinghua.edu.cn); Julie Cairney (julie.cairney@sydney.edu.au)

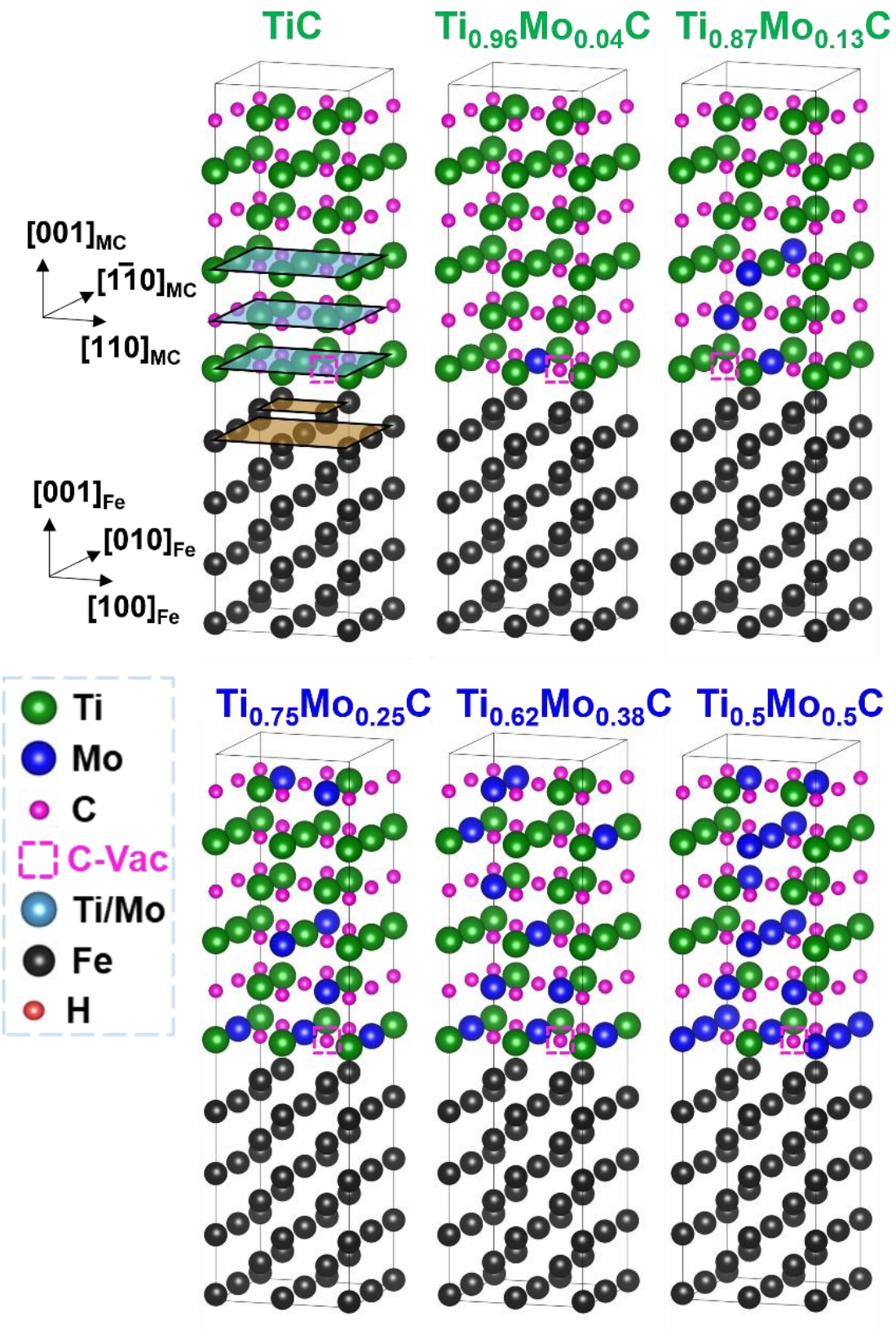

Supplementary Figure 1. Illustrations of the coherent interface models with different compositions of MC.

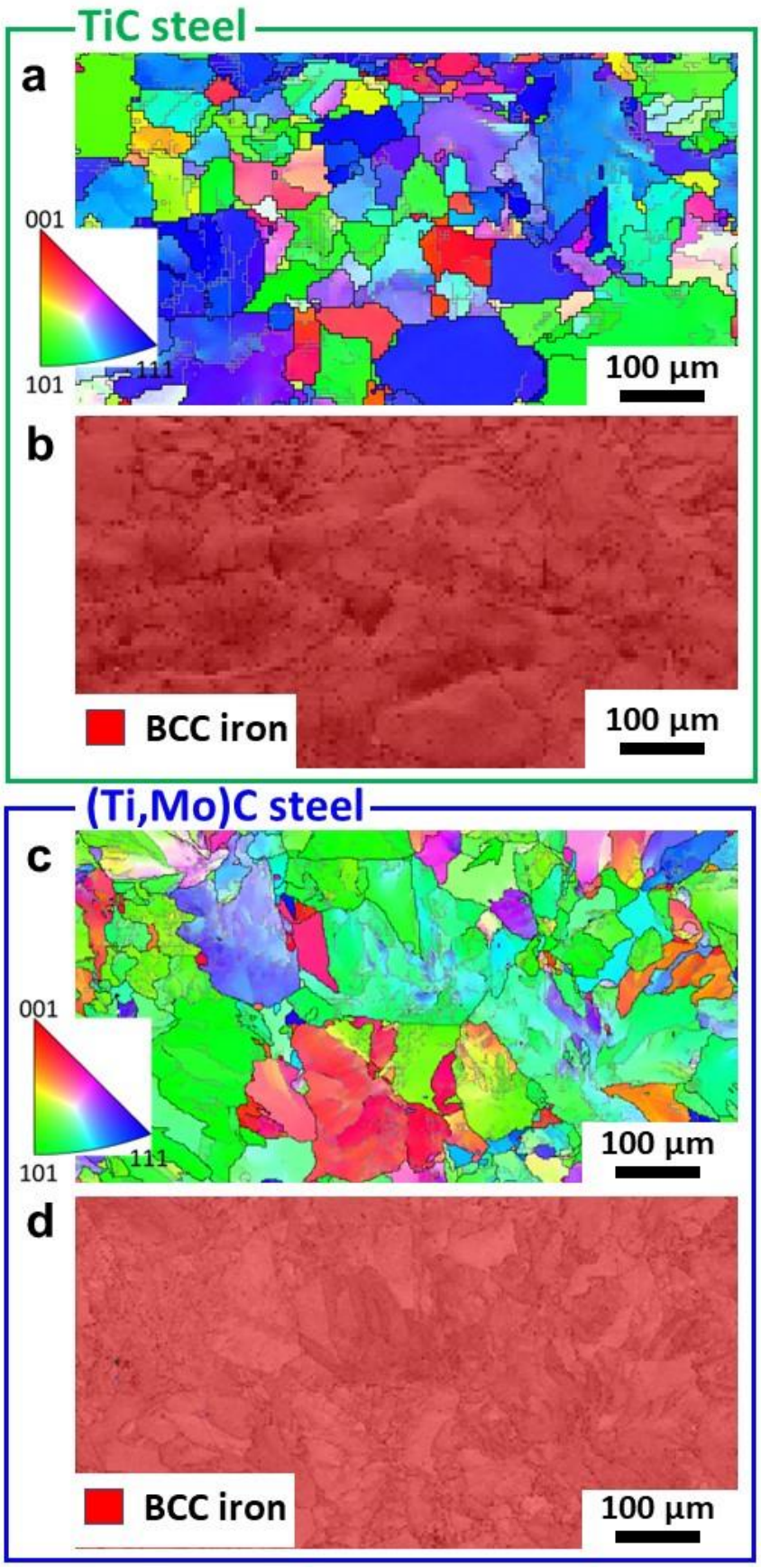

Supplementary Figure 2. SEM-EBSD analyses of (a) TiC steel (grain size: 195 µm) and (b) (Ti,Mo)C steel (grain size: 140 µm).

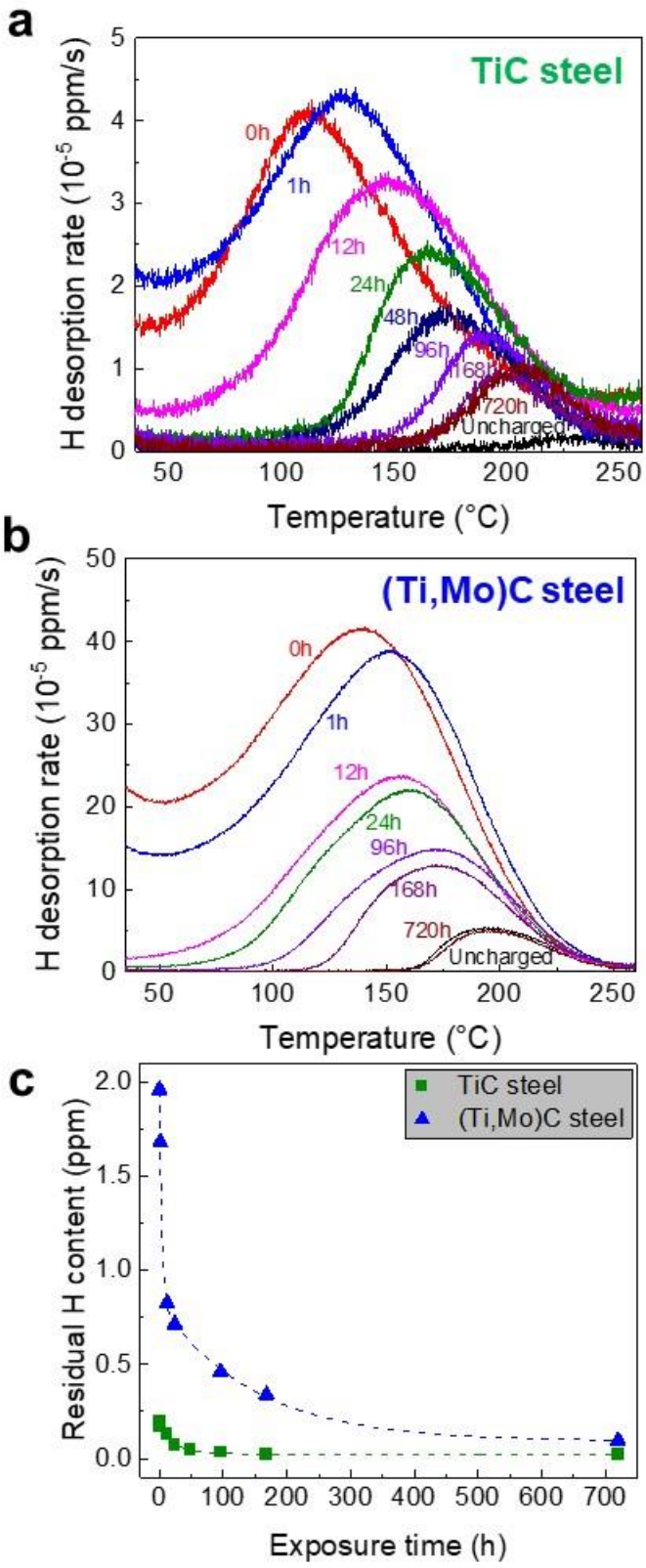

Supplementary Figure 3. TDS data for uncharged samples and hydrogen-charged samples with various desorption durations. (a) TiC steel. (b) (Ti,Mo)C steel. (c) The residual H content determined from desorption below 260 ℃ against the desorption duration after hydrogen charging

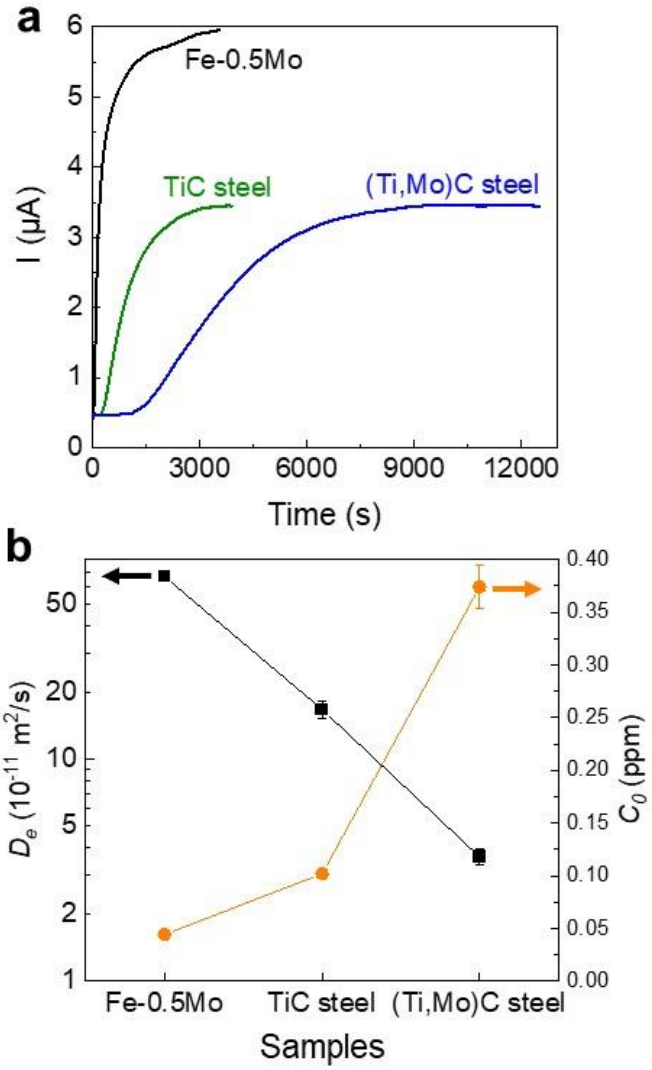

Supplementary Figure 4. Hydrogen permeation tests of the model interphase-precipitate steels in comparison with and the precipitate-free Fe-0.5Mo ferritic steel. (a) Permeation curves showing the current density I as a function of time and the retarded permeability of (Ti,Mo)C steel as compared to other samples. (b) The effective H diffusion coefficient, D_e, and the sub-surface hydrogen concentration, C_0, at the entry side of different samples.

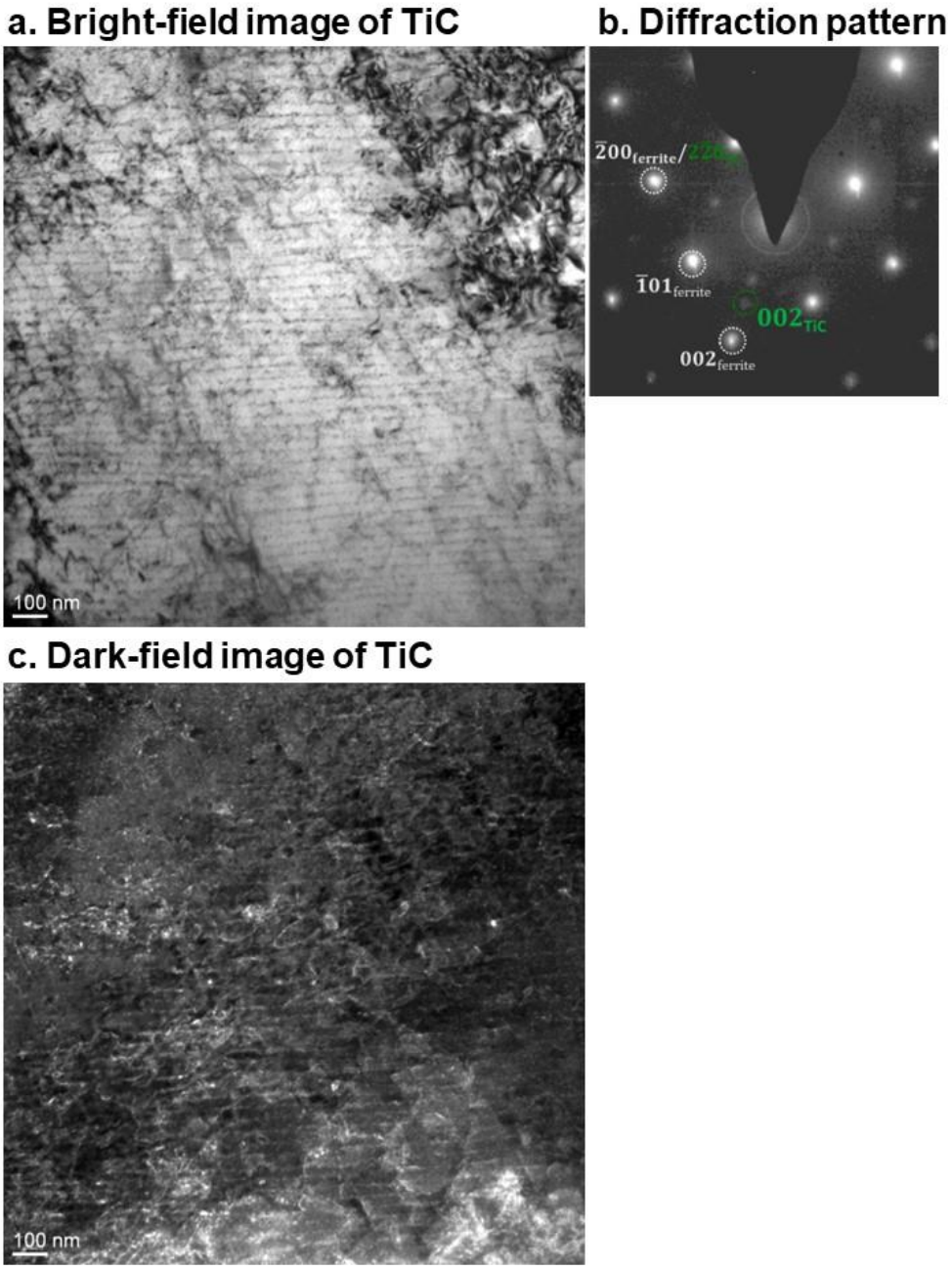

Supplementary Figure 5. TEM analysis of TiC. (a) bright-field image, (b) diffraction patterns, and (c) dark-field image using the (002) of TiC.

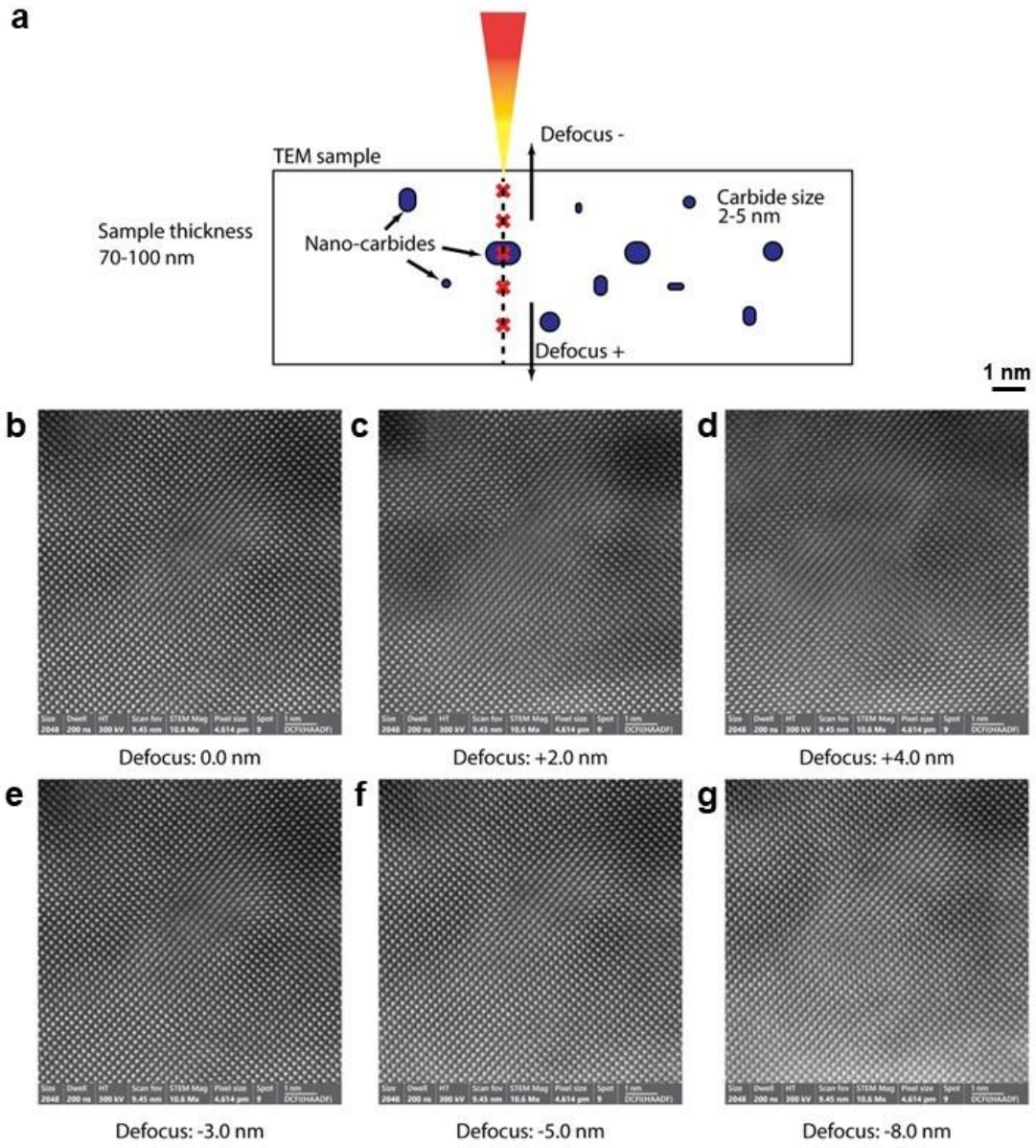

Supplementary Figure 6. Imaging condition for observing nanosized carbides using atomic-resolution STEM. (a) Schematic illustration showing the small MCs (2-5 nm) embedded in a STEM lift-out sample that is usually around 70-100 nm thick. The atomic structure of MCs can therefore overlap with the ferrite matrix. (b)-(g) shows the STEM images at various focal planes in the samples. (b) is in-focus, where the carbide atom column can be seen. Whereas (c) and (d) are over-focused and (e), (f), and (g) are under focused, where the atomic structures relating to the carbides are not visible.

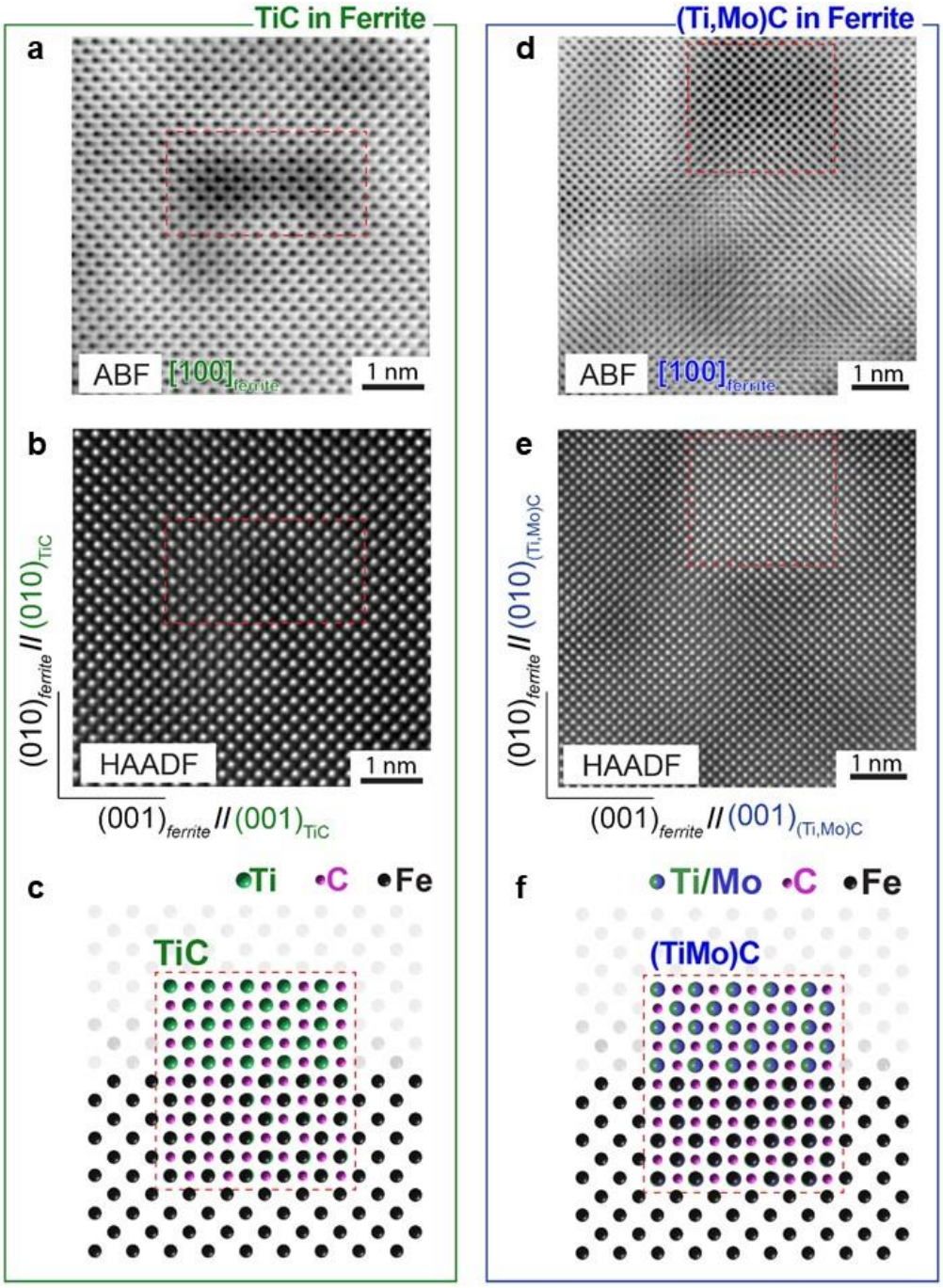

Supplementary Figure 7. Additional atomic-resolution STEM images showing the carbides along [100]$_{ferrite}$ zone axis, corresponding to Fig. 3. (a)-(c) are from the TiC steel, and (d)-(f) are from the (Ti,Mo)C steel. (a) and (d) are ABF-STEM images, showing the atomic columns in the carbides fully coincide with the ferrite lattice along this zone axis. (b) and (e) are the corresponding high-angle annular dark-field (HAADF) STEM images. The red squares highlight that the light Ti atoms in the TiC are slightly darker than the Fe atoms in the ferrite matrix, whereas the heavy Mo atoms are brighter than the Fe atoms, due to their difference in atomic mass. (c) and (f) are corresponding atomic models illustrating the atomic structure under observation, showing the simulated structure of the carbides (colored spheres) embedded in the BCC ferrite matrix (black spheres).

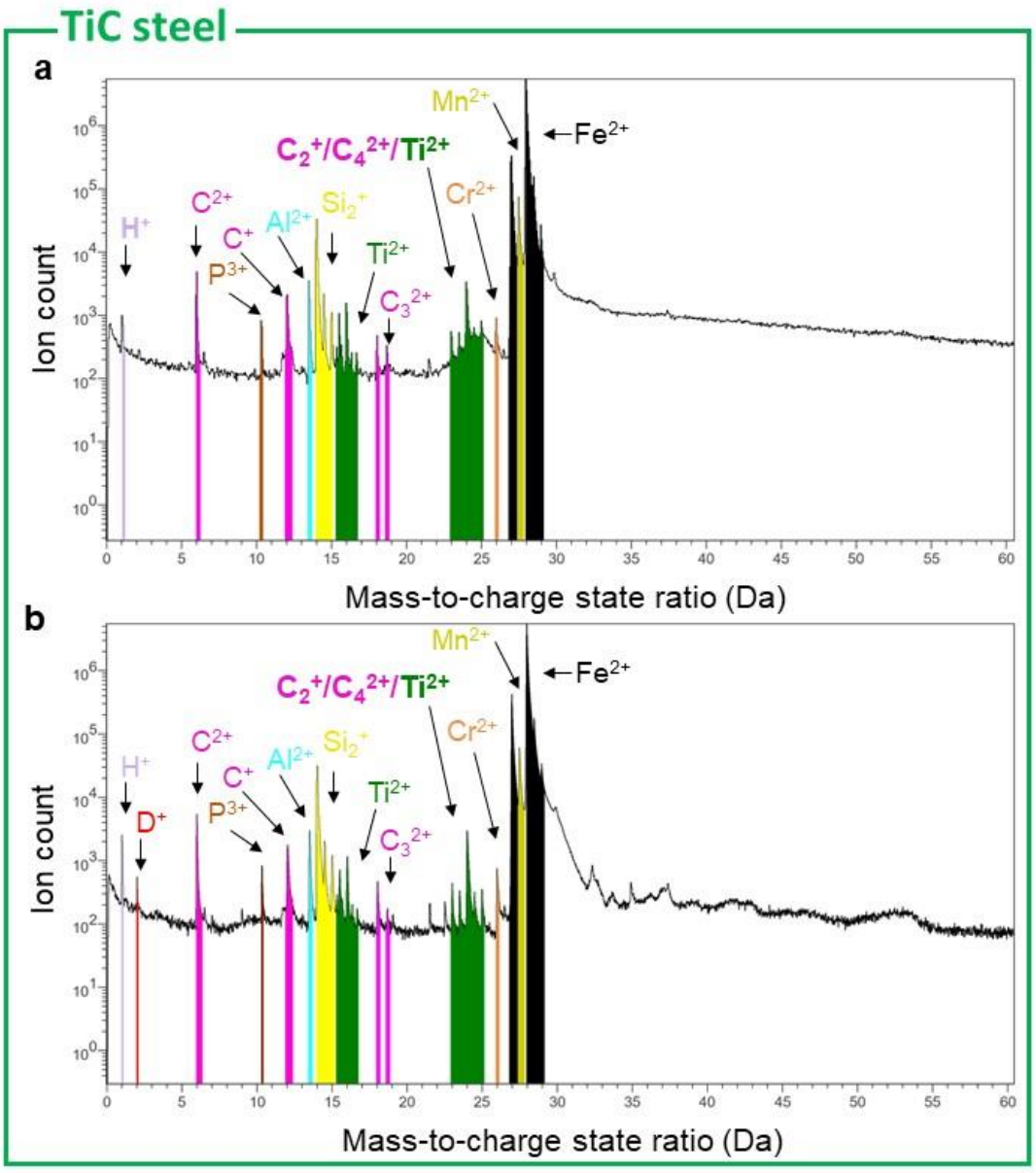

Supplementary Figure 8. APT mass spectra from the (a) uncharged and (b) deuterium-charged TiC steel samples, corresponding to Fig. 4.

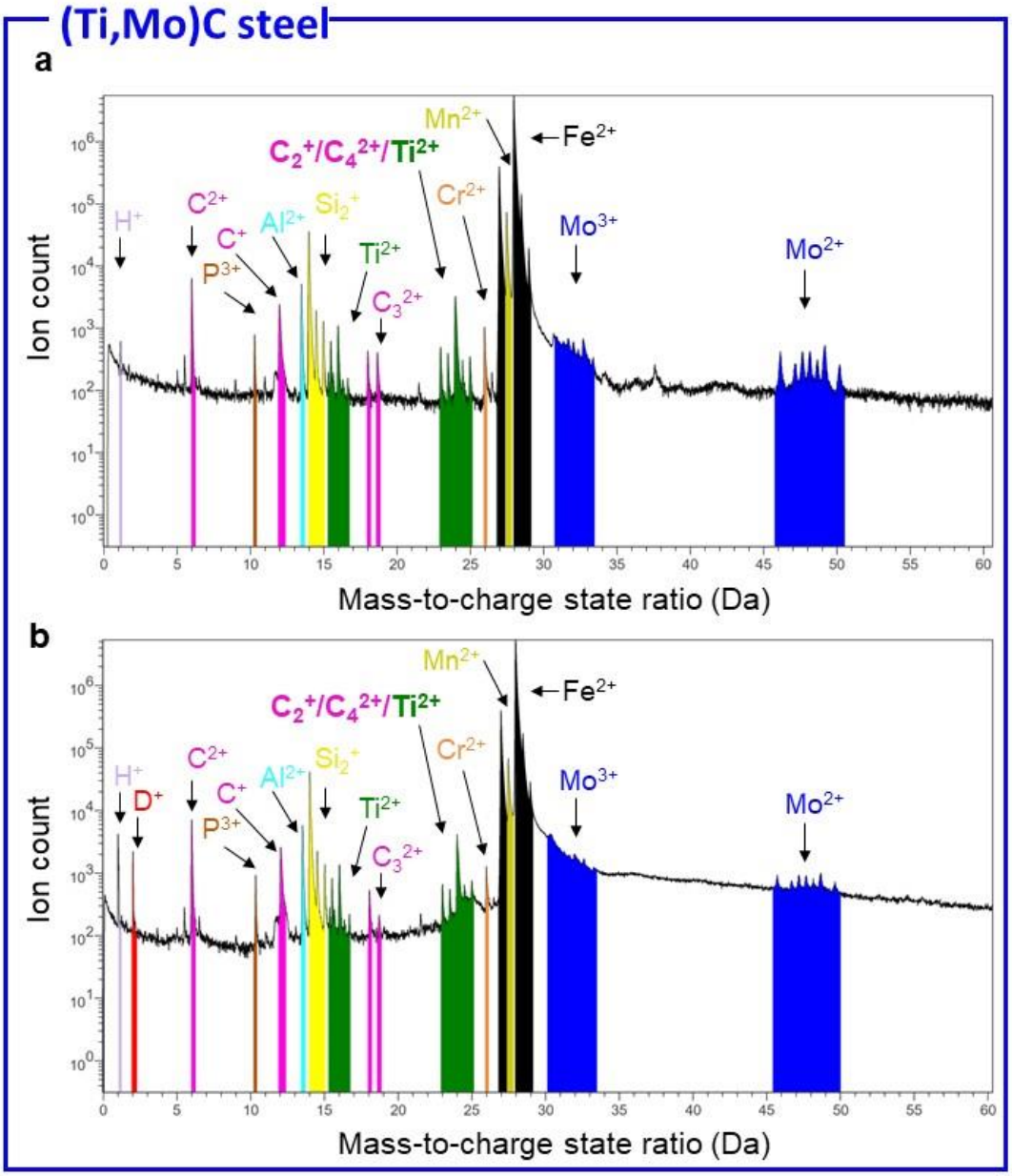

Supplementary Figure 9. APT mass spectra from the (a) uncharged and (b) deuterium-charged (Ti,Mo)C steel samples, corresponding to Fig. 5.

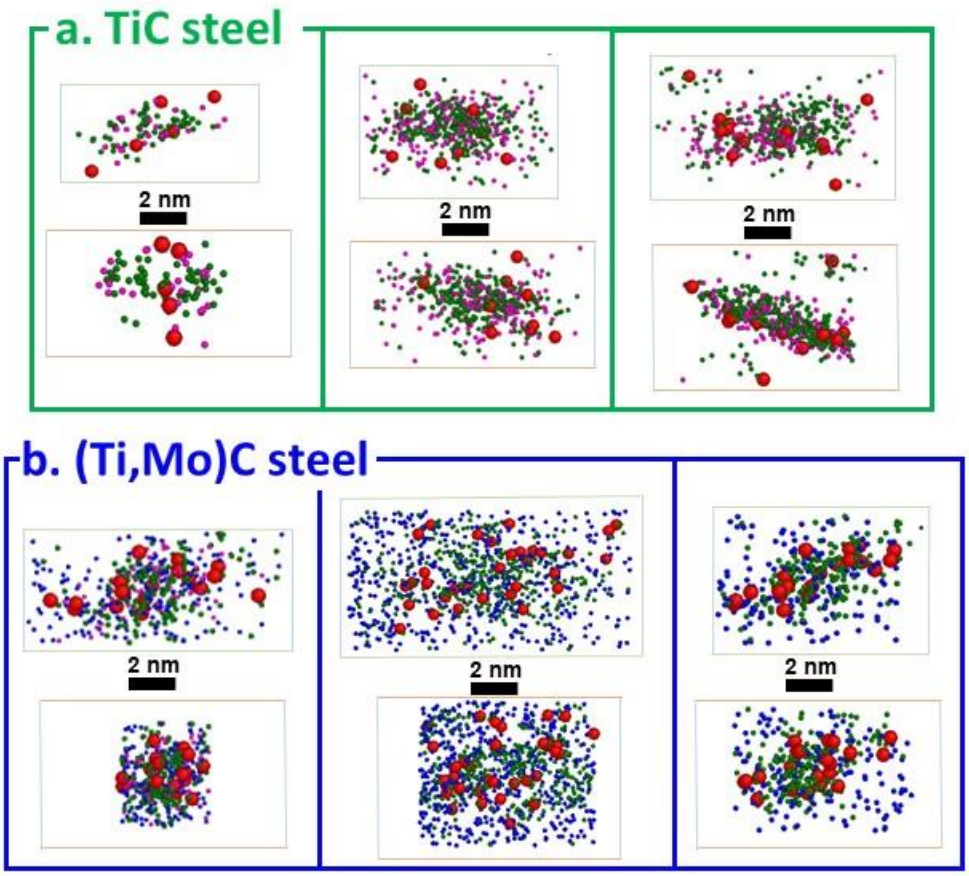

Supplementary Figure 10. Additional atomic views of (a) TiCs and (b) (Ti,Mo)Cs with trapped D atoms (red spheres), corresponding to Figs. 4 and 5, respectively.

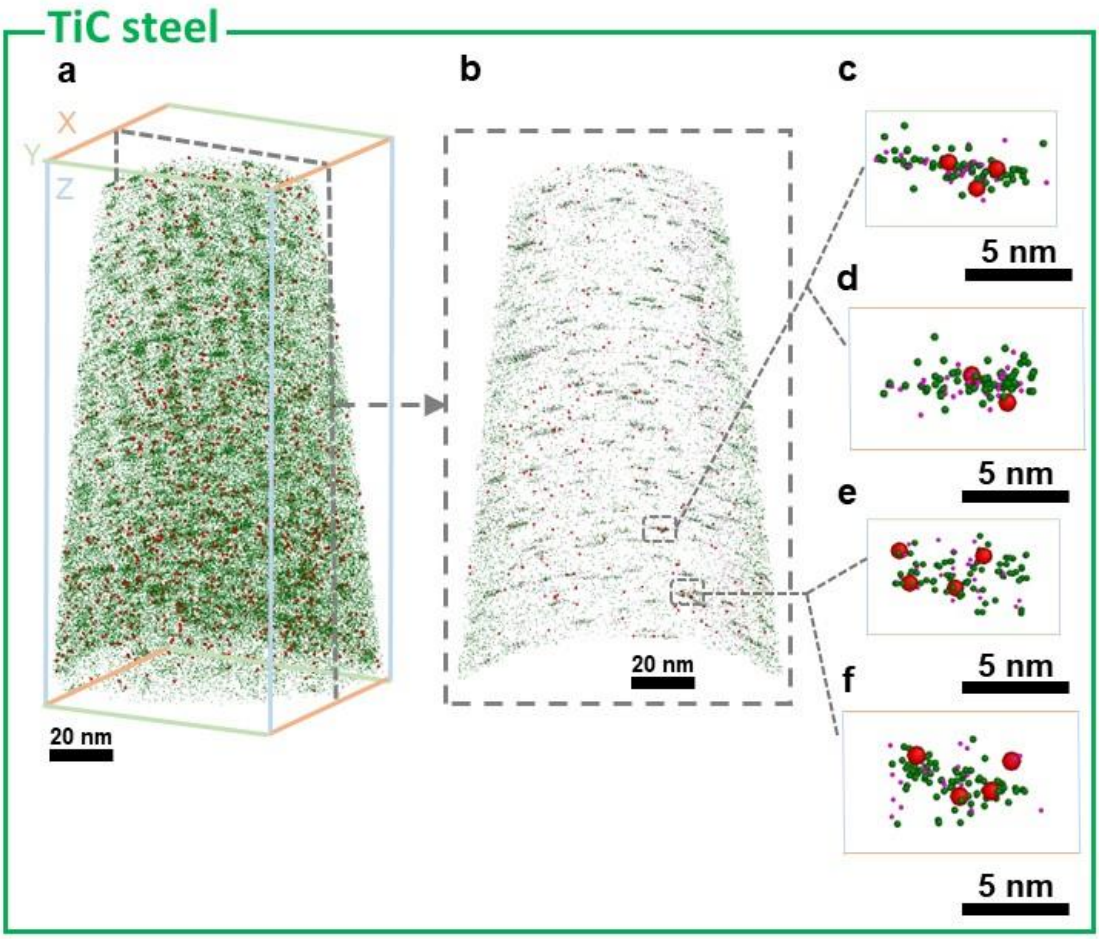

Supplementary Figure 11. Additional APT analysis of D-charged TiC steel using the same condition as the results in Fig. 4.

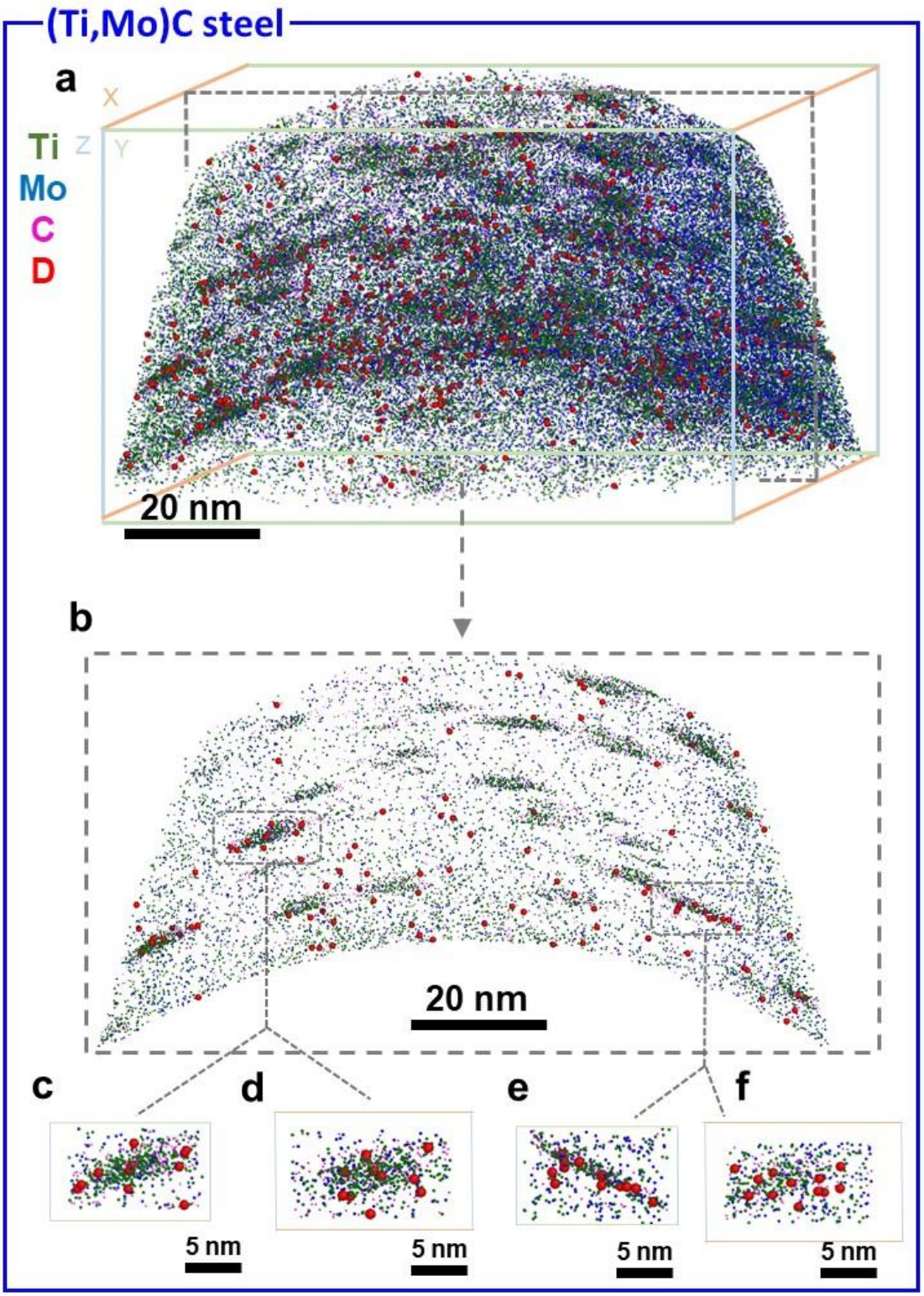

Supplementary Figure 12. Additional APT analysis of D-charged (Ti,Mo)C steel using the same condition as the results in Fig. 5.

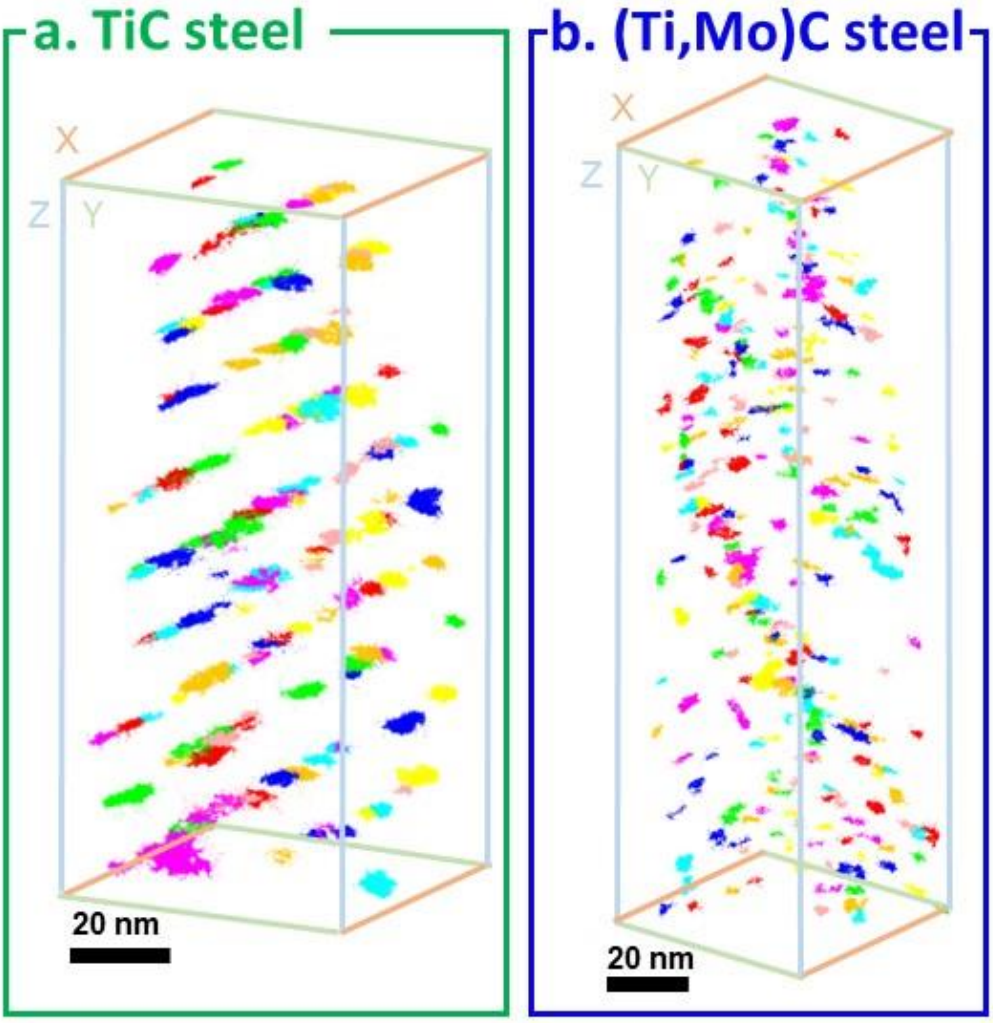

Supplementary Figure 13. Visualizations of the defined clusters in (a) TiC steel and (b) (Ti,Mo)C steel using the Cluster Analysis tool in the APT software.

Supplementary Movie 1. Animated APT data of deuterated TiC steel corresponding to Fig. 4. A 10-nm slice flyover view of the 3-D atom map with deuterium in red, titanium in green, and carbon in magenta.

Supplementary Movie 2. Animated APT data of deuterated (Ti,Mo)C steel corresponding to Fig. 5. b 10-nm slice flyover view of the 3-D atom map with deuterium in red, titanium in green, molybdenum in blue, and carbon in magenta.

Supplementary information for

Chapter 4 - Hydrogen-enhanced deformation in pearlite

Ranming Niu[1,2,7], Hanyu Li[1,2,7], Pang-Yu Liu[1,2,7], Patrick Burr[3], Yi Feng[4], Hung-Wei Yen[5], Mingtu Ma[4], Aimin Guo[6], Hongzhou Lu[6,*], Yi-Sheng Chen[1,2,5,*], Julie M. Cairney[1,2,*]

[1]Australian Centre for Microscopy and Microanalysis, The University of Sydney, Sydney, Australia

[2]School of Aerospace, Mechanical and Mechatronic Engineering, The University of Sydney, Sydney, Australia

[3]School of Mechanical and Manufacturing Engineering, University of New South Wales, Australia

[4]China Automotive Engineering Research Institute Co., Ltd., China

[5]Department of Materials Science and Engineering, National Taiwan University, Taiwan

[6]CITIC Metals Co., Beijing, China

[7]These authors contributed equally to this work: Ranming Niu, Hanyu Li, Pang-Yu Liu.

*Corresponding authors:
julie.cairney@sydey.edu.au (J.M.C.); yi-sheng.chen@sydney.edu.au (Y.S.C.);
luhz@citic.com (H.L.)

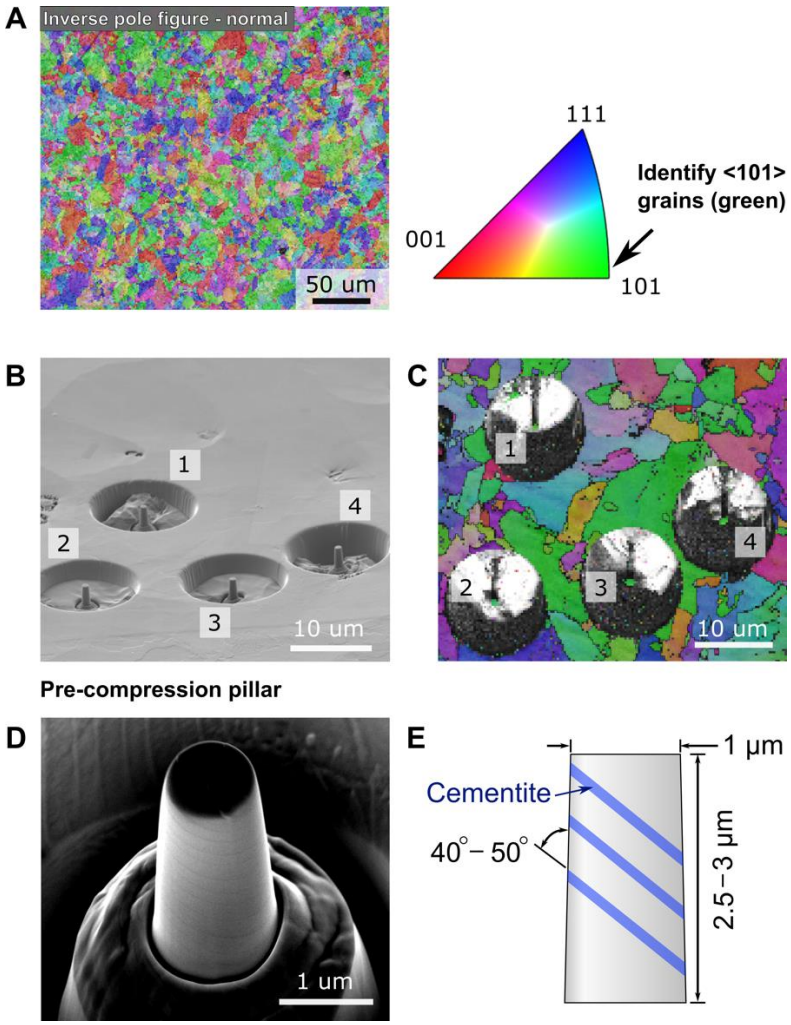

Fig. S1. Micro-compression sample preparation procedure. (A) Grains with normal orientation near <101> were identified with EBSD. (B) FIB trenching and annular milling were undertaken on these grains. (C) The crystalline orientation of the prepared pillars was verified by further EBSD mapping. (D) Pillars with uniformly distributed cementite lamellae with inclination angles between 40 to 50 degrees. (E) Schematic illustration of the desired cementite configuration.

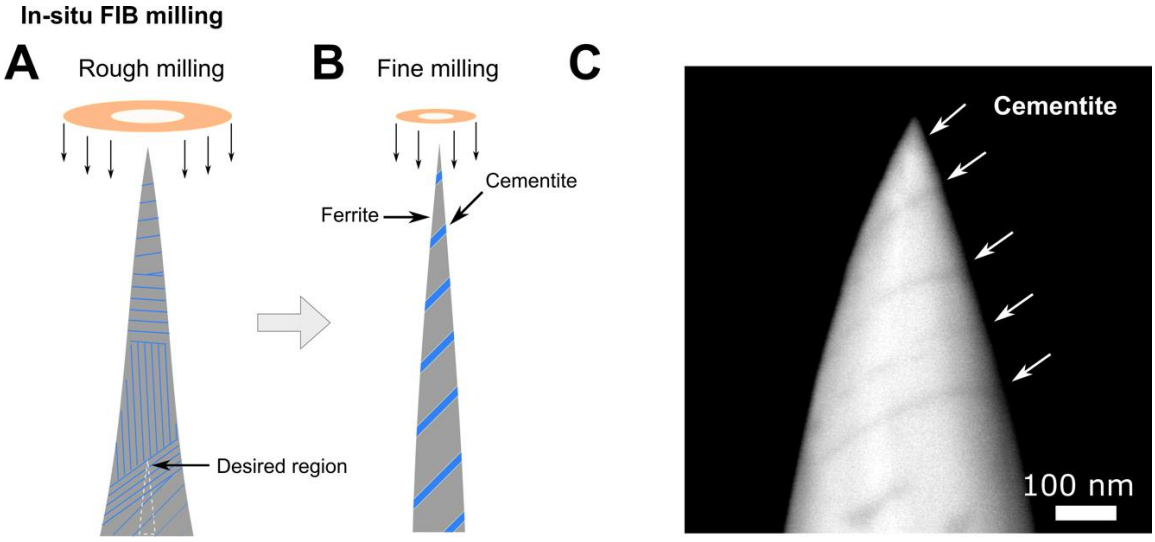

Fig. S2. APT sample preparation. APT tips were prepared by electropolishing followed by in-situ FIB annular milling, locating cementite within the field of view of APT (approximately 200 nm from apex).

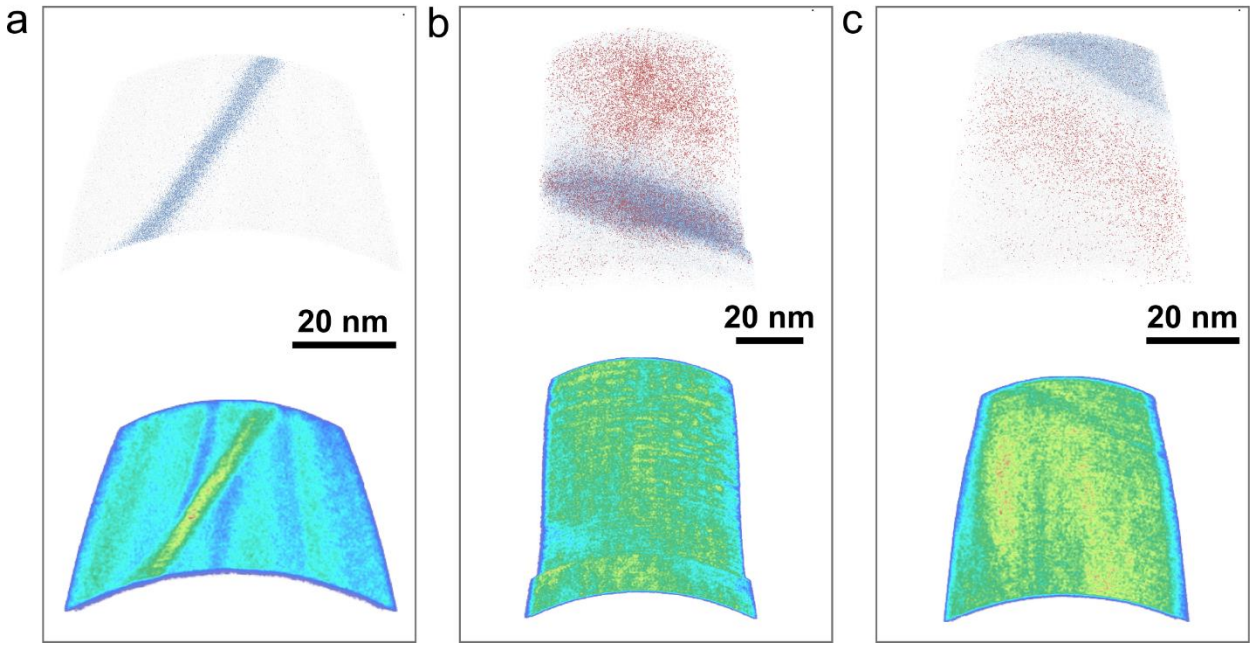

Fig. S3. APT supplementary data – ion-density maps. 2D ion-density maps for APT data presented (A) in Fig.3, (B) and (C) in Fig.6. Maps show that the electric field change between ferrite and cementite was insignificant, which in turns had minor influence on D concentration results.

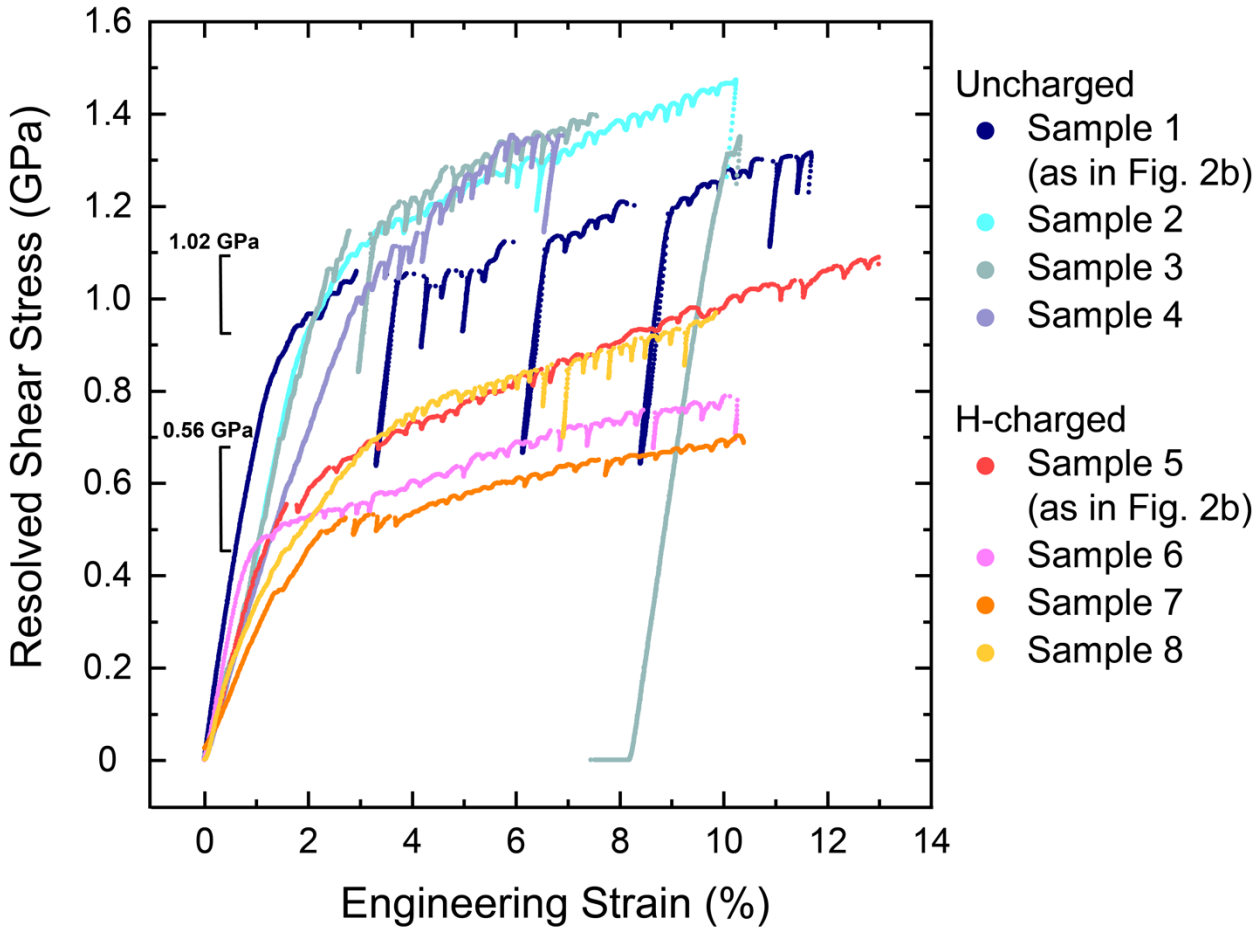

Fig. S4. In-situ micro-compression test supplementary data – engineering shear stress–strain

curves. A lower strength was consistently observed in the hydrogen-charged specimens. The average yield strength values for the uncharged group and the H-charged group were 1.02 GPa and 0.56 GPa, respectively. Uncharged samples commonly show more intermittency in plastic flow than the H-charged ones. The largest strain bursts were observed in sample 3, where a strain burst started at 7% and ends at 10%, spanning across 2% of strain.

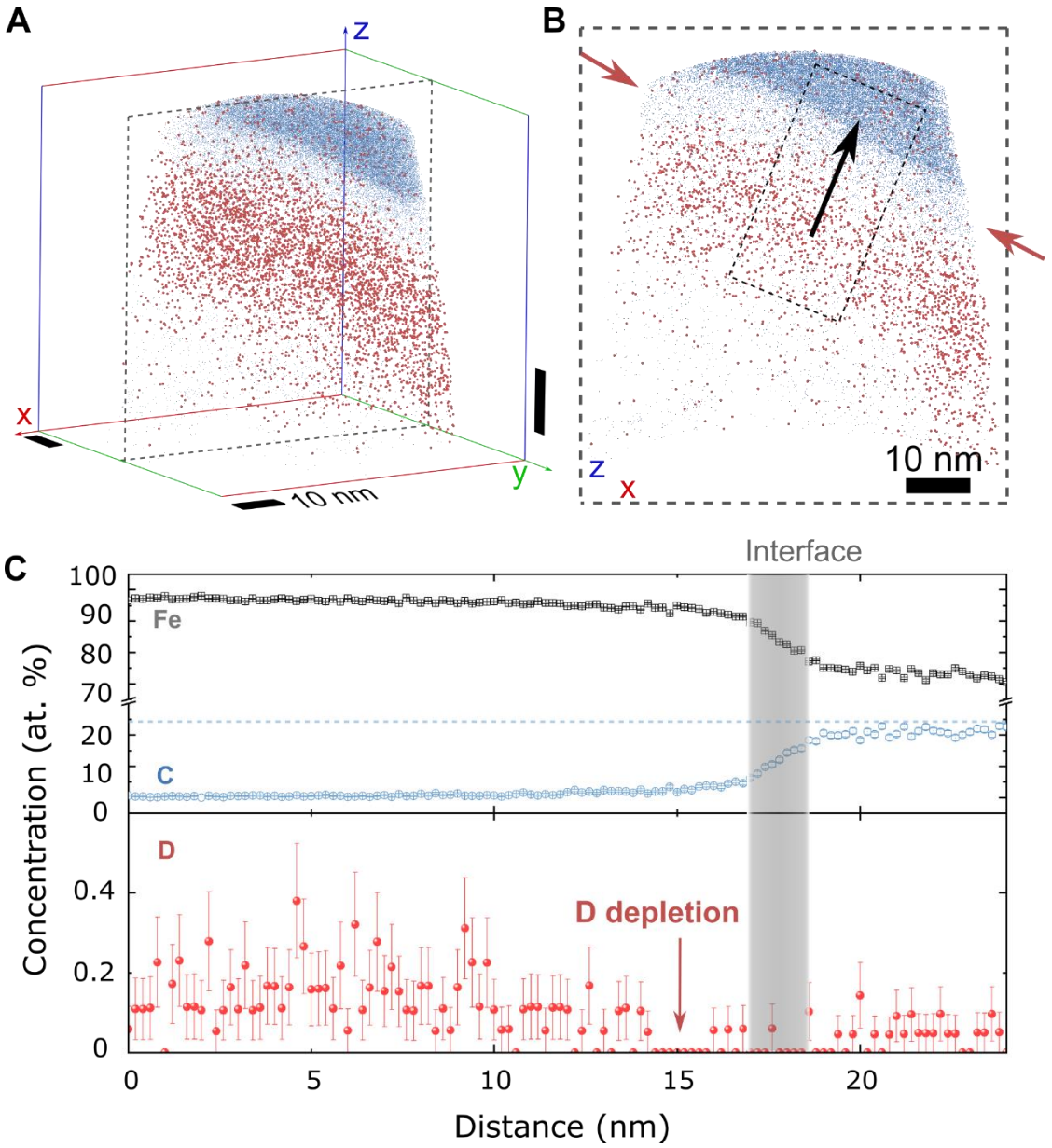

Fig. S5. APT supplementary data *cryo-APT dataset #2*. This dataset captured a part of the cementite at the apex, as shown in the 3-D reconstruction in (A). A depletion zone of hydrogen near the cementite–ferrite interface was observed in both the 2D slice (B) and the 1-D concentration profiles (C) perpendicular to the interface.